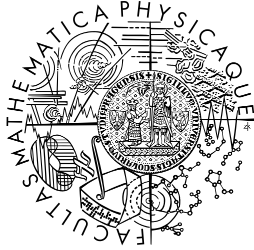

FACULTY OF MATHEMATICS AND PHYSICS
Charles University

MASTER THESIS

Dejan Prokop

Study of optical properties of thin multi-layers based on black metals

Department of Low Temperature Physics

Supervisor of the master thesis: RNDr. Petr Hruška, Ph.D.
Study programme: Physics
Study branch: Physics of Condensed Matter and Materials

Prague 2024

I declare that I carried out this master thesis independently, and only with the cited sources, literature and other professional sources. It has not been used to obtain another or the same degree.

I understand that my work relates to the rights and obligations under the Act No. 121/2000 Sb., the Copyright Act, as amended, in particular the fact that the Charles University has the right to conclude a license agreement on the use of this work as a school work pursuant to Section 60 subsection 1 of the Copyright Act.

In .... date ....

Author's signature

First and foremost, I would like to thank my supervisor RNDr. Petr Hruška, Ph.D., for his guidance, dedicated time, and genuinely kind and inspiring personal attitude, which has been a constant source of motivation in my physics studies.

My acknowledgment extends to all those without whom this work could not have been successfully completed in its current form and everyone who participated in a cooperation project EstAV-21-08 from the Czech Academy of Sciences (CAS) and Czech Science Foundation (GAČR) No. 23-05002S.

My colleagues from the Institute of Physics of the CAS for creating a friendly and heartwarming work environment, namely:
To my consultant Joris More-Chevalier, Ph.D., for his assistance during depositions, advices, and insightful discussions.
To Ing. Michal Novotný, Ph.D., for his helpful approach in solving various problems that I encountered.
To Ing. Jiří Bulíř, Ph.D., for his help with the ellipsometry measurements.
To RNDr. Ladislav Fekete, Ph.D., for his help with the AFM measurements.
To Ing. Jan Drahokoupil, Ph.D. and RNDr. František Lukáč, Ph.D., from the Institute of Plasma Physics, for their help with the XRD data interpretation.
People from the Faculty of Mathematics and Physics, Charles University:
To Prof. RNDr. Jan Valenta, Ph.D., for providing the instrumental equipment for diffuse reflectance measurements.
To the collective of the Department of Macromolecular Physics for their valuable and interesting lectures and for granting me access to their SEM.
To Prof. Mgr. Jakub Čížek, Ph.D., for introducing me into the topic of positron annihilation spectroscopy.
People from the University of Tartu, Estonia, for their assistance during PL and thermally treated SEM measurements, particularly to Prof. Raivo Jaaniso, Prof. Valter Kiisk, and Elyad Damerchi.
To Siim, Taavi, Martin, Honza and Jarda for making our stay in Estonia an enjoyable and memorable experience full of fun.

A big thanks goes to all my friends, particularly those in Galanta. Even though I moved far away to Prague, you never forgot about me, and every time I returned to my hometown, you welcomed me with open arms and warm hearts. Also, I sincerely thank my 'brother-from-another-mother' Aďo, as well as Sára and Kika, who spent the most time in Prague with me - maybe sometimes more than they would have liked.

And most importantly, I would like to express my deepest gratitude to my family who provided me with unwavering love and support throughout my Master's studies, allowing me to fulfill my dreams.

I would like to dedicate this thesis to my grandmother, who passed away during my Master's studies, as an honour to her memory. She supported me through my studies and encouraged me to finish all my responsibilities whenever I felt like I can not do it and also taught me to be a responsible and reliable man. I believe that if she were here today, she would be proud of the person I have become.

Title: Study of optical properties of thin multi-layers based on black metals

Author: Dejan Prokop

Department: Department of Low Temperature Physics

Supervisor: RNDr. Petr Hruška, Ph.D., Department of Low Temperature Physics

Abstract: Thin films of black metals are characterized by their excessively rough, porous, fractal-like nanostructured surface, capable of strong light absorption. In this thesis, thin films of black aluminium and titanium were prepared using pulsed DC magnetron sputtering in a reactive nitrogen and argon mixture. The structural and optical properties were determined by XRD and diffuse reflectance measurements, while their morphology, thermal stability, and chemical composition were investigated by AFM, SEM, and EDX. Thermochromic materials based on transition metal oxides can change their optical with temperature. WO_3 and phosphorus-doped WO_3 films were deposited by PLD at various substrate temperatures and oxygen deposition pressures. The best reversible thermochromic response, characterized by temperature-dependent optical transmittance and spectroscopic ellipsometry measurements up to 500°C, was observed for a WO_3 film exhibiting a tetragonal crystal structure and a band gap shifting from 2.7 eV to 2.4 eV. Based on our findings, we tested a new heterostructured multi-layer appropriately combining a black metal with a thermochromic material, potentially improving its thermochromic response to light absorption and its subsequent conversion into heat. This combination might be utilized for the development of efficient self-controlled smart absorbers. Furthermore, it has been shown that black Al enhanced the photoluminescence of europium-doped ZnO films.

Keywords: thin films, black metals, thermochromic films, multi-layers

Contents

Introduction **3**

1 Physics of thin films **7**
1.1 Definition and classification 7
1.2 Optical properties of thin films 8
1.3 Chromogenism and thermochromism 14

2 Preparation of thin films **17**
2.1 Overview of deposition techniques 17
2.2 Magnetron sputtering 19
2.2.1 Our MS system 23
2.3 Pulsed laser deposition 28
2.3.1 Our PLD system 30

3 Experimental techniques **34**
3.1 Morphological properties 34
3.1.1 Profilometry 35
3.1.2 Atomic force microscopy 36
3.1.3 Scanning electron microscopy 39
3.2 X-ray diffraction 44
3.3 Optical measurements 54
3.3.1 Ellipsometry 61
3.3.2 Photoluminiscence 64

4 Results and discussion **66**
4.1 Prepared samples 66
4.1.1 R-Al and B-Al series 66
4.1.2 R-Ti and B-Ti series 69
4.1.3 WO_3 and WO_3:P series 73
4.1.4 Multilayered films 77
4.2 Morphology of R-Al and B-Al films 78
4.3 XRD results of R-Al and B-Al films 87
4.4 Reflectance of B-Al films 92
4.5 Morphology of R-Ti and B-Ti films 93
4.6 XRD results of R-Ti and B-Ti films 96
4.7 Reflectance of B-Ti films 99
4.8 Morphology of WO_3 and WO_3:P films 100
4.9 XRD results of WO_3 and WO_3:P films 106
4.10 Transmittance of WO_3 and WO_3:P films 110
4.10.1 Transmittance calibration measurements 113
4.10.2 Temperature-dependent transmittance 116
4.11 Photoluminescence of ZnO:Eu@B-Al films 120
4.12 Ellipsometry results 122

Conclusion **127**

Bibliography **128**

List of Figures **140**

List of Tables **144**

List of Abbreviations **146**

Introduction

Black metals (BMs) represent a wide class of materials characterized by a highly developed porous fractal-like rough surface structure, often referred to as moth-like or cauliflower-like, which exhibit reduced reflectivity. The complex broadband plasmonic interaction of electromagnetic radiation[1][2] via localized surface plasmon resonance (LSPR), combined with the trapping of incident light in multiple reflections that leads to its subsequent absorption within their nano- and microstructured surface[3], can be responsible for their black appearance. Their unique light-absorbing capabilities, while still maintaining metallic conductivity, make them a great basis for exceptionally efficient light absorbers throughout the VIS and NIR region and energy converters for solar cells[4]. Addditionaly, a large surface-to-volume ratio provides enough bonding sites for gas molecules, which can be used for electrochemical gas sensing and catalysis[5].

Historically, the first attempts to create black films stemmed from the need to develop suitable materials close to an ideal black body, capable of absorbing incoming light over a wide range of wavelengths, predominantly infrared and radio waves, for the construction of detectors and filters, but also experimentally to confirm Planck's distribution function for black body radiation[6]. In 1930, A. H. Pfund observed that thermally evaporated (TE) bismuth at an appropriate pressure of inert gas ($\sim$ 30 Pa) formed a very dark layer, reflecting only about 1 % of incident light in the infrared region[7], in contrast to the reflective film produced by TE under high vacuum conditions. In the following years, several other BMs were prepared in the similar way, including zinc, selenium[8], antimony[9], platinum[10], aluminium[11], silver, and gold[12]. In particular, substantial attention was paid to the research of gold deposits in numerous works by Harris et al.[13][14]. The proposed mechanism for films prepared by TE suggests that the evaporated source atoms are slowed down by collisions with inert ambient gas atoms at higher pressure due to the shorter mean free path of the collisions, leading to the formation of atomic clusters. Consequently, these clusters impact the substrate with much lower energy, resulting in limited mobility. This further prevents surface migration to more energetically favourable locations, giving rise to the nanoporous columnar growth of the layer.

On the other hand, aluminium possesses several favourable properties compared to gold, such as good wear resistance, adhesion, thermal stability as well as low cost for potential industrial utilization. In 2014, Goldsmith et al. demonstrated improvements in the pyroelectric response of black aluminium (B-Al), suggesting its applications for broadband pyroelectric thermal detectors[15]. Numerous deposition methods for B-Al preparation have been reported, including electrodeposition[1], femtosecond laser surface modification[16], and metal deposition on nanostructured dielectric substrates[17]. However, DC magnetron sputtering (MS) has proven itself to be a reliable technique, allowing for easy tuning of the film's structure by simply modifying the deposition parameters, with good reproducibility (patented by our group at the Institute of Physics of the Czech Academy of Sciences[18]). Like many revolutionary discoveries in the history of science, this finding was unintentional and attracted immediate public attention[19]. Later, equivalent films were successfully prepared by RF

magnetron sputtering with liquid nitrogen cooling (at -170°C) of a substrate holder by the group of Prof. Kawamura at the Kitami Institute of Technology (Hokkaido, Japan)[20].

Despite aluminum being a highly reflective metal, it has been found that introducing an appropriate amount of nitrogen during MS deposition results in a different growth process than for TE[20], leading to the formation of anti-reflective polycrystalline black deposits. The variation in the nitrogen-to-argon ratio shown an optimal percentage of 6 % for the growth of the blackest films, with reflectivity lower than 4 % in UV-VIS-NIR spectral range[21]. Besides, this work provides a detailed description of the growth mechanism, where reflective films tend to follow a V-shaped growth, while black films follow the Stranski-Krastanow growth mode. The morphological, structural, optical and electrical properties of reflective and black Al were investigated for films thinner than 700 nm [22][23] and for films thicker than 1 μm, where it was found that roughness, mean grain, and crystalline size increase as a function of thickness. Positron annihilation spectroscopy revealed that these films contain nanoscopic pores with an average size of 4-6 Å[24]. The thermal stability of B-Al was studied by scanning electron microscopy (SEM) and photothermally stimulated exoelectron emission (PTSE) spectroscopy up to 400°C[25], which confirmed the good thermal stability of the intact films and identified the formation of nanowires from damaged parts. Regarding practical applications, our B-Al film were utilized to improve energy conversion from a light source to an electrical current using the pyroelectric effect[26], which requires temporal temperature oscillations. Recently, we also used B-Al as a basis for quartz crystal microbalance (QCM) sensors, where resolution was shown to be improved by increasing the effective surface of the QCM electrodes, which provided more bonding sites for gas analysis[27].

Inspired by these achievements, we aim to reproduce these results for another material - black titanium (B-Ti). However, due to the high chemical reactivity of Ti, it tends to readily form oxides (TiO_2), nitrides (TiN), oxy-nitrides (TiN_xO_y) and carbides (TiC). Still, Ti and Ti-based thin films have several attractive attributes over Al, such as high mechanical strength, good infrared reflectance and electrical conductivity, outstanding thermal stability, good corrosion resistance, and biocompatibility. Specifically, it stands out as one of the most thoroughly studied thin films, which is stable within a wide composition range ($N/Ti \in (0.6, 1.2)$)[28] and has gold-like reflective properties. It finds wide-ranging applications as a hard coating for cutting tools, decorative coatings for jewellery, anti-corrosive coatings in aerospace industries, and electrical devices[29].

Both conventional pure Ti thin and Ti-based films are preferentially prepared under ultra-high vacuum conditions by various physical vapour deposition (PVD) techniques, primarily MS[30]. However, the high melting temperature of titanium and its tendency to react with melting boats pose challenges to successful film preparation by TE. Supposedly, MS would serve as a suitable method for the preparation of B-Ti with a decreased reflectivity. Fabrications of B-Ti films was successfully demonstrated using ultra-fast pico-[31] and femtosecond[32] laser-assisted texturing. Another promising approach involves utilizing a magnetron-based Haberland-type gas aggregation source[33] to produce titanium nanoparticles[34][35] taking advantage of the LSPR phenomenon. Alternatively, glancing angle deposition (GLAD) presents another viable option

for creating columnar nanostructured morphologies, which enhance the properties of light absorption[36].

Thermochromism is a property of a substance to change colour with a variation in temperature. Transition metal oxides represent a naturally abundant, environmentally friendly, and non-toxic materials that often possess this quality. In recent years, an indirect semiconductor tungsten trioxide (WO_3) is of great interest, as it is being extensively investigated due to its outstanding electrochromic, photochromic, sensing and photocatalytic capabilities, making it a promising material for many scientific and technological applications, particularly for smart windows[37], gas sensors[38], UV detectors[39], and water splitting[40]. WO_3-based nanomaterials have been prepared by a variety of PVD techniques, including TE[41], MS[42] and PLD[43], among others. The last mentioned offers an interesting possibility to tune the optoelectronic properties of WO_3 films by a simple change of oxygen pressure during deposition. Simultaneously, its colour can be altered from dark blue to colourless, with corresponding band gap ranging from 2.6 to 3.3 eV.

Improvements in the tuning of the chromic properties of transition metal oxides were achieved with the help of an appropriate chemical dopant[44][45]. To the best of our knowledge, no results have been published yet on the thermochromic properties of phosporus-doped WO_3. However, the addition of this dopant has already demonstrated enhanced electrochromic performance[46] and has been proposed as an excellent method to improve the energy conversion efficiency of water splitting[47]. Phosphorus acts as a critical factor responsible for this by inducing O^{2-} vacancies that are partially substituted by P^{3-} ions[48]. For crystallised structure at elevated temperatures, this replacement leading to modification of the band gap should be more pronounced, and so the thermochromic effect should be larger. In addition, many efforts have been made to improve the thermochromic properties of smart coatings based on transition metal oxides by designing multilayered structures often involving an antireflective buffer layer[44]. We assume that using an appropriate combination of BM together with a thermochromic film could result in the enhancement and overall efficiency improvement of the thermochromic material.

Zinc oxide (ZnO) is a well-known semiconductor with a wide direct band gap of approximately 3.37 eV with a wurtzite structure at ambient conditions, possessing favourable properties for optoelectronic devices such as UV lasers and photodetectors[49]. Due to their high electron mobility, good electrical conductivity, and transparency to visible light, they have found applications as transparent conductive oxides (TCOs) used in optical coatings for solar cells[50] and flat panel displays[51]. Besides that, it also exhibits piezoelectricity and strong luminescence.

The effect of doping it with rare earth (RE) ions was investigated excessively since it introduces new energy levels in the band gap, allowing their stimulation and subsequent emission of light at a wide range of wavelengths in the VIS region. There were numerous techniques for the preparation of RE-doped ZnO thin films by both physical and chemical deposition[52][53] with different morphologies and band gap values. In particular, pulsed laser deposition (PLD) proved to be useful for high-quality ZnO films doped with trivalent ions of Eu (Eu^{3+})[54] with good reproducibility and the ability to modify the final properties by a simple change

of the deposition parameters. The photoluminescence intensity of the emission lines is sensitive to the local environment and the symmetry of the Eu^{3+} atom sites as well as to the concentration of defects. The effect of elevated substrate temperature during deposition[54] led to quenching of the luminescence, while laser treatment[55][56] with higher laser fluencies showed enhancement of luminescence. It is assumed that the high surface-to-volume ratio of BM could be favourable for enhancing the photoluminescence of these films, making it useful for various optoelectronic devices, such as photoluminescence-based optical sensors.

This work builds on my previous bachelor's thesis[23], where an intensive explanation of morphological, optical, and structural properties was provided as a function of film thickness for both reflective and black aluminium films. However, these properties were only studied for fused silica substrates at room temperature and the influence of depositing on a crystalline substrate has not yet been reported. We aim to expand the knowledge about the B-Al by the implementation of novel characterization techniques.

The main objectives of this thesis can be formulated as follows:

1. Reproduction of B-Al films on various substrates and subsequent characterization of their optical diffuse reflectance, thermal stability and chemical composition.

2. Successful preparation of B-Ti films by MS and the describing the correlation between deposition parameters and their morphological, structural and optical properties

3. Deposition of WO_3 and P-doped WO_3 films by PLD and evaluating their thermochromic properties by means of temperature-dependent optical measurements.

4. Fabrication of multi-layered structures consisting of BM as a basis with thermochromic or photoluminescent oxide film and assessing its impact on these properties.

Optical diffuse reflectance measurements using an integrating sphere were conducted at the Department of Chemical Physics and Optics, while scanning electron microscopy at RT were carried out at the Department of Macromolecular Physics, both within the Faculty of Mathematics and Physics at Charles University in Prague, Czech Republic. Scanning electron microscopy of thermally treated samples and photoluminescence experiments were performed within collaboration with the University of Tartu, Estonia. The film depositions as well as atomic force microscopy, X-ray diffraction, spectroscopic transmittance and ellipsometry measurements were done at the Institute of Physics of the Czech Academy of Sciences in Prague, Czech Republic.

1. Physics of thin films

In this section, we introduce the basic terminology concerning thin films and provide a theoretical explanation of fundamental optical parameters, highlighting their connection to observable quantities. Additional optical phenomena, including luminescence and ellipsometric measurements, will be discussed in Chapter 3.

1.1 Definition and classification

The term "thin films" refers to a small layer of material that is more or less uniformly distributed along the surface of another material. There is no strict definition that establishes the exact range of thicknesses for which a layer is considered thin. Generally, a film is regarded as thin when its thickness ranges from a few nanometres to several tens of micrometres. They are used to improve the surface properties of solid bulk materials, depending on a specific application, including mechanical (e.g. density, adhesion, corrosion resistance), microstructural (roughness, porosity), tribological (hardness, presence of instrinsic stress), optical (reflectivity, absorption, transparency), electrical (resistivity, charge carrier mobility), or magnetic (domain structure and magnetization) properties.

In regions where local fluctuations in atomic density allow the formation of stable nuclei, triggered by a phase transition, in which atoms organise into larger clusters, grains are formed in a process known as nucleation. Based on the structure and size of surface grains, thin films can be divided into three basic groups:

- *Amorphous films*, which do not exhibit a crystal structure, and the atoms have so-called short-range spatial order.
- *Nanocrystalline films* possess a crystal structure, characterized by a periodically repeating long-range spatial order of atoms, with an average grain size ranging from a few nanometers to tens of nanometers.
- *Polycrystalline films* also have a crystalline structure, but in this case, the average grain size is larger and can reach several micrometers.

The structure can be influenced by the presence of defects and/or residual stresses that are induced either thermally (due to different thermal expansion coefficients) or during the growth (caused by interface strain in grain boundaries, different composition, or phase transformation), resulting in a mismatch between the lattice parameter of the film and material. These stresses may be tensile or compressive, and can be released by mechanical deformation such as cracking, buckling, or delamination.

Epitaxial films represent single-crystal thin layers grown on a crystalline material to precisely replicate its crystal structure and orientation. If the film and substrate are of the same material, it is termed a homoepitaxial layer, otherwise it is a heteroepitaxial layer. A multi-layer is composed of multiple thin films placed on top of each other. The arrangement of individual films can be periodically repeated in a regular pattern (such as alternating sandwich multi-layers), gradually transition from one layer to another over a finite distance (so-called gradient multi-layers), or have a completely random structure.

1.2 Optical properties of thin films

An essential quantity describing the propagation of light through a material is the refractive index n given as the ratio of the speed v at which light travels within the material and the speed of light in vacuum c, thus $n = \frac{v}{c}$. It is a function of the light's wavelength $\lambda = \frac{v}{f}$, where f is the frequency of the wave, and this dependence $n = n(\lambda)$ is called a dispersion relation. When light passes from a medium with refractive index n_1 at incidence angle θ_i through a material with refractive index n_2, then some fraction of the light is reflected at the same angle and the rest enters the material at the angle θ_t related by Snell's law $n_1 \sin\theta_i = n_2 \sin\theta_t$. After entering the material, the wave is attenuated due to absorption according to Lambert-Beer law:

$$I = I_0 e^{-\alpha d} \tag{1.1}$$

where I and I_0 are the intensities of transmitted and incident light, respectively, α is the absorption coefficient and d is the optical path length. The rest of the light is transmitted through a sample. More generally, the refractive index is a complex number $\tilde{n} = n + ik$ with the real part n and the imaginary part k[1] representing the extinction coefficient, directly related to absorption coefficient α.

This process can be described by the introduction of complex Fresnel coefficients r and t, representing the ratio between the electric intensities amplitude of reflected and transmitted wave, respectively, to that of the incident wave. If we follow the notation provided in[58] then the Fresnel equation for both $S-$ and P-polarization[2] can be expressed as:

$$r_s = \frac{n_1 \cos\theta_i - n_2 \cos\theta_t}{n_1 \cos\theta_i + n_2 \cos\theta_t} \qquad r_p = \frac{n_2 \cos\theta_i - n_1 \cos\theta_t}{n_2 \cos\theta_i + n_1 \cos\theta_t} \tag{1.2}$$

$$t_s = \frac{2n_1 \cos\theta_i}{n_1 \cos\theta_i + n_2 \cos\theta_t} \qquad t_p = \frac{2n_1 \cos\theta_i}{n_2 \cos\theta_i + n_1 \cos\theta_t} \tag{1.3}$$

Finally from these coefficients, we can express the observable quantities - reflectance R and transmittance T as:

$$R_{s,p} = r_{s,p}\overline{r_{s,p}} \tag{1.4}$$

$$T_{s,p} = \frac{n_2 \cos\theta_t}{n_1 \cos\theta_i} t_{s,p}\overline{t_{s,p}} \tag{1.5}$$

where the overline denotes a complex conjugate. Once we know these quantities, we can proceed to obtain $n(\lambda)$ and $k(\lambda)$. In the special case of normal incidence ($\theta_i = \theta_t = 0°$) and the light coming from air ($n_1 \doteq 1$, $n_2 =$ n) the equations are further simplified to:

$$R_s = R_p = \frac{(1-n)^2 + k^2}{(1+n)^2 + k^2} \qquad T_s = T_p = \frac{4n}{(1+n)^2 + k^2} \tag{1.6}$$

[1]Both n and k are connected by Kramers-Kronig relations[57].

[2]The terms S- and P-polarization refer to the directions of electric field polarization perpendicular and parallel to the plane of incidence, respectively.

Which e.g. for glass in the visible light yields values $R \sim 0.04$ and $T \sim 0.96.$, meaning that only 4 % of light is reflected from the surface and the rest is passing through. For reasonably thick metallic samples (typically highly reflective), the amount of transmitted light is usually negligible so it makes sense to measure their reflectivity. On the other hand, dielectric oxide films are usually fairly transparent even for greater thicknesses, therefore most experiments are measurements of the measurements, which can also be combined with the reflectance measurements.

When incident light reaches a material composed of two or more plane-parallel thin films, the reflected and transmitted waves interfere with each other, resulting in transmittance and reflectance being dependent on the wavelength of light. For simplicity, we shall consider only a single layer with refractive index n_2 of thickness d surrounded by a medium with refractive index n_1. However, more generalized calculations can be performed for a substrate-film system[59] and multi-layered structures employing the transfer-matrix method[60]. Let us assume that a monochromatic plane wave with a wavevector $\vec{k} = \frac{2\pi}{\lambda}\vec{e}_k$, where $\vec{e}_k$ is a unit vector in the direction of propagation, is incident on a thin film surface at an angle θ_i (see Fig. 1.1), then we can express its electric field component as:

$$\vec{E}(\vec{r}, t) = \vec{E_0} e^{-i(\vec{k}\cdot\vec{r} - \omega t)} \tag{1.7}$$

where $\omega = 2\pi f$ is the angular frequency and $\vec{E_0}$ is the amplitude of the wave. Since we are investigating interference at any arbitrary point in space, we can omit the term $\vec{k} \cdot \vec{r}$ and consider the amplitude to be a scalar. The air-sample interface is characterized by Fresnel coefficients r and t. After the first refraction, the wave passes through the sample and can be repeatedly reflected on the bottom and top surfaces of the film. Each successive wave undergoes two additional reflections compared to the previous wave and gains a phase difference φ:

$$\varphi = \frac{4\pi}{\lambda} nd \cos\theta_t \tag{1.8}$$

We can express the varying amplitude E_j^T for each transmitted wave as (similarly for reflected waves E_i^R):

$$\begin{aligned}
E_1^T &= E_0 t_{12} t_{21} e^{i\omega t} \\
E_2^T &= E_0 t_{12} r_{21} r_{12} t_{21} e^{i(\omega t + \varphi)} \\
E_3^T &= E_0 t_{12} (r_{21} r_{12})^2 t_{21} e^{i(\omega t + 2\varphi)} \\
&\vdots \\
E_j^T &= E_0 t_{12} (r_{21} r_{12})^{j-1} t_{21} e^{i(\omega t + (j-1)\varphi)} \\
&\vdots
\end{aligned} \tag{1.9}$$

The final amplitude E^T of the transmitted wave is given as the superposition of each wave:

$$\begin{aligned} E^T = \sum_{j=1}^{\infty} E_j^T &= E_0 t_{12} t_{21} e^{i\omega t} \sum_{j=1}^{\infty} (r_{21} r_{12})^{j-1} e^{i(j-1)\varphi} \\ &= E_0 t_{12} t_{21} e^{i\omega t} \sum_{k=0}^{\infty} \left(r_{21} r_{12} e^{i\varphi} \right)^k \\ &= E_0 t_{12} t_{21} e^{i\omega t} \frac{1}{1 - r_{21} r_{12} e^{i\varphi}} \end{aligned} \tag{1.10}$$

Where in the last step we evaluated this sum, knowing that it corresponds to the geometric series with a common ratio $q = r_{21} r_{12} e^{i\varphi} < 1$ and the first term $a_0 = 1$. The measured intensity of the transmitted wave I_t is given by the product of the amplitude E^T and its complex conjugate $\overline{E^T}$:

$$\begin{aligned} I_t = \overline{E^T} E^T &= \frac{E_0 t_{12} t_{21} e^{-i\omega t}}{1 - r_{21} r_{12} e^{-i\varphi}} \cdot \frac{E_0 t_{12} t_{21} e^{i\omega t}}{1 - r_{21} r_{12} e^{i\varphi}} \\ &= \frac{E_0^2 (t_{12} t_{21})^2}{1 - r_{21} r_{12} e^{i\varphi} - r_{21} r_{12} e^{-i\varphi} + (r_{21} r_{12})^2} \\ &= \frac{E_0^2 (t_{12} t_{21})^2}{1 - 2 r_{21} r_{12} \cos\varphi + (r_{21} r_{12})^2} \\ &= \frac{E_0^2 (t_{12} t_{21})^2}{(1-R)^2 - 2R\cos\varphi + 2R} \\ &= \frac{E_0^2 (t_{12} t_{21})^2}{(1-R)^2 + 4R\sin^2\frac{\varphi}{2}} \end{aligned} \tag{1.11}$$

where we first used the definition of cosine function, $\cos\varphi = \frac{e^{i\varphi} + e^{-i\varphi}}{2}$, then Equation (1.4), and then the trigonometric identity $\cos(\varphi) = 1 - 2\sin^2\frac{\varphi}{2}$. If we further assume the most common case for transmittance spectroscopic measurements at normal incidence so we can use Equation (1.5) and we neglect the absorption of light inside the film (assuming $R + T = 1$), we can finally express the intensity of the transmitted wave as:

$$I_t = \frac{T^2}{T^2 + 4R\sin^2\frac{\varphi}{2}} I_0 \tag{1.12}$$

where we can see that the intensity of transmitted light depends on transmittance T, reflectivity R but also on refractive index n, thickness d, and wavelength λ (through φ). The analogous derivation can be made for reflected waves or we can use the abovementioned assumption $R + T = 1$ and express it as a complement of Equation (1.12). The overall intensity of light forms an interference pattern depicted in Fig. 1.2. The period of the oscillations determines the thickness and optical properties of the film. For interference to occur, the thickness of the film must be comparable or smaller than the coherence length of the source, which is for our films sufficiently satisfied[3].

[3] The coherence length l_c of light can be approximated as $l_c \sim \frac{\lambda^2}{n\Delta\lambda}$ where $\Delta\lambda$ is the linewidth[58].

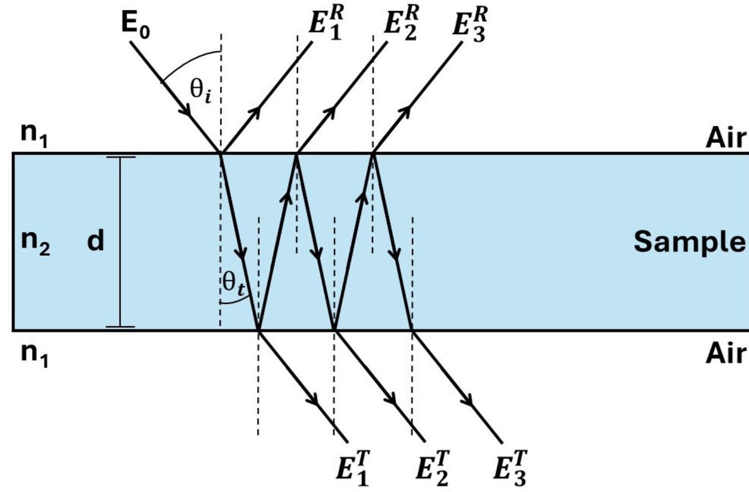

Figure 1.1: Interference of light on a plane-parallel thin film. The light incoming from a medium with refractive index n_1 is incident on a film with thickness d at an angle θ_i and refractive index n_2. At each interface, light is either transmitted or reflected, and the total amplitude of the transmitted or reflected light is given by the sum of the partial amplitudes E_i^T and E_i^R, respectively. Here, the presence of substrate is omitted.

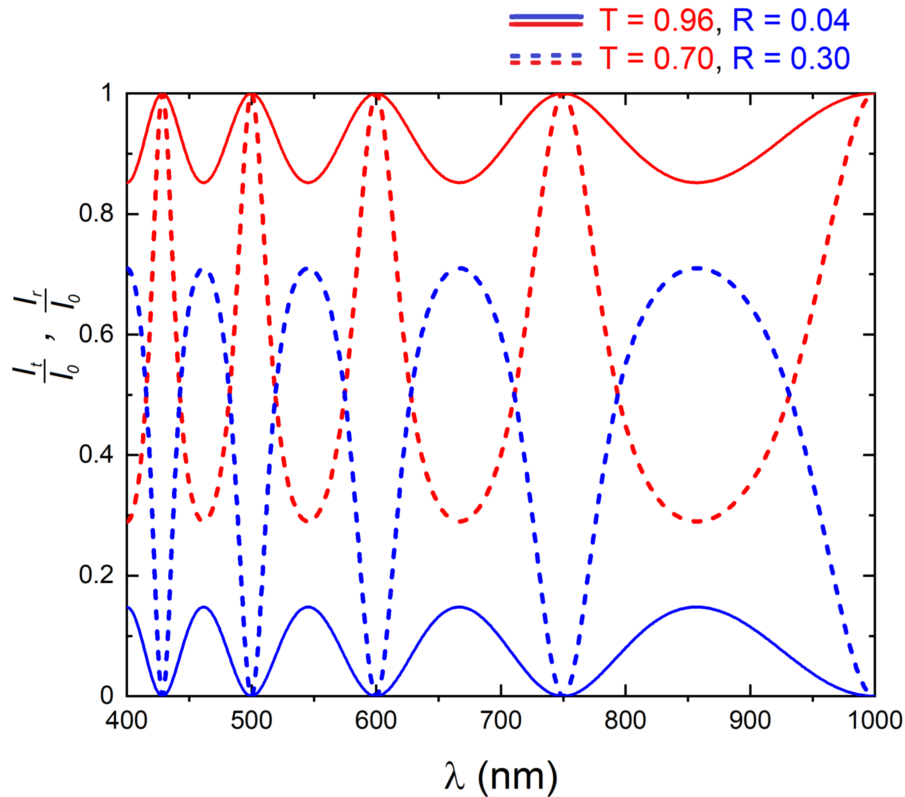

Figure 1.2: The intensity of transmitted light (red) and reflected light (blue) as a function of wavelength according to the Equation (1.12) for a transparent material e.g. glass (solid lines) and a more reflective material e.g. metal oxide layer (dashed lines), both with a thickness $d = 1000$ nm, refractive index $n = 1.5$, and negligible extinction coefficient $k = 0$ for all wavelengths.

To evaluate the optical transmittance T, initially the reference intensity of light I_0 without the presence of a sample is measured and then the intensity of light that passes through a sample I. Also, it is necessary to perform a baseline correction by subtracting the background spectrum I_b arising from illumination from the environment and the thermal noise from the detector. Considering the signal from the background to be negligibly smaller for both I and I_0 the optical transmittance T can be determined as a ratio:

$$T = \frac{I}{I_0} \tag{1.13}$$

The measured intensity of light I for a certain wavelength is proportional to the number of photons that hit a detector in a given time interval, which is a random variable following the Poisson distribution[61]. Hence I corresponds to the mean value and the whole spectrum represents the histogram of these intensities. The probability $P(k)$ that a certain pixel detects k photons is:

$$P(k) = \frac{I^k}{k!} e^{-I} \tag{1.14}$$

It is well-known that the standard deviation of Poisson distribution with mean value of I is $\sigma_I = \sqrt{I}$. Since both I and I_0 are independent variables with absolute errors σ_I and σ_{I_0}, respectively, the formula for propagation of uncertainty yields expression for the absolute error of transmittance σ_T:

$$\sigma_T = \sqrt{\sum_{k=1}^{n} \left(\frac{\partial T}{\partial X_k} \right)^2 \sigma_{X_k}^2} = \sqrt{\frac{T}{I_0} (T+1)} \tag{1.15}$$

where first equality corresponds to a general formula for propagation of error for a function T dependent on the variables X_k and their corresponding errors σ_{X_k}. The second equality, is obtained by rewritting the formula using Equation (1.13) and by substituting the variables. Finally, the relative error of transmittance η_T can be expressed as:

$$\eta_T = \frac{\sigma_T}{T} = \sqrt{\frac{1}{I_0} \left(1 + \frac{1}{T} \right)} \tag{1.16}$$

The optical properties of thin films strongly depend on their electronic structure. The state of each electron is characterized by a unique crystal momentum vector $\vec{k}$ and energy within the Brillouin zone. The energy difference between the top of the valence band and the bottom of the conduction band, mostly expressed in electronvolts, is called the band gap. In other words, there are certain energies within the band structure with no corresponding electronic states, and therefore the electrons need a minimum energy corresponding to E_g to overcome this barrier to be excited from the valence band to the conduction band. Based on the magnitude of E_g we can categorize materials into three categories: conductors (metals, with no band gap, highly reflective in visible wavelength range), semiconductors (E_g from 0.1 to 4 eV) and insulators (typically $E_g > 4$ eV, usually transparent).

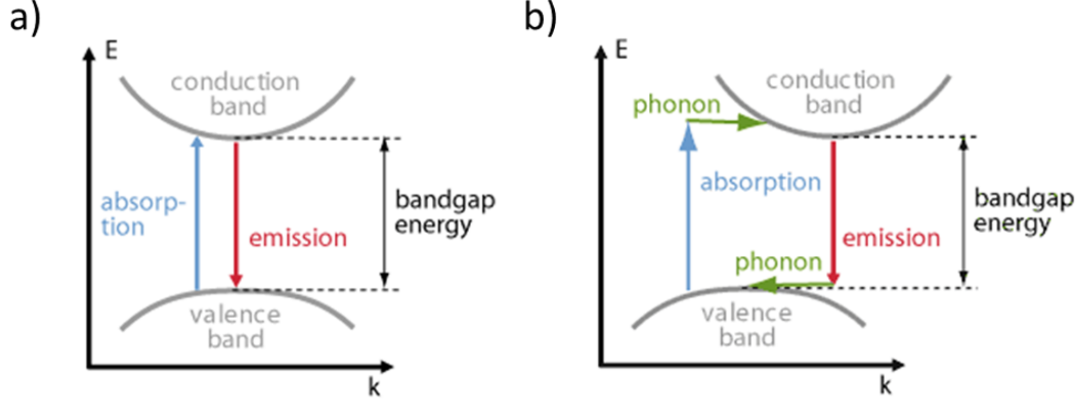

Figure 1.3: Graphical representation of energy E vs. crystal momentum vector $\vec{k}$ for a) a direct band gap and b) an indirect band gap. Taken from [63].

There are two types of band gaps in semiconductors[4]:

- *A direct band gap* - The $\vec{k}$-vectors of the minimum energy state of the conduction band and the maximum energy state of the valence band coincide (see Fig. 1.3a). A photon with energy exceeding E_g can be absorbed during the excitation of an electron, leaving a hole. Conversely, an electron can easily transition from the conduction band to the valence band and emit photons with energy close to E_g.
- *An indirect band gap* - The $\vec{k}$-vectors of the minimum energy state of the conduction band and the maximum energy state of the valence band are different and electrons cannot transition without additional momentum transfer through phonons to satisfy conservation of energy and momentum (Fig. 1.3b). Therefore, these processes occur at a lower rate and are temperature-dependent as temperature affects the population of phonons.

Spectrophotometric transmittance measurements can serve to accurately estimate the band gap value E_g, To measure the amount of light absorbed within the sample, a dimensionless quantity absorbance A is used, defined as a negative common logarithm of transmittance:

$$A = -\log T = -\log \frac{I}{I_0} = -\log e^{-\alpha d} = \alpha d \log e \tag{1.17}$$

where for the equivalent forms we used first Equation (1.13) and then Equation (1.1).

[4]In semiconductors, there is often a distinction between the optical and electronic band gaps. The optical band gap refers to the minimum energy required to create an exciton, a bound state of an electron and a hole, typically derived from optical absorption measurements. However, the electronic band gap represents the minimum energy needed to generate an unbound electron-hole pair and is typically determined using electrical methods. Due to Coulombic attraction between the electron and hole, the electronic band gap is slightly higher than the optical band gap, requiring additional energy, so-called exciton binding energy, to overcome this attraction. However, for most inorganic semiconductors, the Coulombic interaction is negligibly small with exciton binding energies in the order of meV[62].

Considering that the optical path length d is usually taken as the thickness of the film, the absorption coefficient α, commonly expressed in cm^{-1}, can be determined by using a well-known identity $\log_a b = \frac{\ln b}{\ln a}$ as:

$$\alpha = \frac{A \ln 10}{d} \tag{1.18}$$

In 1966 Tauc proposed a method for the estimation of E_g using optical absorption measurements for amorphous semiconductors[64], although it is being also used for other materials, assuming that the energy-dependent absorption coefficient α can be expressed in the following form[65]:

$$(\alpha \cdot h\nu)^{\frac{1}{\gamma}} = B(h\nu - E_g) \tag{1.19}$$

where h is the Plank constant, ν is the photon frequency, B is a constant called band tailing parameter, and γ is a factor dependent on the nature of the electron transition and is equal to 1/2 or 2 for the direct and indirect transition band gaps, respectively. This approach is valid for materials, which do not absorb light for energies lower than E_g. The plot $(\alpha \cdot h\nu)^{\frac{1}{\gamma}}$ against incident photon energy $h\nu$ is known as Tauc plot. This produces an irregular curve with some parts that are in the form of a straight line. The value of E_g can be determined by fitting the experimental data in the region exhibiting linear dependence, followed by extrapolation to the abscissa corresponding to this linear fit.

1.3 Chromogenism and thermochromism

Chromogenism refers to the ability of a material to change its optical properties (transmittance and reflectance) when exposed to certain external agents, leading to its colour change or dimming. Depending on the nature of these agents, we classify chromogenism into different types with their self-explanatory prefixes that are included in Table 1.1 In this section, attention is paid to thermochromism, with an explanation of the discolouration mechanism and a few examples provided.

Chromism type	External agent
Thermochromism	Heat
Photochromism	Electromagnetic radiation
Electrochromism	Electric field or current
Magnetochromism	Magnetic field
Mechanochromism	Mechanical stress or deformation
Solvatochromism	Various solvents
Gasochromism	Various gases

Table 1.1: Classification of various chromic phenomena and the responsible stimuli.

Despite numerous thermochromic materials had been known for a long time, their first systematic investigation is attributed to the work of Houston in 1871[66]

but more attention to its mechanism began to emerge during the 1960s[67]. In fact, every material is thermochromic to some extent, but most show only a subtle change in colour, although the term is used mostly when this change is significant enough. Primarily, thermochromic changes are considered to be reversible, i.e. the colour is restored upon returning back to the original temperature. Reversible thermochromic films have found many applications: from the obvious ones such as temperature indicators (e.g. publically well-known mood rings), thermochromic dyes (for clothing or mugs), anti-counterfeinting inks (bank notes) to more advanced ones such as displays and sensors. However, irreversible thermochromic materials are also highly valuable and frequently reported in the literature[68], particularly in ensuring the quality and safety of food packaging, as they can confirm that food has never been exposed to temperatures above the safe threshold, providing a reliable method of monitoring and maintaining food safety during transport and storage[69].

Thermochromic materials can be organic, inorganic, or a combination of both. The main advantage of organic thermochromes lies in their excellent reversibility, but they are generally applicable to temperatures only up to approximately 100°C because higher temperatures leads to their degradation. On the other hand, most inorganic thermochromic materials can withstand thermal treatment and remain chemically stable under ambient air. At higher temperatures up to 500°C, these requirements are fulfilled for various transition metal oxides (such as V, W, Nb, Mo, etc.) with well-known durability.

The main mechanisms responsible for the thermochromimic behaviour of inorganic transition metal oxides are:

1. *Phase transition* - Transitions taking place at some critical temperature T_c to different allotropic modifications of the same compound give rise to variations in electronic structure. Another similar mechanism is related to order-disorder transitions occurring e.g. for Cu_2HgI_4, which possesses at RT bright red colour, with all Cu^+ and Hg^{2+} ions arranged in alternating layers in ordered tetragonal phase. At higher temperatures (around 70°C), these metal ions start randomly occupying tetrahedral holes throughout I^- array in disordered pseudocubic phase, resulting in dark brown colour[70].

2. *Band gap shrinkage* - The decrease in band gap with elevated temperature leads to different light absorption behaviour (red shift). Semiconductors may undergo a semiconductor-to-metal transitions (SMT), which is associated with removing oxygen atoms, creating a defect centers that leave electrons in intersticial sites, typically observed in ZnO, WO_3, TiO_2[71].

3. *Crystal field effect on $d-d$ orbital transition due to transition metal ions impurities* - The presence of ligand ions affects electronic levels between d-orbitals that are splitted. With increasing temperature this field strength changes due to alternations in ion position. Typical example of this phenomenon is ruby, naturally occurring as corundum (Al_2O_3) with its signature red colour caused by Cr^{3+} ions, that are squeezed in the octagehedral positions, replacing Al^{3+} ions. Upon heating, the chemical bonds between Cr^{3+} and O^{2-} expand, which causes relaxation and change of ligand field energy. Consequently, it turns into green colour characteristic to pure Cr_2O_3[72][73].

The first mechanism is accompanied with an abrupt change in optical properties, while the rest are showing a gradual change in observed optical quantities. For typical temperatures for human environments (below 100°C), applications for smart windows are extensively studied in numerous works, with VO_2 being among the most prevalent materials due to its reasonable critical temperature T_c of 68°C, corresponding to the phase transition from monoclinic ($P2_1/c$) to tetragonal rutile structure ($P4_2/mnm$). Below T_c, VO_2 is transparent to IR radiation, while above T_c it becomes reflective (see Fig.1.4a) and b)). For practical applications, the transition temperature was further reduced closer to RT by doping with various ions, such as W^{6+}, Mo^{6+}, or Nb^{5+}[44]. This makes VO_2 coating a suitable material for the fenestration of buildings with effective energy saving capabilities by reducing the costs related to heating and air conditioning. However, a relatively short environmental stability of VO_2 remains the greatest obstacle, as it transforms into the most thermodynamically stable phase of V_2O_5, which is not thermochromic.

Therefore, appropriate alternatives that could be utilized for large-scale production are still being investigated. For high temperature applications, WO_3 is becoming widely studied, whose thermochromic monoclinic phase for bulk material remains stable before undergoing a transition to a non-thermochromic orthorhombic crystal phase. Fabricating heterostructured multi-layers that use BM as the basis and WO_3 deposited on top (Fig. 1.4c)) could enhance the thermochromic response of the oxide with better efficiency due to the larger effective surface area of black metal. The BM sublayer is expected to absorb light in the VIS wavelength range, which will be converted into heat. The optical properties of the WO_3 will be influenced by the temperature of the BM, which will reduce the light going through the thermochromic layer, therefore reducing the light conversion. This combination allows to obtain a self-controlled light heterostructured absorber.

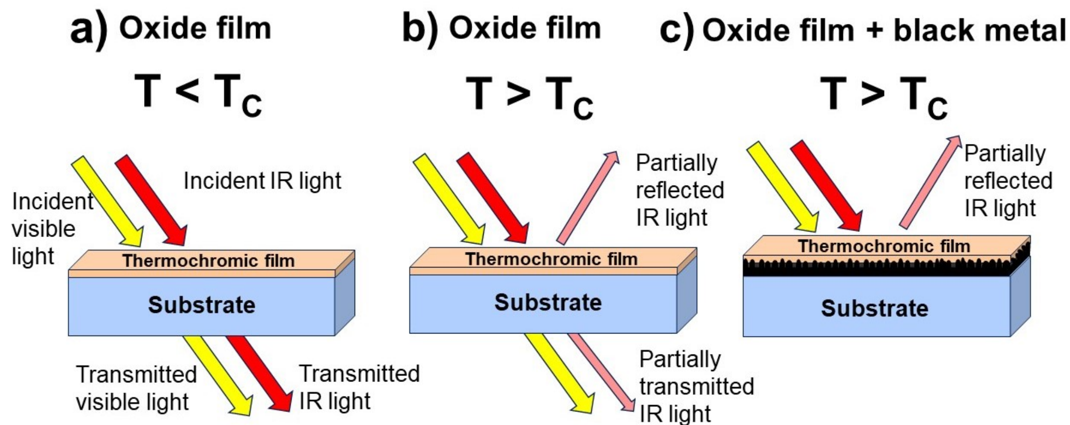

Figure 1.4: Schematic diagram depicting the thermochromic properties of a transition metal oxide film undergoing a phase transition at the critical temperature T_c. a) At temperatures below T_c, the oxide film allows the transmission of VIS and IR light. b) At temperatures above T_c, the oxide film partially reflects IR light while still transmitting VIS light. c) The proposed combination of the oxide film with a BM layer to create a temperature self-controlled light absorber using the conversion of light into heat.

2. Preparation of thin films

The upcoming chapter provides a brief summary of thin film preparation methods, with a focus on those employed in this thesis, particularly magnetron sputtering and pulsed laser deposition. We will discuss the advantages and disadvantages of these techniques and describe in detail the deposition systems used for our thin films.

2.1 Overview of deposition techniques

Deposition is a controlled process of preparing thin films by transferring a desired material, referred to as the target, onto a chosen base material, known as a substrate. Nowadays, there is a wide variety of deposition methods that can be classified according to various criteria, frequently combining several methods simultaneously. To ensure the cleanliness of deposition, it is often carried out in a high or ultra-high environment of vacuum chambers, provided by various vacuum pumps.

Typically, two main categories of vacuum thin film synthesis are distinguished based on whether the deposition mechanism is primarily chemical or physical. In chemical vapour deposition (CVD), one or more volatile vapour reactants (precursors) are introduced into the deposition chamber, which react and/or decompose on the substrate surface to form a film. The substrates are usually heated to activate or accelerate chemical reactions between precursors. The main advantages of CVD are very good homogeneity, chemical purity and wear resistance of resulting films. Because the precursors completely surround the substrate, the film is formed on all surfaces, enabling deposition even on complex-shaped substrates. However, it is rather not environmentally friendly, since formed gaseous by-products can be potentially toxic.

In addition to the conventional CVD method, the chemical reactions can also be accelerated using plasma, generated by an external voltage source, which is referred to as Plasma-enhanced CVD (PECVD). This method is based on increasing the energy of the gaseous phase by ionising it in a plasma discharge between electrodes. Other methods based on this principle include microwave plasma CVD (MPCVD) and remote plasma-enhanced CVD (RPECVD). If organometallic compounds are used as precursors, the method is called metalorganic CVD (MOCVD). Besides plasma, light can also be used as a stimulant, which is then called photo-initiated CVD (PICVD), or if a laser beam is used, it is referred to as laser-assisted (LACVD). A promising technique for the production of outstanding semiconductor materials with atomic-scale precision is atomic layer deposition (ALD), where precursors are introduced into the chamber sequentially.

Physical vapour deposition (PVD) encompasses a large group of techniques, where thin films are fabricated by converting atoms from a solid target into a vapour phase species through mechanical, thermodynamic, or electromechanical processes, which then condense on the substrate. Compared to CVD, PVD is valued for its ability to produce coatings with greater diversity of materials, without necessarily requiring elevated temperatures, and their properties can be tuned just by a simple modification of deposition parameters. Also, the deposition

by-products are usually not hazardous for humans or the environment. Nonetheless, PVD methods are mostly highly directional, usually following cosine spatial distribution[74] in film thickness, which complicates maintaining uniformity for larger or irregularly shaped substrates.

A standard and straightforward example of PVD processes is thermal evaporation (TE), in which the target material is placed into a specially designed boat-shaped crucible and the gaseous phase is produced by supplying heat to the target, causing it to reach the temperature necessary for atom release through sublimation. In this case, heat is supplied, for example, through direct heating via Joule heating using resistive wires positioned underneath the crucible, which is then conducted to the target. Sometimes, chemical reactions between the crucible material (such as W or Ta) with the evaporant could pose an obstacle. A similar effect can be achieved by a high-energy electron beam, emitted via thermoemission from an electron gun (usually made of W filament), impacting a small area of the target and converting its kinetic energy into heat, known as electron beam evaporation or EB-PVD. Alternatively, ion beams or arc can also be used for depositions. A layer-by-layer growth of epitaxial films is obtained during molecular beam epitaxy (MBE) from multiple crucibles placed in Knudsen effusion cells.

The final properties of thin films depend on various parameters influenced by the deposition technology and configuration. These include the composition, pressure, and flow rate of the reaction gas mixture, substrate temperature, plasma characteristics (if applicable), substrate preparation, and others. Among these, one of the most crucial for technological applications is the deposition rate v_d, defined as the ratio of the total film thickness h and deposition time t:

$$v_d = \frac{h}{t} \tag{2.1}$$

To schematically illustrate the influence of various deposition parameters on film morphology and microstructure, structure zone diagrams (SZD) have been introduced. Movchan and Demchishin presented the first SZD in 1969[75] for thick films prepared by TE. They described film properties as a function of their temperature and divided the graph into three separate zones. For lower temperatures, in zone 1, the atom mobility is significantly suppressed and so films posses fine-grained structure of textured and fibrous grains. For higher temperatures in zone 2, surface diffusion becomes dominant and films consist of columnar grains separated by distinct boundaries. At even higher temperatures within zone 3, the bulk diffusion and recrystastalization lead to prominent grain growth and denser films.

2.2 Magnetron sputtering

Sputtering refers to a PVD method in which source material atoms are vaporised in the presence of a glow discharge plasma through a bombardment of energetic positive ions of some inert working gas. This mechanism of thin film preparation was firstly described by W. R. Grove in 1852[76], and nowadays the sputtering-based methods represent the most widely used PVD technique in both academic and industrial applications[77].

A simplified model of sputtering considers this process as an interaction of inert gas ions as an inelastic collision of hard spheres, transferring their momentum to target atoms and ejecting them towards a substrate where they condense (illustrated in Fig. 2.1). The efficiency of sputtering is described by the parameter called the sputtering yield Y, which represents the average number of sputtered atoms per ion of the working gas. It depends on the target material used, the working gas, the applied voltage to the target and the angle at which the ions strike the target[74]. Argon is typically chosen as the working gas[1], which is ionised by a discharge maintained by an applied electric voltage. The Ar^+ ions are subsequently accelerated by the electric field towards the target surface, serving as a cathode. Both working gas ions and sputtered atoms have sufficient energy to be excited, and therefore deposition is accompanied by characteristic light emission during deexcitatation (see Fig. 2.2). However, most of the kinetic energy of the impacting ions is converted into heat, so the target must be cooled continuously to prevent overheating and melting.

To ensure that plasma only in the electric field is self-sustainable, the pressure must be relatively high. To increase the efficiency of ionisation, an additional magnetic field is utilised, causing secondary electrons to be confined in the vicinity of the target, avoiding their loss in the chamber walls. This improvement, known as magnetron sputtering (MS), was proposed and patented by J. S. Chapin in 1974[78]. He used a device called planar magnetron, consisting of a system of permanent magnets placed under the target, forming a magnetic circuit with magnetic field lines in closed loops in a flat geometry, where the target and substrate are positioned parallel to each other. Over the years, a variety of other geometries have been employed, such as cylindrical and sputter-gun[79]. The selective strengthening or weakening of the magnetic field led to the development of imbalanced magnetrons, which changed the plasma configuration and hence modified the properties of the deposited films in a desired way.

In order to explain the effect of the magnetic field, we need to consider an electron with mass m_e moving in combined electric and magnetic fields with velocity $\vec{v}$, which is experiencing the Lorentz force $\vec{F_L}$. Then the equation of motion can be expressed as:

$$\vec{F_L} = e(\vec{E} + \vec{v} \times \vec{B}) = m_e \frac{d\vec{v}}{dt} \tag{2.2}$$

where e is the (elementary) charge of electron, $\vec{E}$ and $\vec{B}$ are electric and magnetic field vectors, respectively.

[1] Other noble gases such as He, Ne, Kr or Xe can be used, although Ar serves a good compromise between its cost and sputtering yield.

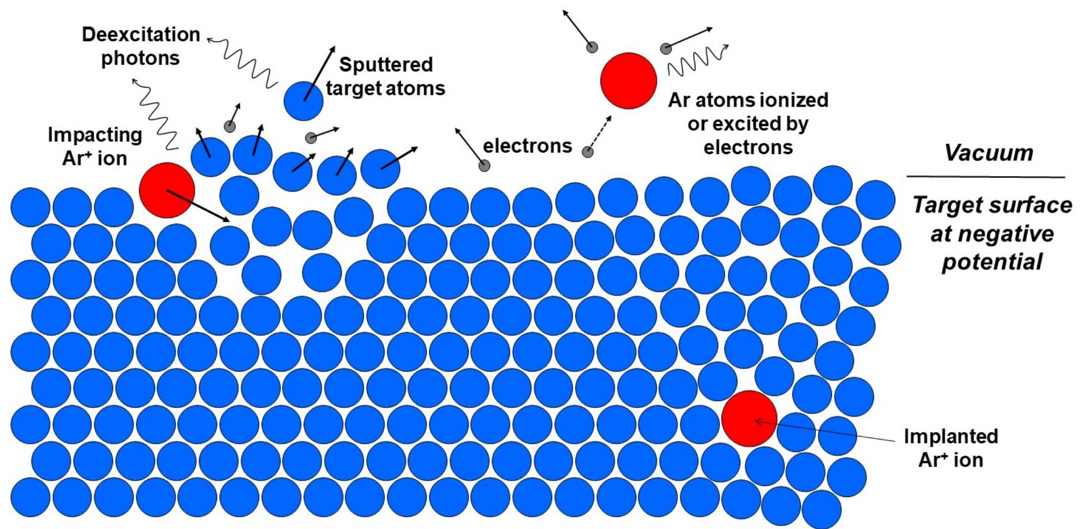

Figure 2.1: Scheme of the sputtering process. Ar^+ ions (red) collide with the target atoms (blue). Upon impact, these ions may be reflected back, stick to the surface, sputter target atoms and secondary electrons, or become implanted under the surface, depending on their initial energy. Secondary electrons can repeatedly excite the Ar atoms. Taken from [80].

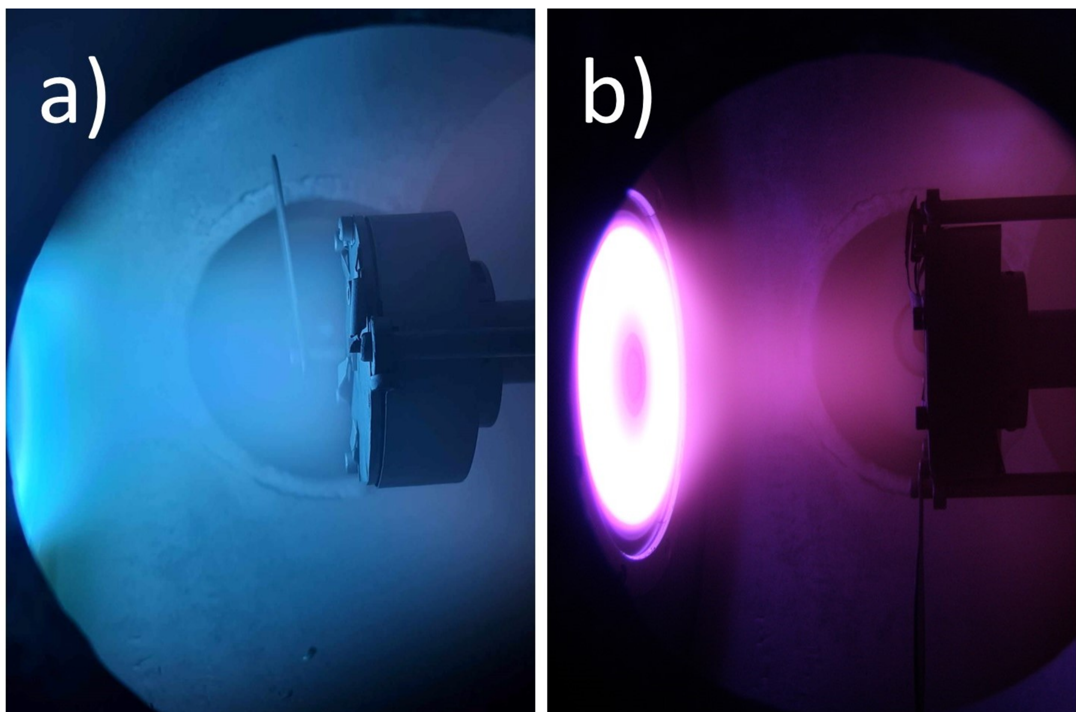

Figure 2.2: Photographs of glow discharge plasma during MS deposition:
a) Ti target in pure Ar atmosphere, b) Ti target in a mixture of Ar and N_2

Solving Equation (2.2 for any arbitrary electric and magnetic field is a challenging task, so we simplify our explanation only for four special configurations of planar magnetrons:

- For a homogeneous electric field in the direction of the z-axis, perpendicular to the target surface and in the absence of a magnetic field ($\vec{E} = (0, 0, E_0)$ and $\vec{B} = \vec{0}$), the electron is accelerated parallel to the direction of the electric field, which is the case of conventional sputtering described above.
- For a homogeneous magnetic field in the direction of the z-axis, perpendicular to the target surface and in the absence of a electric field ($\vec{B} = (0, 0, B_0)$ and $\vec{E} = \vec{0}$), the electron gyrates in a cyclotron orbit in a plane perpendicular to the magnetic field (x-y plane). The Larmor radius of gyration R_L is given by:

$$R_L = \frac{v_\perp m_e}{eB_0} \tag{2.3}$$

  where $v_\perp = \sqrt{v_x^2 + v_y^2}$ is the magnitude of the velocity component in the plane perpendicular to $\vec{B}$. The Ar^+ ions would gyrate in the opposite direction, and due to their mass M_{Ar} being much greater than that of electrons, Equation (2.3) gives significantly larger R_L, making them nearly unaffected by the magnetic field.
- If both homogeneous electric and magnetic fields are present and perpendicular to each other (i.e., for example $\vec{E} = (0, 0, E_0)$ and $\vec{B} = (B_{0x}, B_{0y}, 0)$), then electron undergoes so-called $\vec{E} \times \vec{B}$ drift. The electron, which is emitted from the target, is accelerated by the electric field, which increases the perpendicular velocity component (see Fig. 2.3a). Simultanuosly, the magnetic field extends its Larmor radius, causing it to return back to the target. Hence, for a circular planar magnetron, the elecrons will drift around the target in cycloidal motion.
- If the magnetic field is inhomogeneous (i.e., for example with $B_z(z)$ component varying along z-axis), then so-called magnetic mirroring effect occurs. A classical magnetic moment $\vec{\mu}$ of an electron is an adiabatic invariant, defined through its energy $E = \frac{1}{2} m_e v^2 = \frac{1}{2} m_e (v_\perp^2 + v_z^2)$ as:

$$E = -\vec{\mu} \cdot \vec{B} \implies \mu_z = \frac{m v_\perp^2}{2B_z} = const. \tag{2.4}$$

  Near the region, where the magnetic field lines enter the surface, the magnetic field is the strongest and $\nabla \vec{B} \parallel \vec{B}$. As the electron moves closer to the surface, B_z increases, and to keep μ_z constant, $v_\perp$ must also increase. Because the magnetic field does no work, then v_z must drop. At certain mirroring point is $v_z = 0$ and the electron is reflected back. Additionally, in places where $\nabla \vec{B} \perp \vec{B}$, the $\nabla \vec{B} \times \vec{B}$ is induced that is perpendicular to both $\vec{B}$ and $\nabla \vec{B}$ (Fig. 2.3b). Below the points, where magnetic field lines are parallel to the surface of the target, the sputtering efficiency is the highest, forming an erosion track (Fig. 2.3c). This effect leads to imperfect utilization of the total amount of target material. To minimize this effect, targets can be rotated or other geometries can be used.

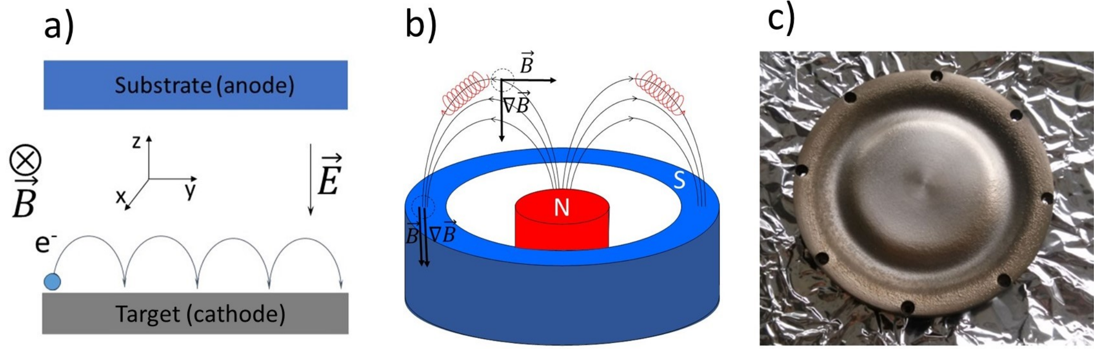

Figure 2.3: The effects of combined electric and magnetic fields in a planar magnetron. a) The cycloidal movement of an electron in $\vec{E} \times \vec{B}$ drift close to the target. b) Inhomogenous magnetic field in circular magnetron. c) Photograph of the erosion track on an aluminium target.

Consequently, the magnetic field combined with the mentioned effects, lead to a higher density of plasma, which allows for film deposition at lower pressures and significantly increases the deposition rate.

According to the type of electric voltage applied to the magnetron, we distinguish several different methods of deposition by MS:

- Applying continuous direct current (DC) to the target is arguably the simplest method, but it requires the target material to be conductive, otherwise a charge builds up on its surface that prevents further ion bombardment. When this charge reaches a certain threshold, arcing can happen, which is generally undesirable. To avoid arcing, the negative bias can be applied in pulses, alternatively switching the voltage on and off with some duty cycle and repetition frequency on the order of tens of kHz. Duty cycle represents the ratio of the time during which voltage is applied, to the total duration of that period. During the negative part of cycle, sputtering takes place, and during the positive phase of the cycle, electrons are attracted to the surface to neutralize any accumulated charge.
- When an alternating current (AC) with low frequency (up to several tens of 10 kHz) is used, the system effectively behaves like DC MS, where the target and substrate (or chamber walls) act alternatively as cathode and anode. During polarity reversal, both ions and electrons oscillate between the electrodes, allowing resputtering of the deposited film atoms.
- In radio frequency (RF) MS the frequency of applied voltage is further increased to MHz (typically 13.56 MHz). If we capacitively couple one of the electrodes to an RF generator, a negative DC-like self-bias develops with respect to the second electrode. The heavier positive ions with low mobility cannot respond to polarity changes and remain almost stationary, while electrons still oscillate between the electrodes, acquiring enough energy to ionize the Ar atoms and generate plasma. As a result, this configuration does not rely on secondary electron emission from the target and the discharge is sustained, allowing deposition from any arbitrary material (including insulators).

Besides using an inert gas, deposition can also occur in a reactive gas atmosphere, such as N_2 or O_2, to alter the composition of the resultant film and form nitrides and oxides. However, the chemical reaction with the target material leads to undesired hysteresis behaviour of the deposition parameters, such as the deposition rate, as a function of the reactive gas flow.

The most widely recognised SZD for films prepared by sputter deposition was published by Thornton[81]. He described their morphology as a function of two parameters: substrate temperature and deposition pressure, dividing the diagram into 4 zones by introducing an additional transition zone T. At lower pressures, the mean free path of the particles is large, and therefore sputtered atoms do not experience any collisions before reaching the substrate with relatively high kinetic energies, leading to the formation of denser fiber-like structures. Conversely, at high pressures, sputtered atoms undergo collisions with the ambient gas atoms, resulting in their much lower energy distribution and columnar growth of the films with significant void fraction. The elevated temperature is responsible for the thermal activation of surface diffusion, leading to a rather smooth growth of randomly oriented crystalline grains, with gradually increasing diameters.

The main advantages of MS compared to other PVD techniques include the high versatility of sputtered materials regardless of their melting temperature. Polymeric and other heat-sensitive films can also be prepared without degradation, as deposition can be carried out at lower substrate temperatures[82]. It is generally a reliable way to produce nanocrystalline films with relatively high deposition rates. Additionally, the films possess great thickness uniformity and better adhesion than for TE because of the higher energy of the sputtered atoms impinging on the substrate. Despite the initial cost of MS equipment being relatively high, MS is scalable from small laboratory setups to large industrial systems. Often times, more targets can be combined in multi-magnetron systems for composite film preparation. To mention some of the drawbacks of MS, the process is not optimal for epitaxial film growth, and reactive sputtering can be complex and challenging to control, often requiring precise process optimization.

2.2.1 Our MS system

The photographs of our MS deposition system used for the fabrication of BMs in this work can be found in Fig. 2.4 and Fig. 2.5, and its schematic diagram in Fig. 2.6. A base pressure of 5×10^{-3} Pa is achieved through a combination of a primary rotary oil pump (capable of reaching ~ 50 Pa) and a secondary diffusion pump, cooled by water and located below the vacuum chamber. The vacuum chamber and the diffusion pump are separated by gate and separation valves.[2] Initially, a sample holder is inserted horizontally into the vacuum chamber at a certain distance, commonly referred to as the working distance, from round-shaped targets with diameters of 10 cm (on a planar magnetron). Although the sample holder is movable, the working distance remains fixed at also 10 cm for our depositions. Ar and N_2 flows are monitored and adjusted by mass flow controllers in the range 0 - 20 sccm, and 0 - 10 sccm, respectively.

[2] The separation valve enables pre-pumping of the vacuum chamber and diffusion pump individually, otherwise a chemical reaction of heated oil with ambient air can lead to the oxidation and degradation of its quality, necessitating replacement.

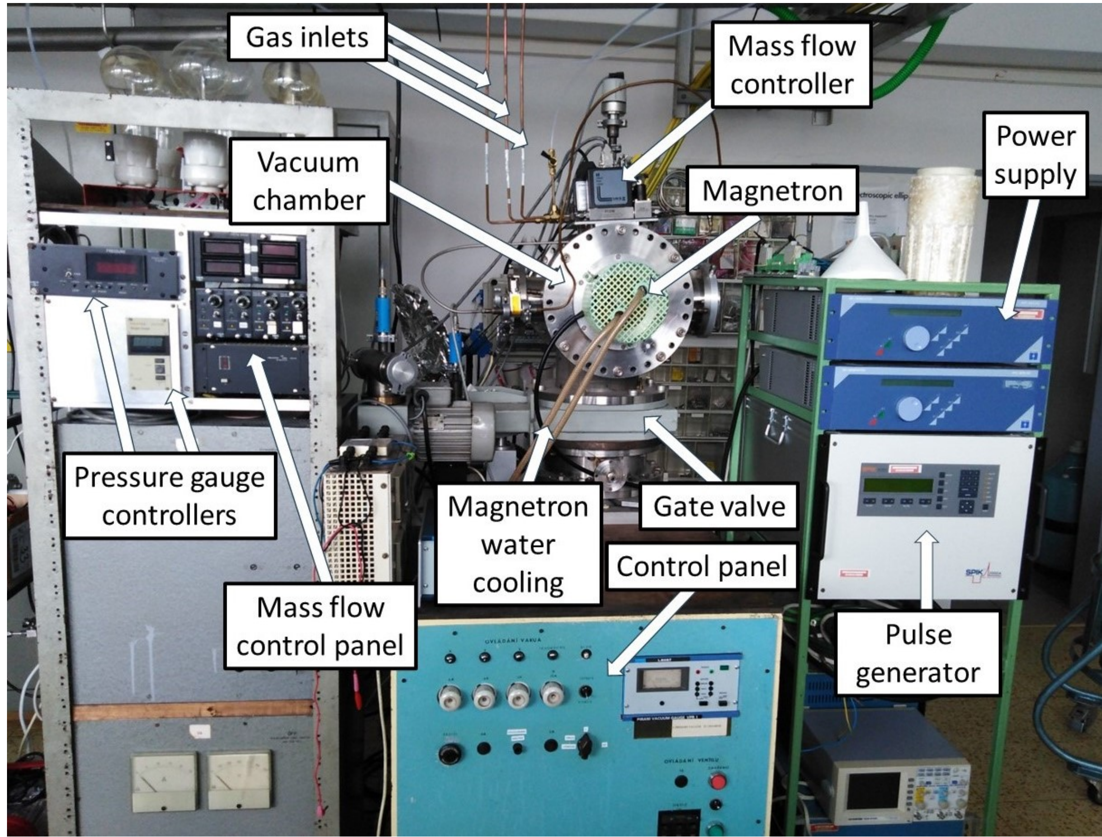

Figure 2.4: Front view of the whole MS deposition apparatus for BM deposition showing most of the key components.

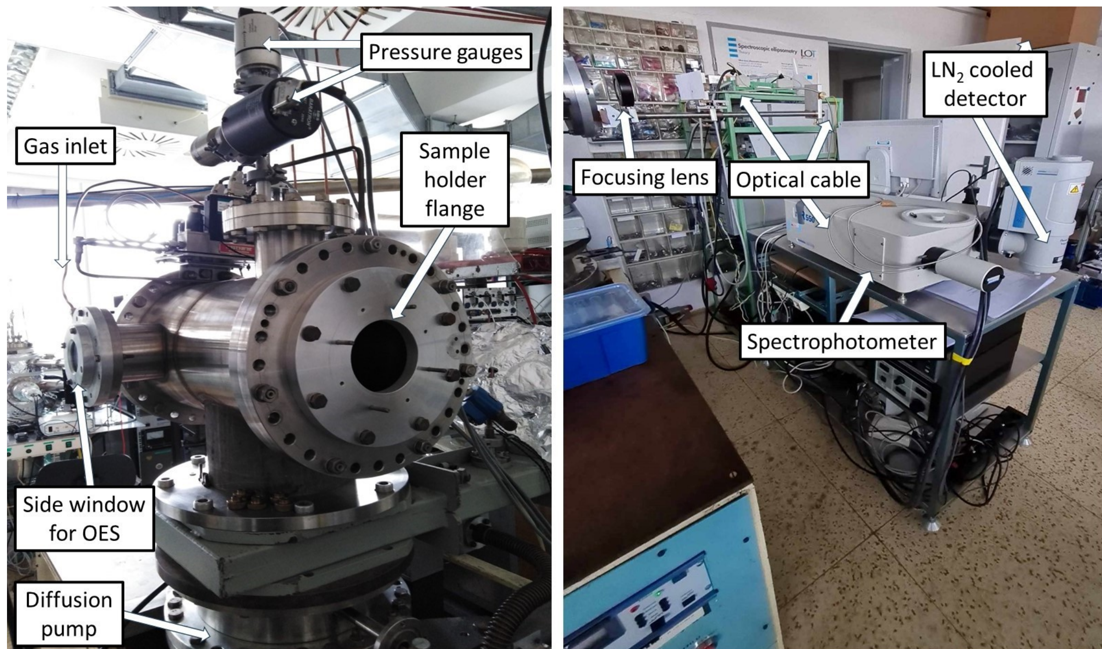

Figure 2.5: Photograph providing detailed views of our MS system for BM deposition. The left image shows a back view from the side, where sample holder is inserted and the right image shows the OES system that can be optionally installed for plasma characterization.

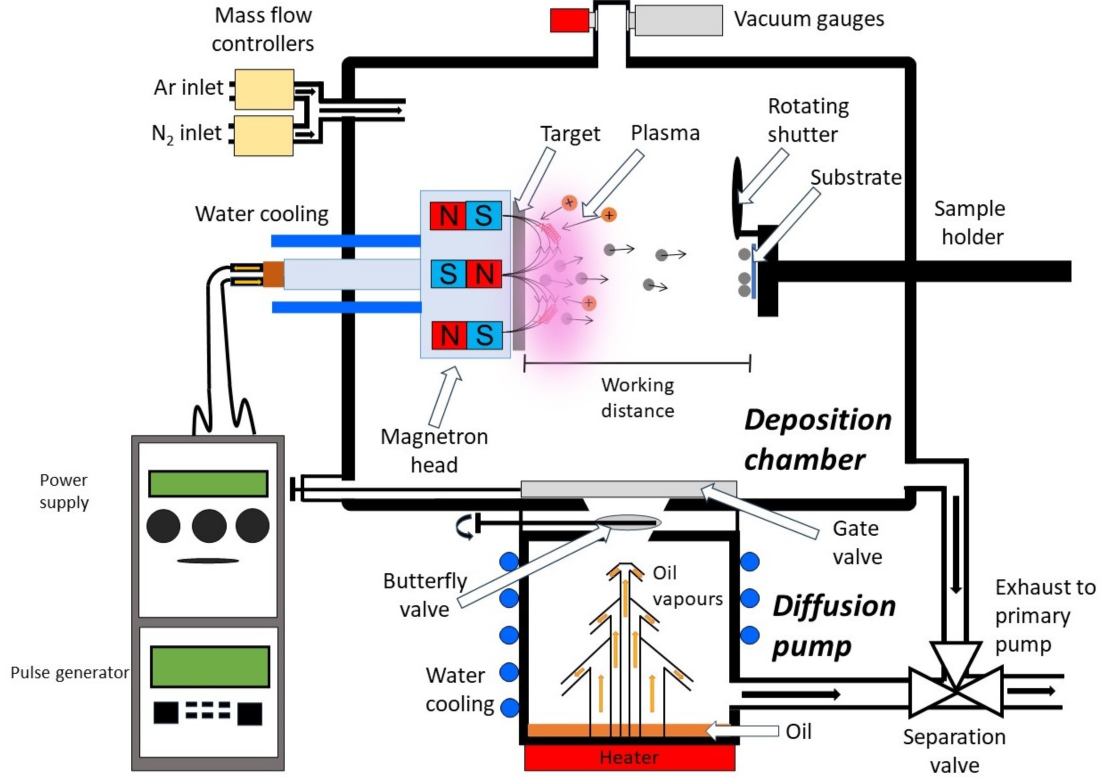

Figure 2.6: Schematic diagram of our MS deposition system for BM deposition.

The deposition pressure of $\sim$ 1 Pa is established by the partial closure of a butterfly valve located between the diffusion pump and the chamber. The pressures higher than or comparable to deposition pressures are controlled by a capacitance gauge (CMR 364 by Pfeiffer) and for a high-vacuum Penning gauge (Balzers Compact FullRange Gauge PKR260) is utilized.

For glow discharge ignition, a DC power supply (Hüttinger 3000) is used together with a pulse generator (MELEC) capable of generating short pulses with a repetition frequency of 10 kHz and a duty cycle of 0.5. At the beginning of the deposition, we set three deposition parameters (voltage U, current I, and power P) and the power supply tries to maintain the maximum power value possible. Before deposition, a presputtering is done to clear the target of adsorbed impurities and oxide/nitride layers that formed as a result of exposure to the atmosphere. During this process, the sputtered atoms are blocked from striking the substrate by a rotating shutter on the sample holder and the deposition parameters (voltage U, current I, and power P) vary over time. Presputtering is considered complete when no further fluctuations in these parameters are observed. Skipping this step could result in the creation of gradient-like films, which are often undesired for their performance, unless specifically studied.

Besides providing a spectacular view of the beautiful plasma, the side window can be used for optical emission spectroscopy (OES) measurements. The emission spectrum of plasma is determined by electronic transitions of target material and working gas and contains important information about its composition and dynamics. The emitted light is collected by a focusing lens and directed through an optical cable via a small aperture. After that, the light is decomposed into

several wavelengths using a diffraction grating and gathered by a Symphony CCD camera (cooled by liquid nitrogen) inside a spectrophotometer (iHR550 Imaging Spectrometer from Horiba). Intensity as a function of wavelength is recorded and for plasma from Fig. 2.2 the spectra in the wavelength range 300 - 930 nm are presented in Fig. 2.7. For such intense plasma, OES serves as a powerful non-perturbative technique for real-time in-situ plasma diagnostics, which can be used to obtain various plasma parameters such as excitation temperature, electron density, etc.[48]. Interestingly, this approach also allows for the investigation of plasma chemistry processes during pre-sputtering, where the intensity of titanium lines usually increases over time as the oxide passivation layer, formed during chamber venting, is removed. During deposition, the plasma remains stable, and the ratio between different emission lines remains constant over time. It is rather challenging to compare absolute emission line intensities for two separate depositions because the film deposited on a window gradually attenuates the intensity, and the transmission spectrum would be required to be measured before every deposition, which is impractical. Therefore, typically ratios of the most significant lines are studied. In this thesis, the OES spectra are omitted from the results, even though it could also fall into the "optical properties" category, but they rather relate more to plasma properties than to our thin films (though they are surely strongly correlated). They are just briefly mentioned here as another potential tool for improving the film quality in future investigations.

The sample holder can support up to four substrates, enabling the simultaneous deposition of multiple films (e.g. on various substrates). This raises the question whether the films are uniform in thickness. To address this, we conducted an experiment to evaluate the homogeneity of our MS deposition system. A glass substrate (of dimensions 6×4.5 cm) was cleaned and masked at 14 locations using a vacuum tape. It was then placed on the sample holder (see Fig. 2.8) and a thin film of black aluminium was deposited for 6 minutes (with the same conditions as will be specified in section 4.1.1). After deposition, the vacuum tape was carefully removed and the thickness of the film was measured using a contact profilometer (will be explained in Section 3.1.1). For a given masked area, at least 10 measurements were taken to compensate for the error caused by the choice of the exact location. The mean value of these thicknesses is then assigned to a single data point, represented by a red circle, with coordinates (x, y) on the substrate's coordinate system, with origin in the lower-left corner. However, since the sample holder has different shape and dimensions, its centre does not align with the substrate's centre (indicated by the white cross). The resulting contour plot (right side of Fig. 2.8) was constructed by extrapolating and interpolating the measured data across the entire substrate area. It shows that the highest thickness is near the centre of the sample holder and is symmetric around this point. Thus, placing multiple substrates (usually we use 1×1 cm) near the centre results in a thickness variation of less than 5 % , meaning that our films can be considered practically equivalent. This offers a significant time-saving advantage compared to techniques like pulsed laser deposition (see the next section), where inhomogeneity is apparent even within a single sample. Since sputtering takes place across a larger area of our fairly large target, several copies of the same sample can be prepared.

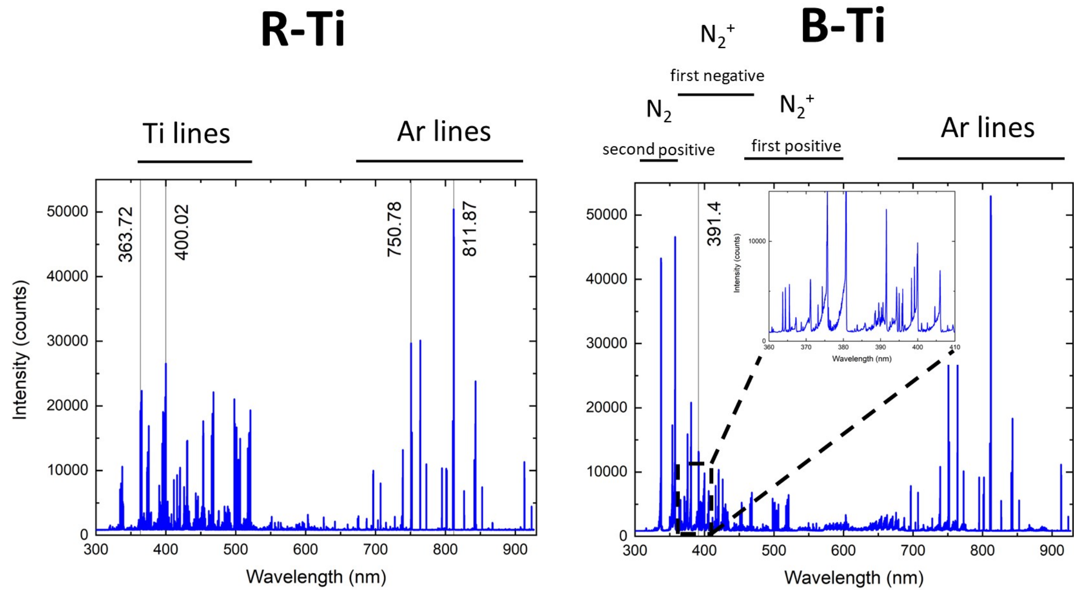

Figure 2.7: An example of OES spectra showing a difference between deposition of reflective (R-Ti) and black titanium films (B-Ti). For R-Ti, the titanium emission lines are distinctly identified from Ar lines (left graph). The strongest lines are denoted by vertical solid lines for Ti I (383.7 nm and 400.0 nm)[83] and for Ar I (750.8 nm and 811.9 nm)[84]. Unfortunately, when plasma contains molecular nitrogen, the N_2 emission from various electronic transition systems[85] overlap with Ti wavelength area. However, a strong line at 391.4 nm that was previously not present is now clearly observed, corresponding to N_2^+ first negative system[86]. A small inset shows detail on the region from 360 to 410 nm, where vibrational transitions are observed.

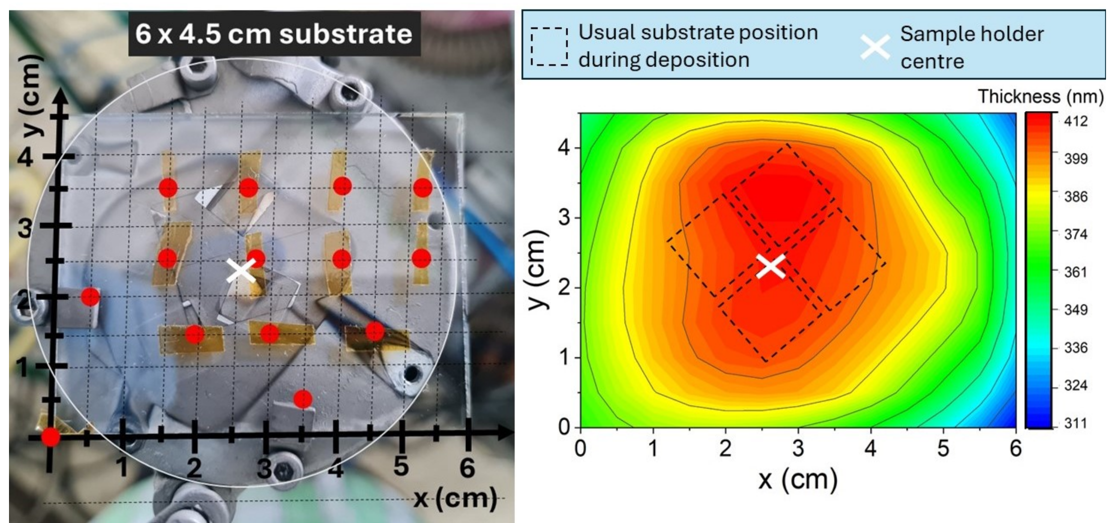

Figure 2.8: Assessment of thickness homogeneity in our MS deposition system. The left image shows a photograph of the glass substrate positioned on the sample holder with measurement points (red dots). The right image presents a contour plot of the film's deposited thickness, indicating the variation in film thickness across the substrate. The dashed rectangle represents the usual substrate positions during deposition, while the white 'X' marks the sample holder center.

2.3 Pulsed laser deposition

Pulsed laser deposition (PLD) is a relatively straightforward yet powerful PVD technique that uses focused high-power laser pulses to ablate a solid target. This method was first employed by Smith and Turner in 1965[87], just five years after the invention of the laser. In their pioneering work, they successfully deposited various single-element and compound materials, demonstrating the remarkable versatility of PLD. The breakthrough in preparing the high-temperature superconductor $YBa_2Cu_3O_7$ (known as YBCO) by T. Venkatesan, his postdoc D. Dijkkamp, and graduate student X. Wu in 1987[88][89], with a quality surpassing that of alternative methods, has fuelled much attention to PLD that remains to the present day.

During PLD, light energy is absorbed by a target material in a small surface area and converted into thermal energy, causing chemical bonds to break. Because most nonmetallic materials exhibit strong absorption in the ultraviolet spectral range, the penetration depth remains low. Consequently, material is vaporized towards the substrate, forming a so-called plasma plume. The plasma plume consists of many excited ions, neutral atoms, molecules, clusters, and electrons that expand further away from the target and condense on a substrate facing the target. The entire process takes place either under ultra-high vacuum conditions or in the presence of certain working gases such as O_2 or N_2 to promote chemical reactions and retain stoichiometry. The exact shape of the plasma plume is then mainly determined by the working pressure (see Fig. 2.9).

There are several factors that influence the quality and properties of the PLD films that need to be considered and specified:

- Laser pulse energy E or laser fluence F
- Repetition rate of laser f and pulse duration τ
- Working distance d
- Deposition pressure p
- Temperature of the substrate T
- Type of substrate (crystalline or amorphous) and target material

For pulsed laser beams, the physical quantity fluence F is defined as the amount of energy delivered per unit area (equivalent to the laser power density). Considering that the laser energy E is uniformly distributed across the circular area $S = \pi r^2$, where r denotes the radius of a laser spot, we can calculate the average fluence $\bar{F}$ as follows:

$$\bar{F} = \frac{E}{S} = \frac{E}{\pi r^2} \tag{2.5}$$

The minimum fluence must exceed an ablation threshold, otherwise the target only gets heated. This threshold is determined by the target material and laser wavelength and is typically in order of ~ 1 J.cm^{-2}[90]. However, fluence depends not only on the size of the laser-affected zone but also on the exact position within this zone, with the highest value on the beam axis, and lower in locations

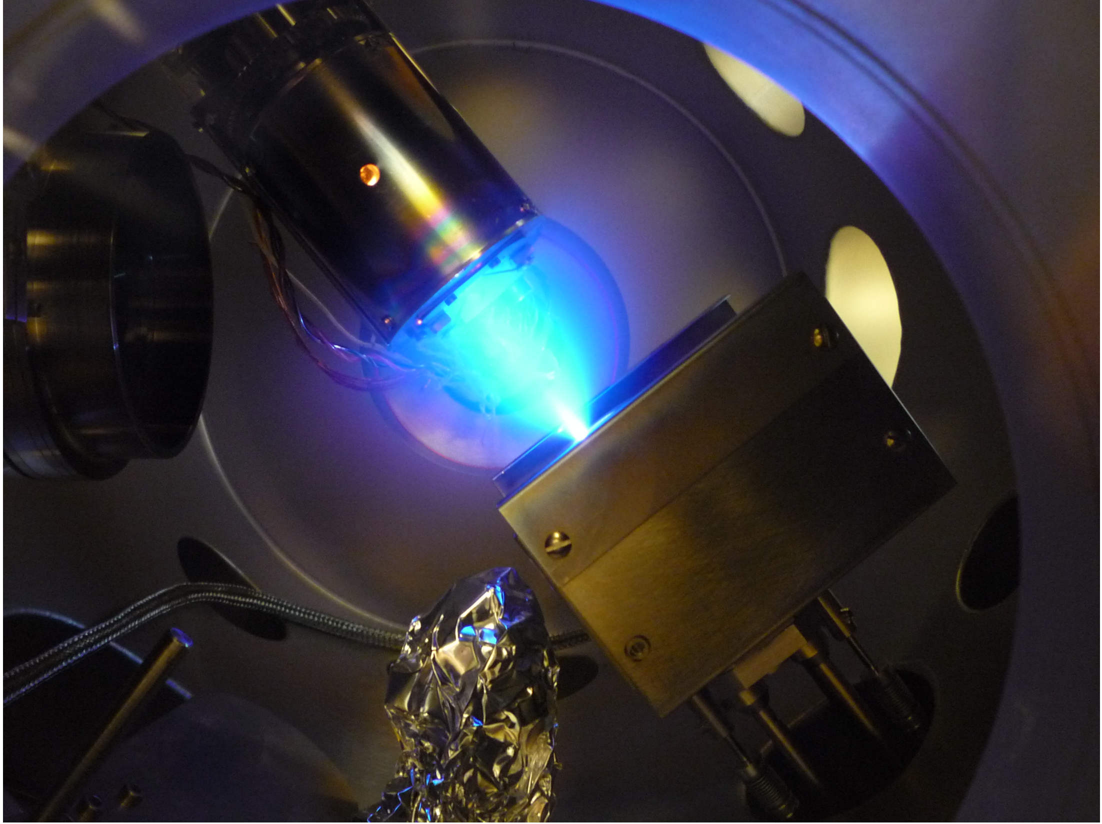

Figure 2.9: Photograph showing the detail of a plasma plume during PLD. In the absence of electric or magnetic fields, the spatial distribution of the ejected species is rotationally symmetric around the normal vector of the target surface.

surrounding this axis. For a typical Gaussian beam profile, the peak fluence F_{peak} is often presented, representing the highest fluence within laser pulse duration, given as $F_{peak} = \frac{E}{\frac{1}{2}\pi w^2}$, where w is the Gaussian beam radius[3].

The main advantage of PLD is the ability to produce multicomponent films with good stoichiometry. Moreover, the material removing source is outside the chamber, unlike the case of MS, providing greater flexibility in the design of the deposition chamber. Unfortunately, there are also a few drawbacks associated with this technique. Perhaps the biggest one is the high directionality of the deposition, which limits the maximum size of substrates that can be homogeneously covered. Because the laser strikes the surface in a small spot, the resulting films are usually quite inhomogeneous, making PLD challenging for large-scale thin film industrial utilization. Nevertheless, for typical applications in a basic research context, these are not generally critical factors.

[3]The Gaussian beam radius w is not the same as laser spot radius r, since the latter mentioned depends on the divergence of the laser beam and the material, where energy is deposited.

2.3.1 Our PLD system

The schematic diagram of our PLD system is depicted in Fig. 2.10. The solid-state Surelite III Nd:YAG (neodymium-doped yttrium aluminium garnet) laser (from Continuum company[91]), placed on an optical table, generates high-power pulses with a wavelength of 266 nm[4]. The Nd^{3+} dopant ions serve as a lasing medium, replacing the Y^{3+} ions in the crystal structure of $Y_3Al_5O_{12}$ garnet, which is optically pumped to create population inversion with a Xe lamp. The photons emitted by stimulated emission bounce between the mirrors of the optical resonator before escaping through a partially reflective mirror. To prevent dangerous exposure to the laser beam, the laser contains a shutter near the exit hole that needs to be opened mechanically. Even though this crystal emits light with a wavelength of 1064 nm, nonlinear optical elements are used to quadruple the frequency, producing a fourth harmonic with a wavelength of 266 nm. The pulse duration was chosen to be $\tau = 5$ ns at the repetition rate $f = 10$ Hz. To ensure safety, another mechanical shutter is placed in the beam path. Both the laser and the mechanical shutter can be controlled via a custom LabVIEW software (see Fig. 2.12).

The laser beam is then directed through a system of three optical mirrors, which reflect it onto a target in the deposition chamber. Before entering the deposition chamber, the laser beam passes through a focusing lens (40 cm focal length), forming a smaller elliptical laser spot with area $S = 0.0455$ cm^2. The size of a single pulse laser spot was determined using a laser alignment paper placed at the same position as the target. By measuring the lengths of the semi-major and semi-minor axes a and b, respectively, the area of the elliptical spot was calculated by formula $S = \pi ab$.

The third mirror can be displaced, allowing the laser beam to strike a detector behind it for laser energy determination. The total laser energy E was measured using a FieldMaxII-TOP™ laser energy meter (from Coherent company[92], depicted in Fig. 2.10d that uses a pyroelectric detector J-50MB-YAG (Fig. 2.10c). The software displays the time-resolved energy value with a sampling rate of 10 Hz (see the upper left corner of Fig. 2.12), showing a sine-like behaviour over time. Therefore, the mean energy value was calculated by averaging a certain number of data points (in our case 200), together with the standard deviation, providing the statistical error of energy $\sigma_{E_{stat}}$. Since the manufacturer states that the measurement accuracy $\sigma_{E_{meas}}$ is $\pm 1\%$ of the reading, the total energy error σ_E is given as $\sigma_E = \sqrt{\sigma^2_{E_{meas}} + \sigma^2_{E_{stat}}}$. Hence, for our depositions the total laser energy and its error corresponded to $E = 90(3)$ mJ.

However, during deposition, the optical path is slightly different compared to that of energy measurement because the laser reflects off an additional third mirror and passes through a laser entrance window, which attenuates the beam and lowers the fluence. The window is made of quartz because it must be transparent to the UV laser wavelength. By measuring the optical transmittance of the window, the total attenuation was estimated to be about 10 %, but in the following text we will always present the value measured by the energy meter. Finally, the average fluence $\bar{F}$ was evaluated from Equation (2.5), considering its error $\sigma_{\bar{F}} = \frac{\sigma_E}{E}\bar{F}$, as $\bar{F} = 2.0(1)$ J.cm^{-2}.

[4] Also, ArF, KrF and XeCl gas excimer lasers are a popular option in PLD applications.

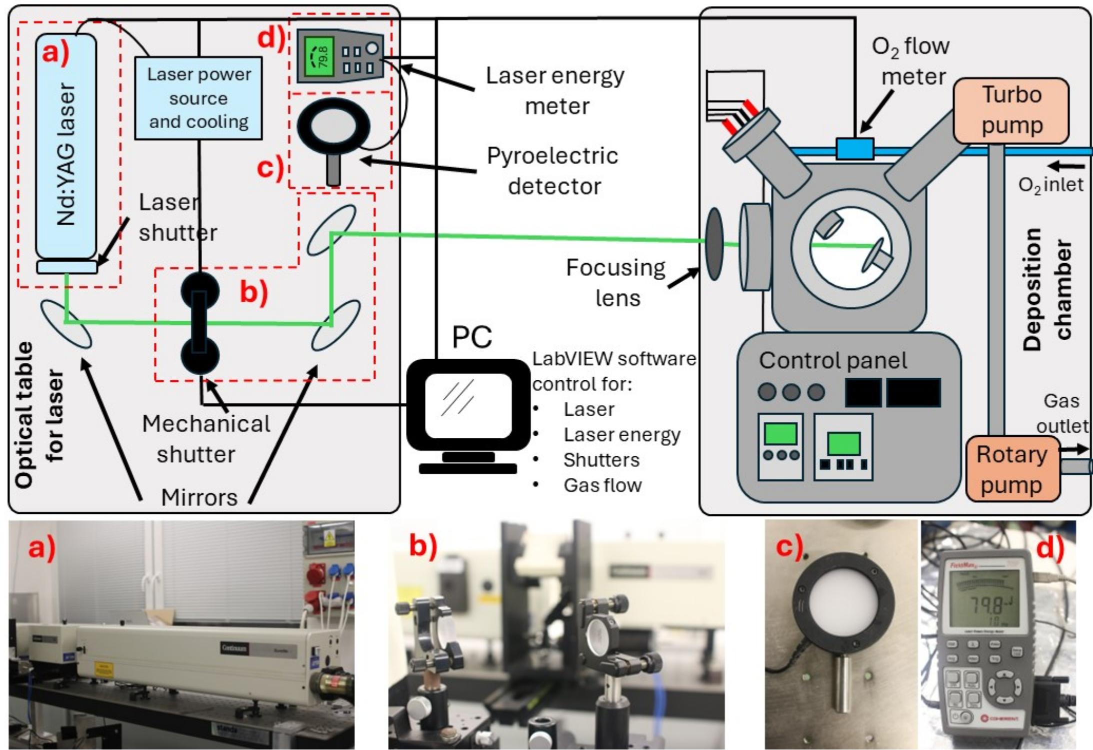

Figure 2.10: Schematic diagram of our laboratory PLD system (upper part) and a few photographs of its components (bottom part) showing a) Nd:YAG laser, b) optical mirrors c) pyroelectric detector, and d) laser power and energy meter.

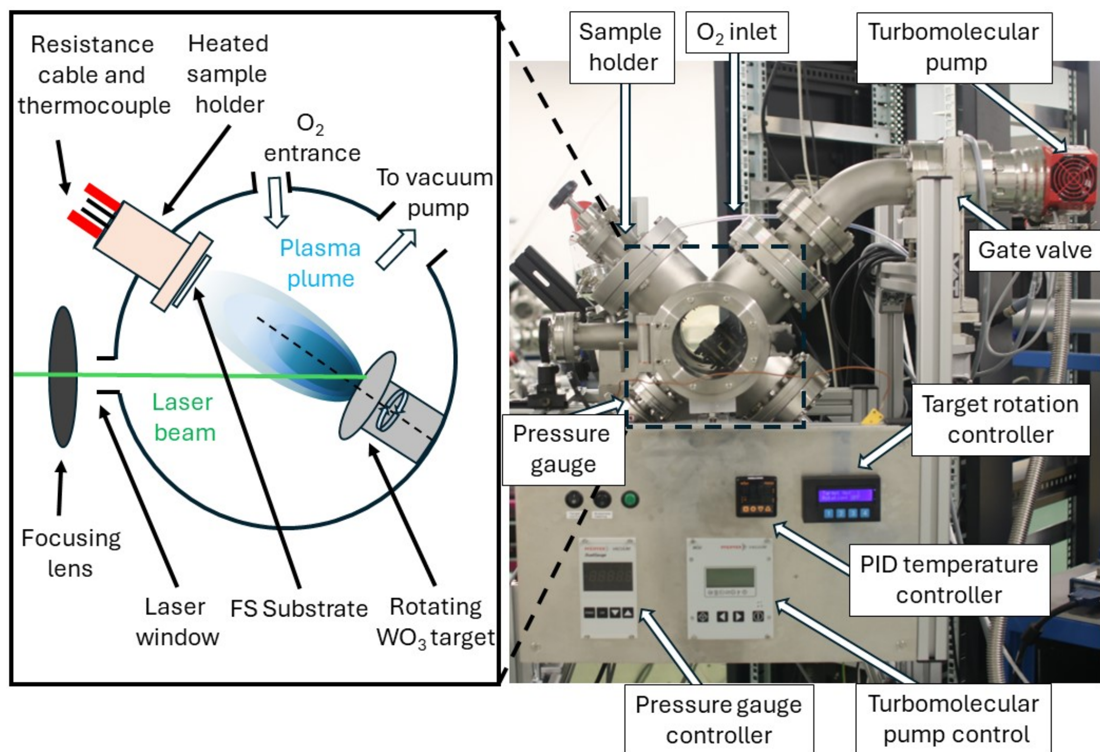

Figure 2.11: Schematic diagram (left) and photograph (right) of our PLD vacuum chamber and its components.

The deposition chamber and its schematic diagram are depicted in more detail in Fig. 2.11. Prior to deposition, the substrate is placed on a sample holder (see Fig. 2.13) and inserted into the chamber using a 40 mm KF flange at a fixed working distance $d = 10$ cm from the target. The vacuum chamber is evacuated to a low vacuum of approximately 20 - 50 Pa using a primary rotary pump (Pfeiffer Duo 1.6)[93], and a base pressure of about 5×10^{-4} Pa is achieved with a secondary turbomolecular pump (Pfeiffer D-35614 Asslar HiPace 80)[94]. Both pumps are separated from the chamber by a manual gate valve. Pressures above 100 Pa are measured by a diaphragm capacitance vacuum gauge (Pfeiffer CMR 364)[95] and pressures below 100 Pa by a Penning gauge (Compact Cold Cathode Gauge PKR260 by Balzers)[96]. For high-temperature depositions, a resistance cable for heating can be mounted to the back side of the sample holder together with a thermocouple for temperature measurements. The temperature is controlled by a proportional-integral-derivative (PID) controller (by Selec)[97]. In the meantime, the laser can be started to heat up and stabilize.

As soon as high-vacuum is reached, the turbomolecular pump is set to stand-by mode, and working gas (in our case oxygen) is introduced into the chamber at a defined flow rate, again controlled by computer software (Fig. 2.12). The desired deposition pressure is adjusted by partially closing the gate valve. To start a deposition, we can either open the mechanical shutter manually or select a specific pulse count, after which the program will automatically close the shutter. During the deposition, the focused laser beam is incident on a rotating target to provide uniform ablation. The plasma plume can be observed from the outside through a window in front. A similar window is also located on the opposite side, allowing for the OES of the hot plasma[21]. After deposition, the chamber is vented with ambient air once the sample cooled back to RT. The laser energy is remeasured once again to ensure that the laser power remained stable throughout the process.

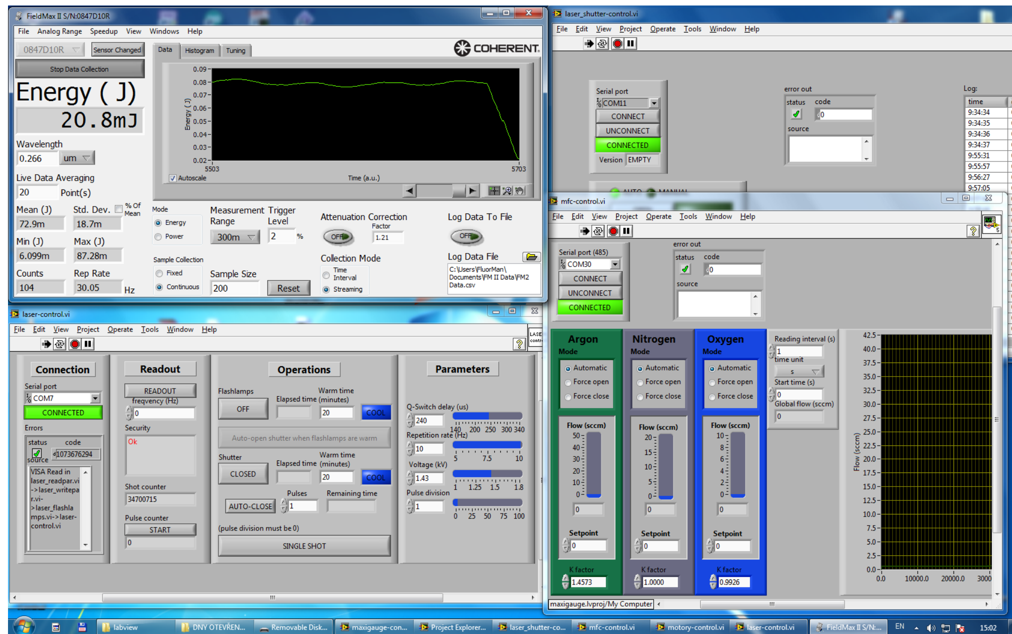

Figure 2.12: Screenshot of the LabVIEW graphical user interface programs developed for PLD showing four windows: Upper left - laser energy over time with statistical metrics such as mean and standard deviation; Upper right - mechanical shutter control and it can be used to set an exact pulse count for deposition; Bottom left - laser operation control; Bottom right - gas flow control allows introduction of various gases into the chamber by setting a flow rate.

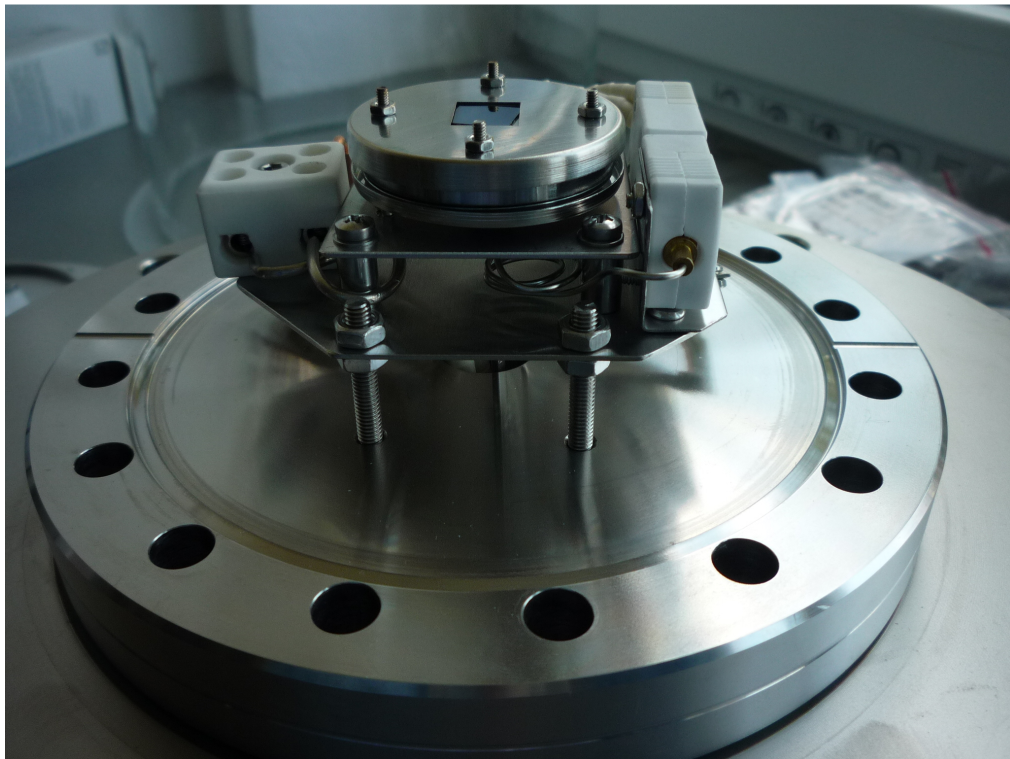

Figure 2.13: Photograph of the PLD sample holder from the inside. The sample is placed in the centre and covered under a mask, preventing heat dissipation and enabling creating a height step for thickness determination. Underneath the sample there is a heating element and thermocouple for temperature measurement.

3. Experimental techniques

In this chapter, we present an overview of the experimental techniques employed for the qualitative characterization of our samples and the quantitative determination of their various physical properties.

3.1 Morphological properties

Roughness is one of the most important technological properties of thin films for various applications and determines the outcome of many physical and chemical processes. In a larger context, it is rather a subjective term - one may describe an apple to be fairly smooth to the touch, but zooming closer to microscopic scales would reveal a wavy structure, and there is no strict distinction between these two terms. But mathematically, the concept of roughness is well grasped. Consider a single-valued function $h(\vec{r},t)$ that describes the surface height with respect to the substrate surface at a specific position given by the position vector $\vec{r}$ at time t. If in addition the sample is stationary and the surface of a film is unvarying then the function $h(\vec{r},t) = h(\vec{r})$ is independent of time. The mean value of this function, denoted as $\overline{h}(\vec{r})$, can be expressed as:

$$\overline{h}(\vec{r}) = \frac{\int h(\vec{r})d\vec{r}}{\int d\vec{r}} \tag{3.1}$$

where the domain of integration corresponds to the substrate two-dimensional domain (x-y) plane and the growth of the film takes place in a vertical (z) direction. However, surface profiles are usually experimentally obtained for a set of finite discrete points $\vec{r} = (x_i, y_j)$, where the domain of the surface is discretized into a chosen number of $N \times M$ ($i \in \{1, ..., N\}, j \in \{1, ..., M\}$) points, so the integral in the expression (3.1) can be replaced by a sum:

$$\overline{h}(\vec{r}) = \frac{1}{NM} \sum_{i=1}^{N} \sum_{j=1}^{N} h(x_i, y_j) \tag{3.2}$$

The surface roughness then quantifies the deviations of the surface height $h(\vec{r})$ from the mean value $\overline{h}(\vec{r})$. if these deviations are negligible then we consider the sample to be ideally smooth; otherwise to some extent rough. There are many roughness parameters but the most common are S_a and S_q being the arithmetic average roughness and the root-mean-square roughness, respectively[98], given by:

$$S_a = \frac{1}{NM} \sum_{i=1}^{N} \sum_{j=1}^{M} \left| h(x_i, y_j) - \overline{h}(\vec{r}) \right| \quad S_q = \sqrt{\frac{1}{NM} \sum_{i=1}^{N} \sum_{j=1}^{M} \left(h(x_i, y_j) - \overline{h}(\vec{r}) \right)^2} \tag{3.3}$$

Roughness can also be calculated along a single line profile for a function of one variable $h(x_i)$, giving rise to similarly defined parameters R_a and R_q, further simplifying Equations (3.3) by requiring only a single summation. It is often useful to redefine the surface height profile so that $\overline{h}(\vec{r}) = 0$ by choosing this average height as a reference instead of the substrate surface.

3.1.1 Profilometry

Profilometry is one of the most widespread experimental techniques thanks to its accessibility and user-friendliness. It allows for direct measurement and evaluation of various surface morphological parameters along a single line profile.

In conventional contact stylus profilometry, a small diamond tip with a radius on the order of tens of nanometres up to several micrometres (called a stylus) is brought in contact with the sample and then moved laterally across its surface. The vertical displacement as a function of position is recorded to obtain a profilometric record with a specific length, applied force, vertical and lateral resolution. The subsequent development in optical methods gave rise to a non-contact profilometry, which provides the same information employing less time-demanding optical or laser-based interferometric measurements. By avoiding direct contact, this method eliminates the risk of damaging the specimen or tip. However, the main advantage of the stylus profilometer lies in the high versatility of studied samples because it is independent of surface reflectance and offers much better resolution.

Profilometric thickness measurements were done using the KLA Tencor P6 contact profilometer with an applied force of 1 mg and a maximal vertical resolution of 13 μm, reaching resolution on the nanometre scale. The sampling speed was chosen to be 50 μm/s and the sampling frequency 50 Hz, resulting in a data point for every μm step. The software displays a real-time profilometric record and for a sample with a thickness of 190 nm it is depicted in Fig. 3.1.

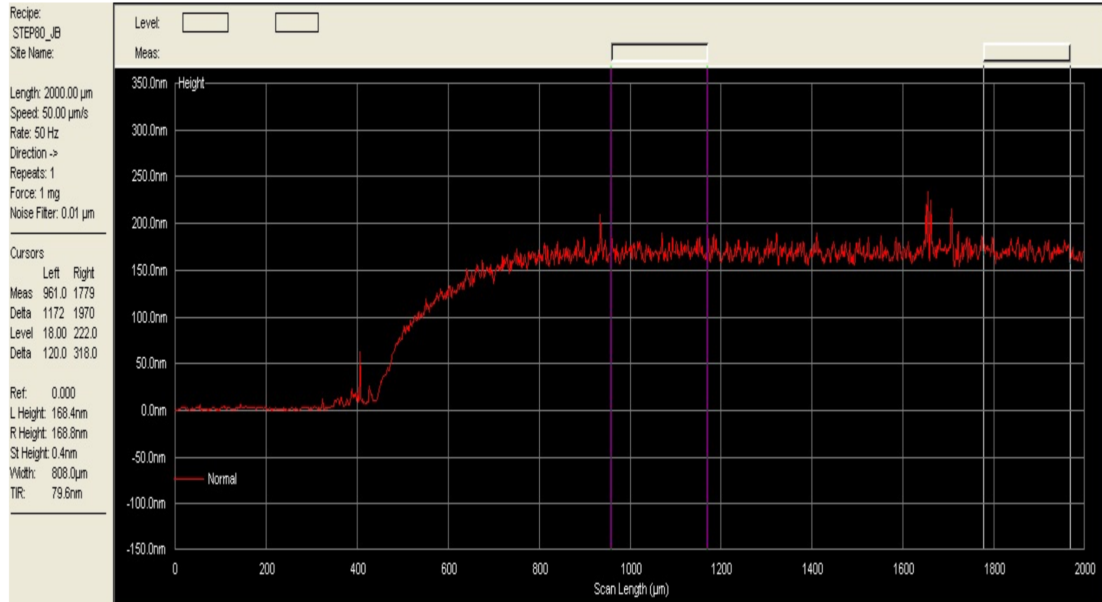

Figure 3.1: An example of a profilometric record with a length of 2 mm for film thickness determination in the Profiler 7.4 program interface. The substrate (left side) was previously covered by a mask during a deposition and the film (right side) was deposited on the exposed part of the substrate. These two plane-parallel regions are separated by a gradually rising vertical step. The thickness of $\sim$ 190 nm is determined as the mean height difference between the baselines of the substrate and the film.

3.1.2 Atomic force microscopy

Atomic force microscopy (AFM), first invented and described in 1986 by G. Binnig, C. F. Quate, and Ch. Herber[99], is a powerful imaging technique that allows visualization and investigation of surface properties of specimens with nanometric spatial resolution. The basic principle is in many aspects similar to profilometry but it relies on the interaction between a small tip and sample via weak van der Waals, electrostatic and other forces[1]. Also, it performs multiple line scans, which enables the formation of a three-dimensional final image.

The tip, much smaller than that used in a profilometer, typically has a radius on the order of several nanometres. It is part of an elastic silicon or silicon-nitride cantilever forming a probe that moves across the sample surface in the (x-y) direction. Either the probe or the sample is driven by piezoelectric scanners responsible for delicate movements (see Fig. 3.2). The forces acting on the cantilever result in its bending and the deflection is measured by the position of a reflected laser beam on a photodetector. The signal is monitored by an electronic feedback system, which continuously adjusts the sample position to control the height of the cantilever according to selected measurement parameters. The signal from the feedback system is then recorded, displayed and analysed by a computer. Additionally, the AFM may be equipped with an integrated optical microscope with a camera to view the position of the tip on the sample.

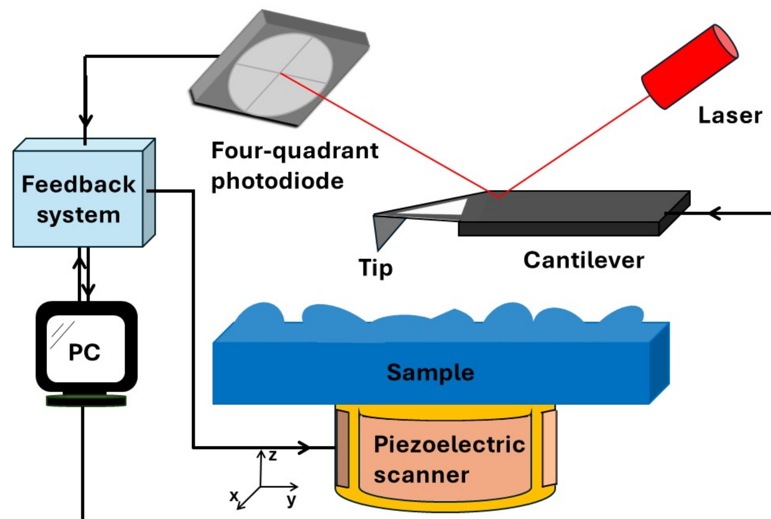

Figure 3.2: A simplified schematic diagram of basic AFM instrumentation. A piezoelectric tube scanner moves in (x-y-z) axes by applying a small voltage to four electrodes on the outside and one electrode on the inside. The upper side of the cantilever is made from highly reflective material to reflect the aligned laser beam onto a four-quadrant detector. The small displacement of the cantilever causes a large change in the laser spot and the difference in detected intensity between the top two and bottom two quadrants is proportional to the vertical displacement. Analogically, the difference between the rightmost and leftmost two quadrants is proportional to the lateral displacement.

[1]These forces acting on the tip are often approximated by Lenard-Jones potential with the magnitude of $10^{-9} - 10^{-12}$ N[100]

AFM can be operated in various measurement modes, the most prevalent are[101]:

- *Contact mode* - the tip is bought into contact with the sample and the interaction force F is determined from the Hooke's law $F = k\Delta z$, where k is the elastic constant of the cantilever and Δz is the tip displacement due to bending. In the constant-force mode, the feedback system maintains the pre-set value of this force and adjusts the height accordingly. The voltage applied to the z-piezo element is measured as a function of tip position. If the feedback system is inactive, then a constant-height mode is utilized, where the cantilever deflection is measured. It is conceptually the simplest and fastest mode, although the dragging of the material of soft samples or sudden jumps on the steep surface features for hard samples may lead to tip or sample damage. Also, capillary and plasticity effects might negatively distort the resulting image.
- *Semi-contact mode* - sometimes also referred to as "tapping mode" the cantilever is excited by forced oscillation near its resonant frequency to reach a certain amplitude of oscillations. As the cantilever approaches the surface it briefly comes into contact with the sample resulting in a change of the oscillation amplitude and phase. The feedback system applies voltage to keep the amplitude at a constant level and this voltage is recorded. Here, the phase-contrast images can be simultaneously obtained identifying regions with different material properties. Since the sample and the tip are in direct contact for a short duration, this technique provides a reduced risk of damage.
- *Non-contact mode* - the tip is brought into proximity of the sample but is kept at a higher distance so that only attractive forces apply. Similarly to the previous case, the oscillating signal with a small amplitude is generated, and the change in resonant frequency and amplitude is measured. The absence of intermittent contact further decreases the tip wear but it is very sensitive to any contamination present on most surfaces under ambient conditions.

The final AFM image is a convolution of a tip shape with a sample surface topography. The usage of unsuitable tips, due to their size, shape, or quality, is responsible for image artefacts (see Fig. 3.3). The source of these artefacts must be recognized beforehand to avoid their misinterpretation. Only after successful identification of these artefacts we can remove them during processing of the images. Other artefacts could be introduced by e.g. piezoelectric scanner nonlinearity, hysteresis or creep[102], incorrect image processing, sample inclination, etc. Since the whole instrument is highly susceptible to any environmental factors, the whole stage is supported on a platform that actively and/or passively reduces noise from external acoustic or mechanical vibrations and stabilises thermal drift effects. Usually, the measurements are performed in ambient conditions and AFM does not require samples to be conductive.

For our data visualization and analysis, Gwyddion[103], an open-source software developed by the Czech Metrology Institute, served as our tool. The program provides a large number of analytical, data, and image processing tools for height fields obtained by AFM, such as levelling, background removal, data correction and transformation, masking, filtering, statistical characteristics, etc. It

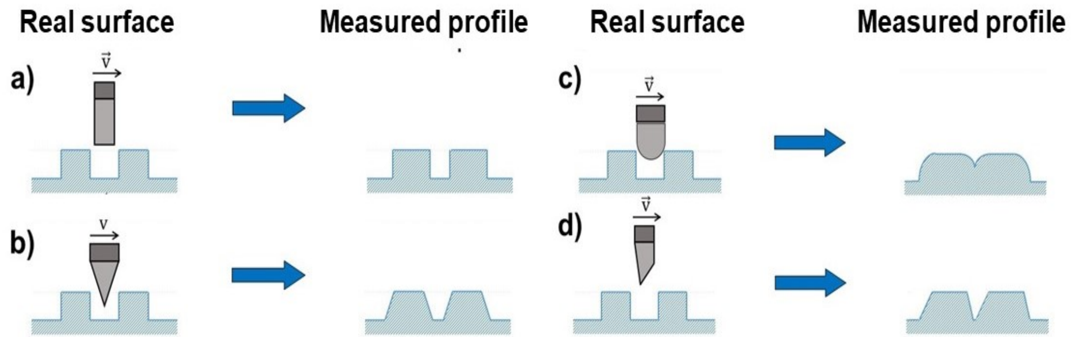

Figure 3.3: Illustration of probe-induced artefacts in AFM: a) The probe with appropriate tip shape and size gives satisfying results and the slight change in the measured surface profile is unavoidable due to the omnipresent finite size of the tip. b) The wrong probe shape also alters the shape of surface features. c) The blunt or contaminated tip makes convex features as grains appear larger laterally, while concave features as cavities tend to appear smaller. d) The broken tip shows repeating features with asymmetric inclination.

provides 2D and 3D false-colour visual representations, although 2D images are usually preferred in the scientific community due to their clarity (see Fig. 3.4). It is important to keep in mind that while the elimination of image artefacts is desired for the final picture quality, it must be done with caution to ensure that we do not affect the real intrinsic properties of the studied sample. Over-processing can potentially alter surface parameters, leading to inaccurate results[104].

The AFM images (of sizes 1 μm $\times$ 1 μm and 5 μm $\times$ 5 μm) were acquired by Dimension Icon - Ambient Atomic Force Microscope from Bruker company using PeakForce Tapping mode with ScanAsyst - Air probe (k = 0,4 N/m, f_0 = 70 kHz and nominal tip radius 2 nm) under ambient conditions. Both detailed and larger images had a resolution of 512 $\times$ 512 pixels^2. The instrument was placed on a several-ton heavy concrete block, which had been isolated from the rest of the building to eliminate unwanted external vibrations.

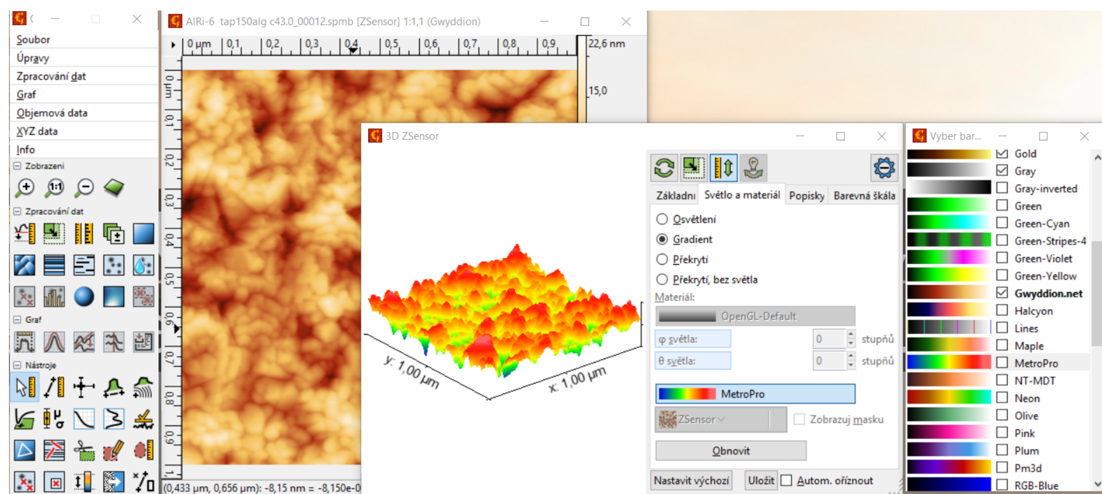

Figure 3.4: An illustration of the graphical user interface of Gwyddion. The toolbar for data processing is located on the left side, while the 3D visualization tool is positioned on the right side, offering a wide palette of colours.

3.1.3 Scanning electron microscopy

Scanning electron microscopy (SEM) is a common imaging technique used to visualize the surface of materials, creating images with high magnification and resolution, and providing useful information about the morphology, overall microstructure, and crystallography of a specimen. The basic principle, first demonstrated by Knoll and Ruska in 1932[105] and developed by von Ardenne in 1937[106], involves the interaction of a finely focused electron beam with the sample.

The resolution of an optical microscope d, often understood as the smallest separation between two point-like objects in which they are still distinguishable, is constrained by the Abbe diffraction limit[107]:

$$d = \frac{\lambda}{2n \sin \alpha} \tag{3.4}$$

where λ is the wavelength of light, and $n \sin \alpha = NA$ is the numerical aperture of the objective (n is a refractive index and α the half-angle over which the light enters objective). Therefore, an optical microscope is unable to resolve objects smaller than roughly 1 μm and the maximal magnification is approximately 1000-times. According to de Broglie hypothesis, an electron has an associated wavelength $\lambda = \frac{h}{p}$, where h is the Planck's constant and p is the momentum of the electron. In SEM, electrons are accelerated by an electric field with voltage U to a kinetic energy $E_k = eU = \frac{1}{2}mv^2$. If we further express momentum $p = mv$ as a product of electron mass m and its velocity v[2], combining these equations we can obtain the expression for electron wavelength:

$$\lambda = \frac{h}{\sqrt{2meU}} \approx \frac{1.23 \times 10^{-9}}{\sqrt{U}} \tag{3.5}$$

In SEM, the acceleration voltage of up to 30 keV is typically used, which yields a wavelength of 7 pm and more. So electrons with significantly shorter wavelengths enable us to achieve practically a resolution of ~1 nm and magnification effectively up to 10^6-times[3]. However, the maximal usable magnification for practical imaging may be limited by factors such as sample preparation, stability, and detector capabilities.

The schematic diagram of the basic SEM is shown in Fig. 3.5a. The electrons are emitted from an electron gun, usually a tungsten filament or a LaB_6 crystal, where electrons are released via thermionic emission. Higher spatial resolution and reliability is achieved by field emission guns utilizing a strong electric field around a very sharp tip. The electrons are then accelerated by an electric field from an anode to chosen energies. Afterward, the electron beam is modified by a system of apertures, magnetic and/or electrostatic lenses and electromagnetic coils that are responsible for beam collimation and diameter reduction. The focused beam subsequently scans the surface of the sample in a lateral raster pattern in an (x-y plane) perpendicular to the beam direction. At each discrete scan location, the electrons interact with the atoms of the sample and generate a signal, which is measured by an appropriate detector. Finally, the signal is digitized and recorded by a computer pixel-by-pixel.

[2]We are neglecting here the relativistic effects.

[3]This estimation takes into account capabilities of electron optics and correction for relativistic effects.

The incident electrons lose energy due to interaction with the sample atoms within an interaction volume (see Fig. 3.5b) divided into various regions corresponding to different penetration depths. The size and shape of the interaction volume depend on the acceleration voltage and the properties of the sample material such as density, chemical composition, etc., leading to very complex structures. However, at 0° tilt, the interaction volume is rotationally symmetric around the beam and can be modelled, e.g. by Monte Carlo simulations[108]. The main types of signal obtained in SEM include (see Fig. 3.6):

- *Secondary electrons (SE)* are inelastically scattered electrons that escape the sample surface after the primary electrons from the beam eject the electron from conduction or valence bands. Since these electrons have low kinetic energy (< 50 eV), they originate only from depths corresponding to a few nanometers up to tens of nanometers. Thus SE provides a so-called topographic contrast, containing information on the surface morphology of the sample.
- *Backscattered electrons (BSE)* are electrons from the primary beam that undergo scattering events due to attractive interactions with atomic nuclei of the sample, which sometimes completely reverse their initial direction and consequently electrons return back toward the sample surface. Since the energy of the incident beam is in order of keV, these electrons can penetrate to much higher depth (approximately hundreds of nanometers) and still lose only a negligible fraction of their initial energy. The amount of lost energy depends on the length of the trajectory within the sample. The interaction cross-section increases monotonically with the atomic number Z, thus BSE distinguish regions with different chemical compositions (often referred to as Z-contrast).
- *X-ray* radiation is produced due to the deceleration of electrons and there are two main mechanisms of X-ray generation. Characteristic X-rays are generated when a primary electron ejects an electron from the inner shell (with binding energy E_1), leaving behind a vacancy and an electron from the outer shell (with binding energy E_2) fills the void, it releases a photon with an energy $E = E_1 - E_2$ corresponding to the transition energy between the two states.[4]. Braking radiation (bremsstrahlung) is a consequence of an energy loss of primary electrons. It has a continuous spectrum and only contributes to the background. The emission depth of X-ray is roughly in order of micrometers.
- *Auger electrons (AE)* are emitted as a result of the Auger effect, which is a three-step process. Firstly, the primary electron ionizes the atom by ejecting the electron from the inner shell leading to a creation of vacancy. Secondly, the electron from the outer shell fills the void. Finally, this transition energy is absorbed by another electron, which is ejected from its shell, leaving the atom with two vacancies. The energy of these AE is even smaller than in the case of secondary electrons, therefore they provide more surface-sensitive information.

[4]In the Siegbahn notation, the energy levels of electrons within the atom are often denoted in the ascending order as K-, L-, M-, and so on atomic shells. The transition energy corresponding to transition (L $\rightarrow$ K) is denoted as K_α, (M $\rightarrow$ K) as K_β, (M $\rightarrow$ L) as L_α, etc.

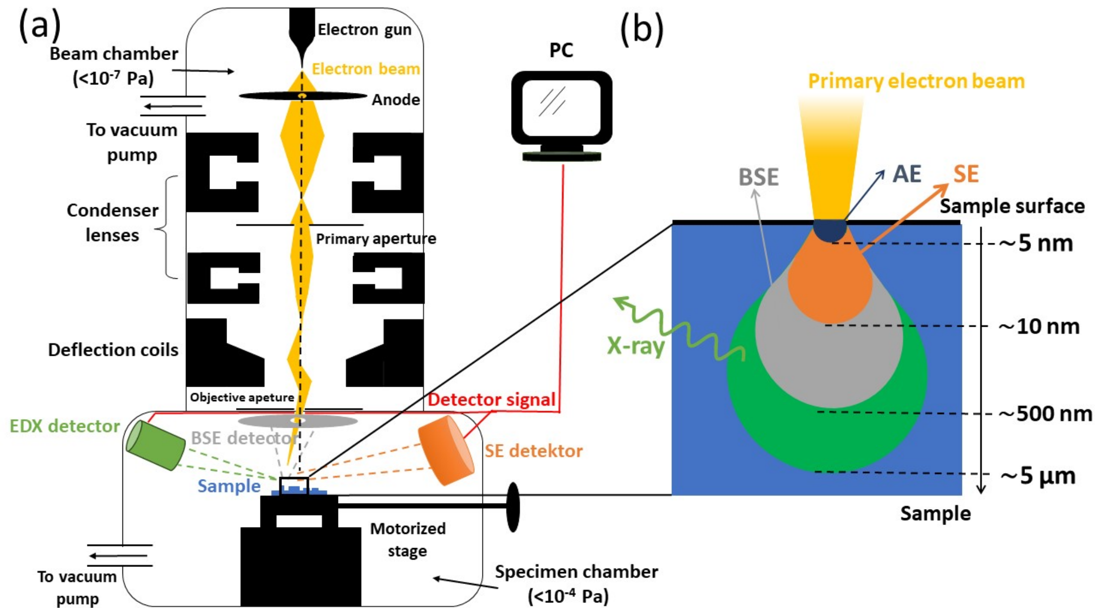

Figure 3.5: (a) Schematic diagram of an SEM instrument. In conventional SEM a high level of vacuum ($< 10^{-4}$) in the specimen chamber is required. Samples must be properly grounded to prevent the development of surface charge, (b) simplified scheme of an interaction volume of electrons with atoms of the atoms within the sample. Different types of signals with a rough estimation of their corresponding penetration depths.

BSE can also be utilized to image the microstructure of different crystalline phases in a polycrystalline sample. Crystallographic orientation may have an impact on the total number of backscattered electron through a phenomenon known as orientation contrast to form an electron backscatter diffraction (EBSD) pattern[108]. Moreover, since characteristic X-rays have specific well-defined energies for electron transition in each atom, by measuring the energies of these X-ray photons we can determine both qualitatively and quantitatively the chemical composition of a sample. However, energy-dispersive X-ray spectroscopy (EDX) is sometimes inappropriate for thin films because of the high emission depth of X-rays and is therefore used rather for bulk materials. During EDX measurement, the working distance[5] needs to be constant to ensure an optimal signal. For our measurements, it was set to 10 cm. An example of EDX spectra is depicted in Fig. 3.7.

Compared to AFM, SEM captures only a 2D image of a sample and cannot provide information about its height, and thus surface roughness. Furthermore, the sample needs to be sufficiently electrically conductive to prevent charging that distorts the image. The built-up charge must be therefore dissipated by e.g. usage of conductive clamps, applying another additional coating, or using a lower vacuum. The first method is non-destructive but often insufficient. In the second case, additional coatings can alter the final properties of a thin film, making it unsuitable for our purposes. The last one might lead to image quality

[5] Working distance refers to the distance between a sample and a detector during the experiment. In the case of the SE measurement mode, it is often desired to have the detector closer to the sample.

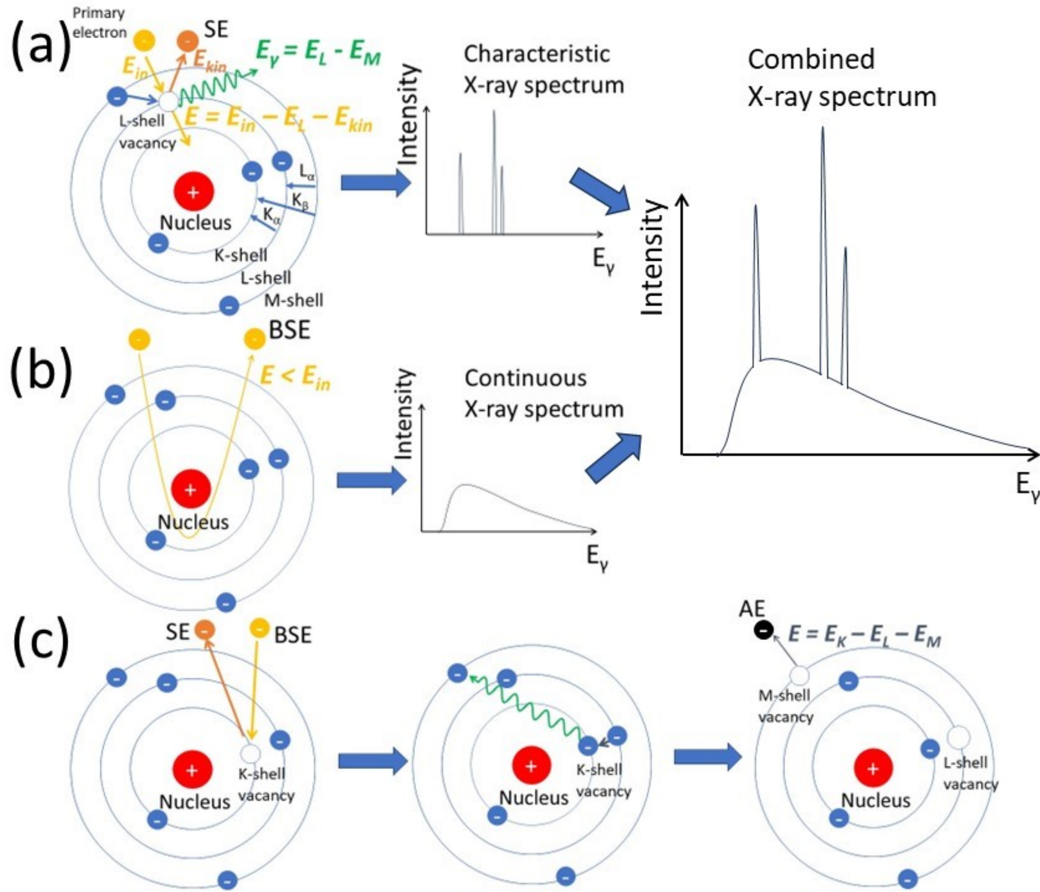

Figure 3.6: Emission of various SEM signals (a) Generation mechanism of SE and characteristic X-rays. Here, a primary electron with kinetic energy E_{in} is inelastically scattered and causes the ejection of L-shell electron while transferring some amount of energy equal to binding energy E_L and kinetic energy of SE E_{kin}. If an electron from the outer shell fills the vacancy, the characteristic X-rays are generated with sharp discrete energies, (b) BSE electrons and resulting continuous X-rays, (c) Generation of AE by Auger three-step process. The resultant kinetic energy of AE is independent of initial electron energy and is given only by a difference in binding energies.

deterioration due to the interaction of the electron beam with gas molecules present in the chamber so it is also not preferred. Overall, sample preparation and high vacuum requirement make this technique more time-demanding than AFM, despite usually faster image capture. Other artefacts can be caused by improper beam alignment, including astigmatism, chromatic aberration or other optical errors. For these reasons, it is beneficial to combine these two methods.

SEM measurements were carried out using the JSM 7200F (see Fig. 3.8a) from Jeol company (SE mode, 15 kV acceleration voltage) to capture images for samples at RT to see the surface morphology. In continuation, the SEM images with thermal treatment were acquired by Nova NanoSEM 450 (see Fig. 3.8b) from FEI company[109] (SE mode, acceleration voltage 20 kV) equipped with a field emission gun and a heating stage (Kammrath & Weiss GmbH), capable of operating at temperatures up to 800°C[110]. The microscope can also capture high-resolution videos, so we can observe real-time temperature-induced changes.

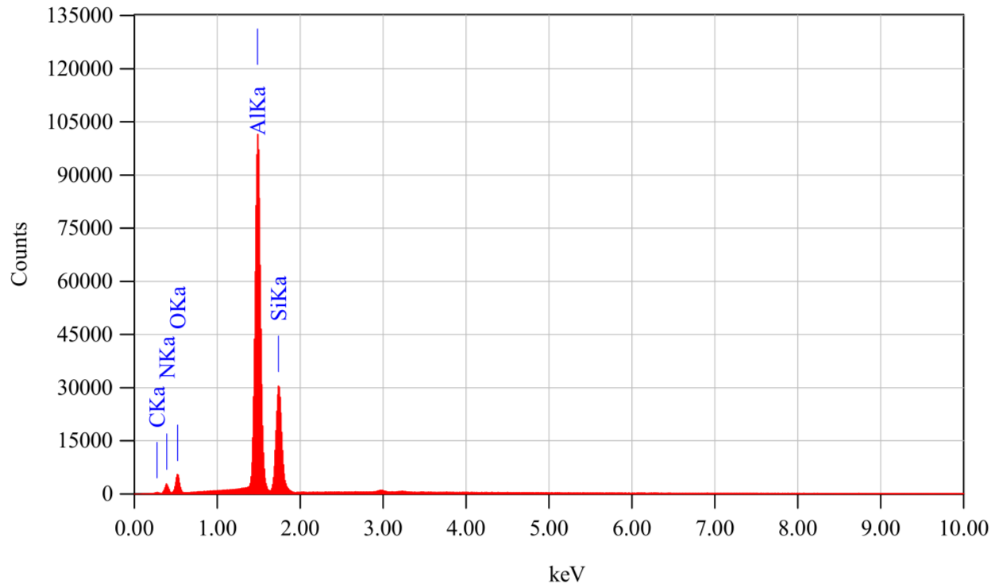

Figure 3.7: Example EDX spectrum of sample B-Al 03. The signal shows the presence of carbon, nitrogen, oxygen, aluminium and silicon both from the thin film as well as the fused silica substrate due to the high emission depth of X-rays. The quantitative analysis can be performed from the intensities of each line, although an accurate quantification is usually limited to only a rough estimation ($\sim$ 1 at.%). For this sample, we also face a problem with overlapping oxygen peaks.

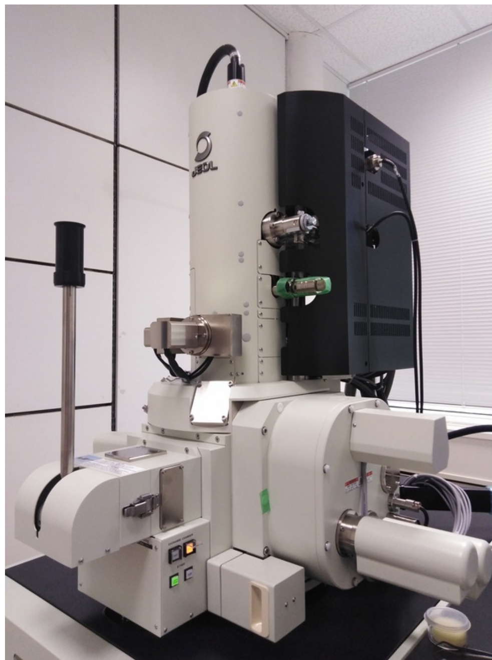

(a) Jeol JSM 7200F SEM located at the Department of Macromolecular Physics at the Faculty of Mathematics and Physics, Charles University.

(b) FEI Nova NanoSEM 450 located at the Institute of Physics, University of Tartu used for heat-treatment measurements.

Figure 3.8: Photographs of the SEM used in this work.

3.2 X-ray diffraction

X-ray diffraction (XRD) is a widely used analytical technique for determining the structural properties of crystalline materials. It has been around for over a century since its discovery in 1912 by M. von Laue, W. Friedrich and P. Knipping [111]. The basic principle of XRD utilizes incident X-rays, in our case monochromatic, as a probe that enters the specimen and interacts with the electrons of the atoms in the crystal lattice. If the wavelength of the X-ray radiation is comparable or smaller than the lattice parameter, then these serve as scattering centres that create a secondary scattered spherical wave propagating to every direction. The scattered waves from each individual atom then interfere with each other, resulting in a diffraction pattern consisting of intensity peaks (also referred to as reflections) that can be detected by a diffractometer. Further investigation of diffraction pattern then allows us to perform various analyses such as qualitative and quantitative structural and phase identification, lattice parameters determination, texture, stress and defects detection, etc.

For an ideal single crystal, the position of every lattice point can be described using a lattice translation vector:

$$\vec{R} = n_1\vec{a_1} + n_2\vec{a_2} + n_3\vec{a_3} \tag{3.6}$$

where n_1, n_2 and n_3 are any integers and $\vec{a_1}$, $\vec{a_2}$ and $\vec{a_3}$ are primitive translation vectors. However, the diffraction is described in a reciprocal space using reciprocal space vectors $\vec{b_1}$, $\vec{b_2}$ and $\vec{b_3}$ constructed so that $\vec{a_i} \cdot \vec{b_i} = 2\pi\delta_{ij}$ for $i, j \in \{1, 2, 3\}$ where δ_{ij} is Kronecker delta, yielding expression for these vectors [57]:

$$\vec{b_1} = 2\pi\frac{\vec{a_2} \times \vec{a_3}}{\vec{a_1} \cdot (\vec{a_2} \times \vec{a_3})} \qquad \vec{b_2} = 2\pi\frac{\vec{a_3} \times \vec{a_1}}{\vec{a_1} \cdot (\vec{a_2} \times \vec{a_3})} \qquad \vec{b_3} = 2\pi\frac{\vec{a_1} \times \vec{a_2}}{\vec{a_1} \cdot (\vec{a_2} \times \vec{a_3})} \tag{3.7}$$

where $V_p = \vec{a_1} \cdot (\vec{a_2} \times a_3)$ is a volume of the primitive cell given by lattice translation vectors. So analogically to Equation (3.6) every point in the reciprocal space can be described as a linear combination of the abovementioned reciprocal space vector as:

$$\vec{G} = v_1\vec{b_1} + v_2\vec{b_2} + v_3\vec{b_3} \tag{3.8}$$

where again v_1, v_2 and v_3 are any integers. A diffraction pattern preserves the symmetry of a primitive cell and the distance between two lattice points in reciprocal space is inversely proportional to their distance in real space.

When the path difference between X-rays scattered by adjacent planes, separated by distance d apart, is equal to an integer multiple of the X-ray wavelength, then the constructive interference occurs and we observe maximum in the intensity of the diffraction pattern. This simple and classical explanation was provided first by W. L. Bragg, yielding the famous Bragg law [112]:

$$2d_{hkl} \sin\theta_{hkl} = n\lambda \tag{3.9}$$

where d_{hkl} is the spacing between two adjacent parallel planes (hkl) corresponding to integers hkl (Miller indices) and θ_{hkl} is the diffraction angle between the incident wave and (hkl) plane for which the condition of constructive interference

is met. In a polycrystalline sample there are many randomly oriented crystallites[6] and therefore the diffraction condition (3.9) will be satisfied for a particular angle θ_{hkl}. If we further denote $\vec{k_0}$ the wave vector corresponding to the incident wave and $\vec{k}$ the wave vector of the scattered wave from the crystal, we can define a diffraction vector $\vec{q} = \vec{k} - \vec{k_0}$. The diffraction condition is satisfied if:

$$\vec{q} = \vec{G}_{hkl} = h\vec{a_1} + k\vec{a_2} + l\vec{a_3} \tag{3.10}$$

and the inter-planar distance d_{hkl} can be obtained by:

$$d_{hkl} = \frac{2\pi}{\left|\vec{G}_{hkl}\right|} \tag{3.11}$$

A coherent monochromatic X-ray beam is generated via an X-ray tube. The thermionically emitted electrons from a heated tungsten cathode are accelerated towards the anode from an appropriate material by an electric field by applying a high voltage between the electrodes on the order of tens of kV. The discrete characteristic X-rays are produced by electron transitions between different energy levels in the anode material. Additionally, continuous bremsstrahlung radiation is also produced due to rapidly decelerated electrons that impact the anode. Upon the impact, electrons convert most of their kinetic energy into heat, and therefore X-ray tubes need to be cooled down by a water cooling system.

The choice of wavelength is crucial and depends on the studied material. Firstly, for samples containing multiple crystalline phases or for crystals with low symmetry, there are many diffraction peaks situated close to each other. In this case, it might be beneficial to increase their separation by using an X-ray tube with a longer wavelength (see Equation 3.9). Secondly, it is desired to avoid wavelengths that could lead to the emission of secondary X-ray fluorescence radiation from a sample which further increases the background signal. Typically, the most intense lines from the entire spectrum, corresponding to transitions between the two lowest energy levels (denoted as K_α lines), are selected, while other wavelengths are filtered out. Most commonly, Cu (K_α = 1.5418 Å), Co (K_α = 1.7902 Å) or Mo (K_α = 0.7063 Å) are used[7]. The X-ray beam then passes through a small beryllium window, emerging from a tube in a divergent cone. To restrict the vertical divergence of the incident beam, Soller slits are placed between the X-ray tube and the sample. They consist of sets of thin parallel slits that absorb most of the entering X-rays while not fluorescing in the energy range of interest. This results in sharper diffraction peaks and reduces background noise, thereby enhancing the signal-to-noise ratio and improving the overall quality of the diffraction pattern, especially at low scattering angles.

The sample is typically mounted on a sample holder or stage at the centre of a goniometer circle, the X-ray tube and the detector rotate around the sample. An XRD pattern represents the intensity of the diffracted X-rays as a function of the double diffraction angle 2θ.

[6] In crystallography, crystallites are referred to as small coherently diffracting domains within a polycrystalline sample. Their sizes can differ from the size of the grains determined by other methods e.g. SEM.

[7] In reality, this transition corresponds to a doublet with two distinct lines with very close wavelength $K_{\alpha 1}$ and $K_{\alpha 2}$. In the case of Cu anode, the intensity ratio of the lines is 2:1, respectively[113].

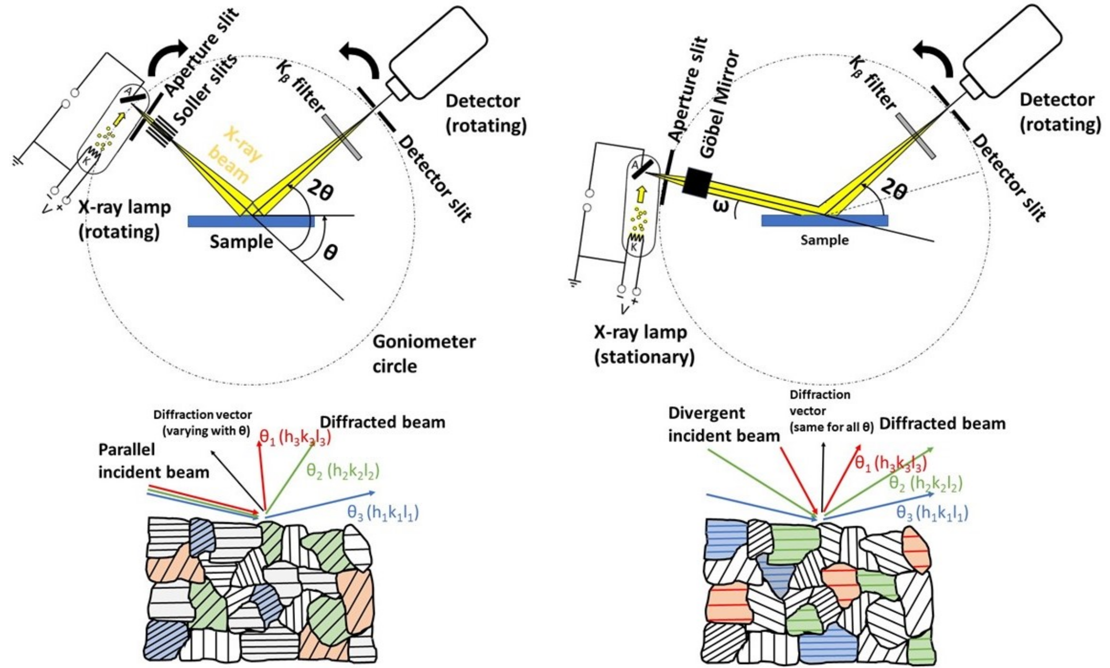

Figure 3.9: Scheme of the two basic XRD geometries used for thin film characterization. X-rays are generated by electrons impacting upon anode (A) from a cathode (K) in an X-ray tube. (a) Bragg-Brentano symmetric geometry and (b) grazing incidence asymmetric geometry. The bottom part of the figure shows different grains that contribute to the diffraction.

XRD measurements can be conducted using various geometries, each with its advantages and disadvantages. In the XRD community, conventional Bragg-Brentano (BB) geometry (see Fig. 3.9) has been dominant for years. In this setup, the divergent incident X-ray beam and the diffracted X-ray beam have the same angle θ relative to the sample surface, so the angle of the diffracted beam is 2θ. The sample is typically mounted on a sample holder or stage in the centre of a goniometer circle. Either both the tube and the detector are moving along the stationary sample with the same constant velocity (in the so-called $\theta - \theta$ scan) or the X-ray tube remains stationary, while the sample rotates by the angle θ and the detector rotates by the angle 2θ in a certain time ($\theta - 2\theta$ scan). Consequently, the diffraction takes place only from the planes (hkl) oriented parallel to the surface for each reflection. This geometry provides reliable information on the preferred orientation of crystallites (texture[8]), lattice strain, and crystallite size.

However, the penetration depth of X-ray radiation significantly increases with increasing diffraction angle, which is not always ideal for thin films, since it can exceed the thickness of the film, leading to an undesired signal from the substrate. Hence, the asymmetric grazing incidence (GI) geometry is widely employed, as the angle between the sample surface and the X-ray tube is fixed at small values (typically in the range of 1°to 5°), resulting in a lower penetration depth in

[8]In a wide sense, texture is the distribution of crystallographic orientations of the crystallites. If the orientation of crystallites is random, then we say that a sample has no texture. Texture significantly impacts the mechanical, optical, or other properties of materials and non-textured materials are usually isotropic.

accordance with the direction perpendicular to the surface and the irradiated volume remains within the film. The detector rotates around the sample. In contrast to BB geometry, in GI geometry a divergent beam is first converted into a parallel one with a negligible divergence. This is achieved by collimating polycapillary optic systems, consisting of many glass capillaries that guide the X-ray through total reflection, or by periodic multilayers bent parabolically made of two alternating materials with varying thicknesses known as Göbel mirrors. Furthermore, the planes (hkl) inclined to the surface are diffracting for each reflection, so the method is complementary in this sense and is suitable for residual stress measurement.

From the individual reflections in a diffraction pattern we are able to extract a lot of important information, namely:

1. *Positions* - enable to perform qualitative phase analysis which contains information about the present crystalline phases and their lattice [9], symmetry and space group of their crystal lattices. The deviation from the bulk value of the lattice parameters could indicate the presence of macrostresses and various defects.

2. *Intensities* - provides information about texture and enables to perform quantitative phase analysis, giving proportions of different crystalline phases.

3. *Widths* - give information regarding mean crystalline size in the irradiated volume. Also, is able to reveal the presence of microstress and type of defects.

4. *Shapes* - can offer further insights into the nature and extent of defects present.

Each reflection in a diffraction pattern can be approximated by an appropriate analytical function. The most widely used functions are described in the Table 3.1. These include mainly Gaussian function $G(x)$, Lorentzian function $L(x)$ or Pearson VII function $P(x)$, a more generalized exponentiated Lorentzian function. Subsequently, it is well justified to prefer Voigt function $V(x)$, which is a convolution of Gaussian and Lorentzian. However, due to its computational complexity, it is being superseded by pseudo-Voigt function $V_p(x)$, a linear combination of both functions $G(x)$ and $L(x)$ with relative weight $q \in [0, 1]$.

The obtained lattice parameters a_{hkl} often vary slightly for each reflection and could be influenced by a systematic error introduced due to a minor misalignment of the specimen from the centre of the goniometer circle. Therefore, a correction function is introduced to eliminate this effect, which in the case of BB geometry is often referred to as the Cohen-Wagner (C-W) plot[114] and takes the following form:

$$a_{hkl} = a_0 + s \cos\theta \cot\theta \tag{3.12}$$

where s is the slope the linear dependence a_{hkl} as a function of $\cos\theta \cot\theta$, which characterizes the amplitude of the systematic error. The correct value of the

[9]Lattice parameters are determined by 6 constants: three lengths a,b and c defining the dimensions of a unit cell and three angles α, β and γ between them .

Analytical function	Formula
Gaussian	$G(x) = A_1 e^{-A_3(x-A_2)^2}$
Lorentzian	$L(x) = \frac{A_1}{1+A_3(x-A_2)^2}$
Pearson VII	$P(x) = \frac{A_1}{[1+A_3(x-A_2)^2]^{A_4}}$
Voigt	$V(x) = G(x) * L(x)$
Pseudo-Voigt	$V_p(x) = qG(x) + (1-q)C(x)$
Description of constants	A_1 - peak height, A_2 - peak position, A_3 - peak width, A_4 - peak shape parameter

Table 3.1: The most commonly used analytical functions for diffraction pattern peak approximation.

lattice parameter a_0 can be calculated by extrapolating the linear fit of Equation (3.12) to the value of $\theta = 90°$.

For further mathematical description of XRD, let us assume that our sample contains m crystalline phases. Then the intensity of reflection I_i from i-th phase depends on multiple factors, which can be summarised in the following relation[115]:

$$I_i = KN_i^2 RA_i LP p_i |F_i|^2 T_i E_i e^{-2M} + I_b \tag{3.13}$$

where:

- K is a scale factor that combines different experimental and instrumental parameters such as the influence of the slit widths, the flux density of the primary beam, etc.
- N is the number of unit cells (simply speaking represents the amount of sample) in the irradiated volume.
- R is a surface roughness factor.
- A is an absorption factor. which is dependent on the absorption coefficient of the sample as well as the used geometry.
- LP factor combines Lorentz factor, which is determined by instrumental configuration, and polarization factor related with elastic Thompson scattering by electrons.
- p is the multiplicity, which is the number of equivalent crystallographic planes that contribute to a particular diffraction peak
- F is the structure factor that describes the intensity of diffracted X-rays by atoms of the crystal lattice. It is usually expressed as:

$$F_{hkl} = \sum_n^N f_n e^{2\pi i(hx_n + ky_j + lz_n)} \tag{3.14}$$

where f_n is the atomic scattering factor and x_n, y_n and z_n are fractional coordinates of n-th atom in a unit cell so the position of each atom can be described by vector $\vec{R} = (x_n\vec{a}, y_n\vec{b}, z_n\vec{c})$. The atomic scattering factor represents the ratio of the amplitude of the diffracted wave from an atom and the amplitude of the incident wave so it is a measure of the atom's X-ray scattering power. If the frequency of the incident X-ray radiation is close to the natural oscillation frequency of the electrons of a given atom, then so-called anomalous dispersion occurs. Consequently, the expression for f_n is modified with two terms, f' and f'', which represent the real and imaginary components, respectively, of the anomalous fraction of the atomic scattering factor so that $f = f_0 + f' + if''$.

- T is a texture factor that takes into account the preferred orientation of crystallites in a certain direction.
- E is an extinction coefficient that takes into account deviations from kinematical approximation[10] We further distinguish primary extinction where secondary diffraction takes place within the same grain and secondary extinction in which diffraction happens in another grain.
- M is a Debye-Waller factor which accounts for the decrease in intensity due to thermal motion of the atoms.
- I_b is the intensity of the background.

The overall intensity I_{hkl} of a reflection corresponding to diffraction from a system of planes (hkl) is given by the sum of the intensities of individual reflections from every present phase in the sample so:

$$I_{hkl} = \sum_{i=1}^{m} I_i \tag{3.15}$$

It is questionable which parameter is ideal to choose as a measure of peak width β (see Fig. 3.10). One would suggest that the peak width at half of the maximum intensity, descriptively named full width at half maximum (FWHM), would be a logical choice. However, in some cases, the quantity integral breadth (IB), which corresponds to the width of a rectangle whose height is the same as the maximum peak intensity I_0 and with the same integrated area of the peak:

$$\mathrm{IB} = \frac{1}{I_0} \int_{-\infty}^{+\infty} I(2\theta)\, d(2\theta) \tag{3.16}$$

seems to be more fitting. For an ideal Gaussian or Lorentzian peak, there is a clear relationship between these two quantities given by:

$$\underset{\text{(Gaussian profile)}}{\mathrm{IB} = \frac{\mathrm{FWHM}}{2}\sqrt{\frac{\pi}{ln2}}} \qquad \underset{\text{(Lorentzian profile)}}{\mathrm{IB} = \frac{\pi}{2}\mathrm{FWHM}} \tag{3.17}$$

[10] The kinematical approximation assumes that each photon is scattered only once and that the transmitted wave is not affected by the scattering process. This assumption is valid if the total path length of a photon in the scattering object is much smaller than the extinction length. This is not satisfied in the case of large perfect crystals or mosaic crystals and the dynamical theory of diffraction needs to be taken into account.

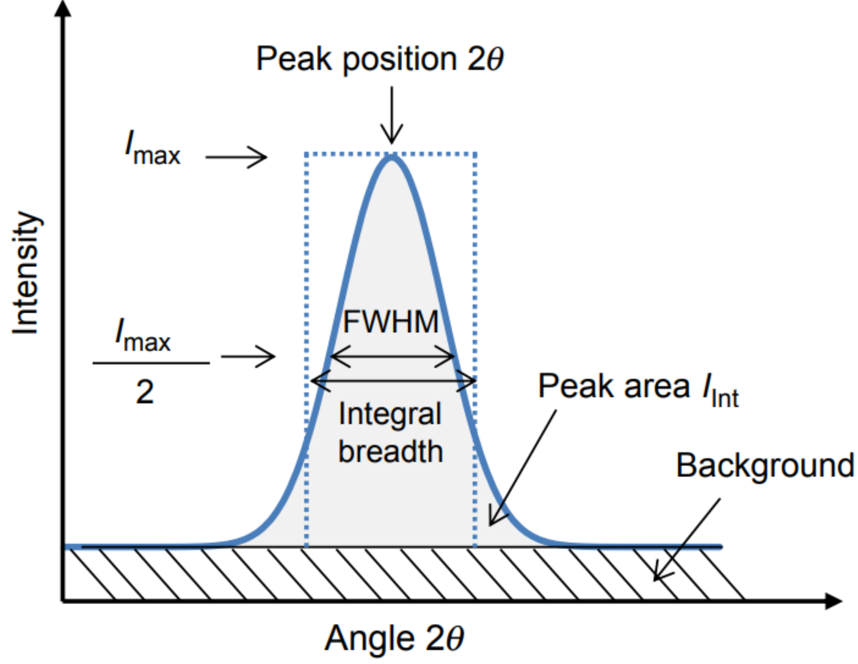

Figure 3.10: Schematic of a diffraction peak showing different peak parameters and comparison between FWHM and IB. Taken from [115].

The width of diffraction peaks is affected by both physical broadening $f(2\theta)$ caused by a sample itself, such as the finite size of crystallites and the presence of microstrain, and by instrumental broadening $g(2\theta)$ mainly due to the source of the X-ray and the X-ray optics used. The final measured profile $h(\theta)$ is given as a convolution of these contributions:

$$h(2\theta) = f(2\theta) * g(2\theta) \tag{3.18}$$

A proper peak profile analysis involves a deconvolution of these two components.

Instrumental broadening is a constant inherent property of every diffractometer and it can be determined by measuring a diffraction pattern of an appropriate standard, usually defectless and textureless crystal with numerous very narrow peaks, where physical broadening can be neglected. Most commonly LaB_6 is chosen. If the reflections of the standard are not situated at the same positions as the studied sample, then it is necessary to do interpolation via a proper interpolation function. The comparison between the standard measured in different geometries and the X-ray sources can be found in Figure 3.11. So by measuring the standard, we can subtract the instrumental broadening and obtain the physical broadening but the peak shape needs to be taken into consideration. For a Gaussian shape, the expression for total FWHM β takes the form:

$$\beta = \sqrt{\beta_{instrument}^2 + \beta_{physical}^2} \tag{3.19}$$

where $\beta_{instrument}$ and $\beta_{physical}$ are FWHM corresponding to instrumental and physical broadening, respectively. For purely Lorentzian profile the expression is modified to a simple sum of these two terms as following:

$$\beta = \beta_{instrument} + \beta_{physical} \tag{3.20}$$

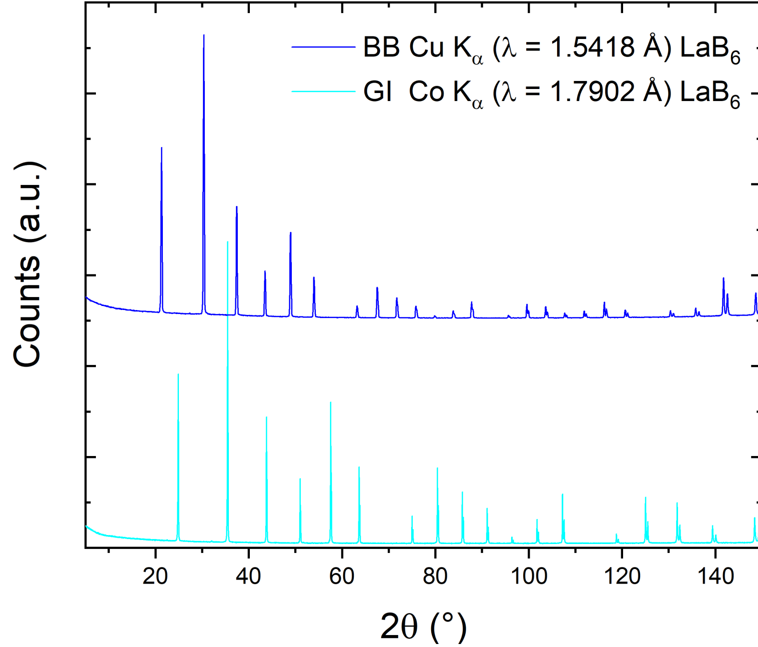

Figure 3.11: Diffraction pattern of LaB_6 standard measured in BB and GI geometries with two different X-ray tubes. The peaks are shifted according to Equation (3.9) and the intensities differ. Since we used a thin film, more signal comes in the case of GI geometry due to lower penetration depth. From the width of each reflection, the physical broadening for each geometry is determined for further analysis.

Physical broadening is predominantly caused by the presence of various defects, such as dislocations, stacking faults, or microstrain as well as the size and shape of crystallites. Microstrain represents the fluctuation of inter-planar distances within the small grains on a microscopic level due to deformation or thermal effects. This results in a change of the lattice parameter a for each individual grain from the expected value a_0, thus broadening the corresponding diffraction peak. The extent of a microstrain is expressed by a dimensionless number $e = \frac{a-a_0}{a_0}$. On the other hand, macrostrain is homogeneous throughout a macroscopic volume, leading to a shift of diffraction peaks towards higher or lower diffraction angles.

The method that separates the contribution of crystalline size D and microstrain e was provided by Williamson and Hall in 1953[116]. It assumes that both of these contributions are independent and that the overall physical broadening of a diffraction peak to hkl reflection is given by a sum:

$$\beta_{hkl} = \frac{k\lambda}{D\cos\theta} + 4e\tan\theta \tag{3.21}$$

where k is a constant characterizing the shape of crystallites[11], λ is the wavelength of used X-ray radiation. Usually, it is represented as a linear dependence of $\beta_{hkl}\cos\theta$ on $\sin\theta$, which is called the Williamson-Hall (W-H) plot. From the slope of the linear regression, we are able to obtain the value of the microstrain

[11]Constant k is e.g. equal to 0.89 and 0.94 for IB and FWHM of spherical crystals with cubic symmetry, respectively.

and the intercept provides information about mean crystallite size. If the value of microstrain is negligible, it can be omitted, giving us an expression already well-known as the Scherrer formula [117]:

$$\beta_{hkl} = \frac{K\lambda}{D\cos\theta} \tag{3.22}$$

However, it is often difficult to properly attribute broadening to either microstrain or crystalline size effect. Therefore, FWHM and IB are combined in various works[118][119], although FWHM nowadays seems more prevalent.

To accurately estimate the above-mentioned parameters of the investigated sample from a measured diffraction pattern, a precise fitting procedure is required. There are two main approaches to fitting a diffraction pattern:

1. The fitting of the individual isolated diffraction peaks, where each peak is approximated via an appropriate fitting function from Table 3.1 and the background contribution is usually considered to be linear in the vicinity of a chosen reflection.

2. Rietveld refinement, where the whole diffraction pattern is approximated at once via a calculated fitting model, which takes into account both the structural properties of the sample and instrumental factors. The parameters of the fitting functions are adjusted to get the optimal match between the refined and measured diffraction patterns.

The Rietveld method, first proposed by Hugo Rietveld in two of his papers [120][121], uses an iterative least-squares method to minimize the difference between the calculated and measured diffraction pattern. The quality of the fit is usually quantified with a certain numerical figure of merit, of which most commonly used is the goodness of fit χ^2[122]:

$$\chi^2 = \frac{\sum_{i=1}^{n} w_i (y_i^{obs} - y_i^{calc})^2}{n-p} \tag{3.23}$$

where y_i^{obs}, y_i^{calc} are the observed intensity and calculated intensity of i-th measured points, respectively, w_i represents the weight of i-th data point and usually taken as $w_i = \frac{1}{\sigma_i^2} = \frac{1}{y_i^{obs}}$ with σ_i being a standard deviation of i-th point, n is a total number of measured points and p is number of adjustable parameters in the fitting model, so $n - p$ represents degrees of freedom. It is worth mentioning that there is no strict rule or agreement for a maximal accepted value of χ^2 to consider our fit as correct. The background is in this case more complicated and also contributes to χ^2 so it is one of the refined parameters. Most popularly, the background is treated as a Chebyshev polynomial. Other refined parameters include e.g. sample displacement, multiple peak shape parameters, unit cell dimensions and occupation of site position by atoms, texture, porosity, absorption and extinction, scale factors for each phase, etc. For mean crystallite size and microstrain estimation, the Rietveld refinement assumes that FWHM of reflections can be globally described by the Caglioti formula[123][12]:

$$FWHM = \sqrt{W + V\tan\theta + U\tan^2\theta} \tag{3.24}$$

[12] Other and more advanced approach is using Le Bail method[124]

where U, V, and W are refined parameters dependent on instrumental settings. The parameters U_{std}, V_{std}, and W_{std} can be obtained from the diffraction pattern of a chosen standard in the same geometry. By comparing the parameters U, U_{std} and V, V_{std} we can conclude the mean crystallite size D and microstrain e using a proper fitting software.

In this work, the XRD analysis was performed using an Empyrean Panalytical Series 2 diffractometer with Cu K_α ($\lambda = 1.5418$Å, 45 kV, 30 mA) X-ray tube and PIXcel^{3D} – Medipix3 area detector in open slit mode. In GI geometry, a parallel beam was created using Göbel mirror (graded W/Si crystal) and Soller slits of 0.04 rad were placed in the way of the primary beam. Also, a horizontal mask of 8 mm and a fixed slit 1/2° were used to ensure that the beam had a smaller width than our sample (less than 10 mm). In the diffracted beam path, a parallel plate collimator of 0.18° was placed. A step size of 0.1°[13], with a time step of 4 s for each step was chosen to obtain a sufficient signal-to-noise ratio. The Rietveld refinement of diffraction patterns was performed in GSAS-II software[125] (see Fig. 3.12) using an appropriate CIF-file from a database[14] that contains all the information about the crystallographic structure of the studied material and can therefore be used as an initial model that is slightly adjusted to obtain the refined parameters. All of the theoretical XRD patterns and unit cell schematic diagrams were generated using VESTA software[126].

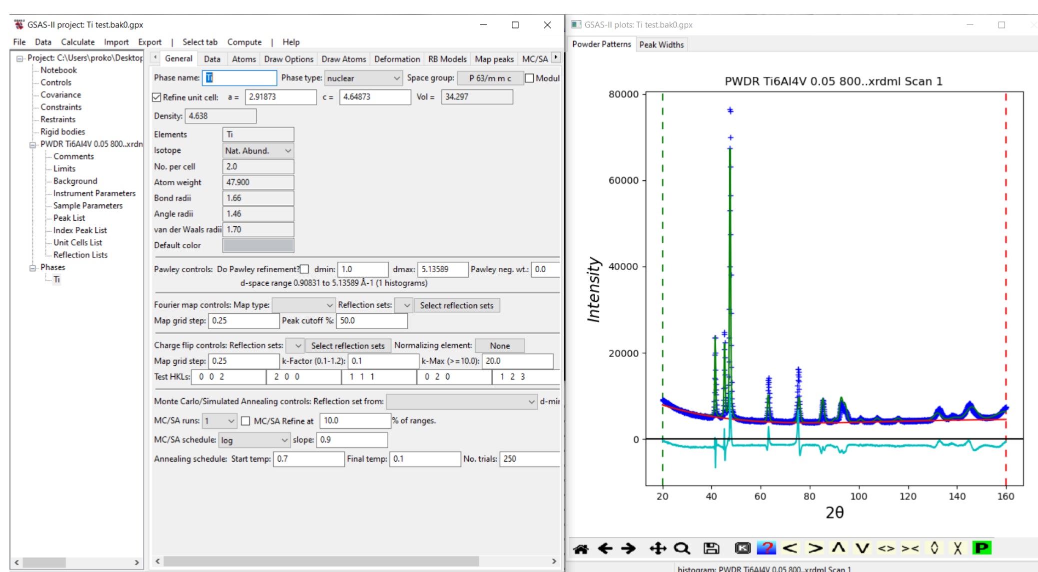

Figure 3.12: An illustration of the graphical user interface of GSAS-II software. The window on the right shows XRD pattern data (blue points) with calculated background (red line), and Rietveld refinement (green line) together with the difference between the data and fit (cyan line). The refined parameters are displayed in the left window.

[13]The step size is usually chosen to be sufficiently small, preferably to contain at least 5 data points per FWHM.

[14]Among these databases Powder Diffraction File (PDF-5+) or Inorganic Crystal Structure Database (ICSD) are the largest and best-known.

3.3 Optical measurements

Optical measurements serve to study the interaction of an electromagnetic field with materials. Particularly, spectroscopy measurements allow us to determine the band structure of thin films. Unfortunately, these properties are not accessible directly and must be obtained from measurements of optical spectra, the dependence of reflectance or transmittance as a function of the wavelength, along with their comparison to theoretical calculations.

The key device for the optical measurements is the monochromator, which is capable of selecting the desired narrow band of wavelength from a polychromatic light source, usually utilizing a diffraction grating. The monochromator can be positioned either before or after the sample. In the former case, a sample is illuminated with a narrow band of wavelength at each measurement step and spectra are acquired. To transition to another part of the light spectrum, the diffraction grating is simply rotated. However, this procedure is more time-consuming, leading to a longer measurement duration. In the latter case, the sample is exposed to a polychromatic light first and the light is separated afterwards. This enables faster spectra aquisition but can be unsuitable for fluorescent samples, as shorter-wavelength light can excite electrons, leading to subsequent de-excitation and emission of light at longer wavelengths, therefore affecting the resulting spectrum.

There are two distinct types of spectroscopic measurements of reflectance:

- *Specular reflectance* measurements, performed by an instrument called spectrophotometer, the reflected light from the surface follows the law of reflection and a detector gathers light in a fixed direction. Typically, specular reflectance is dominant for smooth surfaces creating a mirror-like reflection.

- *Diffuse reflectance* occurs when the reflected light is irregularly scattered in many different directions, hence not preserving the law of reflection. The surfaces that exhibit diffuse reflection are usually rough, resulting in a dimmer appearance due to the lower intensity of light in a certain position. An instrument called integrating sphere[127] is used to collect light from all directions. It consists of a hollow sphere with its inner walls covered with a highly reflective material, assuming negligible intensity loss compared to a reflection from a measured sample. Most commonly, Spectralon, possessing the highest known reflectivity of any materials of >99 % in UV-VIS-NIR spectral range[128], is employed. The sphere also contains two holes for light entrance and exit. The light from a source is guided by an optical cable through the entrance hole and directed onto a sample situated inside the sphere, where it undergoes multiple reflections leaving through the exit hole and finally reaching the detector.

For specular transmittance and reflectance measurements, we used an optical measurement instrumentation shown in Fig. 3.13i. The DT-MINI-2-GS light source was employed that contains deuterium (200 – 410 nm) and tungsten halogen (360 – 2000 nm) lamps. The measurements were carried out in the wavelength range of 200 – 900 nm. The light is guided towards the collimator and is directed towards the sample located on a sample table. The light coming from the sample again passes onto a collimator and is gathered in the spectrometer Ocean Optics

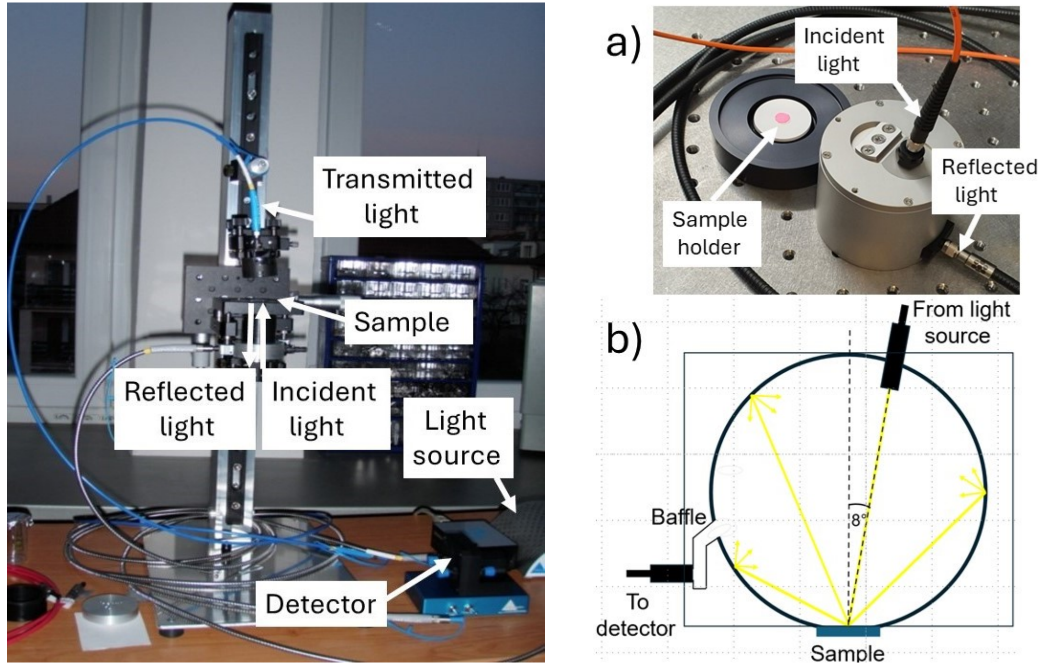

(i) Experimental setup for specular reflectivity and transmittance measurement. In this configuration, transmittance measurement can be performed.

(ii) (a) Photo of the integrating sphere AvaSphere50 used for diffuse reflectance measuerement. (b) Schematic diagram of diffuse reflectance measurement.

Figure 3.13: Instrumentation used for specular reflectance and transmittance measurements.

USB 4000-UV-VIS equipped with a linear CCD detector. The spectra can be displayed in real-time using SpectraSuite software also by Ocean Optics company. For each measurement light (reference - without sample) and dark (background - with closed shutter) spectra were acquired.

Diffuse reflectance measurements were performed using the integrating sphere AvaSphere50 (see Fig. 3.13ii) with the fibre-coupled halogen lamp source Thorlabs SLS201L in the wavelength range of 400 – 1100 nm. Halogen lamp light from the fibre was focused by an aspherical lens to form a spot of approximate size 8 nm in diameter and the sample was placed below the round hole with a diameter of 10 mm under the incidence angle of 8° from the perpendicular direction. The output of an integrating sphere was coupled to a bifurcated fibre bundle with one end going to the UV-VIS-NIR (silicon CCD detector) compact spectrometer (AvaSpec-ULS2048XL-RS-EVO) and the second to the NIR (InGaAs array detector) compact spectrometer (AvaSpec-NIR256-1.7-HSC-EVO). The reflectance was calibrated using the Spectralon standard of diffused reflectance (from LabSphere company). For every measurement, the background and reference spectra were obtained for proper evaluation of spectra.

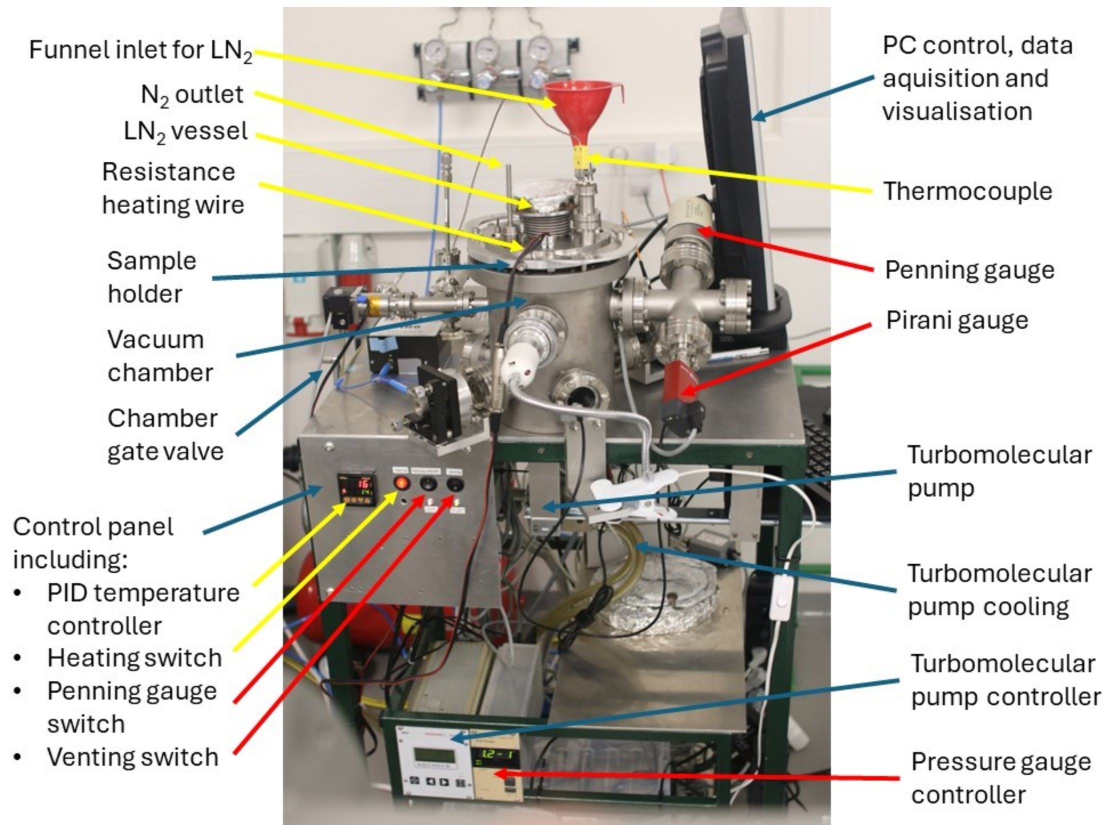

Figure 3.14: The front view of our transmittance measurement system. The basic vacuum chamber components are indicated by blue arrows, while those responsible for achieving high vacuum and different temperatures are denoted by red and yellow arrows, respectively.

Our transmittance measurement system (see Fig. 3.14, 3.15) enables us to conduct measurements at different temperatures, which is crucial for studying the thermochromic properties of our oxide films. The whole apparatus consists of a cylindrical vacuum chamber with a diameter of 155 mm and a height of 200 mm. We perform the measurements under high vacuum conditions ($\sim 10^{-5}$ Pa)[15] to prevent heat transfer between the sample and the environment and to eliminate oxidation caused by residual oxygen in the chamber. This is achieved by a differential pumping system composed of a primary rotary pump (VR 1,5/12 by Lavat[129]) capable of reaching a primary vacuum of ~ 10 Pa and a secondary turbomolecular pump (TMH 071 P by Pfeiffer[130]) located below the chamber. The chamber is separated from the pumping system by a manual gate valve. Following measurement, a compressed air-driven pneumatic valve provides the air venting with ambient air.

After inserting the sample into the sample holder and placing it in the chamber, the primary rotary pump is used to achieve a low vacuum, which usually takes several minutes. The pressure in the chamber is measured by the combined gauge consisting of Pirani and diaphragm capacitive sensor (Compact Pirani Capacitance Gauge PCR280 by Pfeiffer[131]). At higher pressures (above 10^3 Pa),

[15] The value of the base pressure can vary slightly and is influenced mainly by the overall sealing quality of the chamber due to the presence of leaks, pumping time, and the water desorption rate, which is more significant at elevated temperatures.

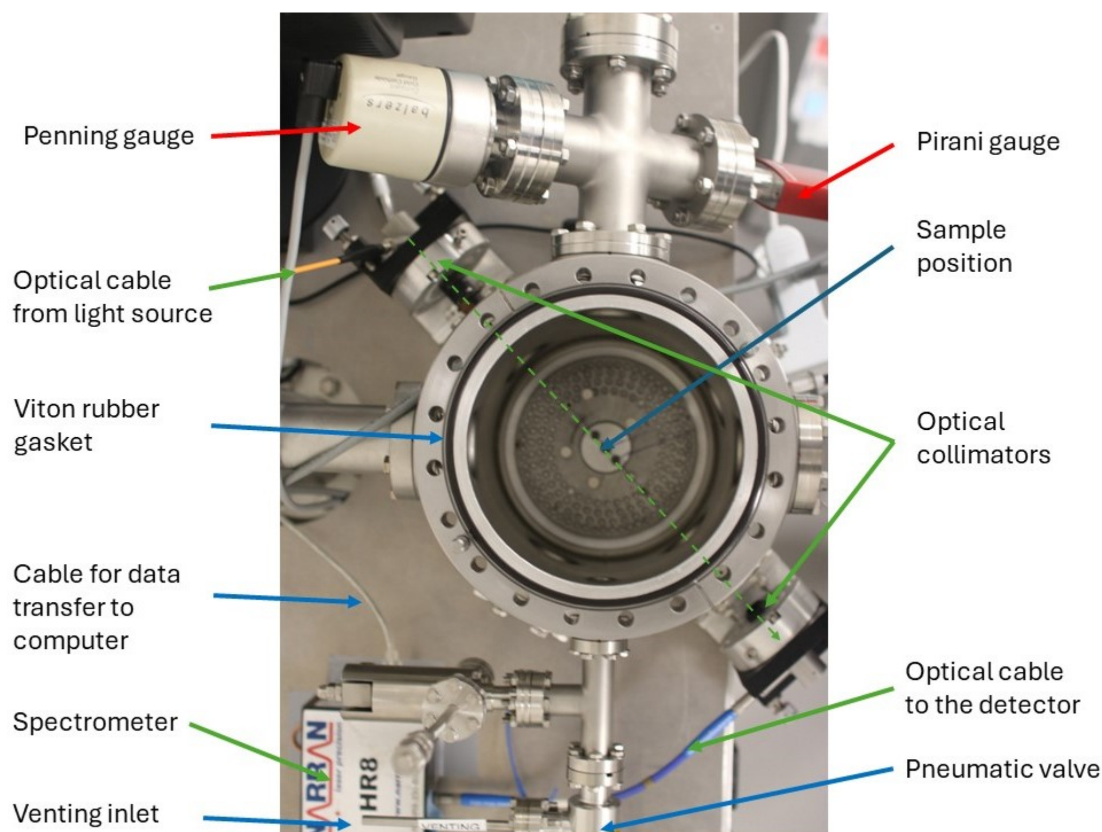

Figure 3.15: The top view of our transmittance measurement system without the sample holder inserted, showing the inside part of the chamber. Additionally from the previous figure, the green arrows denote the optical components. The dashed line indicates the direction of the light beam passing through the sample, located in the middle of the chamber, during the measurement.

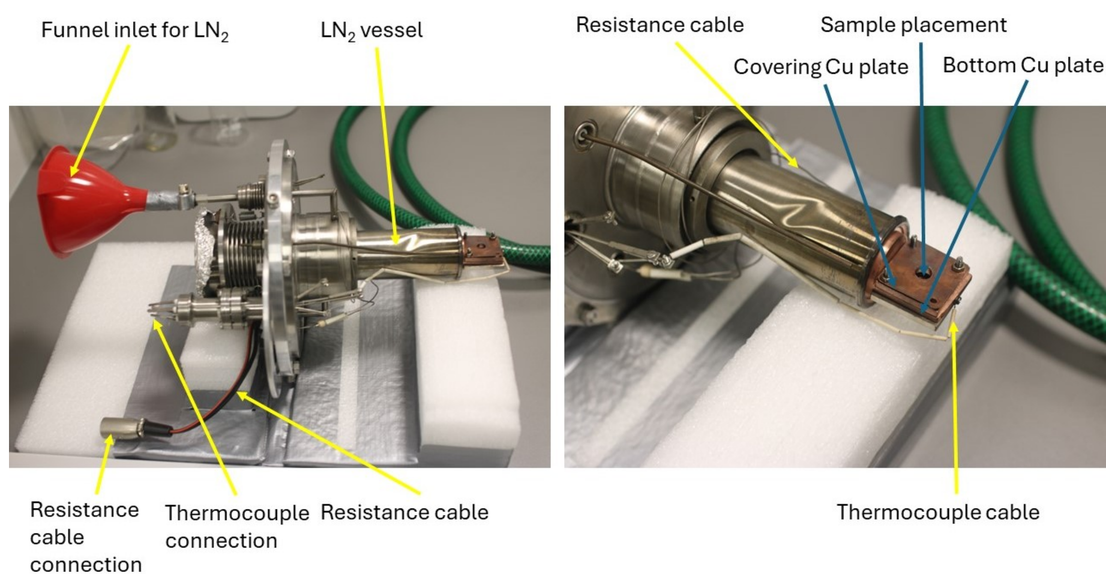

Figure 3.16: A photo of the sample holder used for transmittance measurements: The left figure shows the whole sample holder, while the right one provides a more detailed perspective of the sample placement.

the capacitive diaphragm sensor provides a signal by measuring the capacitance between a thin diaphragm and a fixed electrode. The pressure in the chamber applies a force on the surface of the diaphragm causing its deflection, thus altering the capacitance. To reach lower pressures, the turbomolecular pump is started and the Pirani sensor is utilized (up to 5×10^{-3} Pa). It consists of a metal wire that is heated and exposed to residual chamber gases. The gas molecules transfer heat from the wire due to their thermal conductivity and the heat loss for a given power input is measured, which is a function of the gas pressure. In the crossover range, the signal from both of these sensors is used to determine the pressure. However, for the pressure range in our measurements, another device is used, called a Penning gauge (Compact Cold Cathode Gauge PKR260 by Balzers[96]). It operates on the principle of an inverted magnetron, where a glow discharge is ignited between its electrodes in a crossed electric and magnetic field, causing the ionisation of the residual gases. Consequently, the ions are accelerated towards the electrodes and contribute to the ion current. Because the ion current is proportional to the pressure in the chamber, it can be evaluated.

Usually, within 30–60 minutes, a sufficient base pressure is reached. The temperature of the sample is measured by a thermocouple and controlled by a proportional-integral-derivative controller (PID500 by Selec[97]). Firstly, the sample is cooled down to a temperature of -100°C[16] by liquid nitrogen (LN_2) that can be poured through a funnel into a hollow sample holder vessel (for details see Fig. 3.16). The vessel is in direct contact with the Cu plate, which contains a hole with a diameter of 9 mm in its centre for passing light, where a sample is placed covered with another thinner Cu plate, yet the thermocouple is connected opposite to the vessel. But since copper has the best thermal conductivity among commonly used metals, we assume that heat is quickly transferred onto the sample and the temperature of the sample matches the temperature of the Cu plate. To suffice this condition, for every temperature step we need to wait long enough to reach a thermal equilibrium (usually approximately 5 minutes per step). Subsequently, the heating of the sample is provided by a resistance wire by the mechanism of Joule heat with a power capable of reaching up to 300°C. However, since the time required for obtaining the near-maximal temperatures is gradually increasing, we chose to perform our measurements in the range from -100°C to 250°C with a temperature step of 25°C, yielding a total of 15 measurements with a total time of approximately 4 hours per sample. Additionally, the spectrum before and after the measurement was taken to see if the heating causes reversible or irreversible changes in the optical spectra.

The system is equipped with the duplicate light source (DT-MINI-2-GS) as the abovementioned specular reflectance system at ambient conditions, however here we employ only the halogen lamp (the spectrum can be found in Fig. 3.17). The VIS and NIR light is guided by optical cables towards a primary collimator and is focused on the centre of the sample, creating a beam with a diameter of ~ 3 mm, losing some portion of its intensity in the process. The transmitted light is then passed to a secondary collimator, before being collected by a spectrometer (HR8 Compact Spectrometer by Narran[132]) equipped with a Toshiba TCD1304DG linear array detector with 3648 pixels in the 200–1200 nm wavelength range, pro-

[16]Although LN_2 has a boiling point of -196 °C, we can reach the minimum temperature of only -130°C with our system due to suboptimal thermal isolation.

viding a resolution of 0.3 nm. The signal is acquired and displayed by a computer using its custom application software NarranHR8. The reference spectrum can be loaded a priori and the program then automatically displays transmittance.

Our 16-bit detector has a maximum count limit of 65,536 before reaching saturation. It is desired to choose the optimal integration time so that our reference spectrum is close to this value without exceeding it for any wavelength to minimize relative error η_T from Equation (1.16). For a typical transmittance of a pure fused silica glass with $T \sim 92$ % in the VIS wavelength range, the typical error falls within the range of 0.5 to 1.5 % (see Fig. 3.18) but for less transparent (metallic) films the error tends to increase. Therefore, this limitation makes measuring samples with $T < 10$ % impractical. During our measurements, done in the wavelength range of 400 - 900 nm, taking into account the intensity of our source lamp, the integration time was set to 6000 ms, with a total of 3 spectra collected for each step, and the final spectrum was obtained by averaging them. This approach helps to reduce an error caused by the detection of random cosmic or environmental radiation.

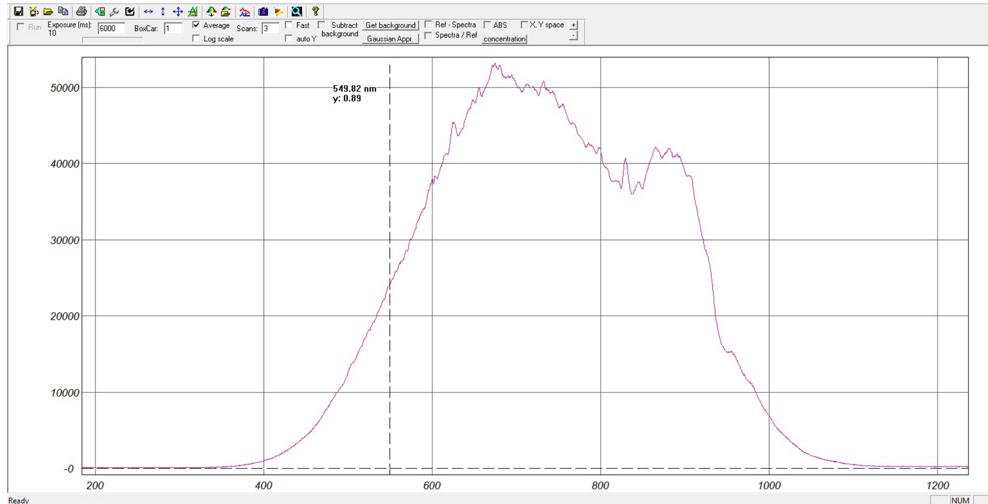

Figure 3.17: Reference optical spectrum of a halogen lamp used for the temperature-dependent transmittance measurements in Narran program interface. The integration time is 6000 ms and 3 spectra are averaged. The intensity drops significantly below 400 nm and above 1000 nm wavelength range. Therefore we performed our measurements only within the range 400-1000 nm.

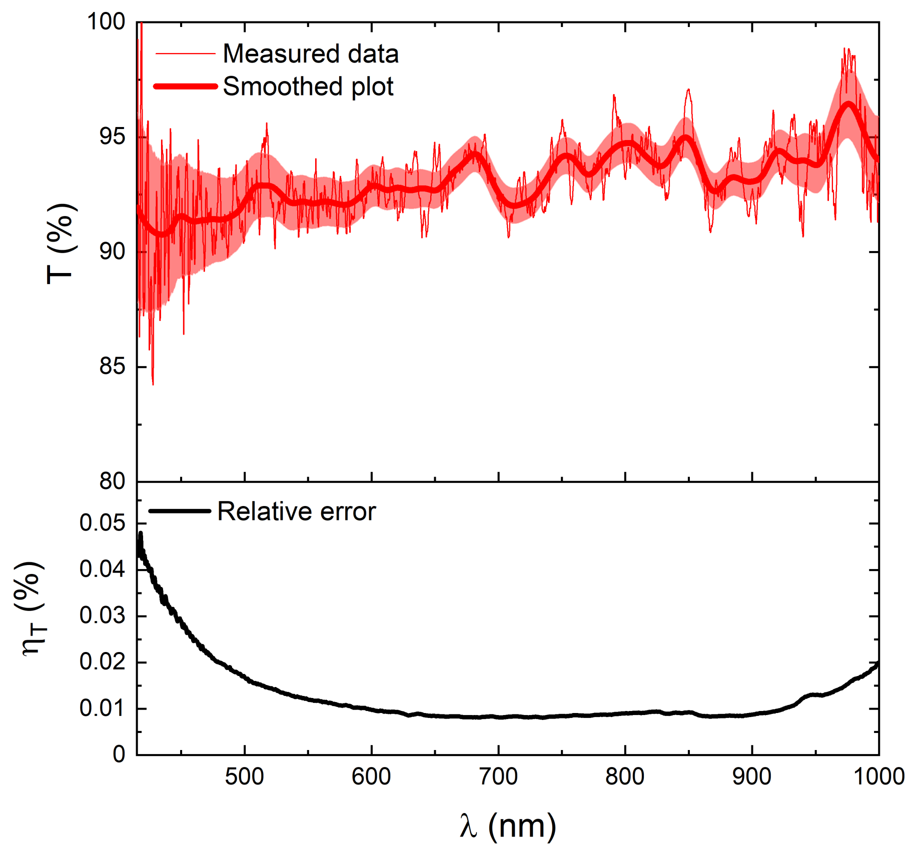

Figure 3.18: Optical transmittance spectrum of a fused silica glass and evaluation of its error. The measured data were smoothed using the adjacent-averaging method and the filled area corresponds to the measurement error according to Equation (1.15). The relative error from Equation (1.16) tends to increase towards the boundaries of our used measurement range.

3.3.1 Ellipsometry

Ellipsometry is an optical, analytical, contactless, and non-denstructive technique that uses elliptically polarised light to study the optical (or dielectric) properties of thin films. Although the basic principles of ellipsometry have been known since 1887 by the works of Drude[133], it has been widely commercialised since the 1990s due to the rapid development of computer technology, which enabled automatization of data processing and fast data acquisition. It allows for high-precision characterization of various properties, including thickness, roughness, composition, band gap, and many others. Additionally, it is one of the few available methods capable of their real-time determination, making it a critical tool for in-situ diagnostics of thin film growth during deposition

In spectroscopic ellipsometry, the change in the polarisation state of light upon reflection or transmission from a sample is measured as a function of its wavelength. The optical coefficients $n(\lambda)$ and $k(\lambda)$ are obtained from the so-called ellipsometric angles Ψ and Δ[17], representing the amplitude ratio and phase difference, respectively, between the S- and P- polarised light components. In a more common reflection setup, the complex reflectance ratio ρ is measured, given as the ratio of r_p and r_s from Equation (1.2):

$$\rho = \frac{r_p}{r_q} = \tan \Psi e^{i\Delta} \tag{3.25}$$

where the angle of incidence is chosen to be close to the Brewster angle, providing maximal sensitivity due to the highest difference between r_p and r_s. Typically, this angle remains fixed or several measurements under a variable angle (VASE) can be performed. Since ρ is defined as a ratio, ellipsometry is not affected by variations in the absolute intensity of the beam and can operate without the need to block other light sources, which usually produce unpolarised light. However, the surface roughness of a sample must be reasonably small and reflectivity fairly high. Otherwise, the reduced light intensity by scattering and/or absorption makes measurement challenging, particularly for black metals. For transparent films, back-reflection from the substrate, as well as inhomogeneity in film thickness typical for PLD samples, might pose some problems.

Ellipsometrical measurements are inherently indirect, meaning Ψ and Δ cannot be directly converted to n and k. Therefore, an appropriate fitting model defined by optical constants must be constructed based on known or assumed characteristics such as the material composition and thickness of each layer and substrate, roughness, porosity, etc. In general, interpreting these measurements tend to be rather difficult, which is considered as the biggest disadvantage of this method and it needs to be combined with other experimental techniques. The choice is greatly determined by the nature of the studied sample depending if the sample is a metal, semiconductor or an insulator. The most popular optical models are Lorentz, Cauchy, Tauc-Lorentz, Cody-Lorentz, among oth-

[17] The meaning of these angles is not straightforward and requires certain coordinate transformations that stem from Mueller matrix formalism. The states of fully, partially polarised, and unpolarised light are described by 4-dimensional Stokes vectors, and the final state after interaction with the sample is given by transformation using 4×4 Mueller matrices. Each polarisation state can be visually represented on a Poincaré sphere[134].

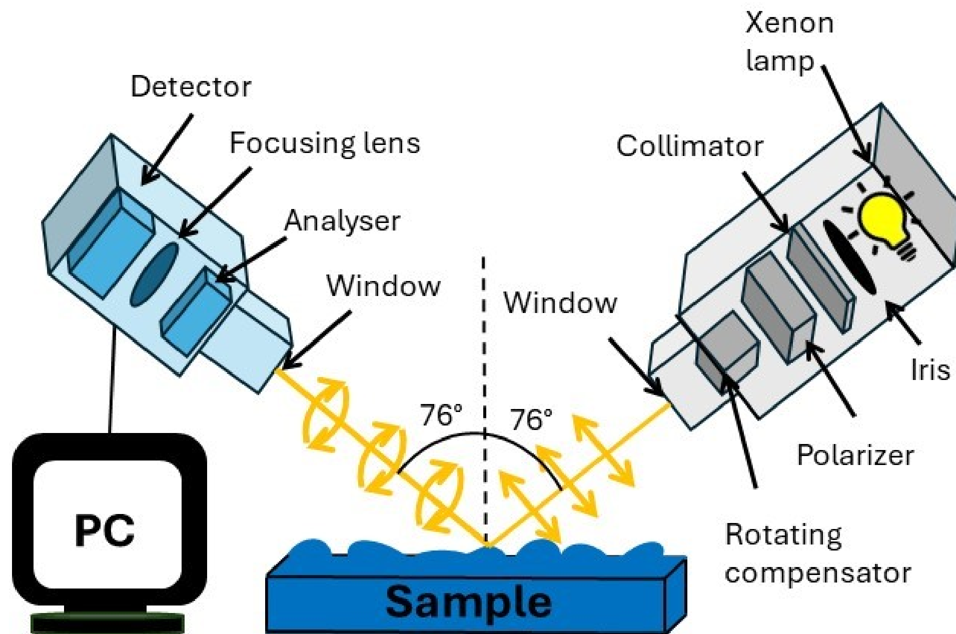

Figure 3.19: Scheme of an RCE type spectroscopic ellipsometry instrument.

ers[18][134] To extract the optical coefficients the model is iteratively improved by modification of initial parameters and compared to the measured data. The best fit is obtained by minimising the mean squared error (MSE) value between the measured and modelled data.

The schematic diagram of an ellipsometric experimental setup is depicted in Fig. 3.19. An iris is placed in front of the light source (in our case Xe lamp), creating a points source. The emitted light is directed onto the sample through a collimator and a polariser, generating a parallel linearly polarised beam. The elliptically polarised reflected light then passes through the analyzer and falls onto a detector. In this configuration, a rotating compensator is placed between the polarizer and the sample (RCE type). Another option would be to use rotating analyzer ellipsometry (RAE), where an optional static compensator or phase modulator can be placed in front of the analyzer to shift the phase of the light wave. Sometimes, a monochromatic laser source is used in single-wavelength ellipsometry for better intensity and focus, but this comes at the cost of reduced wavelength range.

In this thesis, the Spectral Ellipsometer M-2000 (by J. A. Woollam company) (see Fig. 3.20) was used in a UV/VIS wavelength range from 245 nm to 820 nm with a spot size diameter of approximately 4 mm. This ellipsometer is mounted on the vacuum chamber at two tilted flanges at a fixed angle of incidence of 76.0°with two fused silica windows. The measurements were carried out in a high-vacuum ($\sim 10^{-3}$ Pa) provided by a primary rotary pump and a secondary turbomolecular pump. Variable temperature from RT to 500°C was achieved by a resistance heating cable located under the sample holder. The temperature was measured by a thermocouple and controlled by a PID controller. For data analysis, the commercial software CompleteEASE[135] was used (shown in Fig. 3.21).

[18]These models do not necessarily need to be physical e.g. Cauchy model does not satisfy Kramers-Kronig relations

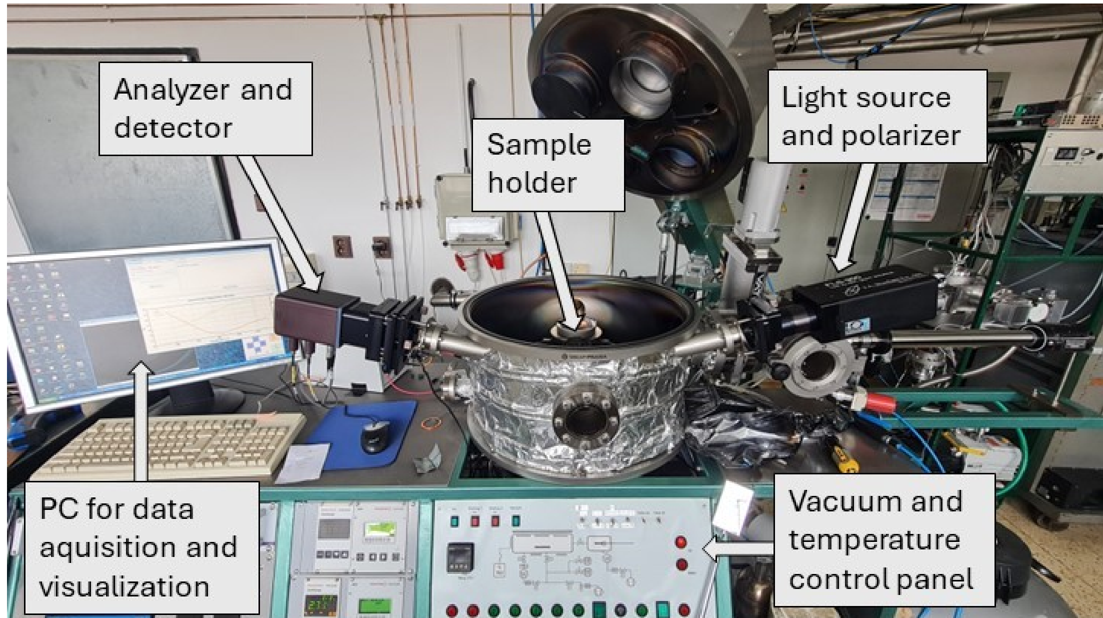

Figure 3.20: Photography of experimental setup for spectral ellipsometry measurements.

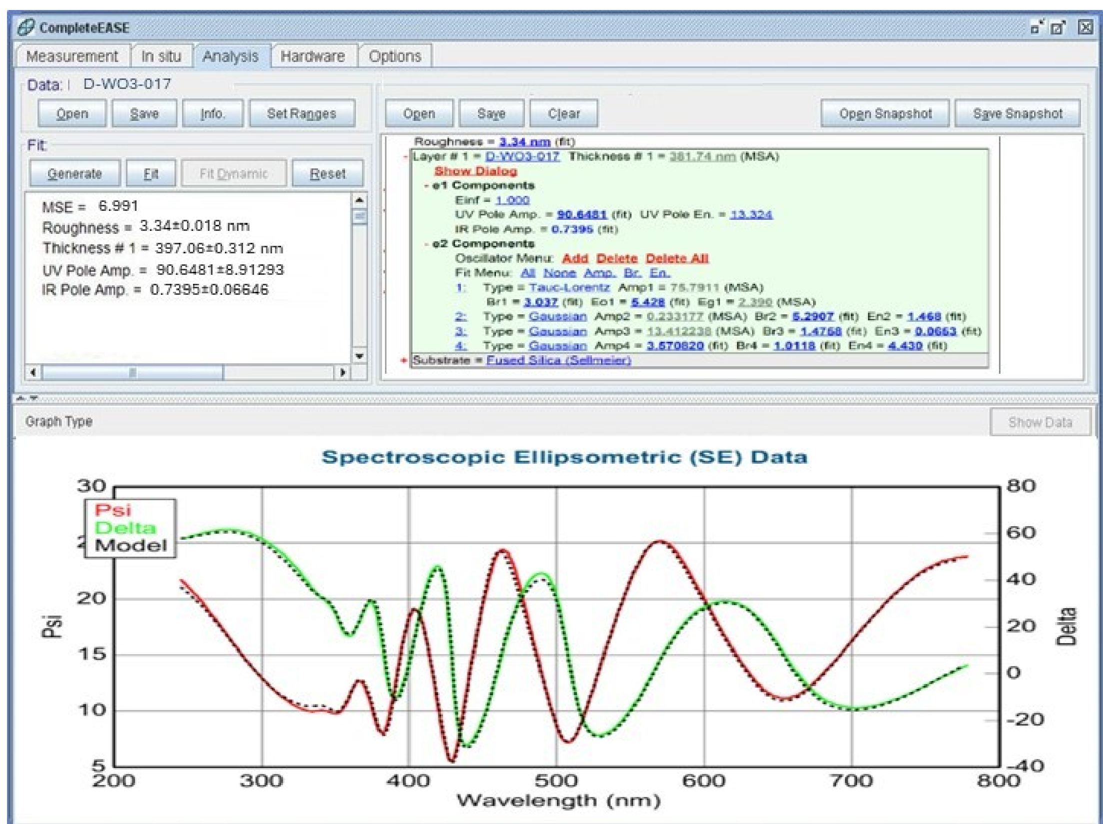

Figure 3.21: An illustration of the graphical user interface of CompleteEASE software, which provides variety of advanced models and material optical constants for spectral ellipsometry spectra analysis. The fitted parameters that can be modified are in bold blue font, displayed in the upper panel.

3.3.2 Photoluminiscence

Luminescence is a physical phenomenon, termed by E. Wiedemann in 1888[136], in which light is spontaneously emitted as a result of excited electrons relaxing from higher energy states to lower energy states, releasing this excess energy in the form of light. Therefore, it is being studied by a collection of analytical techniques that measure the distribution of photons as a function of wavelength, often categorized under optical emission spectroscopy, allowing for the study of the chemical composition and optical properties of a sample.

According to the mechanism in which the excitation of electrons is initiated from an external factor, we can distinguish various types of luminescence with their corresponding prefixes. For example, a sample can be exposed to photons (photoluminescence), heat (termoluminescence), a bombardment of electrons or ionising radiation (cathodoluminescence and radioluminescence), or it can be a result of chemical reactions (chemiluminiscence), mechanical deformation or breaking (triboluminescence), passing electric current (electroluminescence), etc. Among these, photoluminescence (PL) is the most commonly utilized in material research because it provides a very powerful non-destructive method for semiconductor characterization and chemical sensing[137] with outstanding sensitivity.

For a multi-electron system, the state of each electron is specified by quantum numbers L, S, and J, denoting orbital, spin, and total angular momenta, respectively. It is often represented by a term symbol, abbreviated in the form $^{2S+1}L_J$, where L is expressed as a letter "S", "P", "D", and "F" for $L = 0, 1, 2,$ and 3, respectively, and $2S + 1$ is multiplicity. When an electron is excited from a ground state to an excited state with the same multiplicity a part of the light is absorbed within $\sim 10^{-15} - 10^{-16}$ s[138]. Then it may return to the ground state by either a radiative or non-radiative transition. For radiative transitions, when the multiplicity during the process is unchanged we call this process fluorescence, while when the multiplicity is changed we are dealing with phosphorescence. The former distinction of these phenomena arose from the time elapsed between excitation and emission: fluorescence stops immediately (within $10^{-6} - 10^{-9}$ s) as the light source is ceased, whereas phosphorescence is relatively slow ($10^{-6} - 10^{2}$ s). In both cases, the energy of the emitted photons is lower compared to that of the excitation photons, as a consequence of its dissipation during interaction with a crystal lattice by phonons. However, an electron may lose part of its energy by non-radiative processes, including internal conversion or intersystem crossing. In condensed matter, the emission lines are rather broader than in gases, due to a complex interaction of the emitting centres with neighbouring atoms, giving rise to emission bands. The colour of the emitted light depends on the intrinsic characteristics of the sample, mainly on the defect and impurity content, temperature, external electric, magnetic or stress fields, and the size of particles in it.

A simplified schematic diagram of a basic PL experiment is in Fig. 3.22. Usually, the excitation wavelength is picked from a polychromatic light source by a filter/monochromator, or a monochromatic laser source/optical parametric oscillator can be used. Afterward, the light is collimated and guided onto the sample, which is usually placed under a 90° angle to prevent the source light from striking the detector. The emitted light from the sample is then dispersed by a monochromator and detected by a CCD detector. In a conventional PL experiment, the PL intensity as a function of wavelength is recorded, obtaining emission PL spec-

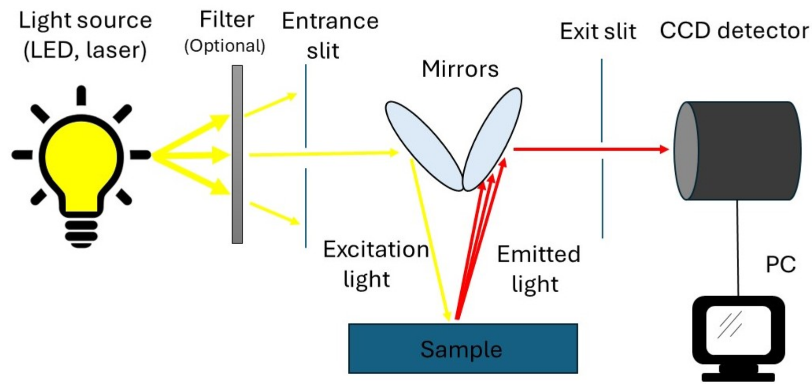

Figure 3.22: Schematic diagram of a PL measurement instrumentation.

tra at constant excitation wavelength. However, one may vary the excitation energy and measure the PL intensity at a constant emission wavelength to get an excitation PL spectrum.

The PL measurements were carried out using a custom self-assembled setup in the Laboratory of Sensor Technologies at the Institute of Physics of the University of Tartu, Estonia (see Fig. 3.23). The PL was excited by either an LED with an excitation wavelength of 365 nm (Thorlabs M365LP1) or pulsed Nd:YAG DPSS laser (Elforlight SPOT-10-100-355, repetition rate 5 kHz, pulse duration 2 ns) emitting at 355 nm. The light from the source was spectrally cleaned by an appropriate band-pass filter. The incident light was not further focused before being incident on a sample located on an optical table at RT. For the LED source, the maximum incident power was 4.0 mW (stability was measured a priori) and the illuminated area was $\sim 5 \times 5$ mm^2. The area illuminated by the laser was smaller, corresponding to $\sim 2 \times 2$ mm^2, and the pulse energy was ~ 1 μJ. The emitted PL photons were collected in a backscattering geometry, dispersed by a monochromator (LOMO MDR-23) and detected by a cooled CCD camera (Andor DU240-BU). The spectra were displayed by software also from Andor company.

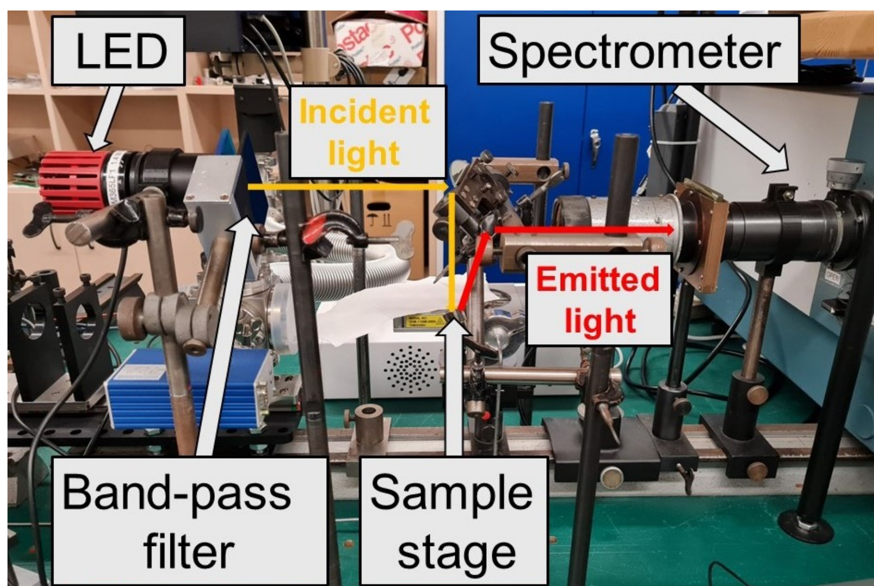

Figure 3.23: Photography of instrumentation used for PL measurements.

4. Results and discussion

In the following chapter, we present the experimental results obtained by the methods from the previous chapter and provide an interpretation and a detailed discussion of their implications.

4.1 Prepared samples

The samples of reflective and black aluminium (denoted as R-Al and B-Al, respectively), as well as reflective and black titanium (denoted as R-Ti and B-Ti, respectively), were prepared by pulsed DC MS. The tungsten trioxide (WO_3) and phosphorus-doped tungsten trioxide samples (WO_3:P) were prepared by PLD on a fused silica substrate (FS) that was kept either at room temperature (RT) or heated to a high temperature (HT) of 500°C.

Substrate cleaning plays an important role in the performance of the resultant films. Before the substrates are inserted into the deposition chamber, it is crucial to remove contaminants such as dust and chemical impurities that could degrade the quality of the films and affect the repeatability of our process. For this reason, ultrasonic cleaning with acetone, isopropanol, and ethanol in sequential order was utilized. After each step, any remaining liquid was removed by blowing compressed nitrogen over the sample.

4.1.1 R-Al and B-Al series

Aluminium thin films were fabricated under the same deposition conditions as in previous work[23] on FS, where the morphology, structural and optical properties of R-Al and B-Al were compared in detail as a function of the film thickness. However, the growth mechanism on other substrates has not yet been investigated. The choice of an appropriate substrate determines the final properties and growth of our films. In this work, eight B-Al films with different thicknesses were prepared in a mixture of Ar and N_2 reactive atmosphere during deposition, with a N_2/Ar ratio of 6-7%, which was shown to be optimal for the growth of the most anti-reflective films[21]. Additionally, one R-Al without the presence of N_2 was deposited for comparison. As substrates, we used either amorphous fused silica (FS) or crystalline Si(111), each with dimensions of 10×10 mm^2. During a single deposition, a total of 4 substrates were inserted into the sample holder (2 of each type), which was held at RT at a fixed working distance of 10 cm from a pure Al target (99.99% purity, 10 cm diameter). As was shown in Fig. 2.8 we can consider each sample equivalent and thus effectively assess the influence of the substrate. After placing the substrates, the vacuum chamber is evacuated to a base pressure of $\sim 5 \times 10^{-3}$ Pa. For plasma generation, the power supply operated initially at 600 V, 2.0 A current, and 800 W power for deposition.

The deposition parameters are listed in Tab. 4.1. After ignition of magnetron discharge, plasma parameters (U, I. P) decreased and the deposition power was slightly lower (330 W) for B-Al samples than for R-Al (360 W), corresponding to a power density of 4.2 W.cm^{-2} and 4.6 W.cm^{-2}, respectively. The constant flow

Sample name	U (V)	I (A)	P (W)	ϕ_{N_2} (sccm)	ϕ_{Ar} (sccm)	t (min)	h_{FS} (nm)	h_{Si} (nm)
B-Al 01						6	264(11)	207(6)
B-Al 02						12	556(15)	425(9)
B-Al 03						18	861(12)	695(13)
B-Al 04						15	651(11)	574(12)
B-Al 05	369	0.90	330	0.5(1)	13.5(1)	9	392(7)	353(16)
B-Al 06						3	112(6)	103(7)
B-Al 07						24	1218(25)	1050(20)
B-Al 08						36	1610(30)	1400(30)
R-Al 01	400	0.89	360	-	14.0(1)	15	879(9)	793(7)

Table 4.1: Deposition parameters for R-Al and B-Al samples prepared by MS.

rates of nitrogen and argon (ϕ_{N_2} and ϕ_{Ar}) combined to a deposition pressure of 0.5 Pa, which was controlled by a manual butterfly valve.

A photograph showing a different appearance of both films is in Fig. 4.1. All of the films have a small section near the corner that was masked with a metal clamp during deposition. This masking creates a step, which serves for profilometric determination of the film thickness. The R-Al sample has a mirror-like surface with high reflectivity, while the B-Al sample has an opaque black surface with minor reflection. However, when viewed from the bottom through the substrate, it is much harder to distinguish between them, as both appear to be reflective. This is due to the not-yet-strongly-developed morphology that is compact near the substrate, which lacks porosity.[22].

For a given deposition, the thicknesses were measured for both types of films deposited on FS (h_{FS}) and Si (h_{Si}) substrates for at least 6 distinct locations along the step by calculating the mean value and its error. Assuming the flux of particles deposited on the substrate surface is uniform in time, then we can expect the mean thickness to be directly proportional to time. When we plot these thicknesses as a function of deposition time t, the deposition rate can be obtained as the slope of the linear fit of the function $h(t)$ (see the graph in Fig. 4.5). We estimated the deposition rate to be 47(2) nm.min^{-1} for on-FS-grown (further denoted as B-Al@FS) films and 40(1)nm.min^{-1} for on-Si-grown films (B-Al@Si), respectively, which is almost two times lower than the rate reported in[23]. This discrepancy may be attributed to unintentional changes in the deposition chamber. We suspect that a primary contributing factor could be the deterioration of the target condition, possibly due to deeper erosion tracks resulting from multiple depositions since the previous depositions. Furthermore, it could be caused by a slight offset in the working distance compared to previous study. The deposition rate of R-Al, determined from a single data point, appears to be higher for both substrates, presumably as a consequence of higher deposition power. This could also be a coincidence or result of a systematic error and to support this claim, more samples would be required.

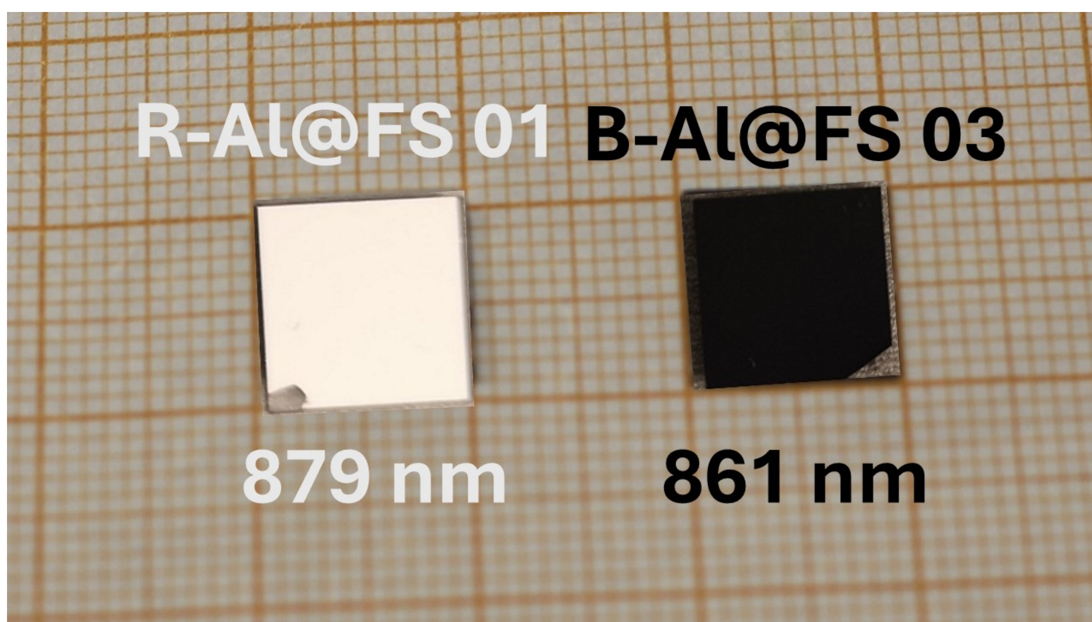

Figure 4.1: A photography of prepared R-Al and B-Al samples on FS substrate.

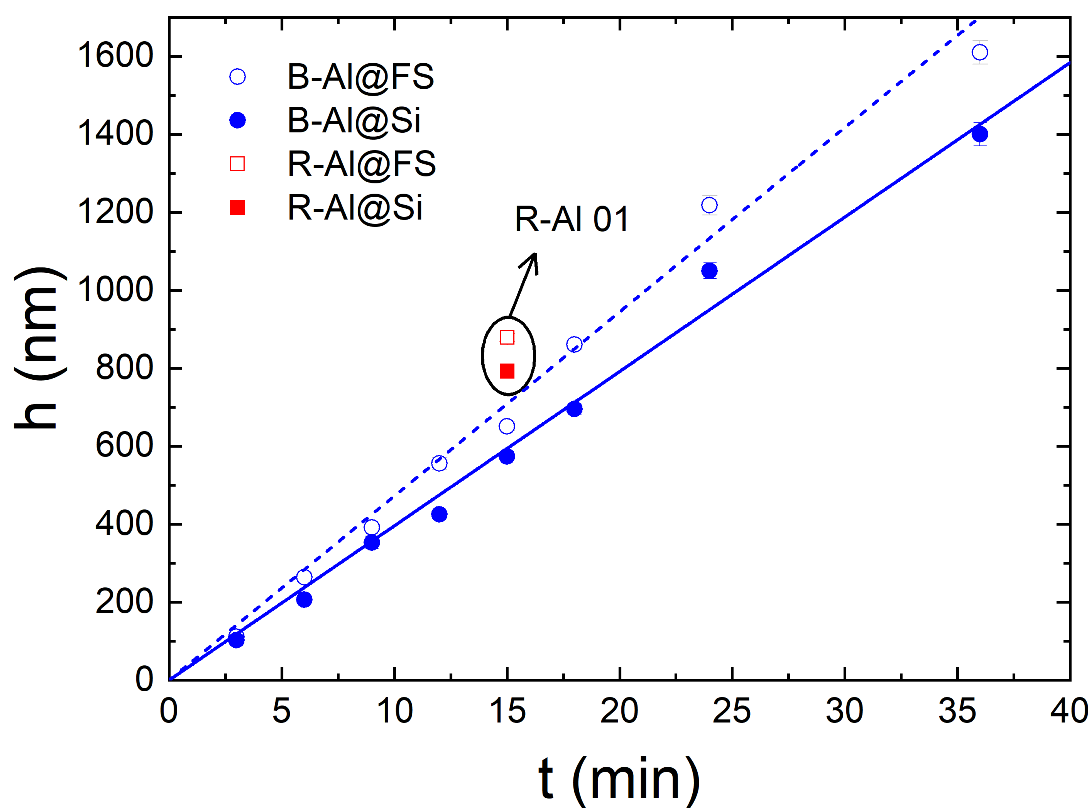

Figure 4.2: Thicknesses of R-Al and B-Al films deposited on FS (empty points) and Si (solid points) substrates as a function of deposition time.

4.1.2 R-Ti and B-Ti series

The titanium films were prepared by pulsed DC MS on FS at RT in the same deposition chamber, utilizing a Ti target (99.999% purity, $\varnothing = 10$ cm). Initially, we used the same deposition conditions as for B-Al. However, the resulting films were quite reflective and the deposition rate was significantly lower. Consequently, several deposition parameters had to be adjusted. To achieve a reasonable deposition rate on the order of tens of nm/s, it was necessary to increase the initial deposition voltage, current and power to 700 V, 2.5 A and 900 W, respectively. The pulse frequency, duty cycle, and working distance remained unchanged.

The chamber was evacuated to a base pressure $p_0 \sim 5 \times 10^{-3}$ Pa. Then nitrogen was introduced into the chamber with the nitrogen flow rate ϕ_{N_2} varying from a minimal available value of 0.6 sccm to 10.0 sccm, achieving the corresponding partial pressure p_{N_2}. Afterwards, argon was added with a flow rate ϕ_{Ar} of either 13 sccm or 19 sccm, resulting in a partial pressure of p_{Ar}. The nitrogen-to-argon (N_2/Ar) ratio could be varied and the actual value was calculated from these pressures according to the formula:

$$\mathrm{N_2/Ar\ ratio} = \frac{p_{N_2} - p_0}{p_{Ar} + p_{N_2} - p_0} \tag{4.1}$$

The photograph comparing the appearance of the prepared films can be found in Fig. 4.3, where the sample B-Ti 09 was chosen as the blackest among the samples by the naked eye. At first glance, we can easily distinguish the reflective and black films, although B-Ti was clearly more reflective compared to B-Al films. R-Ti sample has a more greyish look, typical for Ti films prepared by MS, rather than a mirror-like look typical for B-Al. Likewise, when looking from the bottom side of the substrate, the films appear similar. For an even higher nitrogen content, the films started to appear goldish, suggesting the visible formation of titanium nitride (TiN).

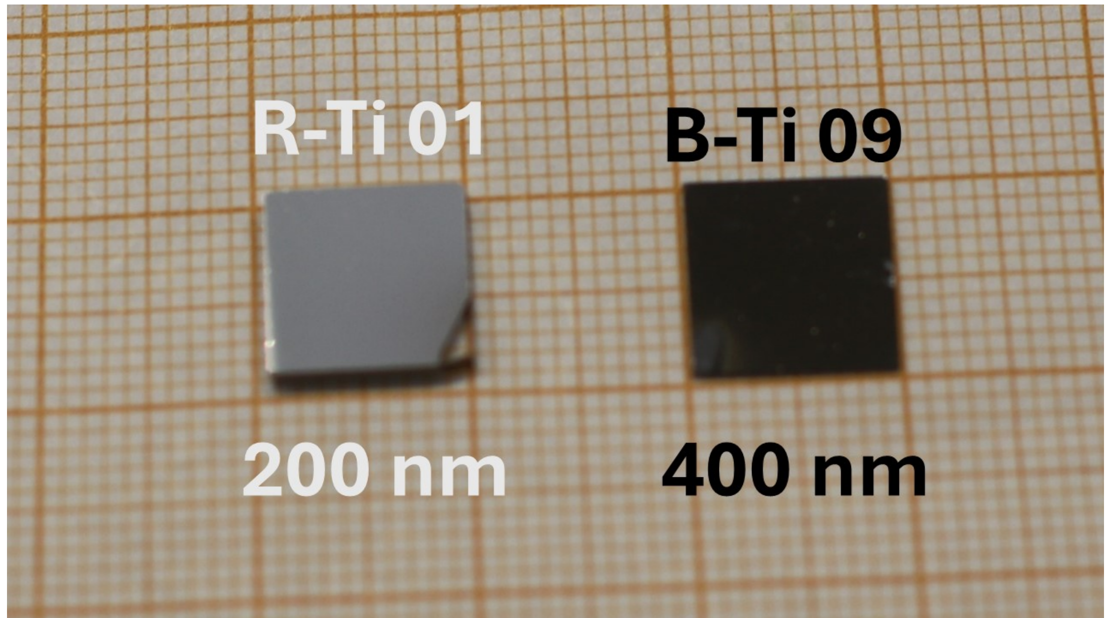

Figure 4.3: A photography of prepared R-Ti and B-Ti samples.

Sample name	U (V)	I (A)	P (W)	ϕ_{N_2} (sccm)	ϕ_{Ar} (sccm)	N_2/Ar ratio (%)	p_{dep} (Pa)	t (min)	h (nm)
B-Ti 01	392	1.13	440	0.6(1)	13.0(1)	4.9(3)	1.0	20	1023(18)
B-Ti 02	423	1.09	460	1.0(1)	13.0(1)	7.4(3)	1.0	20	358(14)
B-Ti 03	439	1.07	470	2.0(1)	13.0(1)	13.0(3)	1.0	20	265(5)
B-Ti 04	443	1.05	470	3.0(1)	13.0(1)	15.0(4)	1.0	20	243(9)
B-Ti 05	447	1.04	460	4.0(1)	13.0(1)	16.2(4)	1.0	20	273(9)
B-Ti 06	451	1.03	460	5.0(1)	13.0(1)	19.9(4)	1.0	20	238(12)
B-Ti 07	455	1.02	460	6.0(1)	13.0(1)	22.9(5)	1.0	20	220(7)
B-Ti 08	447	1.04	460	10.0(1)	19.0(1)	23.8(5)	1.0	30	359(6)
B-Ti 09	427	1.09	470	2.0(1)	19.0(1)	8.3(3)	1.5	20	398(8)
B-Ti 10	431	1.08	470	3.0(1)	19.0(1)	10.5(3)	1.5	20	379(9)
B-Ti 11	435	1.07	470	4.0(1)	19.0(1)	11.9(3)	1.5	20	320(12)
B-Ti 12	439	1.06	470	5.0(1)	19.0(1)	13.8(4)	1.5	20	306(19)
B-Ti 13	443	1.05	470	6.0(1)	19.0(1)	16.3(4)	1.5	20	295(5)
B-Ti 14	447	1.04	460	10.0(1)	19.0(1)	21.1(5)	1.5	30	488(12)
R-Ti 01	369	1.13	420	-	19.0(1)	-	1.0	4	200(15)
R-Ti 02	369	1.13	420	-	19.0(1)	-	1.0	30	1521(40)

Table 4.2: Deposition parameters for R-Ti and B-Ti samples prepared by MS.

The effect of nitrogen content was studied by preparing two series at different deposition pressures p_{dep} of 1.0 Pa (samples B-Ti 01 to B-Ti 08) and 1.5 Pa (B-Ti 09 - B-Ti 14) and the deposition conditions are summarised in Tab. 4.2. Additionally, two samples of reflective titanium R-Ti 01 and R-Ti 02 without nitrogen were prepared with different thicknesses for comparison. The thickness was determined analogously to the B-Al films. Several attempts were made to prepare films at 0.5 Pa but they delaminated immediately upon removal from the chamber. To exclude other factors (such as inadequate substrate cleaning or sudden temperature shock), we repeated the deposition several times with the same result. Partial delamination was also observed on samples prepared at 1.0 Pa after some time (approximately a few days following deposition). This indicates that a lower deposition pressure leads to a deterioration of film quality, so further depositions at pressure 0.5 were discontinued.

The DC power supply deposition parameters as a function of the N_2/Ar ratio are graphically depicted in Fig. 4.4. The deposition voltage U and current I seemingly dropped from their initial values to 369 V and 1.13 A in the case of R-Ti. With higher nitrogen content, the deposition voltage tended to monotonically rise to $\sim$ 450 V, while the current gradually decreased to about 1.02 A, except for sample B-Ti 08 with an argon flow rate of 19.0 sccm. As the plasma parameters are highly influenced by the hydrodynamics of the flowing gas, which are in turn affected by the exact flow rate and the geometry of the deposition system, explaining this behaviour is quite complex and falls beyond the scope of this thesis. However, the deposition power appears to be similar in both cases, corresponding to 420 W for R-Ti and 460-470 W for B-Ti, resulting in a relatively high power density of 5.3 and 5.9-6.0 W.cm^{-2}, respectively.

If we graphically plot the deposition rate v_d with respect to N_2/Ar ratio (see Fig. 4.5), we conclude that the deposition rate of B-Ti is lower than for the B-Al films, except for samples with the lowest nitrogen content (both R-Ti and

B-Ti 01) reaching a maximum value of $\sim$ 50 nm.min^{-1}, which is comparable to the deposition rate of B-Al films. As the amount of nitrogen is negligible, the deposition rate is almost identical to that of R-Ti depositions. However, more N_2 in the chamber causes the growth process to slow significantly, with the deposition rate dropping down to around 20 nm.min^{-1} as the N_2/Ar ratio exceeds 7%, and stabilizing at around 10-15 nm.min^{-1} beyond a certain threshold of nitrogen content. This highlights the impact of nitrogen on the deposition process. The same trend is followed at both deposition pressures, although samples prepared at 1.5 Pa tend to grow slightly faster, possibly due to the higher sputtering yield of the Ti target.

Finally, yet importantly, we should mention that several improvements to enhance the blackness of the obtained film were tested:

1. *Changing the working distance* - we expected that by shortening it, a high-energetic plasma could affect the growth mechanism, favouring surface re-crystallization. Conversely, moving the substrate further from the target could lead to a lower energy of impacting Ti atoms, therefore keeping the substrate at a constant low temperature.
2. *Omitting the pre-sputtering of the Ti target* - we planned to prepare a gradient layer containing more oxygen near the substrate. As the target would eventually clean itself and by so changing the growth mode.
3. *Adding a small amount of oxygen* - we aimed to prepare titanium oxynitride (TiO_xN_y) films. Unsurprisingly, even for the lowest possible oxygen flow, the films instantly turned into transparent films as Ti preferentially reacted with O_2, forming an oxide film.
4. *Controlling temperature or inclination of substrates* - it is suggested that by heating or cooling down the sample holder, or by changing the angle of incidence from normal to glancing angle deposition, we could observe some microstructural changes that could favour light trapping.
5. *Altering the magnetic field of our magnetron head* - it was proposed that implementing changes in the balance of the magnetic field (e.g. using imbalanced magnetron geometry) by adding/removing some permanent magnets at specific locations could influence the plasma properties, which in turn affect the properties of our films.

As for now, modifications 1. and 2. did not contribute to any significant changes in the overall morphological and optical properties of our films. The shortening/lengthening of the working distance only resulted in a higher/lower deposition rate. The 3rd modification was shown to be unsuccessful in obtaining a BM. Unfortunately, approaches 4 and 5 could not be achieved with our current deposition system, as they would require a partial reconstruction of our deposition chamber or at least the sample holder. These ideas serve for future investigation, and their impact remains to be explored.

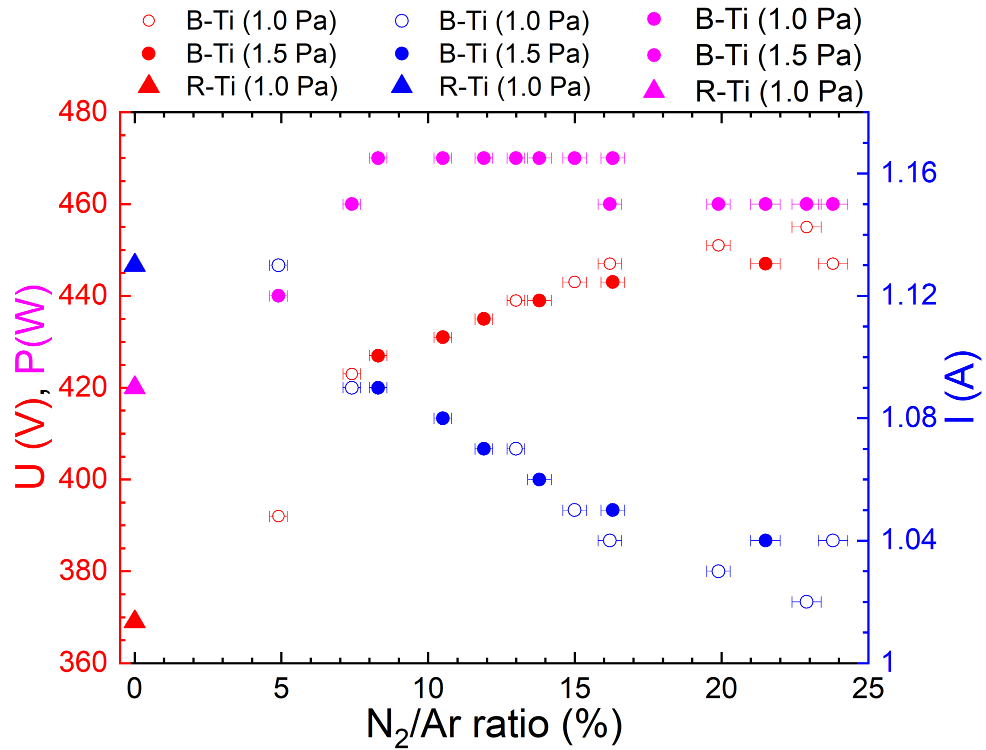

Figure 4.4: Deposition voltage U (red), current I (blue) and power P (purple) as a function of nitrogen content during the deposition of R-Ti and B-Ti films with deposition pressures corresponding to 1.0 Pa and 1.5 Pa.

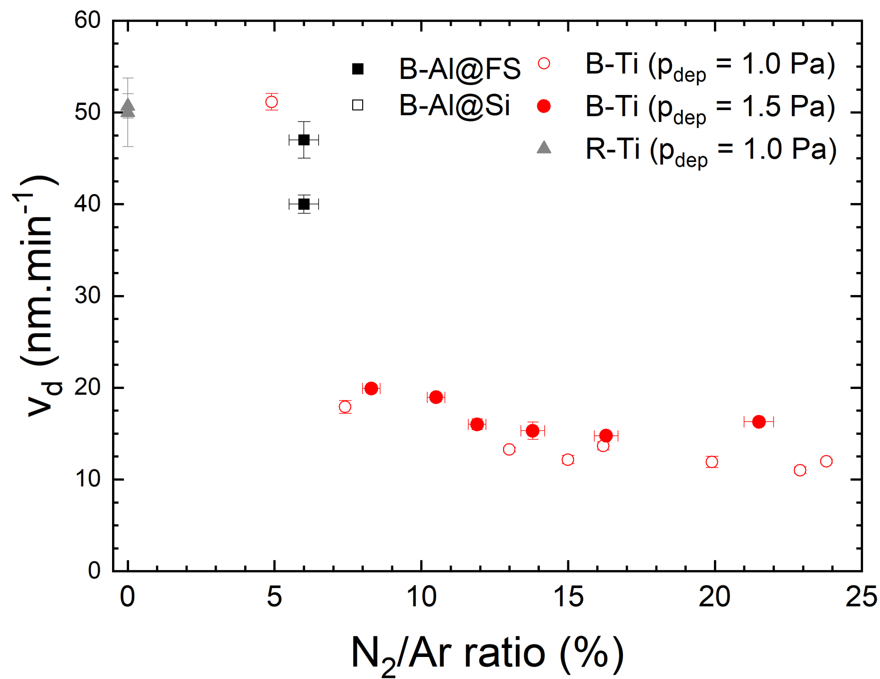

Figure 4.5: Deposition rate as a function of nitrogen content during the deposition of R-Ti and B-Ti films with deposition pressures corresponding to 1.0 Pa and 1.5 Pa. The comparison with B-Al series (black points) is also provided.

4.1.3 WO_3 and WO_3:P series

For each series, a total of 7 tungsten trioxide thin films were deposited with varying oxygen deposition pressure p_{O_2} in the range of 0 to 15.0 Pa. The samples are numerically labelled in ascending order corresponding to the increasing deposition pressure of oxygen introduced to the chamber during the deposition. Initially, the chamber was evacuated to a base pressure of 5.0×10^{-4} Pa for at least an hour. Then oxygen (99.9999 %) was introduced into the chamber with a flow rate of 10 sccm and the pressure was set by partially closing the gate valve, except for samples number 1 of each series. In the meantime, the laser pulses of 10 Hz frequency were adjusted to a minimal energy E_{laser} of 90 mJ, which was measured both before and after deposition. The deposition time was chosen to be 6 minutes for every sample, corresponding to 3600 laser pulses, controlled by the LabVIEW software. A small area of the substrate was masked to create a step that served to determine profilometrically the thicknesses h of the films. The step height was evaluated for at least 10 different places along the substrate-film interface and the thickness was calculated as the arithmetic mean of these values. Owing to the less uniform thickness of the films produced by PLD, the error, calculated as the standard deviation of this mean, is notably higher compared to the films prepared by MS. The relative error of the thickness in these films is around 3-12%.

Sample name	$t_{substrate}$ (°C)	p_{O_2} (Pa)	E_{laser} (mJ)	h (nm)
RT-WO_3 1	RT	0	93(3)	216(15)
RT-WO_3 2	RT	2.5(1)	93(3)	293(21)
RT-WO_3 3	RT	5.0(1)	91(3)	302(15)
RT-WO_3 4	RT	7.5(1)	93(3)	333(35)
RT-WO_3 5	RT	10.0(1)	92(3)	364(24)
RT-WO_3 6	RT	12.5(1)	94(3)	398(47)
RT-WO_3 7	RT	15.0(1)	93(3)	389(28)

Table 4.3: Deposition parameters for RT-WO_3 series prepared by PLD.

Sample name	$t_{substrate}$ (°C)	p_{O_2} (Pa)	E_{laser} (mJ)	h (nm)
HT-WO_3 1	500(20)	0	96(3)	247(19)
HT-WO_3 2	500(20)	2.5(1)	92(3)	324(11)
HT-WO_3 3	500(20)	5.0(1)	93(3)	353(22)
HT-WO_3 4	500(20)	7.5(1)	91(3)	346(19)
HT-WO_3 5	500(20)	10.0(1)	95(3)	362(28)
HT-WO_3 6	500(20)	12.5(1)	92(3)	372(24)
HT-WO_3 7	500(20)	15.0(1)	91(3)	370(27)

Table 4.4: Deposition parameters for HT-WO_3 series prepared by PLD.

In the first RT-WO_3 series, the pure WO_3 target was used and a substrate was kept at RT. The key deposition parameters are summarised in Table 4.3. Alternatively, in the second series HT-WO_3, the substrate was heated with a quick linear ramp, reaching the deposition temperature of 500°C in about 15 minutes

Sample name	$t_{substrate}$ (°C)	p_{O_2} (Pa)	E_{laser} (mJ)	h (nm)
RT-WO_3:P 1	RT	0	92(3)	160(14)
RT-WO_3:P 2	RT	2.5(1)	91(3)	231(16)
RT-WO_3:P 3	RT	5.0(1)	92(3)	265(19)
RT-WO_3:P 4	RT	7.5(1)	91(3)	295(20)
RT-WO_3:P 5	RT	10.0(1)	90(3)	431(15)
RT-WO_3:P 6	RT	12.5(1)	91(3)	498(23)
RT-WO_3:P 7	RT	15.0(1)	90(3)	649(23)

Table 4.5: Deposition parameters for RT-WO_3:P series prepared by PLD.

Sample name	$t_{substrate}$ (°C)	p_{O_2} (Pa)	E_{laser} (mJ)	h (nm)
HT-WO_3:P 1	500(20)	0	90(3)	156(8)
HT-WO_3:P 2	500(20)	2.5(1)	91(3)	234(12)
HT-WO_3:P 3	500(20)	5.0(1)	92(3)	287(15)
HT-WO_3:P 4	500(20)	7.5(1)	92(3)	265(25)
HT-WO_3:P 5	500(20)	10.0(1)	90(3)	262(18)
HT-WO_3:P 6	500(20)	12.5(1)	91(3)	266(18)
HT-WO_3:P 7	500(20)	15.0(1)	91(3)	234(10)

Table 4.6: Deposition parameters for HT-WO_3:P series prepared by PLD.

and then maintained at a constant temperature for an additional one hour to stabilize. However, during this period, the temperature oscillated around the mean value by about 20 ° C, resulting in a temperature error in the Table 4.4. After deposition, we set the PID controller back to RT. The cooling procedure was slower, with an exponential temperature decay with time, reaching a temperature of 50°C[1] in another hour and a half. The photographs of the samples from these two series (Fig. 4.6) show that the transparency of our films increases with deposition pressure because of the transformation from a partially metallic film to an oxide film. The oxygen-depleted samples appear reflective and metallic, whereas the oxygen-rich samples have a visible bluish colour. The samples RT-WO_3 7 and HT-WO_3 7 are almost completely transparent when viewed from normal incidence. The film becomes visible only when the substrate is rotated, revealing a colourful interference pattern.

For the next two series labelled as RT-WO_3:P and HT-WO_3:P, we prepared phosphorus-doped WO_3 films by repeating the same deposition conditions but from a monophosphate tunsten bronze $(PO_2)_4(WO_3)_4$ target, synthesized with the technique described and used by More-Chevalier[48]. The deposition parameters and the thicknesses can be again found in Tables 4.5, 4.6, and the photographs are shown in Fig. 4.7. It is evident that these samples appear significantly more transparent at the same deposition pressure compared to the undoped samples, despite their greater thickness.

[1]This temperature was considered safe for manipulation with the sample holder.

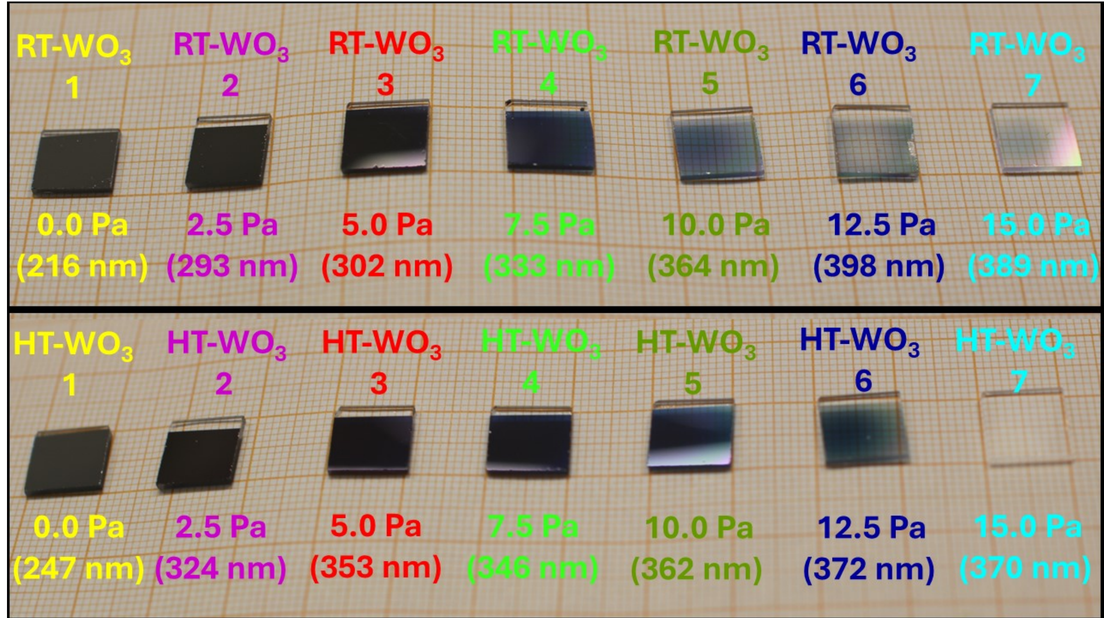

Figure 4.6: A photography of prepared WO_3 thin films. The top picture corresponds to RT-WO_3 series and the bottom one to HT-WO_3. The deposition pressure and the thickness is are shown below each sample.

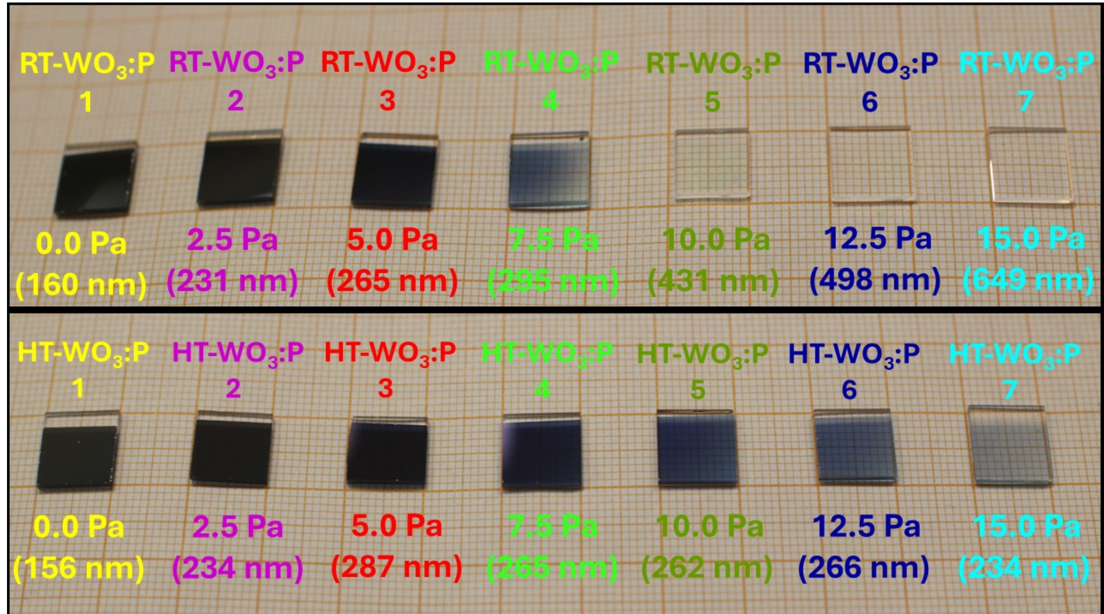

Figure 4.7: A photography of prepared WO_3:P thin films. The top picture corresponds to RT-WO_3:P series and the bottom one to HT-WO_3:P.

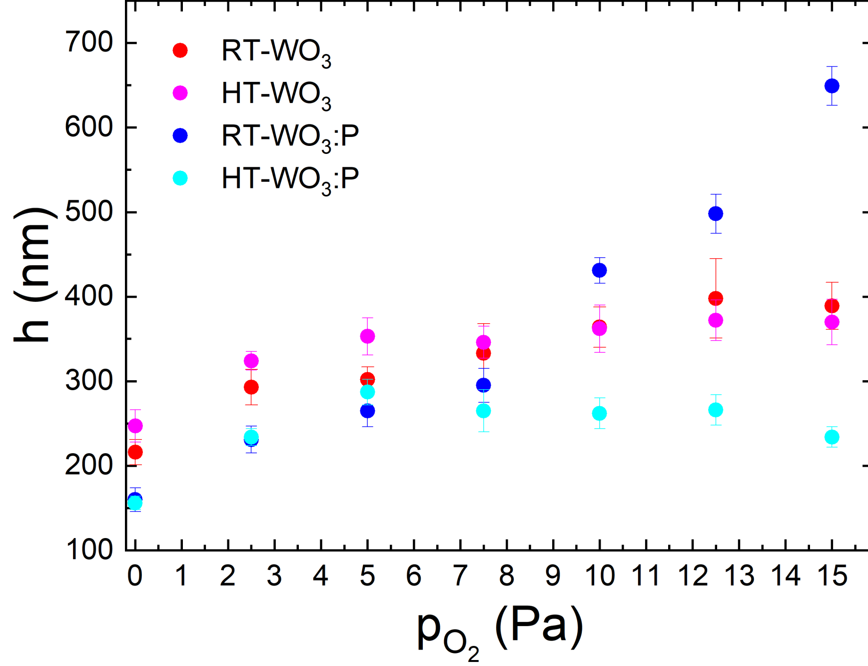

Figure 4.8: Thickness of the WO_3 and WO_3:P films as a function of oxygen deposition pressure.

In Fig. 4.8, we can observe the detailed evolution of the thickness of our films. For the RT-WO_3 films, the deposition rate gradually increases with increasing deposition pressure from approximately 36 nm.min^{-1} to 65 nm.min^{-1}. This trend is even more pronounced for phosphorus-doped samples in the RT-WO_3:P series, where deposition rate spans from 26 nm.min^{-1} to 108 nm.min^{-1}. Thus, at lower deposition pressures, the P-doped films exhibit a slower deposition rate compared to the undoped films, but at higher deposition pressures, the growth rate of the P-doped films increases significantly. The heated substrate affects the growth of the films in both cases, showing a nearly constant thickness independent of pressure, except for the first samples deposited in a vacuum. The undoped films have a higher deposition rate of about 55-60 nm.min^{-1}, while the doped films 40-45 nm.min^{-1}, again excluding the samples deposited in vacuum. To elucidate the growth mechanism of WO_3 films, characterization of laser plasma, employing OES and/or Langmuir probe measurements, needs to be performed similarly as in [48][139].

4.1.4 Multilayered films

To utilize B-Al for photoluminescence measurements, a set of four samples of B-Al combined with ZnO:Eu films with various thicknesses was prepared. The prepared samples are summarised in Table 4.7. Initially, a FS substrate was covered with either 500 nm or 1000 nm thick B-Al film with the same deposition conditions described in Section 4.1.1. On top of this layer, ZnO:Eu films were grown from a Eu_2O_3:ZnO (containing 1% at. of Eu) using the same deposition system mentioned in Section 2.3.1. The deposition was carried out in an oxygen atmosphere with a pressure of 10 Pa and the target was kept at RT. A total of 6000 and 12000 pulses (denoted as 6000p and 12000p) were shot at the target, resulting in a film of thickness approximately 200 nm and 400 nm, respectively. For comparison, 2 additional samples of ZnO:Eu films without the B-Al sublayer were prepared with the same deposition conditions, and the structural, optical and other properties of these films were already excessively studied by Novotný et al.[54]

For temperature-dependent ellipsometric measurements, a multilayered structure consisting of WO_3 on top of B-Ti was prepared (denoted as HT-WO_3@B-Ti). A similar film to sample HT-WO_3 7 sample was chosen as it showed the best thermochromic properties (see Section 4.10.1). For that reason, the same deposition conditions were used, although only a thinner film of 60(10) nm was grown, corresponding to a deposition time of 1 min. Since the deposition temperature of 500°C is too high for B-Al to keep its properties, it could not be used as a sublayer. But B-Ti remains stable at this temperature; therefore, we used a thin film of thickness approximately 500 nm as a basis with the same deposition conditions as for sample B-Ti 09, which were considered the best at the time of preparation (p_{dep} = 1.5 Pa, ϕ_{N_2} = 2 sccm, ϕ_{Ar} = 19 sccm).

Sample name	Description
ZnO:Eu@B-Al 1	500 nm of B-Al 6000p of ZnO:Eu
ZnO:Eu@B-Al 2	500 nm of B-Al 12000p of ZnO:Eu
ZnO:Eu@B-Al 3	1000 nm of B-Al 6000p of ZnO:Eu
ZnO:Eu@B-Al 4	1000 nm of B-Al 12000p of ZnO:Eu

Table 4.7: Prepared multilayers based on B-Al for PL measurements. The top layer of ZnO:Eu film is prepared by PLD and the B-Al was grown by MS.

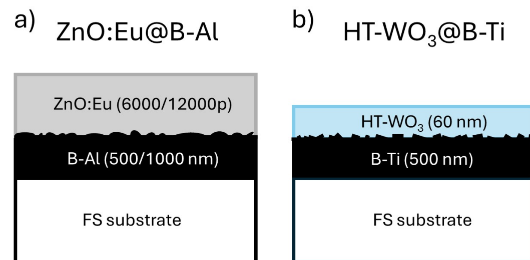

Figure 4.9: A schematic diagram of the prepared multilayers:
a) ZnO:Eu@B-Al films for PL measurements b) HT-WO_3@B-Ti for ellipsometric measurements.

4.2 Morphology of R-Al and B-Al films

The structure of R-Al and B-Al film grown on FS have already been thoroughly investigated by means of SEM and AFM in previous works[23][22] for films thinner than 1 μm as well as for thicker films up to 8 μm[24]. In the first case, it was reported that the surface morphology of reflective films can be characterized as more homogeneous and smoother, with numerous large, well-developed grains possessing fcc crystalline structure. Smaller grains are situated near the substrate and towards the surface their size gradually increases, following the so-called "V-growth mode". On the other hand, black films exhibit much more fine-structured and rough cauliflower-like surfaces with spherically shaped grains that are comparatively smaller. From the substrate, they tend to form high isolated columns separated by pores, following the Stranski-Krastanow growth mode[140]. The mean grain size and roughness increase for both films with thickness, although it was shown that for greater thicknesses these quantities tend to saturate and become independent of thickness. The AFM and SEM observations for our samples R-Al 01 and B-Al 03 on FS (see Fig. 4.10) qualitatively confirm this behaviour. However, in both cases, the surface roughness is comparable. This is likely due to the AFM measurement location, which contains many large grains that coincidentally overestimate the roughness value. By masking these grains and examining only the underlying layer, the roughness decreases, aligning with the findings in the referenced works.

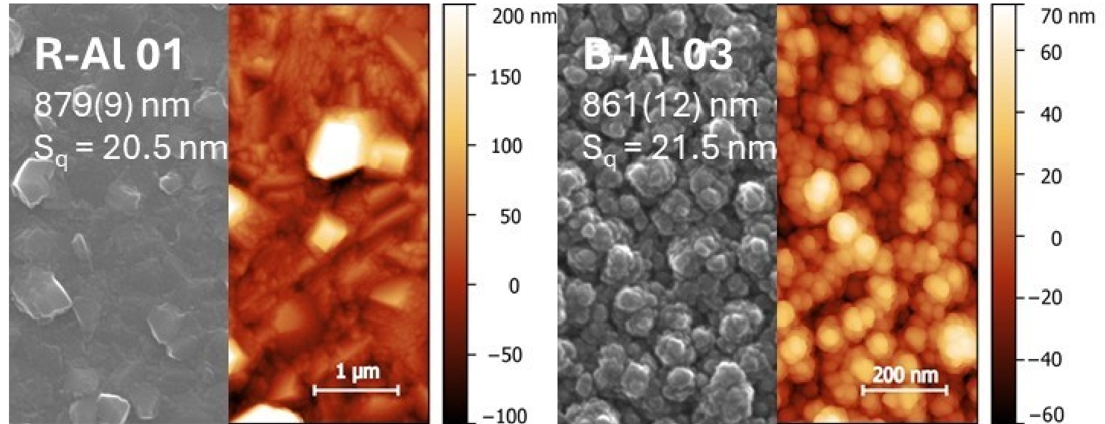

Figure 4.10: AFM and SEM images of R-Al and B-Al for two films with similar thickness, comparing their surface morphology.

To determine whether depositing B-Al on a single crystal Si wafer results in a different outcome, we conducted SE SEM measurements, which are presented in Fig. 4.11 and 4.12. For FS dielectric substrates, we grounded the specimen surface with a conductive vacuum tape to prevent charging. From the images, we were also able to obtain the distributions of grain sizes. The mean grain size distribution for similar B-Al samples grown on FS (B-Al@FS) was already reported[23], so here our focus is only on films grown on a Si(111) substrate (B-Al@Si).

The analysis was carried out using ImageJ software by selecting some number of grains N. For each image, we first set the scale, utilizing the small scale marker present in the image. We then highlighted the boundaries of a large

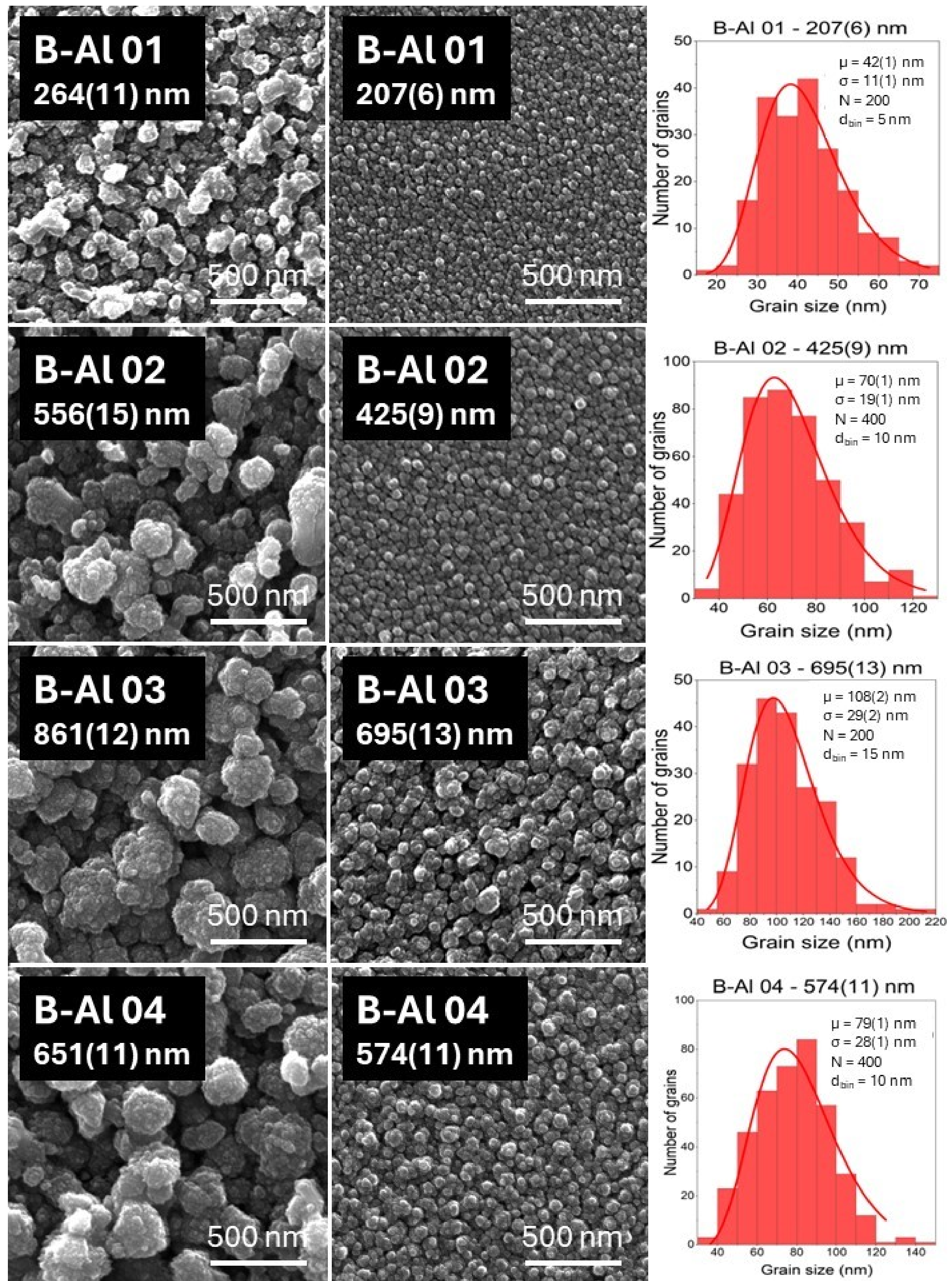

Figure 4.11: SEM images (of dimension 1.8×1.8 μm) aluminium thin films deposited on FS (left column) and Si(111) (middle column) substrates. Each row represents a sample with different thicknesses. The rightmost column shows the histograms of grain sizes obtained from SEM images of Si-grown B-Al. The histograms are fitted with a log-normal distribution, with the distribution parameters listed in the top right corner of each graph.

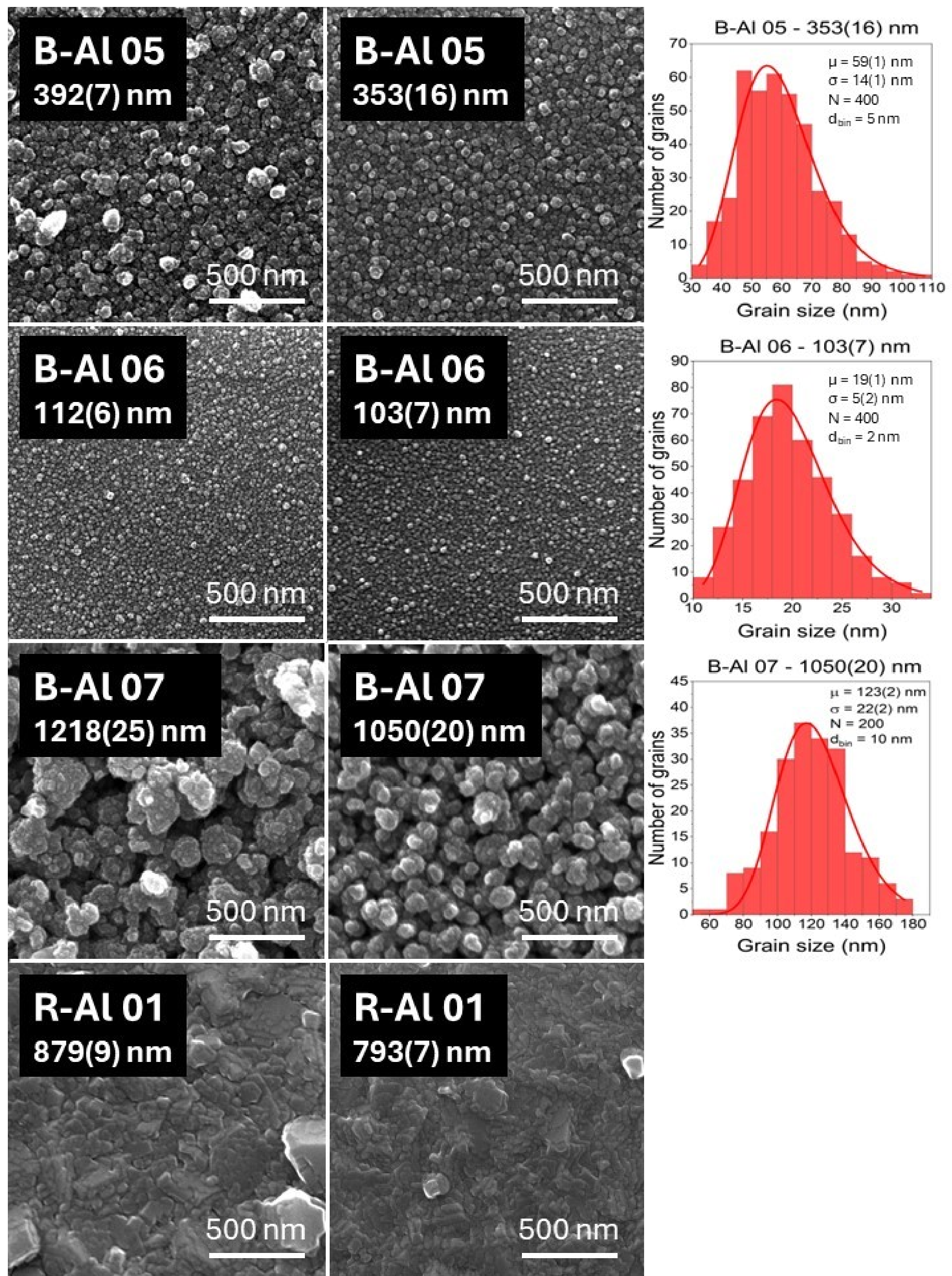

Figure 4.12: SEM images (of dimension 1.8×1.8 μm) aluminium thin films deposited on FS (left column) and Si(111) (middle column) substrates. Each row represents a sample with different thicknesses. The rightmost column shows the histograms of grain sizes obtained from SEM images of Si-grown B-Al. The histograms are fitted with a log-normal distribution, with the distribution parameters listed in the top right corner of each graph.

number of grains, which varied in shape. The software is able to calculate the enclosed areas[2], which we subsequently converted to the corresponding diameters, considering these to be equivalent to grain sizes. Here, some systematic error is introduced due to the subjective determination of grain boundaries, which are affected by the overall image quality. Additionally, since grains are randomly oriented in 3D space and only their 2D projections are visible, sufficient statistics is necessary to ensure statistical accuracy (in our case $N > 200$). We also measured individual grains multiple times to see how the value of area deviates but this deviation was compensated by the large sample size, as overestimated and underestimated grain sizes balanced each other out. Each histogram was then fitted using a log-normal distribution, as these films tend to follow this distribution[141], and the mean grain size μ and the standard deviation σ were obtained.

From these results, it is evident that B-Al tends to grow differently on Si substrate compared to FS. For a given thickness, the Si-grown films appear to be more compact. The smallest grains are comparable in size to the FS-grown films, but they do not tend to aggregate into larger grains that rapidly. The coarsening of the grains starts to be more pronounced for sample B-Al@Si 07 with thickness larger than 1 μm and it starts to resemble the cauliflower-like structure of sample B-Al@FS 07. As a consequence, these films remain more reflective and the threshold where they become black is shifting towards greater thickness. Also, the R-Al@FS 01 film appears to have more developed grains on the surface of two types - larger crystalline grains with sharp edges and smaller ones with rather undefined shape. Yet the underlying layer looks similar to R-Al@Si 01 so the choice of substrate does not affect the growth of R-Al that much.

The mean grain size increases with greater film thickness in both cases. For B-Al@Si (see graph in Fig. 4.13), it follows a power rule $\mu \sim t^{\alpha}$, represented by a dashed line. The parameter α is often reported in the literature, as it indicates various properties of thin films and allows for the prediction of their morphology. This is similar to the behaviour of evolution of the root mean square roughness with the deposition time, a power rule is also commonly observed[142]. Since the mean grain size is correlated with the roughness and the film thickness is directly proportional to the deposition time, this result is not surprising. The value of α was determined to be $\alpha = 0.74(5)$. For thicknesses greater than approximately 700 nm, the mean grain size reaches saturation.

From the EDX spectra that could also be measured with the same SEM, we were able to qualitatively and quantitatively estimate the presence of different chemical elements (refer back to Fig. 3.7). Besides aluminium, the presence of nitrogen, oxygen and carbon was reported using EDX in the past[24] and the formation of AlN in the grain boundaries was confirmed by X-ray photoelectron spectroscopy (XPS) analysis[21]. However, this method provides only a resolution in the order of several percent, due to a high penetration depth of the X-rays (approximately μm for our acceleration voltage of 15 kV), which exceeds the thickness of all our films. Therefore, if the abundance of any element is lower than 1%, we cannot claim its presence with certainty and we consider them to be not present at all. Moreover, since the FS substrate (SiO_2) also contains oxygen, the

[2]Unfortunately, for our samples, the software cannot perform the analysis automatically because it struggles with distinguishing one grains from another, especially if the grains are connected. Hence the described procedure must be used.

signal from it further complicates our analysis, as we cannot accurately estimate the exact oxygen content in the films. This is not a problem for the B-Al@Si samples, where oxygen is located only in a very thin oxide layer on top of Si(111).

The chemical abundance of each element as a function of film thickness is shown in the top part of Fig. 4.14. We can clearly see that the Al content is linearly increasing with thickness in both types of films. This is caused by a higher signal contribution from the film itself and a lesser contribution from the substrate. This effect is also evident in the second graph, illustrating a decrease in oxygen content in FS-grown films. However, this decrease slows down in thicker layers, as our films inherently contain oxygen atoms. The exact value could be obtained by extrapolating this graph, ideally to an infinitely thick film. Nevertheless, the expected oxygen content can be estimated from Si-grown films, where a nearly linear trend is observed again. This can be attributed to oxygen being trapped in the porous fractal-like structure of B-Al, which provides enough binding sites. Therefore, the oxygen content can be considered as a measure of the porosity in B-Al@Si films. The oxygen content reaches almost that of B-Al@FS and for the thickest samples is between 15-20%, consistent with the previously abovementioned published works in thicker films. By examining the O/Al ratio as a function of film thickness, we observe a decreasing trend for FS-grown films, while apparently for Si-grown films it remains almost constant. For films thicker than 900 nm, the difference diminishes. Notably, the R-Al 01 sample contains more Al atoms for a given thickness, likely due to its compactness and higher density compared to B-Al. On the other hand, R-Al@Si sample shows only a negligible amount of oxygen atoms, while some oxygen is present in the R-Al@FS film but less relative to the similarly thick black film. This suggests that oxygen could be present in R-Al in a very thin passivation layer (5 - 20 nm thick) on top of the film.

In B-Al@FS samples, the nitrogen content is higher for lower thicknesses reaching a maximum at approximately 400 nm and then slightly declining before stabilizing at a constant value of 25%. In similar manner, the B-Al@Si films reach this maximum at $\sim$ 900 nm. This difference may stem from the saturation of grain sizes, which is more pronounced in B-Al@FS. Smaller grains provide larger surface for AlN formation but as the growth of grains slows down, the relative amount of nitrogen remains stable. Since the saturation observed for B-Al@FS occurs approximately at twice the thickness, this would also correspond to the observed value of peaking nitrogen content. As expected, the R-Al films do not contain any nitrogen. And finally, by looking at the last graph, we can see that nitrogen atoms are predominantly abundant in thinner films as the growth favours poisoning of grains with nitrogen. However, at around 700 nm, we achieve a stoichiometric ratio of AlN. Beyond this point, this ratio asymptotically approaches a value of 0.5, meaning a nitrogen-deficient state with a higher proportion of metallic Al.

The results may be affected by a huge error caused by surface pollution and the fact, that Al K_α and Si K_α lines are very close to each other. Also, the quantification for lighter elements (below Ar) can be substantially exaggerated by EDX, due to the cascade effect and the low energy needed for K_α excitation[108]. Additional XPS analysis, which is very surface-sensitive, would be required to confirm these statements with certainty.

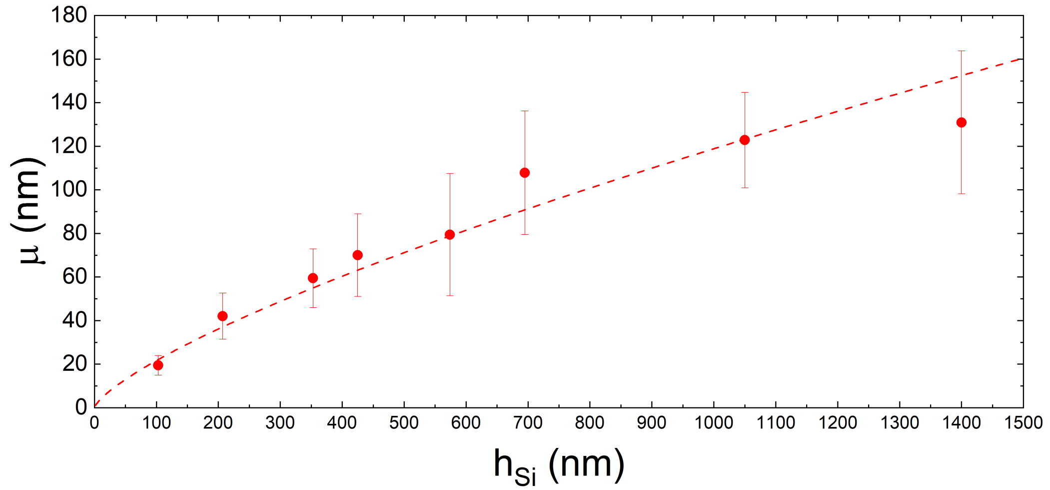

Figure 4.13: Graph showing the evolution of mean grain size with film thickness for B-Al films grown on a Si(111) substrate.

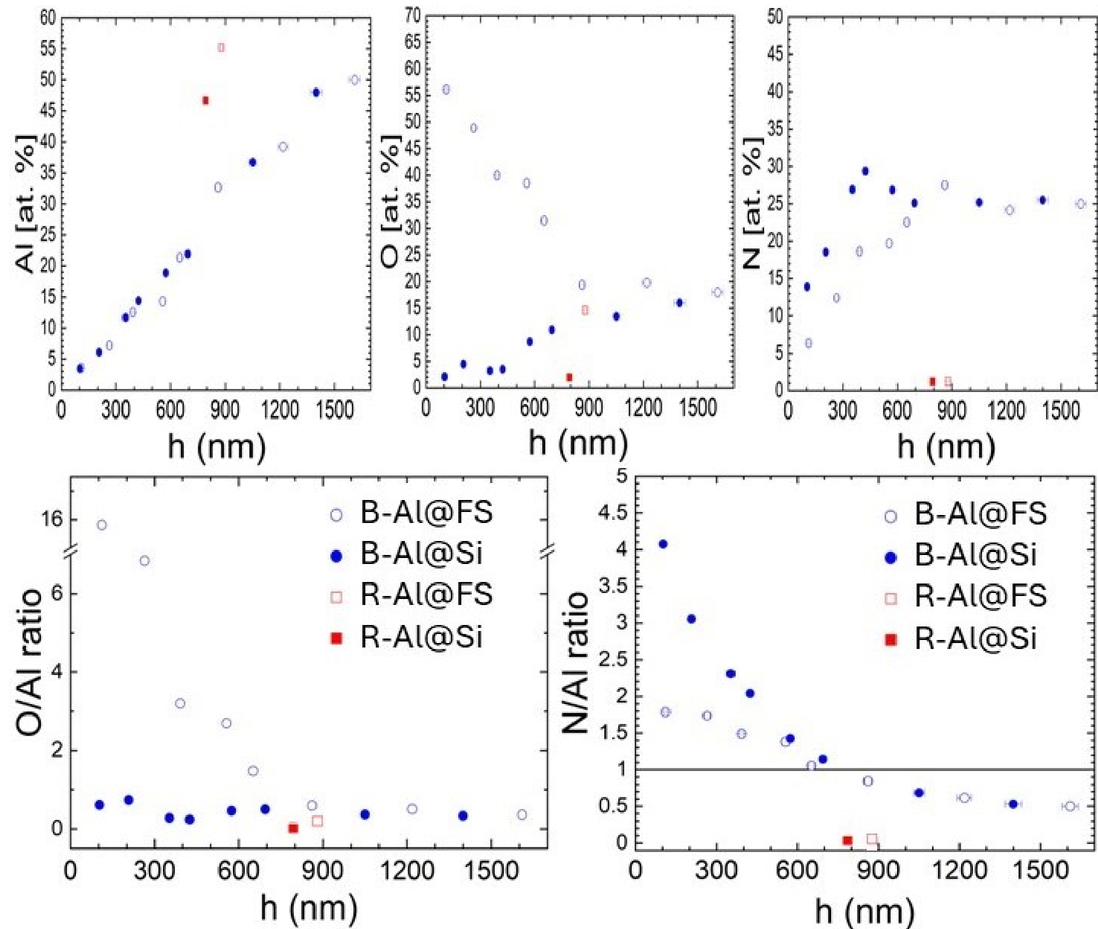

Figure 4.14: Chemical composition obtained from EDX analysis of R-Al and B-Al films: aluminium (top left), oxygen (top middle), and nitrogen (top right) content. The oxygen-to-aluminium (bottom left) and nitrogen-to-aluminium (bottom right) ratios are calculated for perspective. Vertical error bars are missing, although one can expect them to be ∼1% for each data point. Also, the concentration of Si is not listed, but it roughly represents the complement of the sum of Al, O, and N concentrations.

The thermal stability of B-Al films was investigated by SEM during thermal annealing up to 500°C in a vacuum, with a slow temperature ramp of 20°C/min. The SEM images for B-Al 04 grown on FS and Si substrate are shown in Fig. 4.15 and Fig. 4.16, respectively. These images were acquired at intervals of 100°C after maintaining each temperature constant for a dwelling time of 15 minutes. Recently, the formation of spiral-shaped nanowires above 200°C was reported for equivalent B-Al films prepared by MS on an unheated FS substrate[25].

Already at RT, the B-Al@FS 04 sample shows the presence of a few short nanowires of average length < 10 μm. The growth of these nanowires originates from surface scratches and abrasions. While our films exhibit relatively good wear resistance and adhesion, especially compared to those B-Al films prepared by TE, such imperfections are always present due to potential damage by improper handling. It is assumed that they likely occurred during sample transport, as they were not spotted in previous SEM measurements (compare with Fig. 4.12). The nanowires lengthen just negligibly for lower temperatures, and their concentration remains unchanged. During this time, thermal stress is generated, arising from the larger thermal expansion coefficient of Al (24.6×10^{-6} K^{-1}) than that of FS (0.56×10^{-6} K^{-1}). This stress cannot be relieved because of the compact Al_2O_3 film on top of the B-Al film, so thermally-induced diffusion of Al atoms to places of minimal energy is dominant. However, defects in this layer act as weak spots, where accumulated Al atoms push upwards other atoms, causing the formation of these nanowires.

However, the growth of nanowires begins to be significantly pronounced at around 250°C and ends at approximately 375°C. In this temperature range, twisting into spiral-like shapes accompanied by recrystallization is prevalent. For most single-phase metals, the temperature of primary recrystallization, according to Movchan and Demchishin[75] for films prepared by TE, falls within the range of $0.22T_M$ - $0.3T_M$, where T_M denotes the melting temperature (for Al $T_M = 660$°C). For sputtered films, Thornton extended this interval to $0.3T_M$ - $0.5T_M$[81], which aligns with our observed temperatures. However, the intact part of the film remains unchanged even above 400°C, preserving its antireflective properties. It illustrates the importance of proper manipulation with the films on their overall quality and performance. It was also demonstrated that applying scratches intentionally to specific areas on previously annealed films did not induce nanowire growth, likely due to stress release in the layer.[25].

For B-Al@Si 04, morphology evolution with temperature is different. Starting at RT, no nanowires are visible. The first nanowires start appearing at a temperature of 200°C and end at around 350°C, which is notably lower than in the FS case. Considering that the thermal expansion coefficient of Si is 2.6×10^{-6} K^{-1}, almost ten times lower than that of FS, we would expect that the thermally-induced stress is significantly lower, and therefore it should appear at higher temperatures, if at all. However, it is uncertain whether the Al_2O_3 layer has a comparable thickness and thus provides similar stress resistance. The possibility of a thinner Al_2O_3 layer would make it more vulnerable to break. Resolving this question would require additional measurements such as XPS with ion beam sputtering or high-resolution transmission electron microscopy (HRTEM)[143] to accurately determine the thickness of the Al_2O_3 layer. Furthermore, we notice the emergence of surface features much larger than the nanowires at temperatures

exceeding 400°C. The film cracks and forms a filament structure (as seen in the high-magnification image). The size of these structures, estimated to be on the order of several tens μm (see the low magnification image), indicates that these are formed on top of impurities such as dust particles, that were previously invisible. This underlines the critical role of a proper substrate cleaning process as it also affects the final properties of BM for possible high-temperature applications.

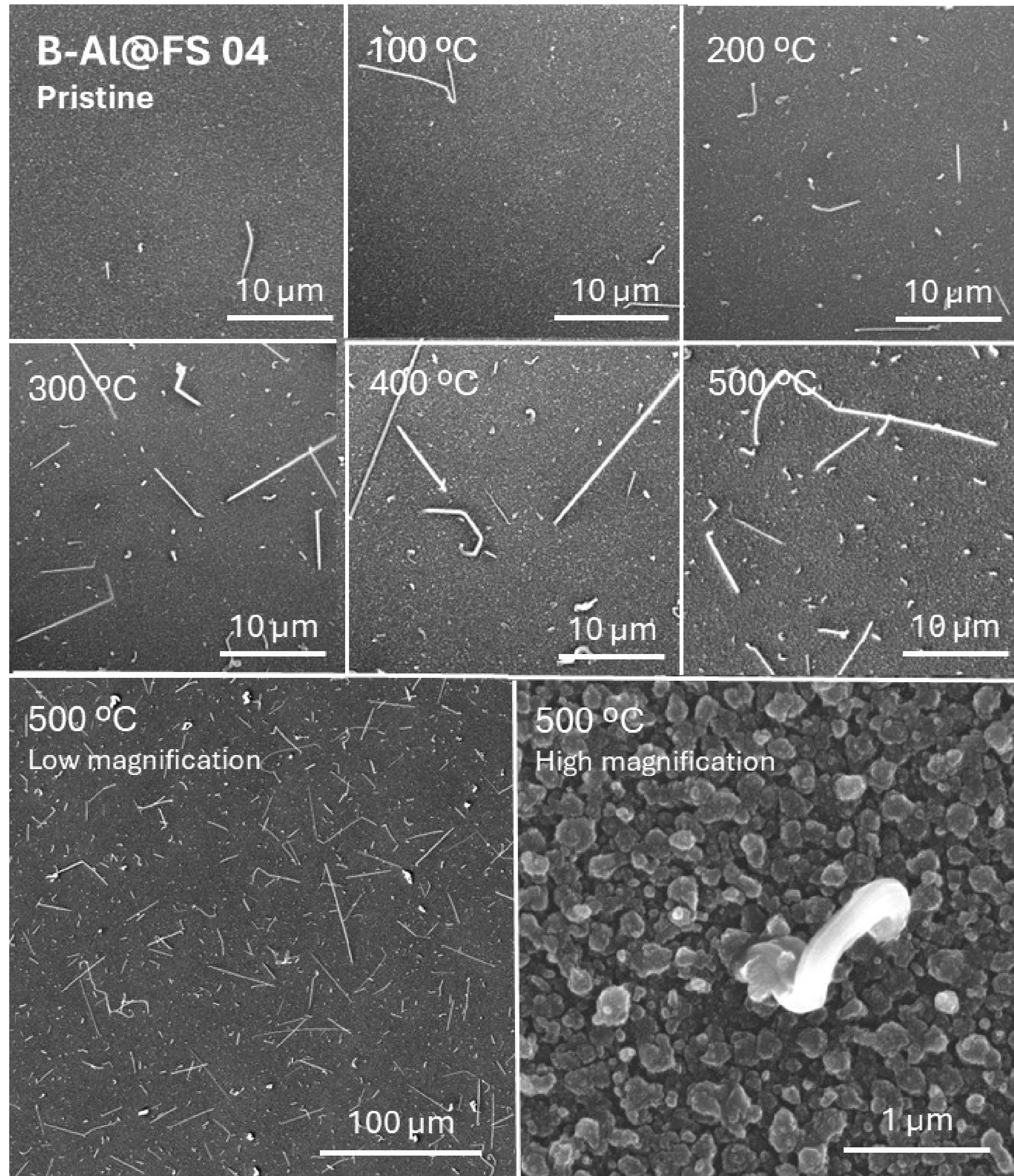

Figure 4.15: SEM images of B-Al 04 film deposited on FS at different temperatures. The mechanically undamaged areas remain stable up to 500°C, while a formation of straight and spiral-shaped nanowires starts from $\sim$ 250°C in surface defects. The concentration and elongation of the nanowires continue to increase up to $\sim$ 375°C, after which no remarkable changes are observed.

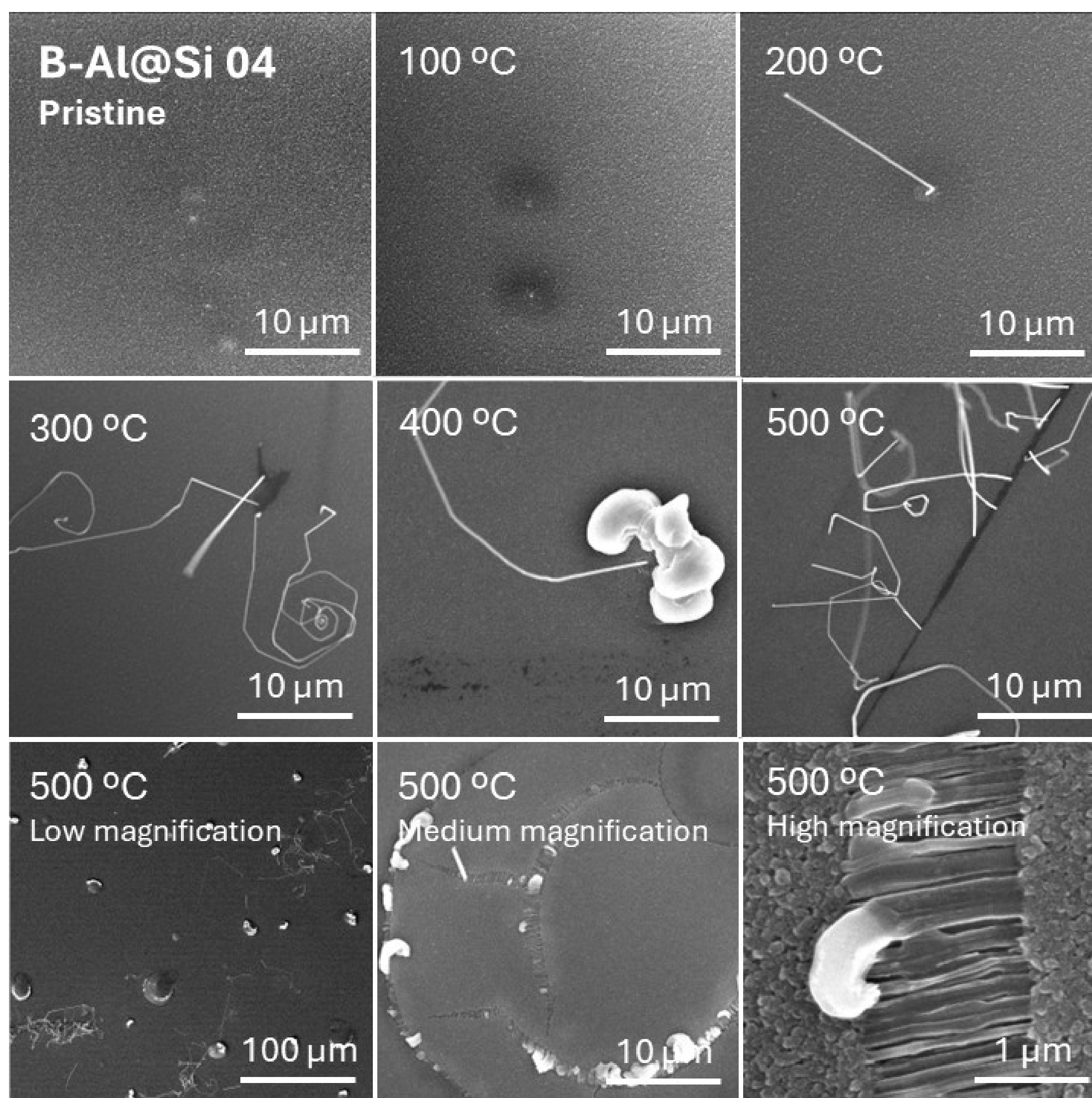

Figure 4.16: SEM images of B-Al 04 film deposited on Si(111) at different temperatures. At the beginning, no wires are present until $\sim 200°C$, when nanowires start appearing from surface imperfections, and their concentration gradually increases up to 350°C. Since this film possesses less scratches, the total concentration of nanowires is smaller than for FS. From this point on, the mechanism differs from FS-grown films, as larger features emerge on top of impurities, while other areas stay unaltered. Al begins to recrystallize/reconstruct because of its high diffusive energy[144][145].

4.3 XRD results of R-Al and B-Al films

Microstructure of R-Al and B-Al films deposited on FS with various thicknesses have been studied by XRD using BB geometry in the past[21][23][24]. Despite their different compositions and surface morphologies, it has been proved that both types of films crystallize in the FCC structure corresponding to bulk Al ($Fm\bar{3}m$ space group, see Fig. 4.17) with the same lattice parameter a_0 = 4.049(7) Å, i.e. without other crystalline phases. A larger mean crystallite size was observed for R-Al films, while a small microstrain value was reported in B-Al due to the presence of open-volume lattice defects. We can demonstrate these conclusions using both BB and GI geometry (fixed angle of incidence 3°) for our samples R-Al 01 and B-Al 03, with a similar thickness of approximately 870 nm. The measured XRD patterns in the 2θ range 30-90° are in Fig. 4.18. We can see that in both geometries we get more signal for reflective films. As expected, the signal from the GI geometry is enhanced, due to the lower penetration depth of the X-rays.

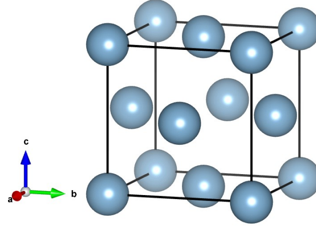

Figure 4.17: Unit cell of Al with space group $Fm\bar{3}m$ (225) depicted using VESTA software.

Five peaks are observed at 2θ = 38.5°, 44.7°, 65.1°, 78.2°, and 82.8°, corresponding to (111), (200), (220), (311) and (222) planes, respectively, but the last mentioned is indistinguishable from the background in B-Al. The increase in intensity towards the lower diffraction angles corresponds to a broad amorphous diffraction peak originating from the FS substrate with a maximum located at 22°. For GI this peak is suppressed, as less signal comes from the substrate. Indeed, AlN, Al_2O_3 nor other crystalline phases are present, implying they must be either amorphous or their content is not sufficient enough to be detected by XRD. Also, for BB geometry it is possible to evaluate texture coefficient T_{hkl} for each hkl plane that is used to describe preferred orientation and it is defined by the formula:

$$T_{hkl} = \frac{\frac{I_{hkl}}{I^0_{hkl}}}{\frac{1}{N}\sum_{i=1}^{N}\left(\frac{I_{hkl}}{I^0_{hkl}}\right)_i} \tag{4.2}$$

where I_{hkl} is the measured intensity, I^0_{hkl} is the normalized intensity from CIF-file and N is the number of reflections considered into analysis. If the T_{hkl} is remarkably higher than 1, it indicates a higher abundance of crystallites oriented in the corresponding direction. Conversely, $T_{hkl} < 1$ suggest absence of a crystallites in a given direction. Since for our samples, all of the reflections exhibit a texture

coefficient of approximately 1 with a small variation we can conclude that there is no texture present.

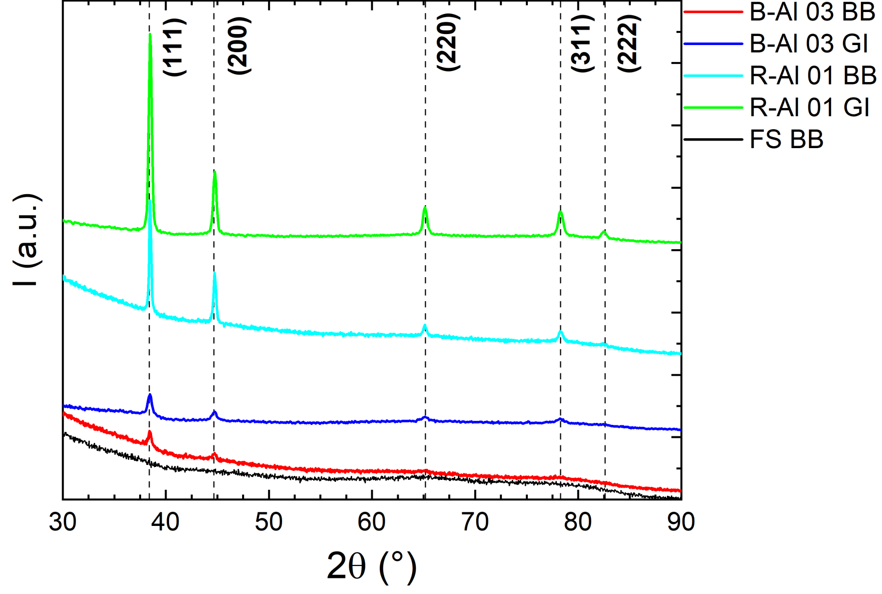

Figure 4.18: XRD patterns of R-Al and B-Al films deposited on FS substrates, measured in BB and GI geometry. The intensities are shifted vertically to present the patterns in a single graph. The dashed lines represent the position of diffraction peaks corresponding to Al ($Fm\bar{3}m$) structure with lattice parameter $a_0 = 4.049(7)$ Å.

During isolated peak analysis, the diffraction pattern peaks were fitted individually by Pseudo-Voight functions with the background approximated locally in the vicinity of the peaks by a linear function. From the positions of the peaks, we can construct a C-W plot (Equation (3.12)) to obtain the value of the lattice parameter a_0, corrected for possible misalignment of the sample in the vertical direction, as the value of the intercept of the linear fit. The d_{hkl} from Equation (3.11) for cubic structure is determined from the Miller indices hkl as:

$$d_{hkl} = \frac{a_{hkl}}{\sqrt{h^2 + k^2 + l^2}} \tag{4.3}$$

Using this equation and the Bragg law (Equation (3.9)) we can determine d_{hkl} and subsequently a_{hkl} and its error $\sigma_{a_{hkl}}$ from the propagation of uncertainty formula as:

$$\sigma_{a_{hkl}} = \frac{\sigma_\theta cot\theta}{\sin\theta} a_{hkl} \tag{4.4}$$

The C-W are in Fig. 4.19i. The linear regressions for all samples have intercepts of $a_0 = 4.05(1)$ Å, which is the same as for the bulk Al[146], indicating the absence of macrostrain that would be responsible for a change in lattice parameter.

From the peak widths, we also constructed W-H plots (see Equation (3.21)) by determining the FWHM value of each peak β_{hkl} together with its error $\sigma_{\beta_{hkl}}$, to evaluate the mean grain size D and microstrain e. These plots can be found in Fig. 4.19ii and the calculated values from this isolated peak fitting are summarized

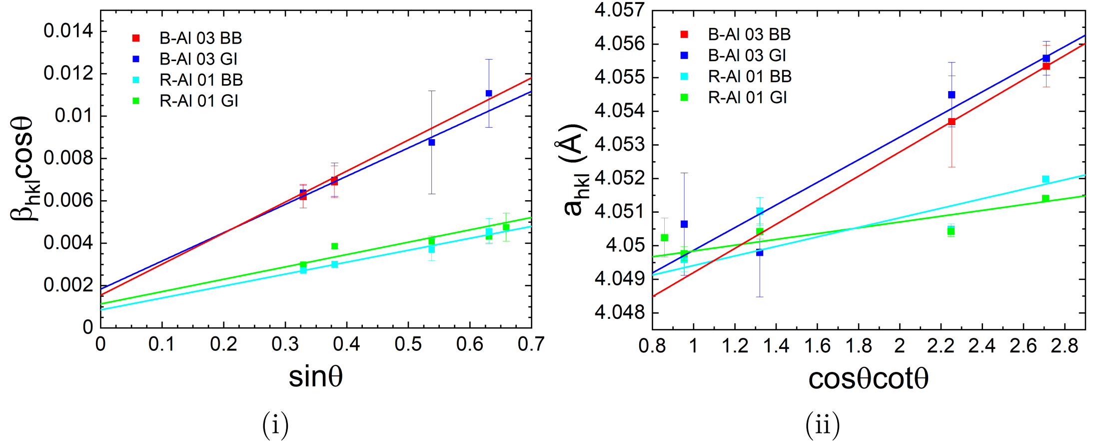

(i) (ii)

Figure 4.19: (i) C-W plot and (ii) W-H plot of R-Al and B-Al films from XRD diffraction pattern in Fig. 4.18. For B-Al in BB geometry only two peaks are available for analysis.

in Table 4.8. The magnitude of vertical error bars $\sigma_{\beta_{hkl}\cos\theta}$ varies for each peak since it was calculated once more via the propagation of uncertainty formula as:

$$\sigma_{\beta_{hkl}\cos\theta} = \sqrt{\cos^2\theta\sigma^2_{\beta_{hkl}} + \beta^2_{hkl}\sin^2\theta\sigma^2_\theta} \tag{4.5}$$

XRD measurements			Isolated peak analysis			Rietveld refinement		
Sample name	Geometry	h (nm)	a_0 (Å)	D (nm)	e (%)	a_0 (A)	D (nm)	e (%)
B-Al 03	BB	861(12)	4.05(1)	75(25)	0.33(8)	4.049(5)	79(10)	0.40(5)
B-Al 03	GI	861(12)	4.05(1)	89(16)	0.37(3)	4.050(3)	70(8)	0.39(4)
R-Al 01	BB	879(9)	4.048(2)	160(19)	0.14(2)	4.048(1)	167(5)	0.07(1)
R-Al 01	GI	879(9)	4.049(1)	120(28)	0.15(1)	4.049(1)	159(4)	0.09(1)

Table 4.8: Parameters obtained from XRD patterns in Fig. 4.18 using isolated peak fitting through C-W and W-H plots, and Rietveld refinement.

There are two main conclusions to be made. Firstly, the microstrain value e, given by the slope of the W-H plot, is notably higher for B-Al films, likely due to the higher density of lattice defects. Secondly, the crystallite size D, obtained from the intercept value of the plot, is larger for reflective samples. The equivalent parameters were also derived from Rietveld refinement, listed in the last three columns of the table, using a CIF-file for aluminium (ICSD-18839)[146] with a 5-th order Chebyshev polynomial as a background. Both analyses yield the same results within their margin of error, although Rietveld refinement is usually more precise and reliable. The results are coherent with previously published articles.

To study the influence of the Si substrate on the crystalline structure of the B-Al film, we measured and compared the XRD patterns in GI geometry for each pair from the same deposition. The results for selected pairs are shown in Fig. 4.20. Qualitatively, the positions of peaks and their relative intensities are identical, implying that B-Al crystallizes on Si in the same crystal structure as for FS with no preferential orientation. Also, the peak positions remain unshifted, meaning there is no tensile or compressive stress present as a result of a mis-match between the Si lattice parameter (approximately 5.43 Å) and Al. This is

XRD measurements			Isolated peak analysis			Rietveld refinement		
Sample name	Substrate	h (nm)	a_0 (Å)	D (nm)	e (%)	a_0 (A)	D (nm)	e (%)
B-Al 08	FS	1610(30)	4.0494(11)	56(3)	0.10(1)	4.0491(2)	56(2)	0.09(2)
B-Al 08	Si	1400(30)	4.048(1)	27(3)	0.12(3)	4.0486(2)	35(2)	0.09(4)
B-Al 07	FS	1218(25)	4.049(2)	101(10)	0.27(6)	4.0487(4)	105(5)	0.33(2)
B-Al 07	Si	1050(20)	4.048(2)	49(9)	0.29(3)	4.0482(7)	59(4)	0.30(2)
B-Al 03	FS	861(12)	4.05(1)	89(16)	0.37(3)	4.050(3)	70(8)	0.39(4)
B-Al 03	Si	695(13)	4.05(1)	33(12)	0.5(1)	4.048(2)	35(4)	0.4(1)

Table 4.9: Parameters obtained from XRD patterns in Fig. 4.20 using isolated peak fitting through C-W and W-H plots, and Rietveld refinement for different substrates.

often the case in epitaxial films but since ours is polycrystalline with a columnar non-continuous vertical growth, the stress can be released and this result seems reasonable.

The intensity of reflections for deposition B-Al 01 (with thicknesses of around 200-250 nm) is significantly suppressed, simply because there is not enough material available for a sufficient signal. As the thickness increases, the intensity rises, but it is generally lower for samples deposited on Si substrates. An exception is the thickest sample, B-Al 08, where the diffraction intensity for B-Al@Si 08 is higher than for B-Al@FS 08. This could be explained by either a generally lower thickness of our Si-grown films compared to FS-grown ones or it might suggest that depositing B-Al on a crystalline Si wafer with a very small roughness favours crystallization less than depositing on a rougher FS amorphous substrate. This effect was also observed with other substrates of even greater roughness, such as aluminum foil. The reversed behaviour for the B-Al 08 sample could possibly be explained by contamination from some unknown impurity, probably introduced from the sample holder. This hypothesis is supported by the emergence of a broad peak at $2\theta \sim 36°$ in both films, which was previously not present. This impurity may have altered the initial surface roughness of the substrate, thereby enhancing crystallization during growth. Notably, the peaks are consistently broader for B-Al@Si, which could be attributed to smaller mean crystallite sizes that correlate with the observed mean grain size. This was already apparent from the SEM images for surface grains but since X-rays penetrate deeper into the material, it gives an average value throughout the whole film. This further confirms that smaller grains are located near the substrate. The determined values are again provided in Table 4.9 and the corresponding C-W and W-H plots, constructed in the same manner as before, can be found in Fig. 4.21i and 4.21. The extraordinary behaviour of sample B-Al 08 is also visible, as the mean grain size unexpectedly plummeted, despite it being expected to be higher with thickness. Additionally, the microstrain is significantly lower, even more than previously discussed R-Al 01 from both independent analyses. There was definitely some process during the deposition that modified the film's properties and XRD has proved to be a useful and effective method for identifying those discrepancies.

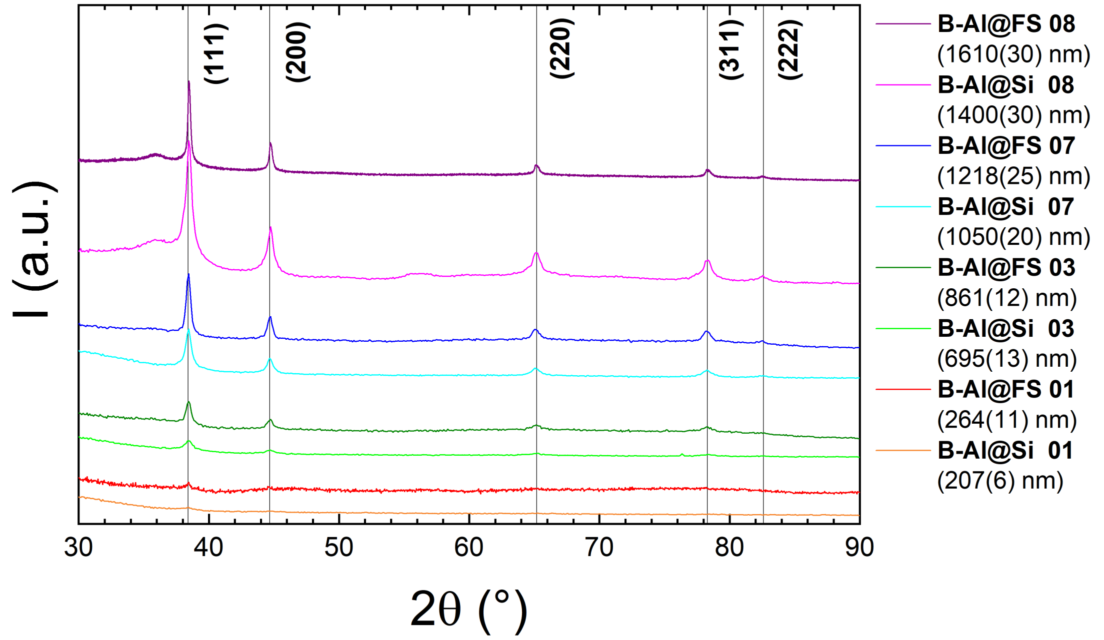

Figure 4.20: Comparison of XRD patterns measured in GI parallel beam geometry of B-Al samples deposited on FS and Si(111) substrates for various film thicknesses. The intensities are shifted vertically to present the patterns in a single graph. The solid lines represent the position of diffraction peaks corresponding to Al ($Fm\bar{3}m$) structure with lattice parameter $a_0 = 4.049(7)$ Å.

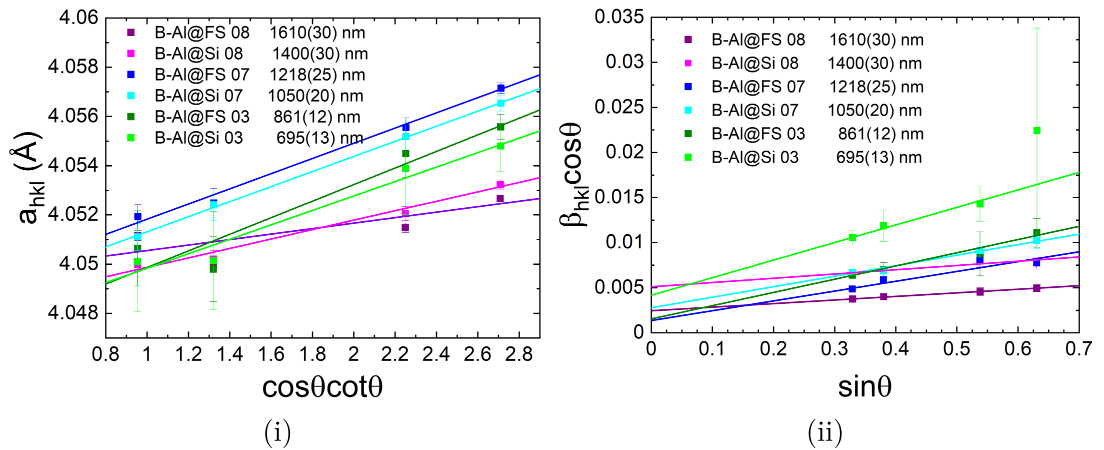

Figure 4.21: (i) C-W plot and (ii) W-H plot of B-Al films from XRD pattern in Fig. 4.18.

4.4 Reflectance of B-Al films

Comparison between the optical properties of R-Al and B-Al films with similar thicknesses prepared on FS have been extensively studied in the past. It was demonstrated that spectrophotometric specular reflectance for B-Al drops exponentially with increasing thickness, reaching $R_{spec} < 5\%$ for films thicker than 300 nm, while reflectance of R-Al films remains just a bit lower than the bulk Al value[23]. Diffuse reflectance measurements[21][22][24] further confirmed strong light absorption in the porous and rough structure of B-Al with $R_{diff} < 4\%$ for film thicker than 500 nm in the UV-VIS-NIR spectral range up to 1200 nm.

Figure 4.22 provides a comparison between the diffuse reflectivity of B-Al films deposited on FS and Si substrate. Notably, the reflectivity of our samples is slightly higher than previously reported and it increases towards the NIR region. This could be due to a slightly modified N_2/Ar ratio from the optimal one during deposition, leading to the formation of a film with a higher fraction of amorphous phases with higher reflectivity, or it may be caused by the degradation of the reference Spectralon standard, which might have lost its reflectivity over time due to extensive use. A clear dependence of the decreasing reflectivity is noted with an increase in film thickness. However, the FS-grown films possess lower reflectivity in each case, which is not a consequence of a smaller thickness, as the thinnest B-Al@FS film still remains less reflective than the thickest B-Al@Si.

In contrast, when looking from the bottom side through the substrate, the reflectivity is generally higher and it tends to further increase with more film. This highlights once again the significant difference in B-Al surface morphology and porosity near the substrate.

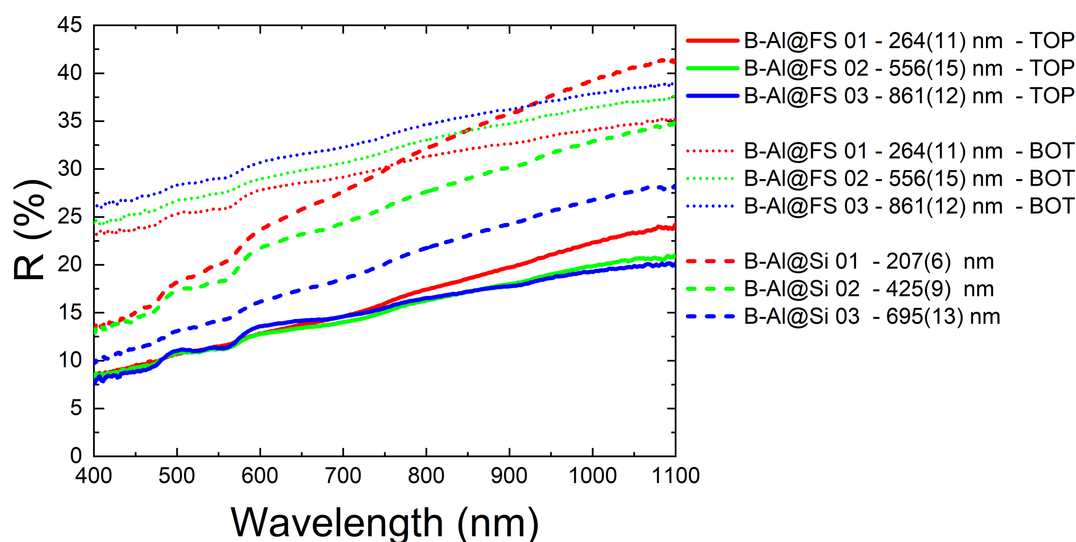

Figure 4.22: Spectrophotometric diffuse reflectance of B-Al films. The graph illustrates distinct reflectance behaviour depending on the substrate and film thickness, with FS-grown films consistently exhibiting lower reflectance from the top surface (denoted as TOP) compared to Si-grown films. Since Si substrate is not transparent, only reflectance from the top surface can be measured. The comparison with reflectance from the bottom surface (BOT) measured through the substrate is presented for FS.

4.5 Morphology of R-Ti and B-Ti films

Initially, morphological properties were investigated at RT using both AFM and SEM to see the difference between R-Ti and B-Ti films of the same thickness. For a proper comparison, two samples with similar thicknesses were chosen: R-Ti 01 and B-Ti 02, both deposited at a deposition pressure of 1.0 Pa. The combined SE SEM and AFM images are presented in Fig. 4.23. These results reveal significantly different surface morphologies between the samples, yet the surface remains relatively uniform and smooth with a similar roughness in both cases, contrary to B-Al. The R-Ti 01 sample exhibits a fine structure with numerous crystalline closely packed grains, each several tens of nanometers in size, and with various shapes ranging from round to angular. The B-Ti 02 sample displays smaller, more densely packed grains, mostly spherical in shape, that coalesce into larger clusters. At first glance, it may resemble a cauliflower-like surface structure. However, the surface waviness appears to be less pronounced in comparison to B-Al, maintaining a relatively low surface-to-volume ratio.

To examine the thermal stability of B-Ti films we again performed SEM measurements under heat treatment for samples deposited at 1.5 Pa with various N_2 content, namely B-Ti 11 and B-Ti 14 (4 and 10 sccm N_2) and the results are compared with the reflective sample R-Ti 02 (0 sccm N_2). The temperature ramp was chosen to be 40°C/min with 100°C steps. The dwelling time was 15 minutes between each measurement. The measured SEM images are presented in Fig. 4.24. For the R-Ti 02 sample, we decided to capture pictures from nearly the same area. Consequently, this region was subjected to continuous electron beam exposure, which must be considered in our analysis. We observed slight modifications in the bombarded area beyond the charging effect.

At RT, the surface of the R-Ti 02 seems more structured with more pronounced grains compared to R-Ti 01 in Fig. 4.23. This might be an intrinsic property of the film due to its significantly greater thickness, or it could be attributed to the lower resolution of the SEM, as the grains are very small. To rule out either possibility, it would be necessary to measure the sample using the same SEM device. However, the sample underwent changes due to annealing in a vacuum, making such confirmation measurements impossible. Below 300°C, the sample does not exhibit any visible changes. However, at 400°C, the surface starts undergoing noticeable changes, which correlates with the transition temperature of bulk Ti ($\sim$ 430°C) where it rapidly loses its mechanical properties[147]. The annealing causes recrystallization, forming larger grains as a result of the increased diffusion of Ti atoms on the surface. The polycrystalline surface becomes rougher with grains reaching sizes of 100 - 200 nm. At 500°C the recrystallization is even more enhanced, and the densely-packed granular surface microstructure resembles that of R-Ti 01 at RT, but with much larger grains.

For B-Ti 11 and B-Ti 14, the scanned area was changed after each measurement to eliminate the impact of the electron beam on the final image. As can be seen, there is no visible change in the surface structure of either film with elevated temperature. This is due to formation of TiN, which has excellent thermal stability up to temperatures well above our range. Some larger surface features are present, which were beneficial for focusing, since it was difficult to focus on the underlying structure. Overall, the surface appears similar to that of B-Ti 02.

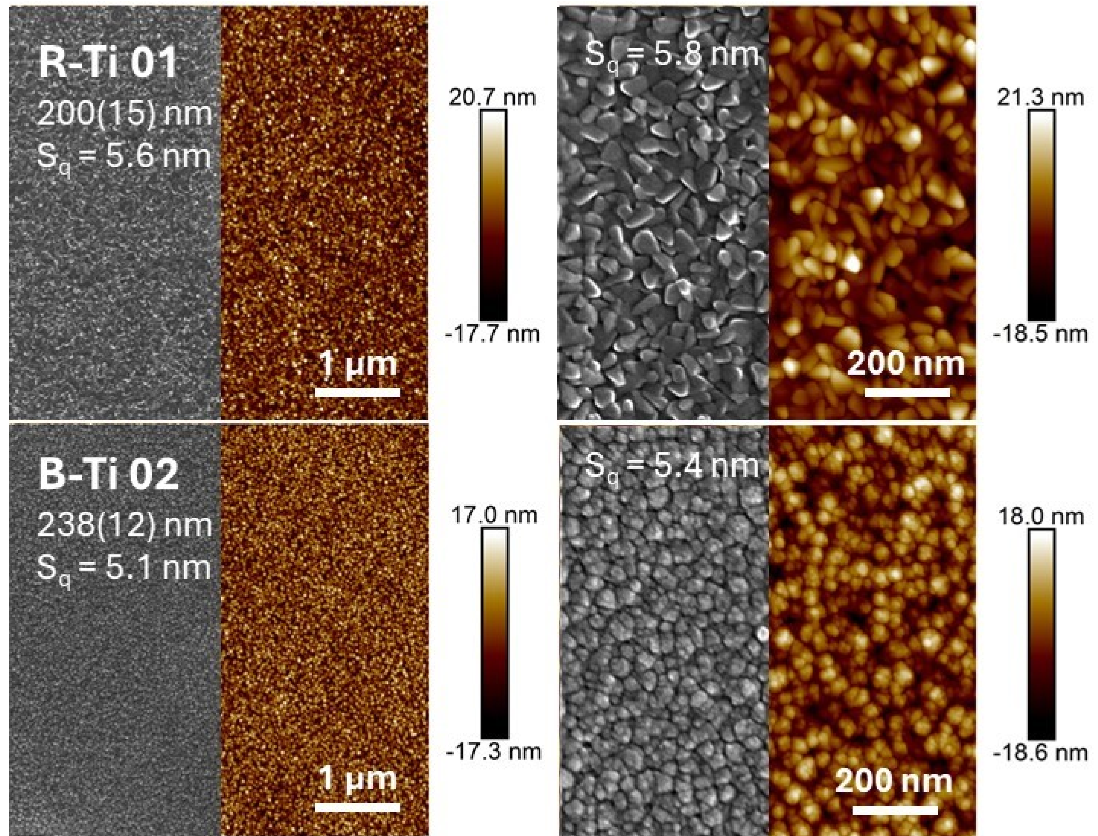

Figure 4.23: AFM and SEM images of R-Ti and B-Ti at RT. The left pictures have dimensions of $5 \times 5\ \mu\text{m}^2$. The inset in the upper-left corner contains information about the sample name, thickness and root-mean-square roughness. The right pictures have dimensions of $1 \times 1\ \mu\text{m}^2$ and the root-mean-square roughness value is again provided.

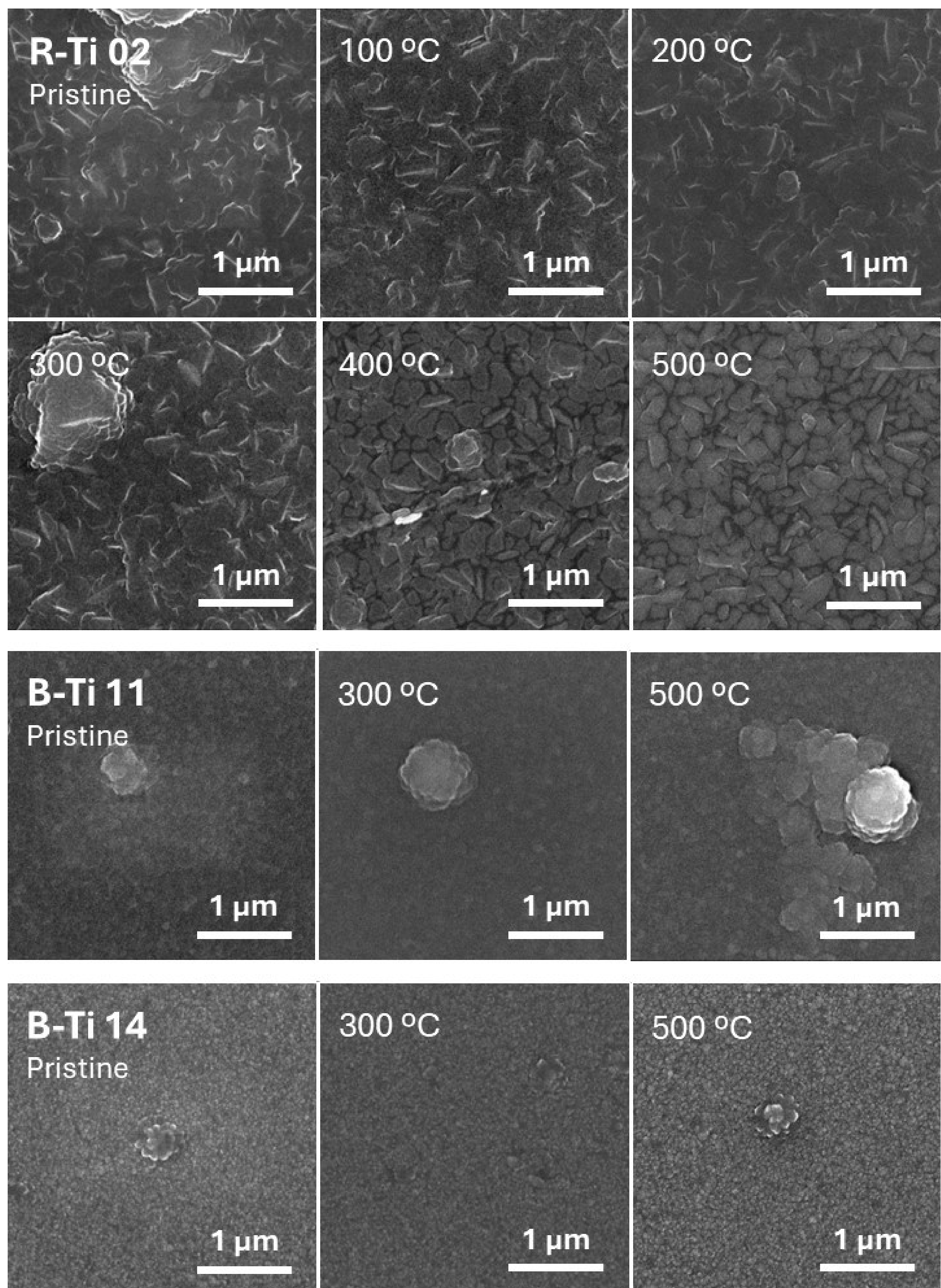

Figure 4.24: SEM images of R-Ti and B-Ti taken at different temperatures. For R-Ti 02 (upper half), the surface microstructure starts to recrystallize above 400°C with substantial grain growth. The surface of B-Ti 11 (third row) and B-Ti 14 (fourth row) remains unchanged, showing a good thermal stability due to formation of TiN.

4.6 XRD results of R-Ti and B-Ti films

It is well-known that bulk titanium appears in two allotropic forms. At low temperatures up to 880°C, it crystallizes in a hexagonal close-packed (HCP) crystal structure (space group $P6_3/mmc$ and lattice parameters $a = 2.951(6)$ Å and $c = 4.684(1)$ Å), known as α phase[148], which is of our interest. For Cu K_α source lamp, the most intense diffraction reflections occur at 35.6°, 38.6°, 40.7°, 53.5°, 64.0°, 71.2°, 77.3°, and 78.7° corresponding to the (010), (002), (011), (012), (110), (013), (112), and (021) planes, respectively (see Fig. 4.25). On the other hand, TiN possesses an FCC lattice with the space group $Fm\bar{3}m$ and lattice parameter $a = 4.244(1)$ Å, similarly to Al (see Fig. 4.26), hence the position of the diffraction peaks is slightly shifted to smaller diffraction angles.

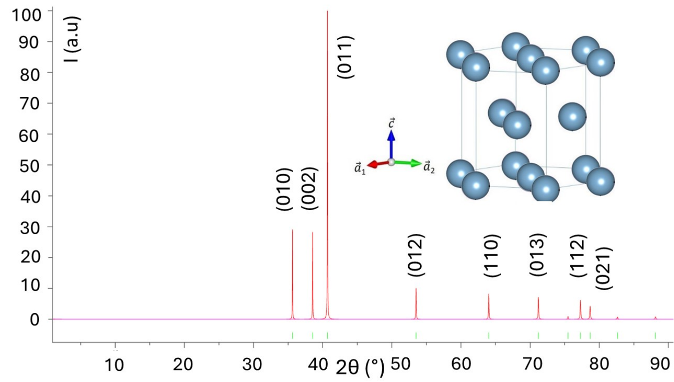

Figure 4.25: Theoretical diffraction pattern and unit cell of Ti with space group $P6_3/mmc$ (194) generated by VESTA software.

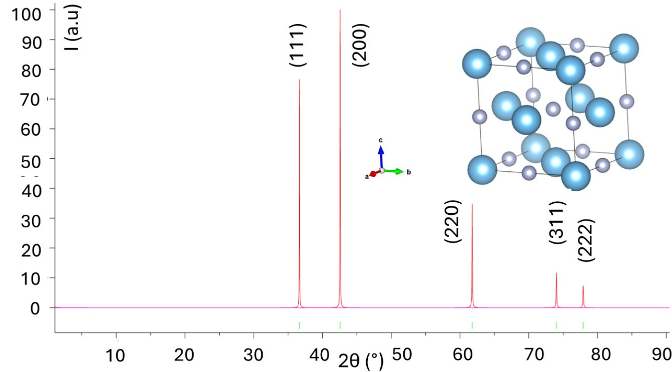

Figure 4.26: Theoretical diffraction pattern and unit cell of TiN with space group $Fm\bar{3}m$ (225) generated by VESTA software.

XRD patterns for our R-Ti and B-Ti films were acquired in GI geometry across the 2θ range of 10-90°, shown in Fig. 4.27. Again, all samples exhibit a wide amorphous peak with a maximum of 22°, originating from the FS substrate. Due to the constant penetration depth of X-rays, the intensity of this peak is inversely proportional to film thickness, which further supports our profilometric measurements, at least relatively, as a decrease of the thicknesses with elevated nitrogen content for deposition pressure of 1.0 Pa is apparent. At first glance, the results reveal that peak intensities vary for different samples, with some peaks

even completely disappearing into the background. Since mostly only two or three peaks are intense enough, this makes W-H analysis difficult to perform. Therefore only Rietveld refinement using appropriate CIF-file for Ti[149] and TiN[150] was utilized. The refined parameters are presented similarly as for B-Al in Tab. 4.10.

Firstly, by examining the R-Ti 02 sample (grey line at the bottom), we can see that it consists solely of the pure Ti phase crystallizing in the HCP lattice from Fig. 4.25. However, not all the peaks are visible, with the majority of them being suppressed in the background. This signifies a strong preferred orientation for the (002) (along the vertical c-axis) and (013) planes, resulting in a texture in two close but non-equivalent crystallographic directions. This is not an uncommon result for polycrystalline films, particularly for those prepared by MS, as similar behaviour has been reported as a consequence of changing bias voltage or deposition rate[151]. The lattice parameters are just slightly higher than those listed in the literature, indicating small tensile stress, and the sample is polycrystalline with an estimated mean grain size of 44 nm.

Adding the smallest feasible amount of nitrogen quickly transforms the film from a pure Ti phase, which is no longer present, into a TiN phase. Yet for the B-Ti 01 sample, the peak positions are shifted towards higher angles, corresponding to a substoichiometric TiN_{1-x} phase, where the value of x was determined to be about ~ 0.4. This implies that not all nitrogen positions are occupied due to a low nitrogen concentration in plasma, and the smaller lattice parameter is caused by N-vacancies in the lattice. Unfortunately, as 0.6 sccm is the lowest possible nitrogen flow available in our sputtering system, we could not investigate this transition for even lower N_2 partial pressure.

For higher N_2/Ar ratios, our B-Ti films crystallize in the TiN phase but the texture continuously changes from a preferred (111) orientation at a lower nitrogen content to (002) at higher nitrogen flow. This is interesting because we are able to tailor the films with the desired pre-defined texture simply by altering the N_2 partial pressure. The switch occurs for samples made at 1.0 Pa at a N_2/Ar ratio of about 13.0%, where the second peak appears for the first time. This change is more sudden for samples prepared at 1.5 Pa, appearing already at a N_2/Ar ratio of 11 %. This effect of texture switching is often observed in TiN films at elevated temperatures, exceeding temperatures 100°C[152]. Our substrate is kept at RT, although we used a very high power loading for our plasma discharge. So it is possible that nitrogen atoms may influence the efficiency of energy transfer between the plasma and the Ar^+ ions due to their different thermal conductivities, or they modify the energy of sputtered atoms, leading to an increase of substrate temperature. Or it could be a consequence of lower defect concentration for films at higher pressures, favouring a certain growth direction. This would require additional analytical techniques, such as positron annihilation spectroscopy, to affirm this hypothesis. The exact mechanism behind this phenomenon remains an open challenging question due to the complexity of the problem.

When comparing the samples prepared at 1.0 Pa and 1.5 Pa, we can see that peaks are broader in the former case, indicating smaller crystallite sizes. For lower pressure, there is clear trend of decreasing D with increasing N_2/Ar ratio, despite their thickness, along with generally higher lattice parameter a. For 1.5 Pa deposition pressure, the crystallites are comparable in size and are not affected by the amount of nitrogen in the chamber, with an exception of sample B-Ti 10.

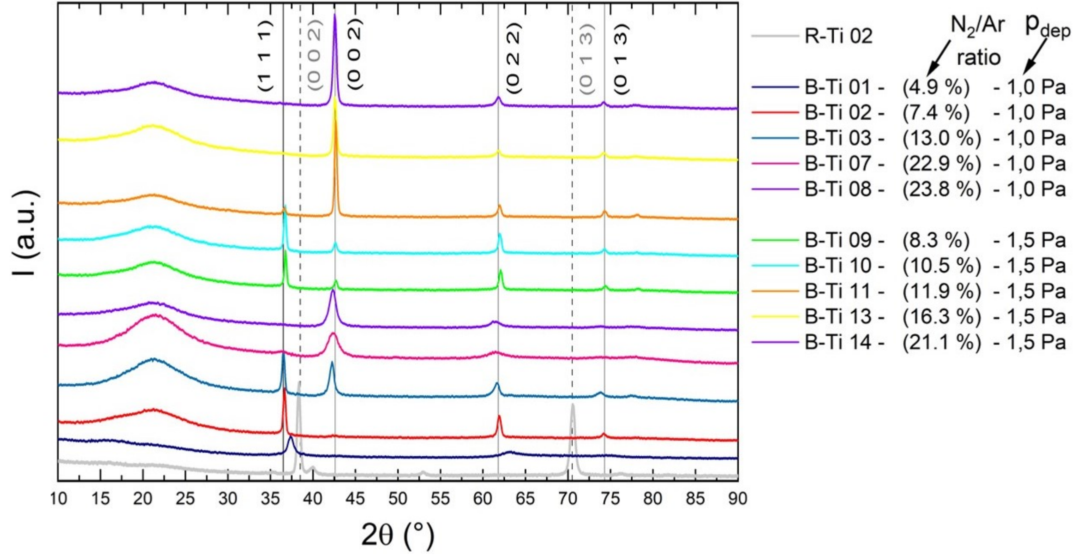

Figure 4.27: XRD patterns of R-Ti and B-Ti films deposited at different nitrogen content and deposition pressures. The solid lines represent the positions of TiN reflections, while the dashed lines show the positions of the most intense Ti diffraction peaks.

Sample name	h (nm)	N_2/Ar ratio (%)	a (Å)	c (Å)	D (nm)	e (%)
R-Ti 01	1521(40)		2.9530(5)	4.6950(2)	44(2)	0.144(3)
B-Ti 01	1023(18)	4.9(3)	4.17(2)		17(3)	0.39(4)
B-Ti 02	358(14)	7.4(3)	4.232(1)		70(11)	0.145(8)
B-Ti 03	265(5)	13.0(3)	4.257(3)		27(3)	0.20(2)
B-Ti 07	220(7)	22.9(5)	4.24(3)		9(8)	0.50(3)
B-Ti 08	359(6)	23.8(5)	4.26(1)		11(5)	0.20(3)
B-Ti 09	398(8)	8.3(3)	4.225(1)		45(3)	0.089(7)
B-Ti 10	379(7)	10.5(3)	4.2301(8)		65(7)	0.124(7)
B-Ti 11	320(12)	11.9(3)	4.238(3)		43(3)	0.10(1)
B-Ti 13	295(5)	16.3(4)	4.242(2)		37(2)	0.10(1)
B-Ti 14	488(12)	21.1(5)	4.238(4)		36(2)	0.137(8)

Table 4.10: Parameters obtained from XRD patterns in Fig. 4.27 through Rietveld refinement.

4.7 Reflectance of B-Ti films

The optical diffuse reflectance spectra in the UV-VIS spectral range of B-Ti films, which appeared darkest to the naked eye, were collected to quantitatively assess their blackness from both sides and are presented in Fig. 4.28. The films deposited at 1.0 Pa showed higher overall reflectivity and some of them underwent partial delamination that deteriorated the film quality. Therefore, only a comparison for films prepared at 1.5 Pa is discussed. Additional specular transmittance measurements showed negligible transmittance ($T < 0.5\%$) for all inspected samples, meaning that the light is either absorbed or reflected. The theoretical reflectance value calculated from the optical constants[153] and Equations (1.2), (1.4) of the air/TiN/FS interface (300 nm of TiN) is provided for comparison by a dashed line.

The reflectance spectra qualitatively display the same behaviour as theoretically predicted, with a minimum between 400-520 nm corresponding to an absorption peak attributed to the charge transfer between the N-2s and Ti-2p states[154] and then a gradual increase of reflectance towards the NIR region. However, the overall reflectivity remains fairly high compared to B-Al, with $R > 20\%$, which is too high to be considered as a BM. Reflectance on the order of a few percent was previously successfully achieved by femtosecond laser pulses[16][155]. Moreover, the peak position seems to be red-shifted for our films. A similar shift was observed as a function of varied N_2/Ar content for DC sputtered films[28] with changing stoichiometry, magnetron power[156] for RF MS, and due to oxidation and creation of TiO_2 layer[157].

Surprisingly, the top surface reflects more light than the bottom surface measured through the substrate, which is the opposite behaviour as was observed for B-Al films. This can possibly be explained by the combined effect of different morphology at the film-substrate interface and the absorption of light due to multiple reflections within the substrate.

In both cases, it can be seen that the reflectivities are lower for our sample than for theoretical TiN and the trend of decreasing reflectivity with increasing film thickness is evident. The highest reflectance corresponds to sample B-Ti 03, deposited at 1.0 Pa with a N_2/Ar ratio in the middle of our studied interval. This high reflectance is likely due to its thickness rather than being directly related to the deposition pressure, as no deviation from this trend is expected. Most likely, if the sample had a greater thickness it would possess a comparable reflectance to the other samples. However, the lowest reflectance is observed for the second thickest sample B-Ti 09. Here, the B-Ti 14 film, with the highest N_2 content, stands out of this trend by showing a higher average reflectivity. This implies that above a certain threshold, the films recover some of their reflectivity, which can be attributed to the improved stoichiometry of the film.

Therefore, maintaining a lower nitrogen flow rate during deposition is desirable. This is also supported by the highest overall reflectance observed from the bottom side. Here, differences between spectra are less pronounced compared to the top side, and for some samples the dependence on thickness is diminished. However, it is important to note that reflectance can be influenced by impurities and dirt. Since the bottom side is always in contact with the sample holder, there is a possibility of some residual particles located on the substrate, which further complicates the interpretation.

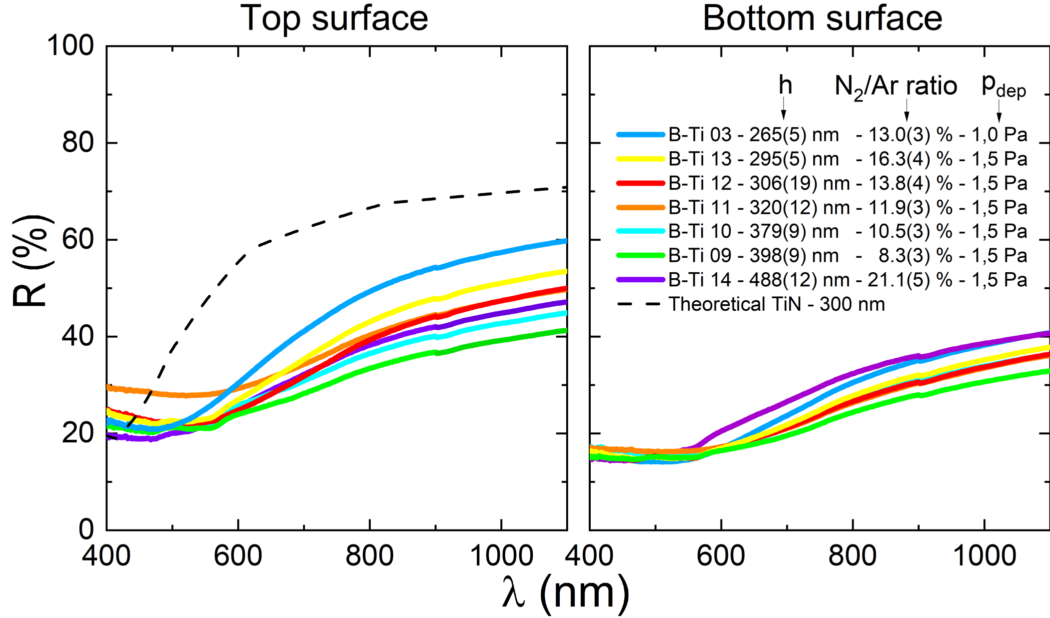

Figure 4.28: Spectrophotometric diffuse reflectance of B-Ti films. The dashed line represents theoretically calculated reflectance from literature optical constants of TiN.

4.8 Morphology of WO_3 and WO_3:P films

The surface morphology of WO_3 and WO_3:P deposited at pressures range 7.5 - 15.0 Pa were investigated. However, as these samples became highly dielectric with increasing oxygen content, they could not be investigated by SEM. This was due to a significant charge accumulation by the electron beam on their surface, which distorted the final image. Several attempts to eliminate the charging, including the use of a conductive tape, a lower acceleration voltage, and a reduced probe current, were unsuccessful. Consequently, only AFM measurements were employed for these samples because AFM is capable of analyzing dielectric films on dielectric substrates effectively.

The AFM images are shown in Fig. 4.30, 4.31, 4.32 and 4.33 with two different dimensions. The smaller images, of size 1×1 μm^2, provide more detailed insight into the fine structure of individual grains and texture, while the larger image areas of 5×5 μm^2 offer a broader overview of the sample surface. By looking at the RT-WO_3 samples deposited at lower pressures (7.5 and 10.0 Pa), their surface morphology exhibits very similar smooth features with some small particles on top. At 12.5 Pa we can already see the emergence of granular structures and a slight increase in overall roughness. However, at the highest pressure of 15.0 Pa, mostly spherical particles tend to create bigger aggregates, suddenly increasing the roughness value to 6.5 nm. At the elevated temperature of 500°C for HT-WO_3 series, a similar behaviour is observed for lower pressure. However, crystallization into rather elongated nanocrystallites with higher density is visible, accompanied by only a minor increase in roughness from $S_q = 1.2-1.3$ nm to $S_q = 1.7-1.8$ nm.

For P-doped films, the development of aggregates already starts with lower pressures of 7.5 Pa for RT-WO_3:P series and 10.0 Pa for HT-WO_3 series. At RT, the grain size as well as roughness develop significantly with oxygen pressure.

On the other hand, the surface of high-temperature films shows different surface morphologies, as they appear to be more homogeneous with less pronounced granularity and the roughness remains comparable, independent of oxygen pressure.

The evolution of roughness as a function of deposition pressure is depicted in Fig. 4.29. For the sake of clarity, only the larger scans were taken into account because these provide sufficient area to compensate for local extremes and sudden changes in surface height. It is important to perform the same image processing procedures for each of the measurements and in the same order. Otherwise, the estimated roughness value could lead to inaccurate results. It is evident that the roughness value depends on the specific position on the sample and the size of the scanned area. Although taking multiple measurements at various locations would be ideal, it is very time-consuming. Nonetheless, we can reasonably expect the exact value to be within a 10-15 % margin of error[142]. Overall, high-temperature deposition results in smoother, more uniform films for both undoped and P-doped tungsten oxide, while room-temperature deposition, leads to significantly rougher surfaces. A further densification of grains for WO_3 films prepared by various PVD methods, especially MS, was reported at even higher temperatures[158] and also for P-doped WO_3 by PLD[48],

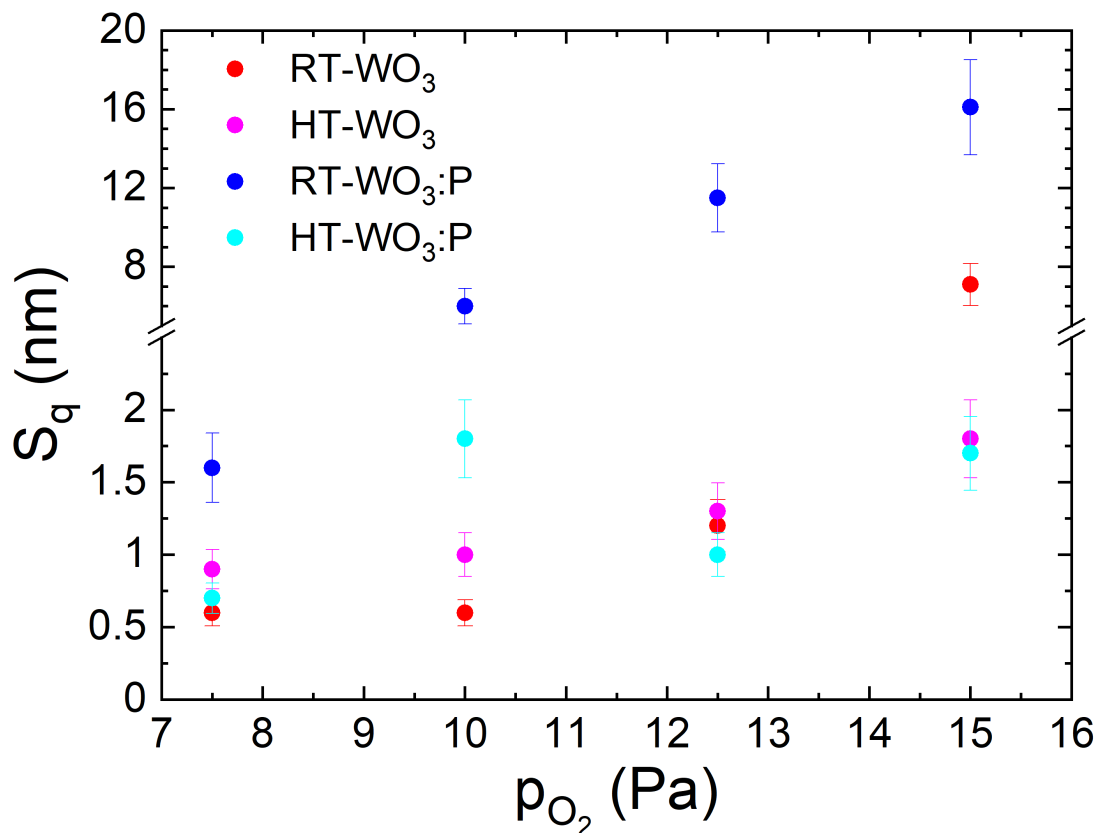

Figure 4.29: Root-mean-square roughness obtained from AFM as a function of oxygen deposition pressure for WO_3 films.

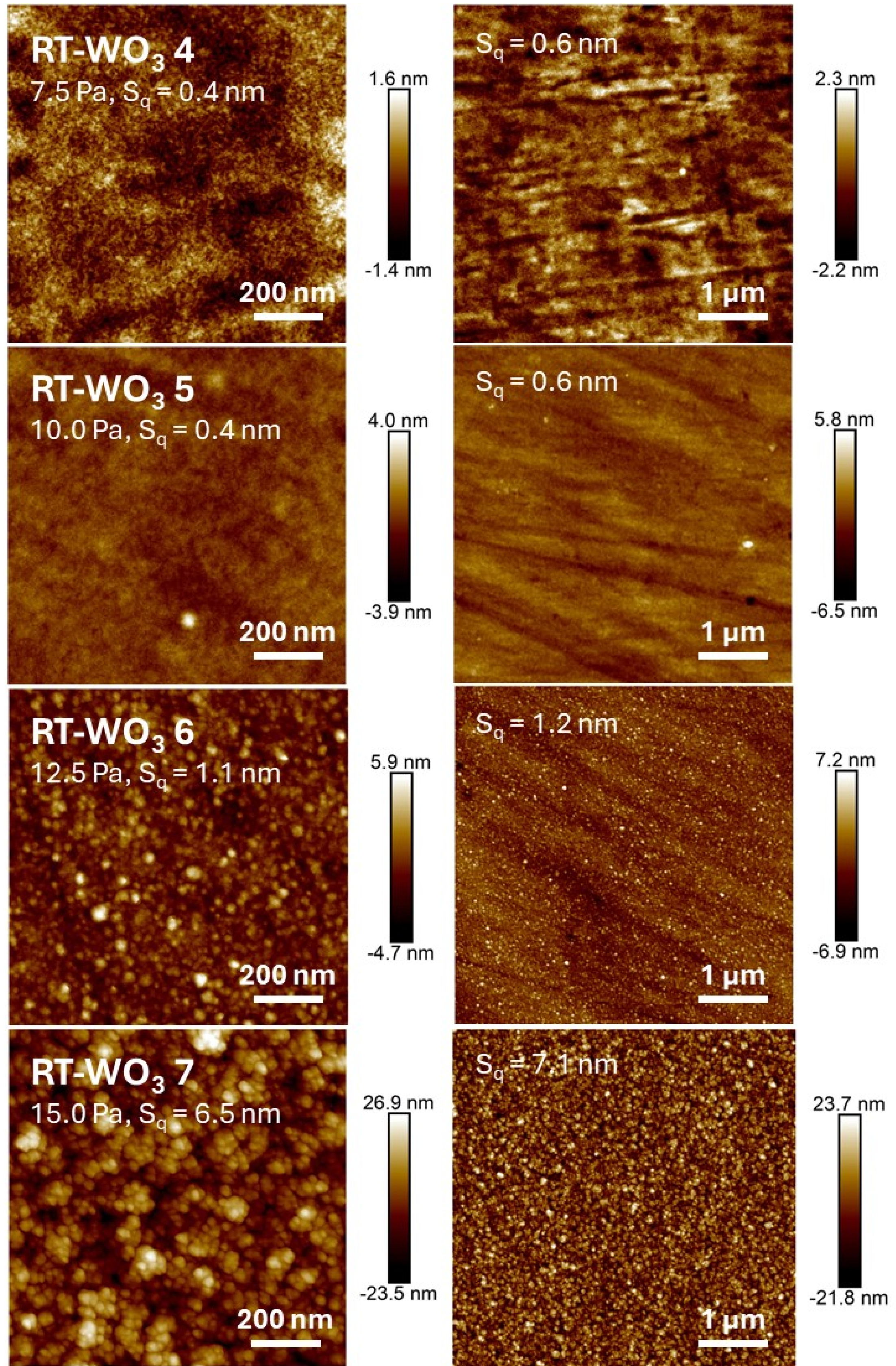

Figure 4.30: AFM images of RT-WO_3 series. The left pictures have dimensions of 1×1 μm^2. The inset in the upper-left corner contains information about the sample name, deposition pressure, and root-mean-square roughness. The right pictures have dimensions of 5×5 μm^2 and the root-mean-square roughness value is again provided.

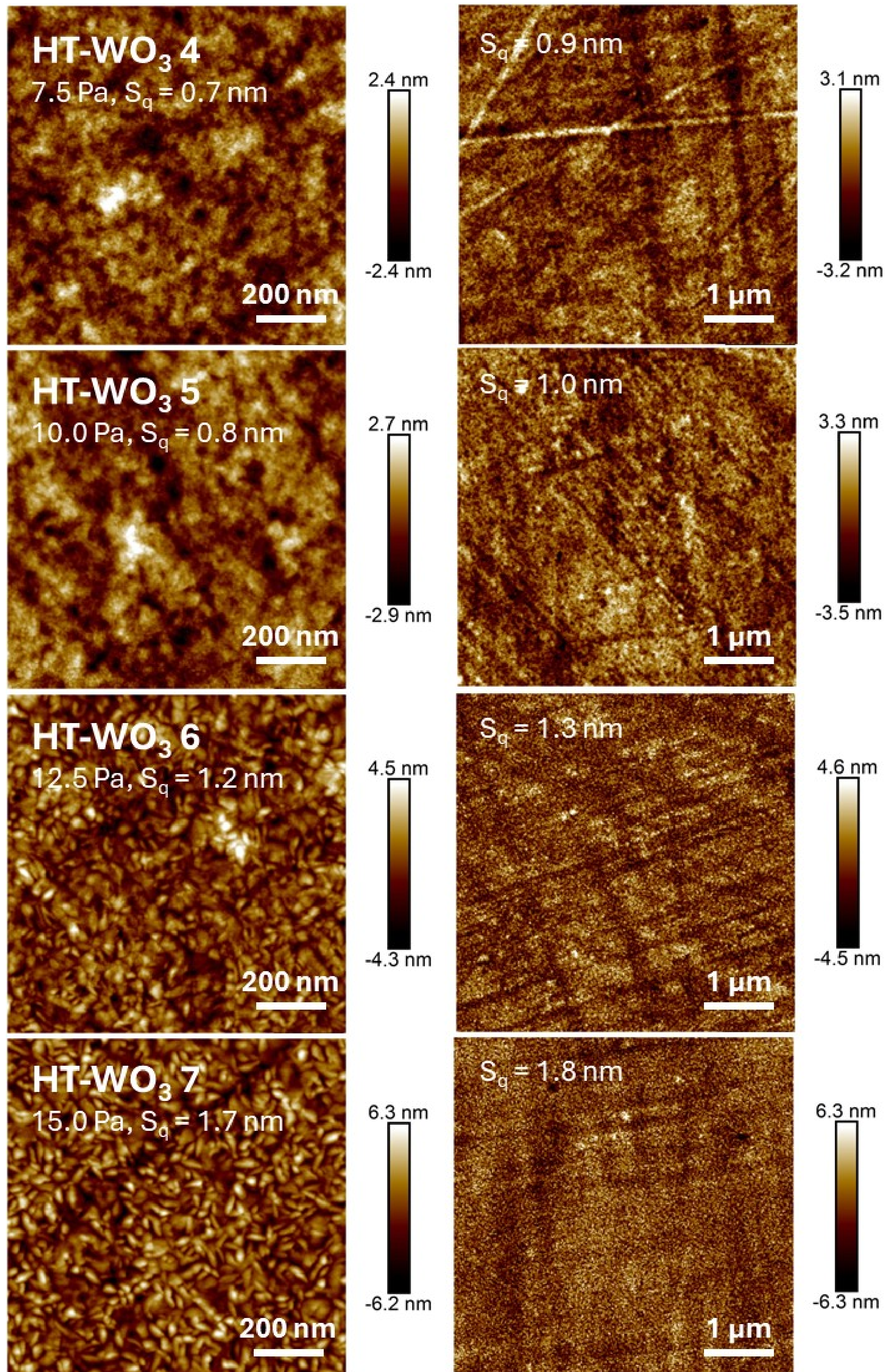

Figure 4.31: AFM images of HT-WO_3 series. The left pictures have dimensions of 1×1 μm^2. The inset in the upper-left corner contains information about the sample name, deposition pressure, and root-mean-square roughness. The right pictures have dimensions of 5×5 μm^2 and the root-mean-square roughness value is again provided.

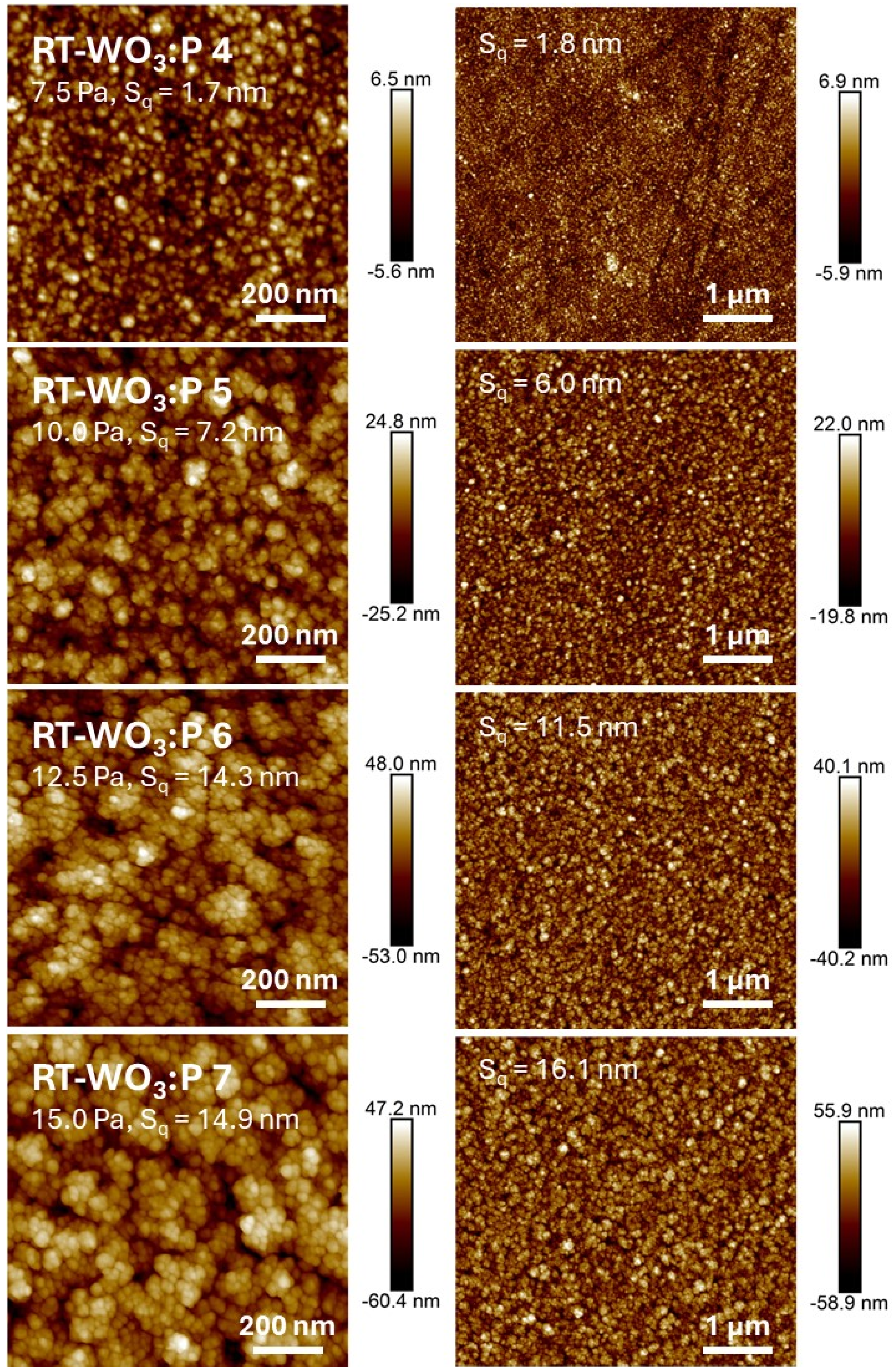

Figure 4.32: AFM images of RT-WO_3:P series. The left pictures have dimensions of 1×1 μm^2. The inset in the upper-left corner contains information about the sample name, deposition pressure, and root-mean-square roughness. The right pictures have dimensions of 5×5 μm^2 and the root-mean-square roughness value is again provided.

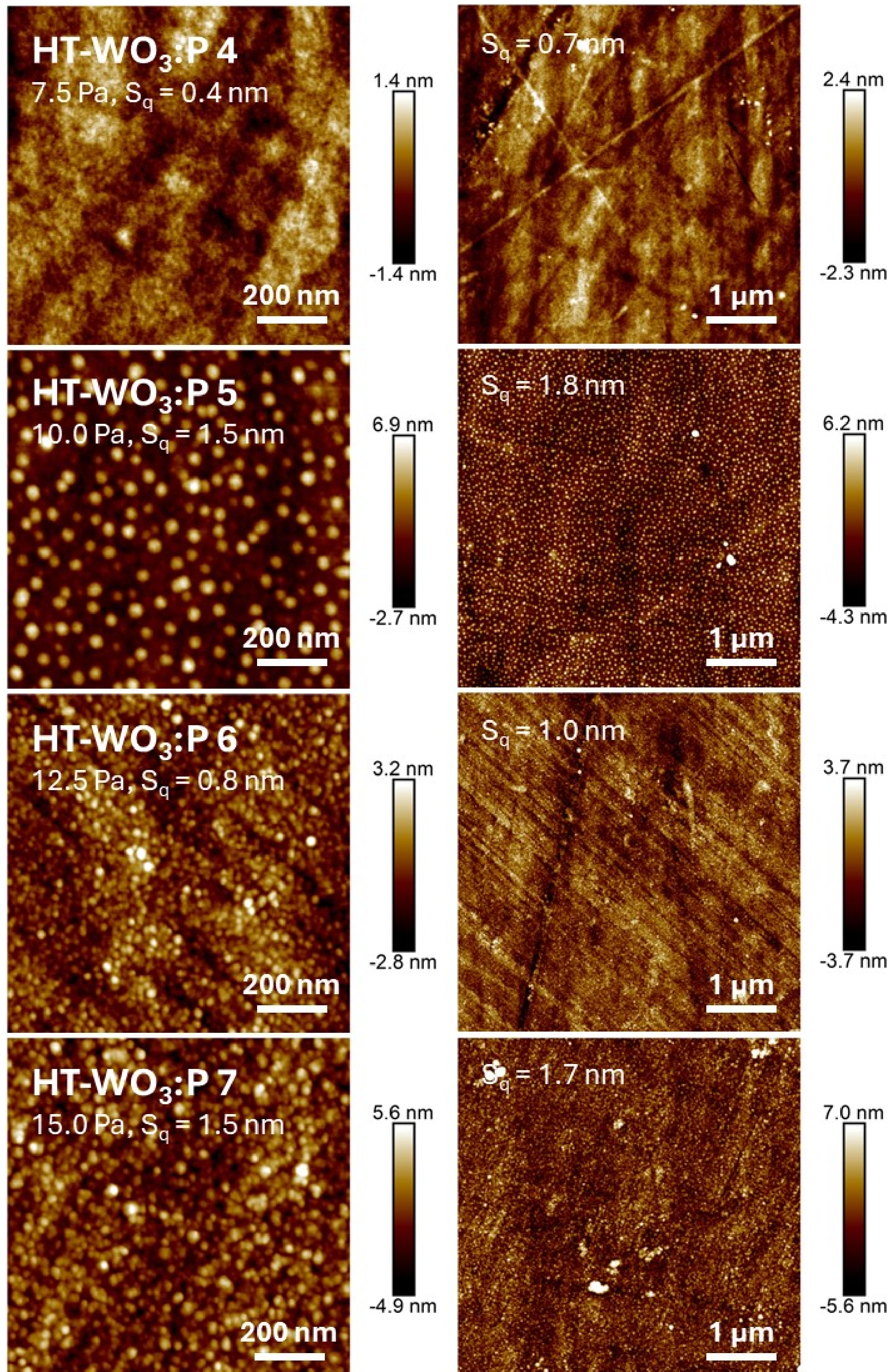

Figure 4.33: AFM images of HT-WO_3:P series. The left pictures have dimensions of 1×1 μm^2. The inset in the upper-left corner contains information about the sample name, deposition pressure, and root-mean-square roughness. The right pictures have dimensions of 5×5 μm^2 and the root-mean-square roughness value is again provided.

4.9 XRD results of WO_3 and WO_3:P films

The structure of WO_3 is rather complex as it exists in several allotropic modifications. The most prevalent form is monoclinic with the space group *P2₁/n*, where each W^{6+} atom, located at octahedral sites, is bonded to six O^{2-} atoms (see Fig. 4.34). This phase exhibits thermochromic properties[68] and it is stable from 17°C to 330°C. The monoclinic phase is also formed for low temperatures from -140° C to -50°C and other crystal structures include triclinic (from -50°C to 17°C), orthorombic (330 - 740°C) and tetragonal (above 740°C)[159] (see Fig. 4.35). Even though the last mentioned should not be stable at RT, it was many times reported to be prepared by MS or PLD techniques[42][158][159]. Considering also the oxygen-deficient states $WO_{3\text{-x}}$ with $x \in (0, 1)$ the number of possible structure modifications in the W-O phase diagram[160] rises significantly.

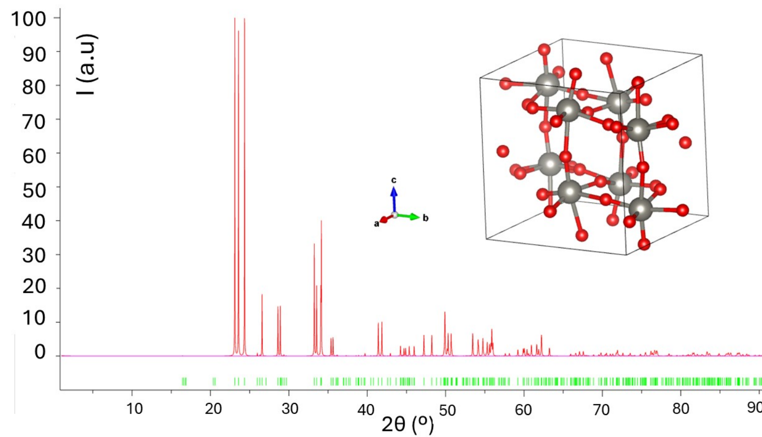

Figure 4.34: Theoretical diffraction pattern and unit cell of WO_3 with monoclinic crystal lattice and space group $P2_1/n$ (14).

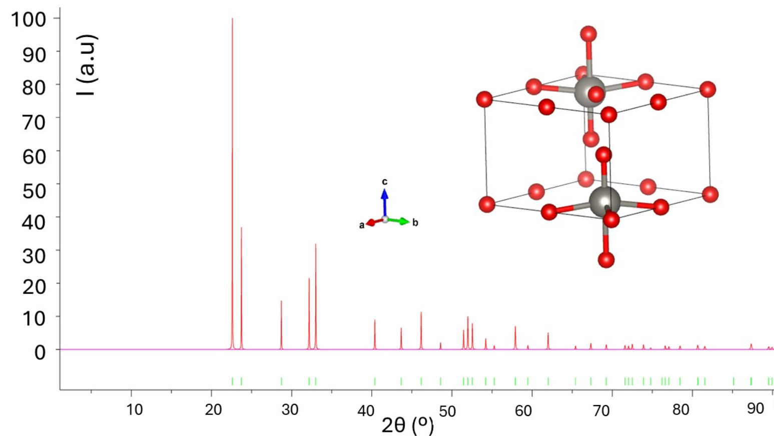

Figure 4.35: Theoretical diffraction pattern and unit cell of WO_3 with tetragonal crystal lattice and space group $P4/nmm$ (129:2).

The XRD measurements of the WO_3 and WO_3 films were carried out in GI geometry for 2θ from 10° to 90°. For three of the four series, namely RT-WO_3, RT-WO_3:P and HT-WO_3:P, a set of broad peaks were observed (shown in Fig. 4.36). These peaks were located between 18° - 30°, which is our well-known peak from

the diffuse scattering of the FS substrate, and between 30° - 40°, 45° - 60°, 75° - 85° that correspond to the diffraction of the nano-polycrystalline film in an amorphous matrix. The presence of latter peaks was confirmed by measurements of the FS substrate by flipping the sample upside-down and the XRD pattern from the substrate was substracted from film patterns. Despite their different appearance, there is no effect of the deposition pressure noted in XRD patterns, which is consistent with previously reported results for P-doped WO_3 films prepared at elevated temperatures, where these films become crystalline at 900°C[48]. It seems likely that the presence of phosphate during the deposition inhibits the grain growth, leading to nano-crystalline layers.

For the HT-WO_3 series samples, different behaviours depending on the deposition pressure were recorded, and the XRD patterns can be found in Fig. 4.37. For the highest pressure of 15 Pa (HT-WO_3 7), a crystalline phase with sharp peaks is recognized. However, the pattern symmetry definitely indicates a higher symmetry than that of the monoclinic lattice (compare with Fig. 4.34). The exact phase was not identified completely using the PDF5+ database, likely due to non-stoichiometry of the film. Therefore, the lattice parameters could not be determined with the desired accuracy. However, it shows a strong similarity to the tetragonal symmetry phase from Fig. 4.35, although the positions of all peaks do not match (see Table 4.11). Our pattern has a small peak at 35.2°, which cannot be attributed to any reflection (hkl) from the database. On the other hand, there should be more peaks that are present in the database structure. Among these, relatively strong reflections at 23.7° and 32.2° are not found in our XRD pattern. This could indicate that our sample is a weakly-textured polycrystalline film, as suggested by the intensity ratio of the other peaks. It is likely a special case of a tetragonal phase, where the position of W atoms is slightly shifted from its original position, as a result of relaxation caused by sub-stoichiometry and a phase with higher symmetry than monoclinic arises. Possibly, even cubic with ordered defects cannot be excluded as well. To determine the exact structure more accurately would require a more time-demanding and systematic approach, which was not the main focus of our work, and hence it is beyond the scope of this thesis.

With increasing deposition pressure, the samples become gradually more amorphous, as evidenced by the decreasing intensity of the reflections. Additionally, an apparent broadening of peaks reveals the increasing crystallite size. The HT-WO_3 6 film still exhibits the same crystal structure as the HT-WO_3 7 sample, where smaller peaks are lost in the background. The mean grain size can be roughly estimated by W-H plot for these two samples, shown in Fig. 4.38. For higher diffraction angles, the FWHM value of the peaks is systematically above the linear fit, which could be the consequence of the broadening by the secondary peak from the Cu K_β line, which is insufficiently filtered. Overall, the mean grain size and microstrain value for HT-WO_3 7 were estimated to be $D = 32(3)$ nm and 0.11%, respectively. As can be seen from the slope of linear fit for HT-WO_3 6 film, the value of microstrain is negligible, and therefore the mean grain size could be calculated by Equation (3.22), corresponding to 18(4) nm.

The two most intensive peaks completely disappear for the HT-WO_3 5 sample as it eventually transforms into a nano-crystalline film with wide peaks. The rest of the more metallic samples resemble the amorphous phases in Fig. 4.36.

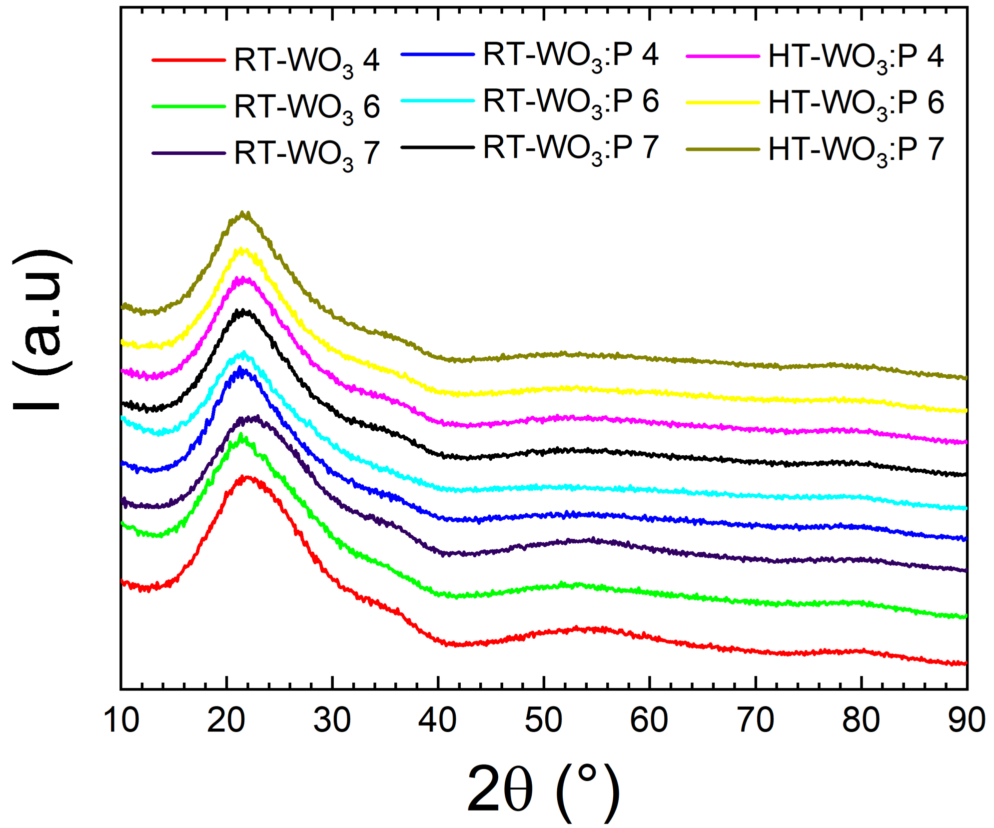

Figure 4.36: XRD patterns of RT-WO_3 and WO_3:P films.

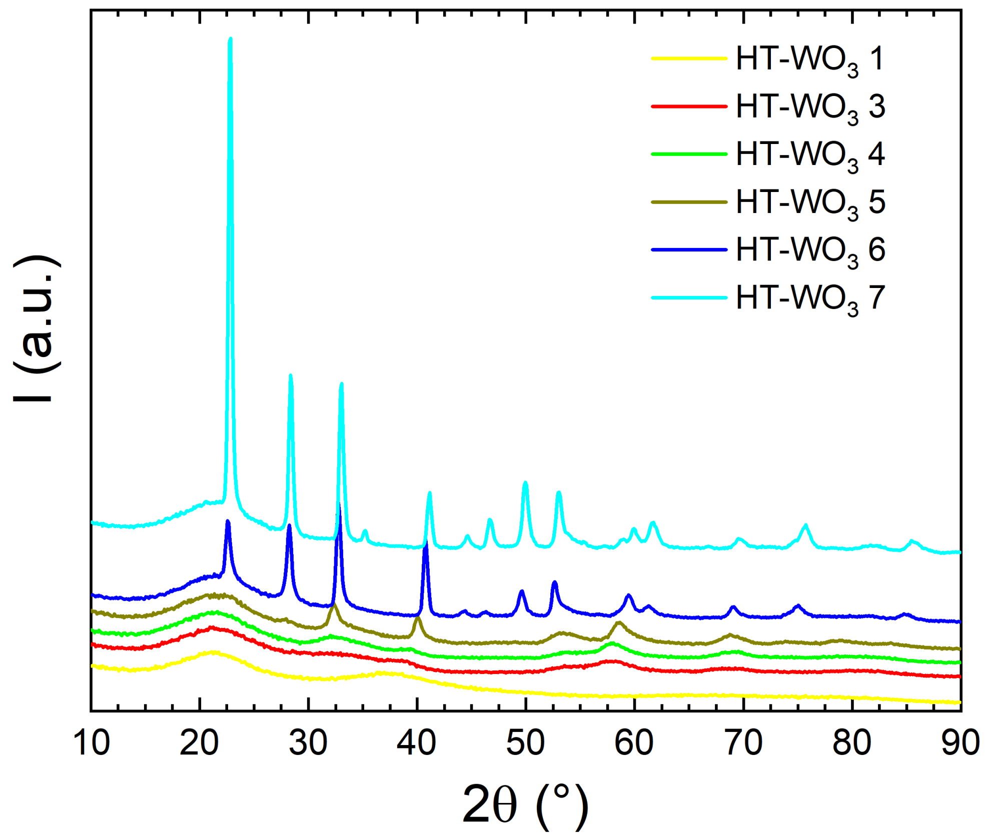

Figure 4.37: XRD patterns of HT-WO_3 films.

Measured				From database					
2θ (°)	I (%)	2θ (°)	I (%)	2θ (°)	I (%)	2θ (°)	I (%)	2θ (°)	I (%)
22.79	100	49.92	13	22.60	100	46.16	3	67.33	4
28.36	33	52.97	11	**23.74**	36	51.46	10	**69.25**	3
33.01	32	61.67	5	28.72	16	51.99	17	**71.59**	3
35.18	2	69.62	2	**32.18**	26	**52.55**	13	72.49	4
41.10	11	75.62	4	33.01	37	**54.21**	6	**76.60**	3
44.60	2	85.55	2	40.38	13	**57.91**	13	**80.67**	4
46.68	6			43.67	10	62.00	10	87.34	4

Table 4.11: Comparison between measured position 2θ and relative intensity I of diffraction peaks with the database tetragonal structure of WO_3 from CIF-file[161]. For database data, only peaks with $I > 3\%$ are listed. The peaks that do not match, because they are either missing in our data or in the database structure, are highlighted in bold.

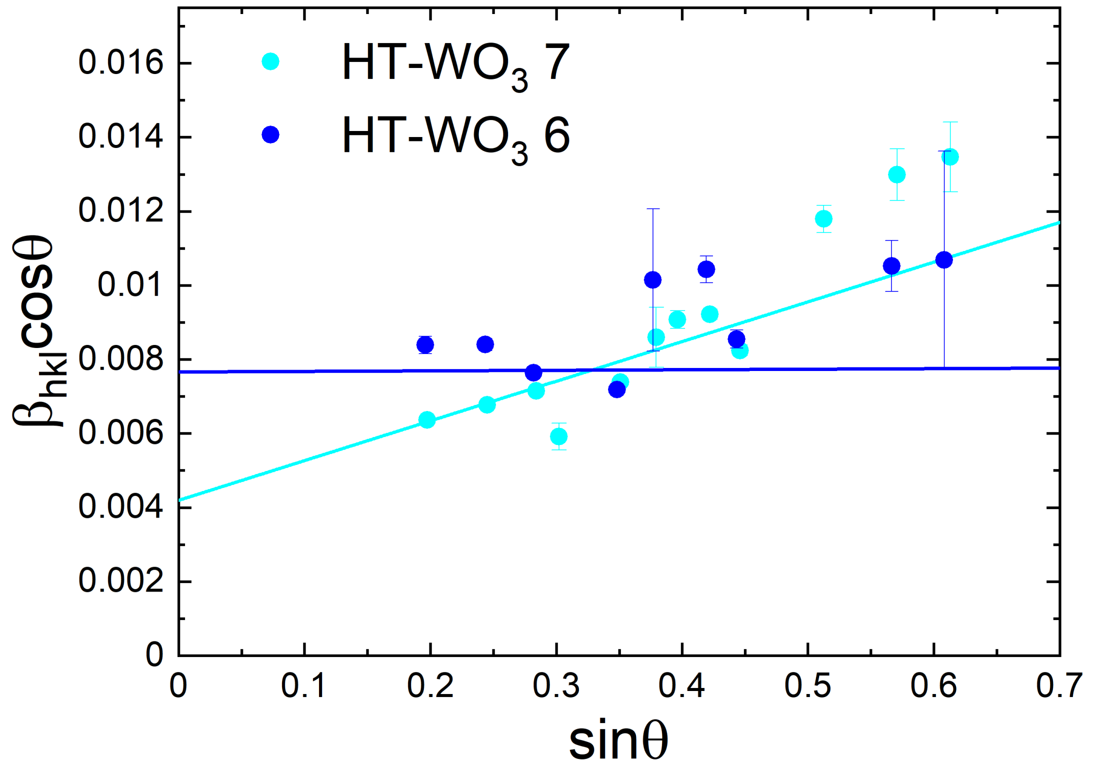

Figure 4.38: W-H plot for HT-WO_3 7 and HT-WO_3 6 samples from the XRD patterns in Fig. 4.37.

4.10 Transmittance of WO_3 and WO_3:P films

The optical properties of metallic films differ from those of oxide films, due to their different electronic structure. When light interacts with a metallic surface, possessing high electrical conductivity and no band gap, the free electrons interact with the oscillating electric field of the light waves. At certain frequencies, these electrons can respond quickly enough to the local changes in the electric field, leading to absorption and re-emission of the light, causing their characteristic shiny appearance. However, a dielectric oxide film with a significant band gap allows light to pass through without being absorbed, because the energy of visible light photons cannot excite electrons from a valence band to the conduction band. For this reason and because of the simpler experimental setup, it is beneficial to study the optical transmittance of oxide films rather than their reflectance.

The acquired optical transmittance spectra were measured under ambient conditions right after deposition using the instrumentation from Fig. 3.13i in the wavelength range of 250 - 800 nm. These spectra provided an initial (further referred to as pristine) state of our samples to compare the transmittance with the following temperature-dependent measurements. Also, they served to determine whether the varied temperature leads to reversible or irreversible changes in transmittance. The results are shown in Fig. 4.39. It is clear that optical transmittance tends to increase with increasing oxygen content. The transmittance drops to < 20 % for deposition pressures lower than 7.5 Pa for WO_3 samples, although for WO_3:P samples remains considerably higher.

The region of shorter wavelengths also indicates a change in the band gap value. Additionally, oscillations in transmittance are observed as a consequence of interference corresponding to Equation (1.12) for longer wavelengths, and the period of these oscillations could be used to estimate the optical thickness of our films. Because the spot size of the light is on the order of millimeters, the thickness may vary slightly from place to place due to the thickness inhomogeneity of films produced by PLD. The determined thickness mostly agrees with our profilometric measurements within the margin of error.

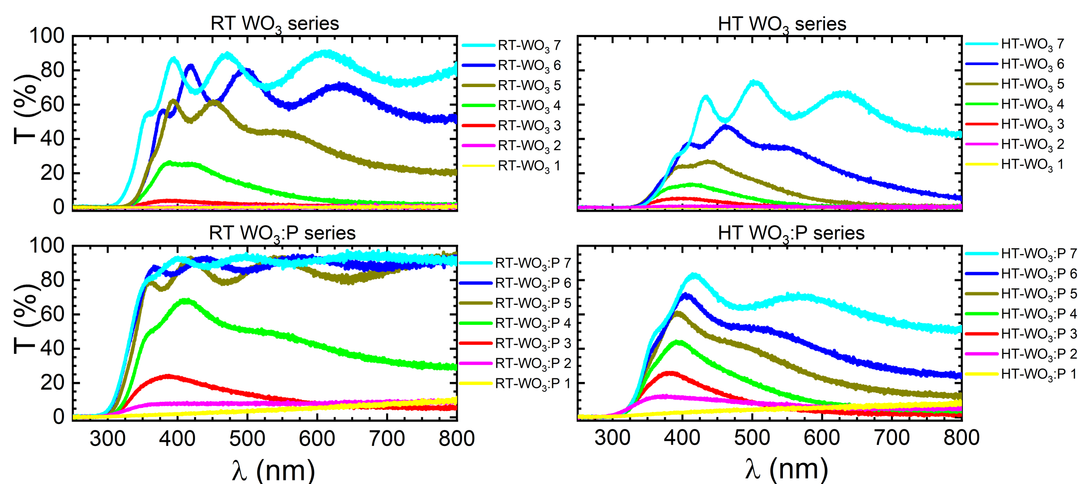

Figure 4.39: Optical transmittance spectra of pristine WO_3 thin films at ambient conditions acquired immediately after deposition.

From these spectra we constructed Tauc plots (shown in Fig. 4.40) from Equations (1.18) and (1.19) by plotting $(\alpha \cdot h\nu)^{\frac{1}{2}}$ as a function of photon energy $h\nu$, since WO_3 is an indirect band gap semiconductor ($\gamma = 2$). The photon energy was calculated from nm to eV by a conversion:

$$h\nu \text{ (eV)} = \frac{1239.8}{\lambda \text{ (nm)}} \tag{4.6}$$

For $E < 3$ eV, the plot remains almost constant with some interference oscillations, since they were also present in transmittance data. A similar plateau appears for $E > 4$ eV, although occasionally we can see a small decrease at the highest energies. This is the effect of the so-called Urbach tail, where the material absorbs light at energies below E_g near the optical absorption edge with an exponentially decaying absorption coefficient as a function of energy[162]. In the 3 - 4 eV range, a linear behaviour is observed, which is used to estimate the band gap E_g. With decreasing deposition pressure for each series, the linear part gets shorter, until it completely disappears for samples deposited at 2.5 Pa and 0 Pa. Therefore, these samples are not included, as the reduced number of data points increases the error in E_g, making it difficult to evaluate accurately.

Table 4.12 presents the extracted optical band gap values E_g, which are affected by two factors that need to be considered when evaluating the error of E_g:

1. Statistical error, which arises from the subjective choice of the fitting boundaries. By choosing different data points that are used for the fitting, the slope and intercept can vary, which brings some statistical inaccuracy. This inaccuracy was estimated for each case by performing fit several times with changed boundaries and subsequently evaluating the standard deviation for each measurement.
2. Error of absorption coefficients due to uncertainty in film thickness, as the absorption coefficient depends on the thickness through Equation (1.18, although this factor is less pronounced than the previous one.

These results show a decreasing E_g for smaller deposition pressures, due to worse stoichiometry with more oxygen vacancies, evidenced by the changing colour of the films as they turn more metallic and conductive. The E_g is systematically smaller for samples prepared at 500°C, which can be associated with improved crystallization of the film.

For undoped WO_3, the E_g from 3.3 eV to 2.6 eV are in good agreement with the previously reported values for WO_3 films prepared by PVD methods[42][159]. The phosphorus doping leads to the replacement of O^{2-} vacancies with P^{3-} ions, creating bonds with W^{6+} ions, modifying the apparent band gap by the Burstein-Moss shift. However, our E_g values are slightly lower than previously reported for similar films[48]. To evaluate E_g more rigorously, it would be beneficial to use other optical methods such as reflectance measurements combined with spectroscopic ellipsometry to consider the contribution from reflection and scattering.

Sample	E_g (eV)	Sample	E_g (eV)	Sample	E_g (eV)	Sample	E_g (eV)
RT-WO_3 7	3.26(6)	HT-WO_3 7	2.83(6)	RT-WO_3:P 7	3.40(5)	HT-WO_3:P 7	3.16(6)
RT-WO_3 6	3.09(10)	HT-WO_3 6	2.86(8)	RT-WO_3:P 6	3.38(6)	HT-WO_3:P 6	3.10(7)
RT-WO_3 5	3.02(7)	HT-WO_3 5	2.85(8)	RT-WO_3:P 5	3.35(6)	HT-WO_3:P 5	3.08(7)
RT-WO_3 4	2.93(8)	HT-WO_3 4	2.80(5)	RT-WO_3:P 4	3.20(7)	HT-WO_3:P 4	3.05(9)
RT-WO_3 3	2.59(9)	HT-WO_3 3	2.68(8)	RT-WO_3:P 3	3.00(9)	HT-WO_3:P 3	2.97(7)

Table 4.12: Band gap from Tauc plots in Fig. 4.40 for WO_3 and WO_3:P films.

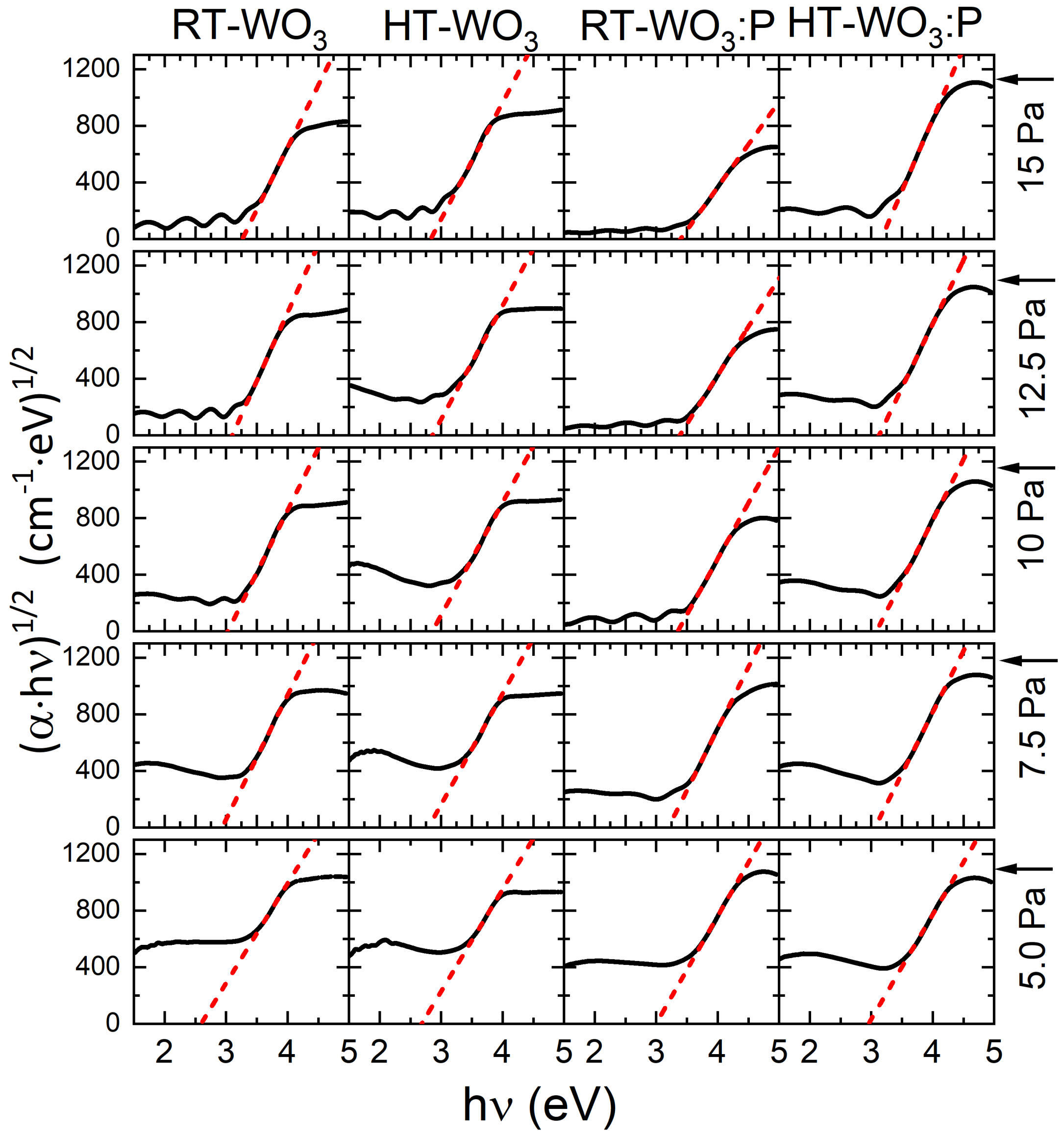

Figure 4.40: Tauc plots for WO_3 and WO_3:P samples. Each column represents a series of films, while each row corresponds to a specific deposition pressure. The red dashed line represents the linear fit used to determine the optical band gap by extrapolating it to the abscissa. Both the horizontal axis and vertical axis are scaled equally to visualize the band gap shift with increasing deposition pressure.

4.10.1 Transmittance calibration measurements

It was necessary to perform a set of calibration measurements to ensure that our transmittance system (Fig. 3.14, 3.15 and 3.16) provided valid results. Firstly, the wavelength calibration was done using an Ar/Hg calibration source with corresponding emission peaks at well-defined wavelengths provided by the source manufacturer[84][163]. For this purpose, we connected the source directly to the spectrometer using the primary optical cable and measured the spectrum. Since the source was intensive enough, the exposure time of 0.1 ms was sufficient with 10 averages per scan. The obtained spectrum of the lamp is presented in Fig. 4.41a. The position and intensity of lines correspond to the predicted values with just a small constant shift of 2.3 nm for each line, so we created a calibration file that was loaded at the start of each measurement. Taking this shift into account, we can consider the peak position to be well calibrated.

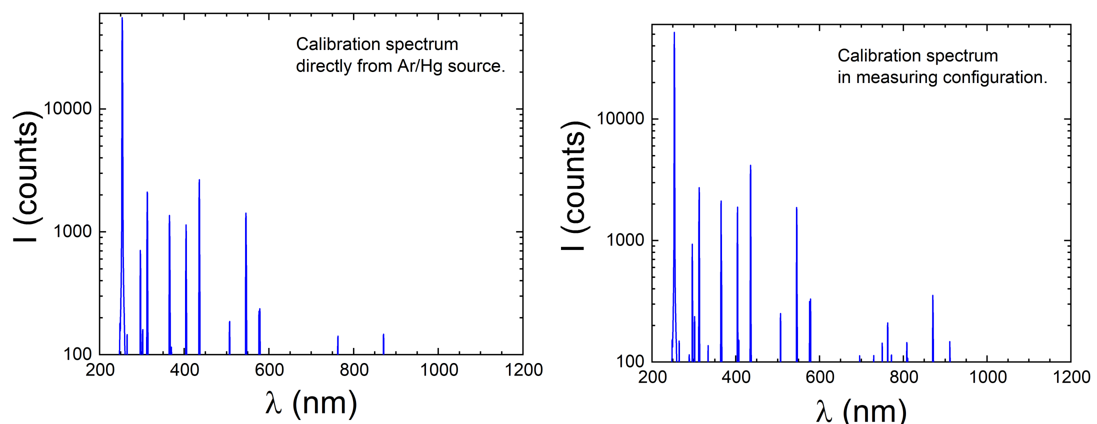

(a) Spectrum of the source connected via a single optical cable.

(b) Spectrum of the source connected in measuring configuration.

Figure 4.41: Optical spectra of Ar/Hg source for wavelength calibration. The vertical axis is in logarithmic scale to enhance low-intensity peaks.

Next, we wanted to evaluate the magnitude of intensity loss due to light passage through the system's optical path, so we repeated the measurement with the light source connected to the optical system consisting of optical cables and collimators. This loss was already notably significant, approximately by a factor of 300 for the most intensive line. Consequently, to achieve a similar intensity for the lines, we adjusted the exposure time to 30 ms, maintaining 10 averages per scan. The obtained spectrum is depicted in Fig. 4.41b. Comparing this spectrum to the previous one, we observe that the intensity of lines corresponding to longer wavelengths (Ar lines) shows different attenuation compared to the lines for shorter wavelengths (Hg lines), which remain similarly intense. Therefore, additional intensity calibration was necessary to compensate for the spectral attenuation of our optical system. Then we compared the measured spectra from this system with those obtained by the transmittance system under ambient conditions (Fig. 3.13i) for a selected film to verify the precision of our calibration. As will be shown in the results, the spectra matched within the margin of error.

Due to the specific design of our system, it is not possible to measure the reference spectrum at every temperature step because it would require removing

the sample from the sample holder, thereby breaking the vacuum. As a result, the reference spectrum needs to be measured beforehand and after each measurement. During that time, the lamp intensity must remain constant. Otherwise, it would be difficult to distinguish, whether the spectra changed due to real intrinsic properties of the studied sample or due to fluctuations in source luminosity. Additionally, there is a concern about the detector itself. A potential drift in background intensity, caused by factors such as thermal noise from internal heating, could also affect the spectra.

To clarify these questions, we conducted a series of reference and background spectra measurements at various times after the lamp was turned on to see if there were any changes (see Fig. 4.42) with the exposure time of 1000 ms, 10 averages per scan. Figure 4.42a shows that the lamp slowly heats up during the first few minutes, resulting in a slight increase in intensity. However, after approximately 20 minutes, the spectra stabilize and no longer change significantly over time. This indicates that a minimum waiting time of 20 minutes is required before starting the measurements. On the other hand, we did not observe any significant drift in the background (see Fig. 4.42b), meaning the detector is ready to use almost immediately.

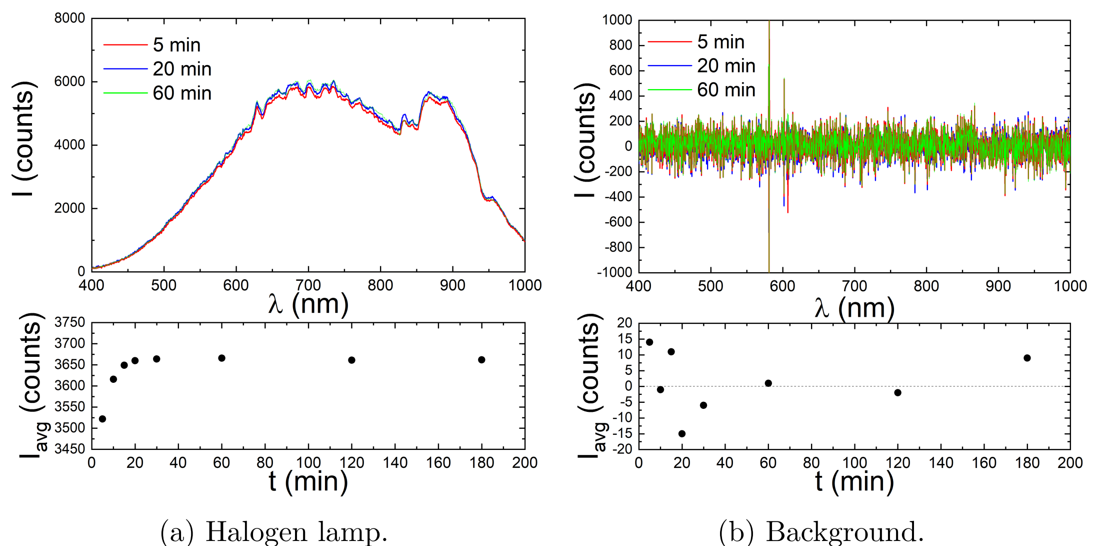

(a) Halogen lamp.

(b) Background.

Figure 4.42: Time-stability optical transmittance measurements. The top two graphs show the measured spectra for three chosen times after the lamp was turned on, while the bottom two graphs represent the average intensity over that wavelength range for times of 5, 10, 15, 20, 30, 60, 120, and 180 minutes.

Next, we needed to verify the linear response of the detector to the incident signal by measuring the reference spectrum as a function of the exposure time, as can be seen in Fig. 4.43. Otherwise, it would be necessary to correct it through a correlation function. From the measured reference spectra (top graph) for 8 selected times, we can calculate the integral intensity, which is the area under the spectrum, to construct the final calibration curve (bottom graph). We observe that the points lie on a linear plot with a relative uncertainty below 0.1 %. An increase in exposure time by 1 ms leads to an increase in the overall integral intensity by approximately 2275 counts, and doubling the exposure time results

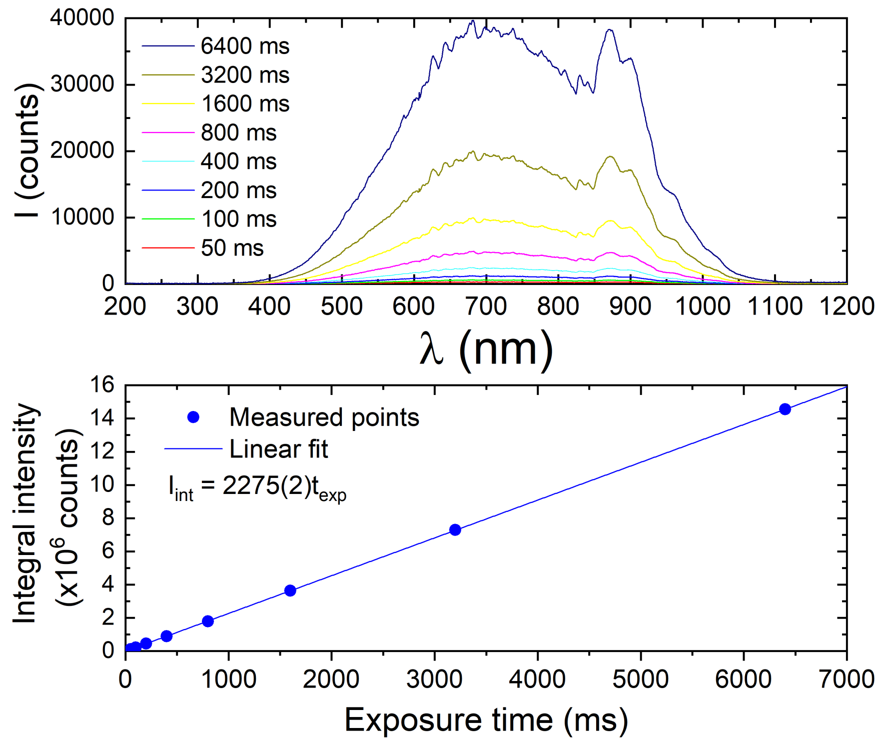

Figure 4.43: Transmittance measurement for verifying the detector signal linearity. The spectra were taken for 8 different times (top graph) to obtain a calibration curve (bottom).

in a doubling of the intensity. The same conclusion holds if we choose to use the single-wavelength maximal intensity instead.

Last but not least, we needed to test whether changes in temperature or pressure alone could affect the transmittance of a fused silica glass. In theory, its optical properties should remain unaffected by the absence of ambient atmosphere and elevated temperatures within the range we used in our experiment. Any alteration in transmittance at temperatures below 0°C could possibly be attributed to water from residual air humidity condensing on the glass surface. However, if we observed changes in spectra at higher temperatures, it could indicate the diffusion of atoms from the sample holder material into the sample.

The measured transmittance of the FS glass is shown in Fig. 4.44. All of the spectra are normalized to the measurement of the same glass at ambient conditions (red line). We can see that most of the data lie within the $\pm$ 2 % range, denoted by the dashed horizontal lines, except for the wavelengths shorter than $\sim$ 500 nm due to the lower intensity of the reference spectrum. This corresponds to the demonstrated relative error from Fig. 3.18 as a result of Equation (1.16). So we can conclude that the changed temperature does not influence the appearance of the substrate and any change in the spectra can be related to the thermochromic properties of thin films.

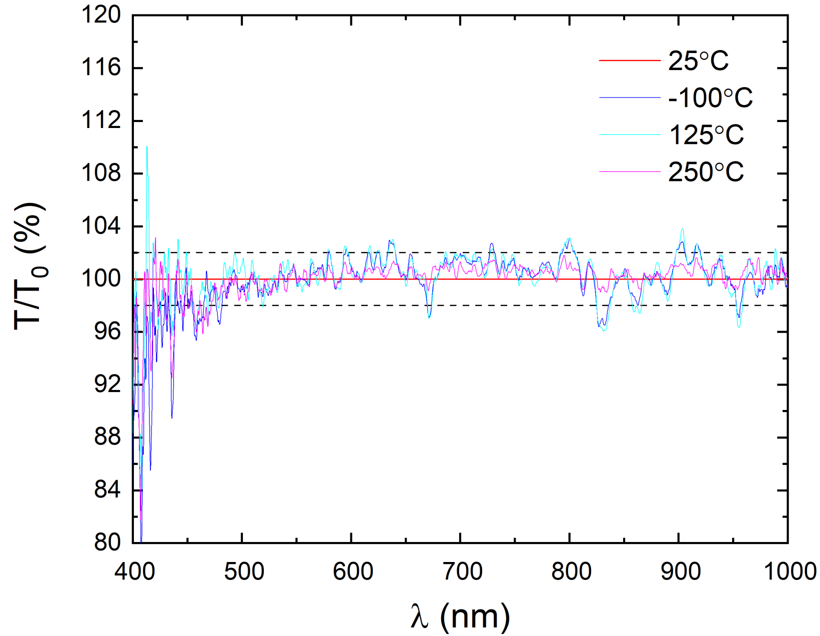

Figure 4.44: Optical transmittance spectra for fused silica glass at different temperatures relati. The reference spectrum was taken at ambient conditions (with temperature $T_0 = 25°C$). No significant change in spectra is apparent, as the data fluctuate within the system's margin of error, except for the short-wavelength region due to the lower intensity of the reference.

4.10.2 Temperature-dependent transmittance

After a successful calibration and testing, we were ready to proceed to the results of our oxide films, presented in Figures 4.45, 4.46, 4.47 and 4.48. As was shown in Fig. 4.39, the transmittance drops rapidly with decreasing oxygen pressure, so measuring those oxygen-depleted samples would result in considerably higher error. Therefore, only the four samples corresponding to the highest deposition oxygen pressure were measured for each series. For each measurement, the samples were first cooled down to -100°C and then heated up to 250°C. After that, the heating was turned off and the sample cooled down freely to room temperature (within approximately 45 min). The final spectra were retaken for comparison.

Firstly, Fig. 4.45 shows a very negligible change for RT-WO_3 4 and RT-WO_3 5 samples in our temperature range and these are not thermochromic. However, already at 12.5 Pa for sample RT-WO_3 6, we can detect minor changes, where its transmittance tends to slightly decrease/increase for higher/lower temperatures. For the sample RT-WO_3 7 deposited at 15.0 Pa, we already observe an apparent shift of interference maxima towards shorter wavelengths with increasing temperature. This could possibly be explained by the thermal expansion of our films. Furthermore, it is evident that heating leads to irreversible changes, as the spectra obtained after the measurement differ from the initial ones, probably due to some internal structural changes in the material. It becomes even more significant for temperatures higher than $\sim$ 175°C. At the highest temperature, we observed a slow change in the spectra, so we decided to keep the sample at the same temperature for 30 additional minutes (30 min dwell time). The final spectrum after the measurement does not show any recovery of the optical ap-

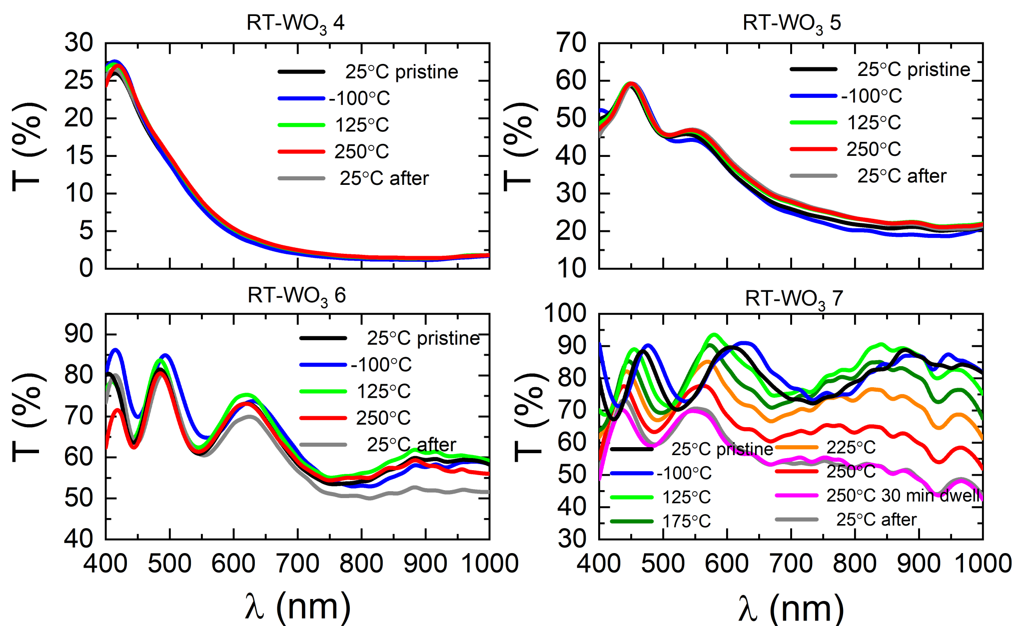

Figure 4.45: Optical transmittance spectra of RT-WO_3 series thin films as a function of temperature.

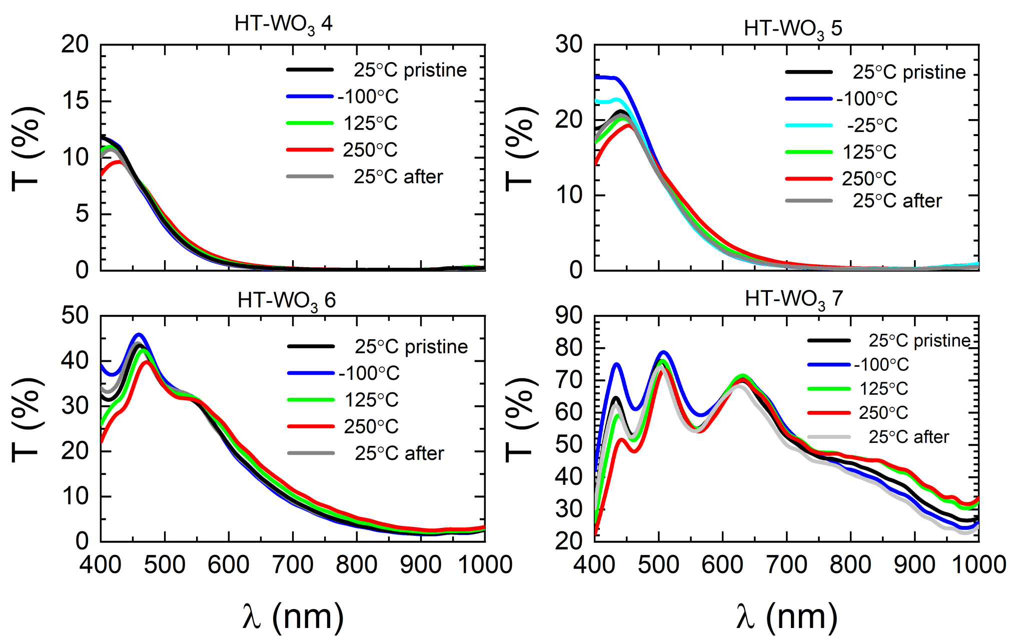

Figure 4.46: Optical transmittance spectra of HT-WO_3 series thin films as a function of temperature.

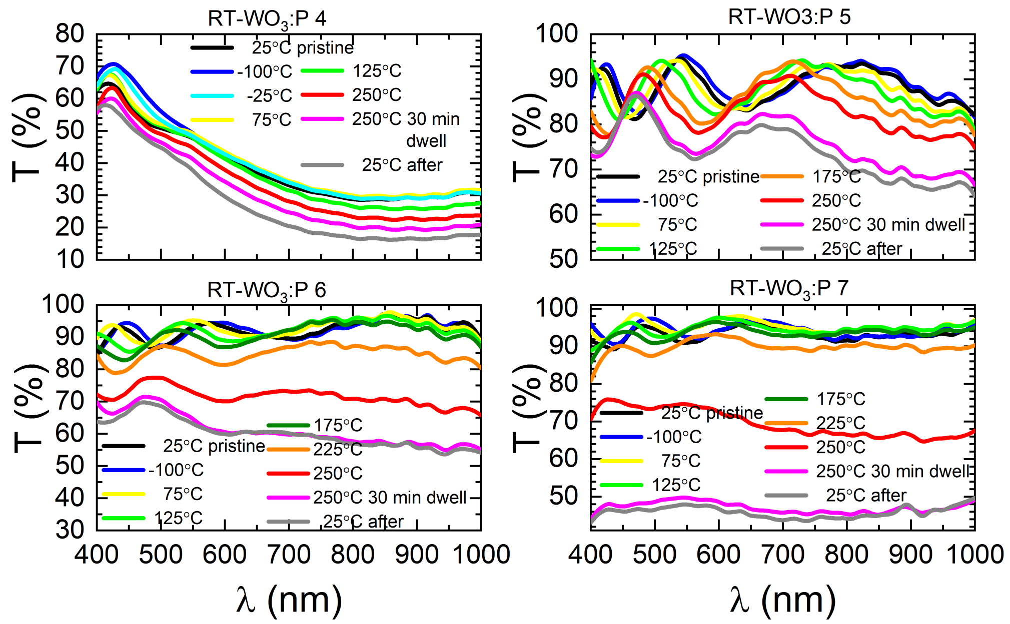

Figure 4.47: Optical transmittance spectra of RT-WO_3:P series thin films as a function of temperature.

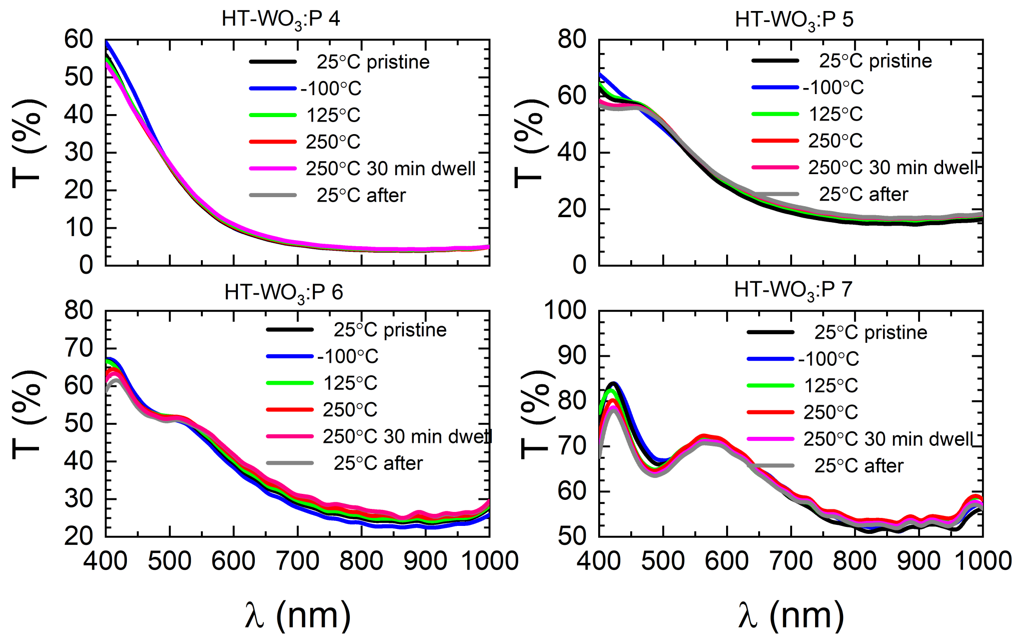

Figure 4.48: Optical transmittance spectra of HT-WO_3:P series thin films as a function of temperature.

pearance, and the sample was seemingly darker with the naked eye. This effect may be caused by recrystallization or oxygen loss in the films. The crystallized WO_3 is more stable in this measurement temperature range. Unfortunately, it limits the repeated utilization of these films for thermochromic applications.

The HT-WO_3 series prepared at elevated temperatures (see Fig. 4.46) reveals a typical thermochromic behavior comparable to the work of Simchi et al.[42], except for the HT-WO_3 4 sample, again showing a minor difference between the spectra. Equivalently to the previous series, transmittance decreases towards the UV part of the spectrum and increases in the NIR region with increasing temperature. This effect is more pronounced in the films that are oxygen-rich. Conversely, this process appears to be at least partially reversible, as evidenced by the similarity between the initial and final spectra, even after a prolonged dwell at maximum temperature. There was no visual variation observed after retrieving the sample. Naturally, they are expected to withstand elevated temperatures up to 250°C, since the films were made at deposition temperature of 500°C. It is possible that the critical temperature, from which the change starts to be irreversible is above our reachable temperature. Depositing the films at heated substrates helps to maintain their optical properties during repetitive exposure to heat. Especially interesting results were obtained for the sample HT-WO_3 7, showing the most significant thermochromic response, despite not possessing a monoclinic crystal structure. To the best of our knowledge, it is for the first time that thermochromic properties are reported for a WO_3 film with a tetragonal phase.

For RT-WO_3:P series (Fig. 4.47) the transmittance does not vary significantly for temperatures between -100°C – 75°C but the colour change accelerates as the temperature exceeds this threshold, where the sample undergoes irreversible change leading to a darkening of the studied sample. This effect is less noticeable for oxygen-depleted sample RT-WO_3:P 4 but becomes more apparent for samples rich in oxygen. For example, samples RT-WO_3 6 and RT-WO_3 7 show a decrease in transmittance by 20 % at 250°C compared to the pristine state. Additionally, keeping the sample at 250°C for 30 min led to a drop of transmittance by half for the sample prepared at the highest deposition pressure. Also, this sample demonstrates a uniform intensity of transmitted light across the UV-VIS-NIR spectrum without any recovery, even after cooling.

Finally, all specimens from the HT-WO_3:P series (Fig. 4.48) do not exhibit any remarkable thermochromism during the experiment, and the transmittance remains almost unchanged, except for a short-wavelength region where the error of data points increases, as explained above (see Fig. 3.18). Similarly to the undoped case, deposition at higher temperatures leads to increased resistance to heat.

4.11 Photoluminescence of ZnO:Eu@B-Al films

This experiment aimed to determine whether the B-Al, acting as a substrate layer, could increase the PL intensity or lead to its quenching due to the interaction of ZnO:Eu films with its porous structure. At first, the photoluminescence spectra were taken using an LED lamp with excitation wavelength of 365 nm and are presented in Fig. 4.49. The features reveal the presence of Eu^{3+} with characteristic emission lines in the red part of VIS spectrum corresponding to transitions $^5D_0 \rightarrow {^7F_J}$ with $J \in \{0, 1, 2, 3, 4\}$, namely at 580 nm ($^5D_0 \rightarrow {^7F_0}$), 593 nm ($^5D_0 \rightarrow {^7F_1}$), 617 nm ($^5D_0 \rightarrow {^7F_2}$), 654 nm ($^5D_0 \rightarrow {^7F_3}$) and 700 nm ($^5D_0 \rightarrow {^7F_4}$)[54]. Yet, not all the lines are easily distinguished from the background signal, especially for multilayers with a thicker B-Al layer. By examining at the most intense $^5D_0 \rightarrow {^7F_2}$ emission line[3] we observe that in all cases the higher intensity is obtained for a thinner film of ZnO:Eu (6000 pulses). This result is counterintuitive, as one would expect that a greater number of Eu-emitting centers would lead to higher intensity. This suggests that the energy transfer is more efficient in thinner ZnO:Eu samples, possibly due to a higher concentration of defects near the surface[164]. The width of this peak is broadened by the splitting of the J = 2 state into three energy (a non-degenerate and two doubly-degenerate) levels that are hard to resolve.

The results also indicate that using a B-Al sublayer of a specific thickness can enhance the PL intensity. This increase was clearly observed in the thinner film, whereas the thicker film resulted in luminescence quenching. However, this measurement is less reliable, because of the larger spot of LED and the inhomogeneity of the films. For that reason, we repeated the measurement using a smaller spot size using a 355 nm excitation laser. Also, the laser possesses a higher intensity, increasing the signal-to-noise ratio that further improve the resolution of our spectra. The obtained PL spectra are depicted in the same manner in Fig. 4.50. Here, the splitting of the most dominant line is visible, and the peak intensity for ZnO:Eu films is comparable. Again the same trend is observed, where a B-Al enhanced the photoluminescence of ZnO:Eu films. The ratio of integrated PL intensities for the most intense emission line at 617 nm is 4.1 for ZnO:Eu@B-Al 1 compared to ZnO:Eu 6000p, and 2.4 for ZnO:Eu@B-Al 2 compared to ZnO 12000p. It is likely that preparing a sample with an even smaller thickness of B-Al could even more improve the PL properties. Using a thinner film would reduce the cost for potential industrial utilization for various photodetectors and sensor applications. Also, we expect the ZnO:Eu layer to penetrate deeply into the porous structure of black metal rather than creating a compact film on its top. However, verifying these claims would require further investigation. In particular, photoluminescence excitation measurements with variable source energy would be of interest combined with a positron annihilation spectroscopy to study the concentration and chemical environment of present defects.

[3]This line corresponds to the forbidden electric-dipole transition that is allowed when Eu^{3+} atoms occupy a site with low symmetry. This suggests that Eu^{3+} atoms probably substitute the Zn site.

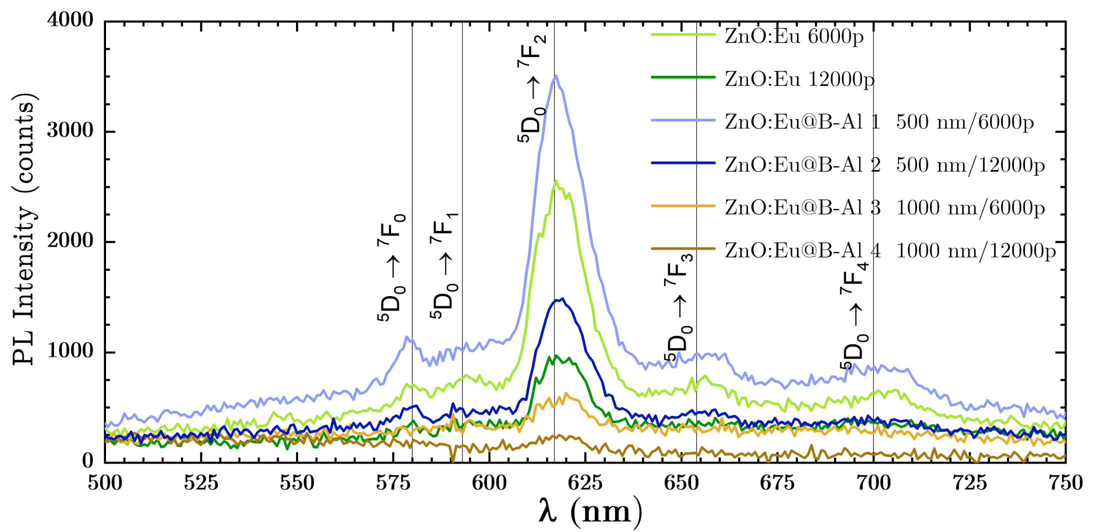

Figure 4.49: PL spectra of ZnO:Eu films and ZnO:Eu@BAl multilayers with various thicknesses excited by 365 nm LED lamp.

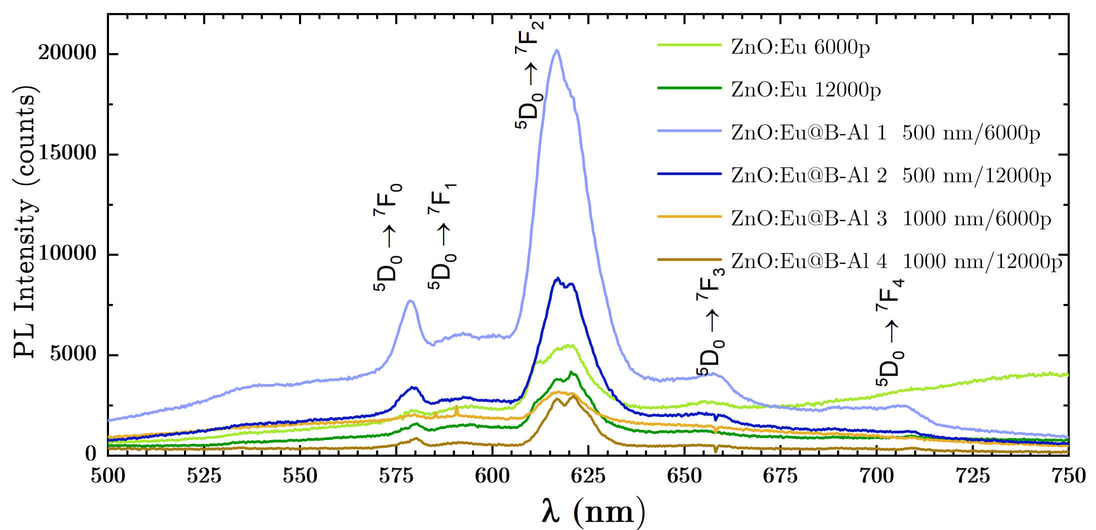

Figure 4.50: PL spectra of ZnO:Eu films and ZnO:Eu@BAl multilayers with various thicknesses excited by 355 nm laser.

4.12 Ellipsometry results

Temperature-dependent ellipsometric measurements were conducted to determine whether the optical properties (refractive index n and optical extinction coefficient k) change due to exposure to elevated temperatures and to assess the impact of the black film on these changes. To investigate this, the measurements of single-layer samples HT-WO_3 7 and B-Ti 09 were performed to obtain optical coefficients, which serve as initial parameters for the analysis of the multilayered structure HT-WO_3@B-Ti. Each of these samples was measured in two cycles: heating up from RT to 500°C, and subsequently cooling down from 500°C to RT with a step of $\sim$ 50°C.

We begin our discussion with the results of sample HT-WO_3 7, which already exhibited reversible thermochromic properties in transmittance spectra (refer to earlier Fig. 4.46). The spectroscopic ellipsometry spectra are shown in Fig. 4.51. The ellipsometric angles Ψ and Δ show visible gradual variation as a function of temperature, suggesting alterations in optical parameters, although there are certain temperature regions where this change is enhanced. The biggest jump occurs between RT and 130°C, which is most likely caused by the desorption of the water previously adsorbed on the surface from air moisture. Another relatively sudden change occurs between 160°C and 200°C, corresponding to the same temperature interval, where the most substantial change in transmittance was observed as well, indicating the strongest thermochromism in this region.

We utilized the Tauc-Lorentz model, often employed for many TCOs[134], for the evaluation of the optical coefficients n and k. This model, first developed by Jellison and Modine in 1996[165][4], is an extension of a classical Lorentz model, although it accounts for the asymmetry of the peak in the imaginary part of the dielectric function ε_2. However, two additional harmonic oscillators (Gaussians) were required to be added to the model to obtain a reasonable fit. The first oscillator was needed near the absorption-onset region with photon energy higher than E_g (positioned at about 5.5 eV), due to the already mentioned Urbach tail[162]. Similarly, this correction could be done using the Cody-Lorentz model, slightly modifying the previous one with the Lorentzian-shape oscillator included[135]. The second oscillator was added for longer wavelengths (positioned at about 1.4 eV) in the NIR region, where k is supposed to be zero, but our sample exhibits an extra absorption band with k progressively ascending for higher wavelengths. This could be a consequence of higher electric conductivity, where free charge carriers could cause this behaviour.

Nevertheless, this model was sufficient enough (with MSE $\sim$ 7) to yield the optical coefficients in the third row of Fig. 4.51. The ellipsometric roughness was estimated to be 3.34(2) nm, which is considerably higher than the R_q determined previously by AFM (see Fig. 4.31). The other important fitting parameters are included in Table 4.13, namely band gap E_g and ellipsometric thickness h_{SE}. The decrease in E_g with increasing temperature is again apparent. The E_g at RT is slightly lower than that determined from transmittance spectra. This difference can be caused by factors mentioned in Section 4.10, although the difference is reasonably small to consider them comparable, proving the usefulness of el-

[4]Although they laboriously derived the expression for the dielectric function, they needed to correct their calculations in the same year[166].

lipsometry in the study of transparent oxide films. The E_g is fully recovered after cooling to its former value. This shift from 2.7 to 2.4 eV for temperature interval up to 500°C, is more significant than what has been reported for monoclinic phase[42][159]. Moreover, h_{SE} agrees well with our profilometric thickness $h = 370(27)$ nm. Here, the difference can be explained by different methodologies during the measurement. Ellipsometry measures thickness in the beam spot (located in the centre) but profilometry measures a step closer to the edge of the film, where the thickness is typically smaller because of the inhomogeneity of films prepared by PLD. Additionally, h_{SE} seems to decrease with increasing temperature below 200°C and then remains constant. This highlights the previously stated assumption of adsorbed water. This change is not observed during the cooling cycle as the sample stays in the vacuum so it is likely that a $\sim$ 15 nm layer of adsorbed water was removed during the heating.

The variation in the refractive index is not as significant as in other published studies for WO_3 films prepared by PLD[167][168], yet it is clearly detected by our ellipsometer. Because even a small change in the refractive index can greatly influence the opacity of the film, transmittance measurements are more sensitive to these changes. To elaborate on this, we present the differences in optical coefficients (Δn and Δk) between the first measurement (at RT prior to heating) and the last measurement (at RT after cooling) at the bottom of Fig. 4.51 (magenta lines). If these changes were completely reversible, we would expect both $\Delta n(\lambda) = 0$ and $\Delta k(\lambda) = 0$ for all λ, which is not the case for $\lambda < 350$ nm, where the initial and final states differ, although for $\lambda > 350nm$ this difference diminishes. This is likely due to the thin layer of adsorbed water. To eliminate this effect, it would be beneficial to perform the same measurement again in two cycles, where the second cycle would ensure no residual adsorbed water. However, this was not known prior to the experiment, as the thermal stability and reversibility of the film had previously been tested only up to 250°C.

On the other hand, when examining the difference Δn and Δk at the highest temperature and at RT during heating (red lines) and cooling (blue lines), we can confirm that these changes in colour are reversible, as both curves look qualitatively the same. The refractive index n_{20} at RT for λ near UV is initially lower and then gets higher for $\lambda > 300nm$ than the refractive index n_{500} at 500°C with a difference of 0.03 - 0.04. Meanwhile, the absorption coefficient k_{20} at RT always remains lower than k_{500} at 500°C, and for $\lambda > 500$ nm their values are the same. Assuming that the temperature change is reversible and the thickness of the film is constant, both red and blue curves should be identical. In our case, there is a hysteresis present, which could be caused again by the removal of adsorbed water or the fact that the temperature of the sample is not exactly the same as the temperature of the sample holder measured by a thermocouple due to thermal conductivity of the FS substrate. Therefore, during the cooling, the real temperature of the sample could be slightly different by a few degrees Celsius. In an ideal scenario, it would be required to perform ellipsometric measurements in situ in the same chamber where the film was deposited to avoid exposure to atmospheric moisture or use vacuum transport boxes. However, in practical applications, this effect is unavoidable.

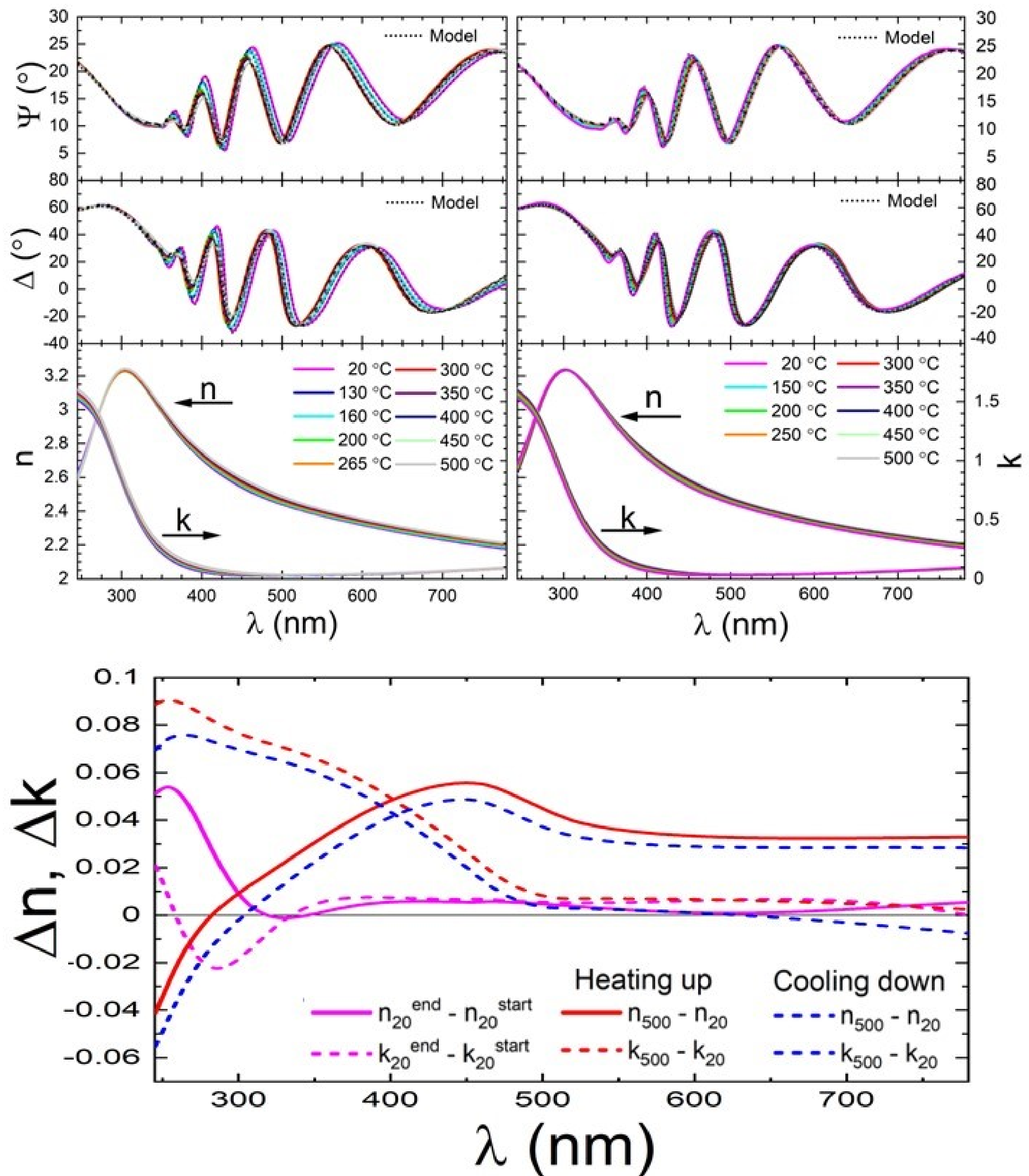

Figure 4.51: Spectroscopic ellipsometry results of HT-WO_3 7 sample at different temperatures. The top graphs show the ellipsometric angles Ψ and Δ, with the left side corresponding to the heating cycle and the right side corresponding to the cooling cycle. The dotted line represents the best fit using the Tauc-Lorentz model to evaluate the refractive index n and the absorption coefficient k presented in the third row. The bottom graph shows the differences in refractive index Δn (solid lines) and absorption coefficient Δk (dashed lines) at temperature denoted in the lower right index of each optical coefficient in the legend.

Heating up			Cooling down		
T (°C)	E_g (eV)	h (nm)	T (°C)	E_g (eV)	h (nm)
20	2.68(1)	397.1(3)	500	2.43(1)	382.2(4)
130	2.63(1)	390.7(3)	450	2.45(1)	382.2(4)
160	2.61(1)	390.6(3)	400	2.49(1)	382.7(4)
200	2.57(1)	383.2(3)	350	2.49(1)	382.7(4)
265	2.53(1)	381.7(3)	300	2.52(1)	382.7(4)
300	2.50(1)	381.4(3)	250	2.56(1)	382.4(4)
350	2.48(1)	381.8(3)	200	2.60(1)	382.3(4)
400	2.45(1)	381.3(3)	150	2.63(1)	382.0(4)
450	2.43(1)	382.0(3)	20	2.71(1)	382.0(4)
500	2.39(1)	381.7(3)			

Table 4.13: Fitting parameters (band gap E_g and ellipsometric thickness h_{SE}) obtained from the Tauc-Lorentz model of ellipsometric data from Fig. 4.51 for the HT-WO_3 7 sample.

Finally, when a thin film of WO_3 (60 nm) is combined with a B-Ti (500 nm), the interpretation of ellipsometric data becomes considerably more complicated. For the single-layered sample B-Ti 09, ellipsometry did not show any variations in Ψ and Δ as a function of temperature. This is expected, as the thermal stability of this film was already proven by SEM. However, even for this film, we were unsuccessful in finding an appropriate model for our black film. Several approaches were tried including the simplest models for TiN, to more advanced effective medium approximations (EMA)[169]. In this model, the roughness and porosity of the black film are compensated by incorporating ambient air as another component, with some volume fraction, into our film. Despite these efforts, the best fit resulted in a substantially high MSE value, making it not good enough to obtain satisfactory optical coefficients. Most likely, our films are gradient layers composed of Ti, TiO_2 and TiN with crystalline and amorphous phases mixed together. Additionally, there is an effect of localised surface plasmon resonance (LSPR) on small metallic nanoparticles, and the film was partially transparent (as evidenced by the interference pattern). All of these factors provide severe limitations for EMA, since ellipsometry is quite sensitive to any surface structures where Equation (1.2) is no longer valid.

Adding another layer of WO_3 on top resulted in an even poorer fit. The measured data are shown in Fig. 4.52, where slight variations with temperature are observed. The most significant change occurs between 100°C and 150°C, which we again attribute to adsorbed water on the surface, and this change becomes less pronounced thereafter. During cooling, this change seems to be smaller than in case of HT-WO_3 7 film. Consequently, it remains challenging to determine whether the black film enhances or diminishes the oxide's thermochromic properties. The film thickness, chosen to maximize the black film's effect, may also be too small for this effect to show. For future improvements, it would be necessary to perform additional ellipsometric measurements in transmission mode to account for the transparency of the film.

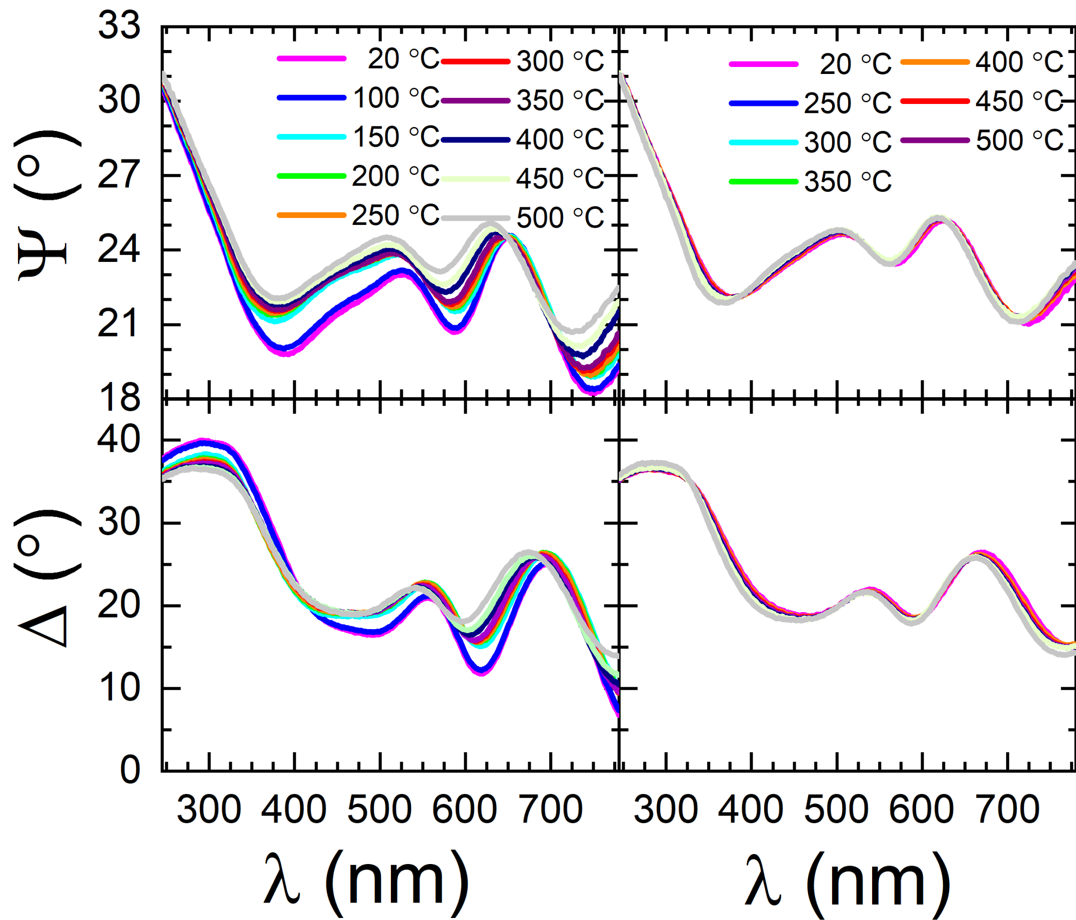

Figure 4.52: Spectroscopic ellipsometry results of HT-WO_3@B-Ti sample at different temperatures. The ellipsometric angles Ψ and Δ on the left side correspond to the heating cycle and the right side correspond to the cooling cycle.

Conclusion

Thin films of B-Al were successfully reproduced on amorphous FS and crystalline Si substrates using pulsed DC MS with varying thicknesses. Despite having the same crystalline structure and chemical composition, the growth mechanism differs for the Si-grown films compared to previously reported works. This results in a lower deposition rate, a higher overall reflectivity, and a more compact morphology characterized by smaller grains for films with the same thicknesses as FS-grown films. At elevated temperatures, the formation of nanowires and other large surface features was observed, beginning to emerge at temperatures around 200°C, arising from the thermal stress relief in damaged surface spots.

By optimization of the deposition parameters, B-Ti films were also prepared by pulsed DC MS using various deposition pressures and altering N_2/Ar ratio. Lower deposition pressures led to delamination. Introducing even a small amount of nitrogen gave rise to the formation of TiN films, which is responsible for a rapid decrease in the deposition rate and improved thermal stability. The optimal N_2/Ar mixture appears to be approximately 8 %, although the diffuse reflectance remains still higher compared to B-Al or other BM. Their texture can be tailored to switch between two crystallographic orientations by altering the N_2 content. Rietveld refinement of XRD patterns revealed a relation between the lattice parameters, mean crystallite sizes, and microstrain values for films deposited at 1.0 Pa and 1.5 Pa. Their relatively smooth morphology does not resemble the desired moth-eye structure, which is capable of efficient light absorption.

WO_3 and P-doped WO_3 films were deposited by PLD at RT and HT of 500°C for various oxygen deposition pressures. The transition from the oxygen-deficient metallic state to the transparent oxide state, accompanied by a gradual change in their appearance, was noted with increasing deposition pressure. The surface morphology is also greatly affected by altered stoichiometry and temperature-induced surface recrystallization. The unheated WO_3 as well as P-doped films show an amorphous structure and consequently do not exhibit reversible thermochromism. However, HT-WO_3 samples at higher deposition pressure possess a tetragonal-like crystal structure, unlike a monoclinic phase, for which thermochromic properties have been reported. The sample with the best reversible thermochromic response possessed an optical band gap of 2.7 - 2.8 eV at RT, as determined independently by optical transmittance measurements in our custom-made vacuum system and spectroscopic ellipsometry. Additionally, the band gap shifted with increasing temperature up to 500°C to 2.4 eV.

Fabrication of a multi-layered structure consisting of B-Al and Eu-doped ZnO films manifested enhanced photoluminescence for a certain thickness of B-Al. Conversely, increasing this thickness leads to quenching of luminescence. The combination of the best thermochromic WO_3 film with the most anti-reflective B-Ti, did not provide convincing results to evaluate the effect on the thermochromic properties. Although minor changes in the ellipsometrical angles were apparent, we were unable to construct an appropriate optical model to obtain optical parameters as a function of temperature. This makes the investigation of BM-based thermochromic multi-layers challenging and will therefore require other approaches that can be employed in future studies.

Bibliography

[1] X. Zhang, F. Shan, H. Zhou, et al. Silver nanoplate aggregation based multifunctional black metal absorbers for localization, photothermic harnessing enhancement and omnidirectional light antireflection. *J. Mater. Chem. C*, 6:989–999, 2018.

[2] M. Kobayashi, Y. Katori, M. Yamaguchi, et al. Broadband light absorber of gold-coated moth-eye film. *Opt. Mater. Express*, 9(9):3744–3752, 2019.

[3] J. Cizek, O. Melikhova, P. Hruška, et al. Positronium Formation in Nanostructured Metals. *Acta Physica Polonica A*, 132:1579–1584, 2017.

[4] X. Liu, P. R. Coxon, M. Peters, et al. Black silicon: fabrication methods, properties and solar energy applications. *Energy Environ. Sci.*, 7:3223–3263, 2014.

[5] J. Kejzlar, J. More-Chevalier, M. Hruška, et al. Black Gold Layers: Preparation, Material and Optical Properties, Application Potential for Electromagnetic Absorbers and Gas Sensors, 2024. Submitted article.

[6] H. Mavani and N. Singh. A Concise History of Black-body Radiation Problem, 2022. [Online] `https://arxiv.org/pdf/2208.06470`. Accessed on June 20th, 2024.

[7] A. H. Pfund. BISMUTH BLACK AND ITS APPLICATIONS. *Review of Scientific Instruments*, 1(7):397–399, 07 1930.

[8] H. S. Seifert and H. M. Randall. Transmission and Reflection of Plastics and Metal Blacks in the Far Infra-Red. *Review of Scientific Instruments*, 11(11):365–368, 1940.

[9] H. C. Burger and P. H. Van Cittert. Die Herstellung von Wismut-Antimony Vacuum Thermoelementen durch Verdampfung. *Zeitschrift Für Physik*, 66:210–217, 1930.

[10] F. Kurlbaum. Aenderung der Emission und Absorption von Platinschwarz und Ruß mit zunehmender. *Annalen der Physik*, 67:846–858, 1899.

[11] W. O. Milligan and A. B. Focke. The crystal structure of aluminum black. *American Chemical Society*, 1:107–108, 1941.

[12] L. Harris. *The Optical Properties of Metal Blacks and Carbon Blacks*. Massachusetts Institute of Technology, Cambridge, 1967.

[13] L. Harris, R. T. McGinnies, and B. M. Siegel. The Preparation and Optical Properties of Gold Blacks. *Journal of the Optical Society of America*, 38:582–589, 1948.

[14] L. Harris and J. K. Beasley. The Innfrared Properties of Gold Smoke Deposits. *Journal of the Optical Society of America*, 42(2):134–140, 1952.

[15] J. Goldsmith, V. Vasilyev, J. Vella, et al. Black aluminum: a novel antireflective absorbing coating. In *NAECON 2014 - IEEE National Aerospace and Electronics Conference*, pages 69–70, 2014.

[16] H. Huang, L. Yang, S. Bai, et al. Blackening of metals using femtosecond fiber laser. *Applied Optics*, 54:324, 2015.

[17] A. Christiansen, G. Caringal, J. Clausen, et al. Black metal thin films by deposition on dielectric antireflective moth-eye nanostructures. *Scientific Reports*, 5:10563, 2015.

[18] M. Novotný, J. Bulíř, J. Lančok, et al. A method of preparation of black aluminium by magnetron sputtering and its application in thermal absorption coating of anodes, Patent PV 2016-378/307110, Dec. 2017.

[19] Hospodářské noviny. Dva studenti provedli špatné výpočty při pokusu. A vytvořili unikátní černý hliník (Newspapper article in Czech), 2011. [Online] `https://domaci.hn.cz/c1-52694250-dva-studenti-provedli-spatne-vypocty-pri-pokusu-a-vytvorili-unikatni-cerny-hlinik`. Accessed on June 21st, 2024.

[20] P. Pokorný, M. Hruška, M. Novotný, et al. Thermally stimulated exoelectron emission from the surface of black aluminum layers prepared by PVD methods. *Vacuum*, 221:112880, 2024.

[21] J. More-Chevalier, M. Novotný, P. Hruška, et al. Fabrication of black aluminium thin films by magnetron sputtering. *RSC Adv.*, 10:20765–20771, 2020.

[22] C. A. Corrêa, J. More-Chevalier, P. Hruška, et al. Microstructure and physical properties of black-aluminum antireflective films. *RSC Adv.*, 14:15220–15231, 2024.

[23] D. Prokop. Štúdium štruktúry a vlastností tenkých vrstiev čierneho hliníka pripraveného pomocou magnetrónového naprašovania (in Slovak). *Bachelor thesis. Charles University*, 2021.

[24] P. Hruška, J. More-Chevalier, M. Novotný, et al. Effect of roughness and nanoporosity on optical properties of black and reflective Al films prepared by magnetron sputtering. *J. Alloys Compd.*, 872:159744, 2021.

[25] M. Romanova, J. More-Chevalier, M. Novotny, et al. Thermal Stability of Black Aluminum Films and Growth of Aluminum Nanowires from Mechanical Defects on the Film Surface during Annealing. *Physica Status Solidi (b)*, 259:2270024, 2022.

[26] J. More-Chevalier, P. V. Yudin, Ch. Cibert, et al. Black aluminum-coated $Pt/Pb(Zr_{0.56}Ti_{0.44})O_3/Pt$ thin film structures for pyroelectric energy harvesting from a light source. *J. Appl. Phys.*, 126(21):214501, 2019.

[27] M. Hruška, J. More-Chevalier, D. Prokop, et al. Surface Enhancement Using Black Coatings for Sensor Applications. *Nanomaterials*, 12(23):4297, 2022.

[28] M. R. L. Glew, A. Vollmer, S. L. M. Schroeder, et al. The characterization of TiN thin films using optical reflectivity measurements. *Journal of Physics D: Applied Physics*, 35(20):2643, 2002.

[29] S. Borah, H. Bailung, A. Pal, et al. Study on the influence of nitrogen on titanium nitride in a dc post magnetron sputtering plasma system. *Journal of Physics D: Applied Physics*, 41:195205, 2008.

[30] Y. L. Jeyachandran, B. Karunagaran, Sa. K. Narayandass, et al. Properties of titanium thin films deposited by dc magnetron sputtering. *Materials Science and Engineering: A*, 431:277–284, 2006.

[31] B. Zheng, W. Wang, G. Jiang, et al. Fabrication of broadband antireflective black metal surfaces with ultra-light-trapping structures by picosecond laser texturing and chemical fluorination. *Applied Physics B: Lasers and Optics*, 122(6):180, 2016.

[32] K. Wöbbeking, M. Li, E. G. Hübner, et al. Conical microstructuring of titanium by reactive gas assisted laser texturing. *RSC Adv.*, 9:37598–37607, 2019.

[33] H. Haberland, M. Karrais, and M. Mall. A new type of cluster and cluster ion source. *Zeitschrift fur Physik D Atoms, Molecules and Clusters*, 20(1-4):413–415, 1991.

[34] M. Drábik, A. Choukourov, A. Artemenko, et al. Morphology of Titanium Nanocluster Films Prepared by Gas Aggregation Cluster Source. *Plasma Processes and Polymers*, 8(7):640–650, 2011.

[35] A. Shelemin, O. Kylián, J. Hanuš, et al. Preparation of metal oxide nanoparticles by gas aggregation cluster source. *Vacuum*, 120:162–169, 2015.

[36] S. Liedtke, Ch. Grüner, A. Lotnyk, et al. Glancing angle deposition of sculptured thin metal films at room temperature. *Nanotechnology*, 28(38):385604, 2017.

[37] G. Leftheriotis, M. Liveri, M. Galanopoulou, et al. A simple method for the fabrication of WO_3 films with electrochromic and photocatalytic properties. *Thin Solid Films*, 573:6–13, 2014.

[38] M. Epifani. Mechanistic Insights into WO_3 Sensing and Related Perspectives. *Sensors*, 22(6):2247, 2022.

[39] P. V. Karthik Yadav, B. Ajitha, Y. A. K. Reddy, et al. Effect of sputter pressure on UV photodetector performance of WO_3 thin films. *Applied Surface Science*, 536:147947, 2021.

[40] T. H. Wondimu, A. W. Bayeh, D. M. Kabtamu, et al. Recent progress on tungsten oxide-based materials for the hydrogen and oxygen evolution reactions. *Int. J. Hydrogen Energy*, 47(47):20378–20397, 2022.

[41] S. Durrani, E. Khawaja, M. Salim, et al. Effect of preparation conditions on the optical and thermochromic properties of thin films of tungsten oxide. *Solar Energy Materials and Solar Cells*, 71:313–325, 2002.

[42] H. Simchi, B. E. McCandless, and T. Meng. Structural, optical, and surface properties of WO_3 thin films for solar cells. *J. Alloys Compd.*, 617:609–615, 2014.

[43] F. Wan, L. Lequn, Y. Chujun, et al. Plasma assisted pulsed laser deposition of WO_3 films for thermochromism. *Materials Chemistry and Physics*, 314:128880, 2024.

[44] T. Chang, X. Cao, S. Bao, et al. Review on thermochromic vanadium dioxide based smart coatings: from lab to commercial application. *Advances in Manufacturing*, 6(1):1–19, 2018.

[45] L. Lu, Z. Wu, C. Ji, et al. Effect of Fe doping on thermochromic properties of VO_2 films. *Journal of Materials Science: Materials in Electronics*, 29:5501–5508, 2018.

[46] K. Bon-Ryul, K. Kim, and H. Ahn. Novel tunneled phosphorus-doped WO_3 films achieved using ignited red phosphorus for stable and fast switching electrochromic performances. *Nanoscale*, 11:3318–3325, 2019.

[47] R. Guo, X. Lai, J. Huang, et al. Phosphate-Based Electrocatalysts for Water Splitting: Recent Progress. *ChemElectroChem*, 5(24):3822–3834, 2018.

[48] J. More-Chevalier, S. A. Irimiciuc, L. Volfova, et al. Tailoring pulsed laser deposition of phosphorus doped WO_x films from $(PO2)_4(WO3)_4$ target by space-resolved optical emission spectroscopy. *Thin Solid Films*, 742:139042, 2022.

[49] M. Willander, O. Nur, Q. X. Zhao, et al. Zinc oxide nanorod based photonic devices: recent progress in growth, light emitting diodes and lasers. *Nanotechnology*, 20(33):332001, 2009.

[50] V. Kumar, O. M. Ntwaeaborwa, T. Soga, et al. Rare Earth Doped Zinc Oxide Nanophosphor Powder: A Future Material for Solid State Lighting and Solar Cells. *ACS Photonics*, 4:2613–2637, 2017.

[51] T. Minami, T. Miyata, and Y. Ohtani. Optimization of aluminum-doped ZnO thin-film deposition by magnetron sputtering for liquid crystal display applications. *physica status solidi (a)*, 204:3145 – 3151, 2007.

[52] R. Kumar and H. S. Dosanjh. A mini-review on rare earth metal doped ZnO nanomaterials for photocatalytic remediation of waste water. *Journal of Physics: Conference Series*, 2267(1):012139, 2022.

[53] Y. İpek and N. K. Ayhan. Rare Earth Element Doped ZnO Thin Films. *International Journal of Pure and Applied Sciences*, 7:305–313, 06 2021.

[54] M. Novotný, M. Vondráček, E. Marešová, et al. Optical and structural properties of ZnO:Eu thin films grown by pulsed laser deposition. *Applied Surface Science*, 476:271–275, 2019.

[55] Š. Havlová, M. Novotný, P. Fitl, et al. Effect of pulsed laser annealing on optical and structural properties of ZnO:Eu thin film. *Journal of Materials Science*, 56:11414–11425, 2021.

[56] M. Novotný, J. Remsa, Š. Havlová, et al. In Situ Monitoring of Pulsed Laser Annealing of Eu-Doped Oxide Thin Films. *Materials*, 14(24):7576, 2021.

[57] Ch. Kittel. *Introduction to Solid State Physics*. Wiley, New York, 2004.

[58] P. Malý. *Optika*. Karolinum, Praha, 2014.

[59] M. Kubinyi, N. Benkö, A. Grofcsik, et al. Determination of the thickness and optical constants of thin films from transmission spectra. *Thin Solid Films*, 286(1):164–169, 1996.

[60] M. Jafar. Comprehensive formulations for the total normal-incidence optical reflectance and transmittance of thin films laid on thick substrates. *European International Journal of Science and Technology*, 2:274, 2013.

[61] Photon Counting. [Online] `https://www.cis.rit.edu/class/simg713/notes/chap5-photon.pdf`. Accessed on April 4th, 2024.

[62] M. O'Kane. Exciton: An introduction. [Online] `https://www.ossila.com/pages/what-is-an-exciton`. Accessed on June 2nd, 2024.

[63] RP Photonics. Band gap. [Online] `https://www.rp-photonics.com/band_gap.html`. Accessed on June 2nd, 2024.

[64] J. Tauc, R. Grigorovici, and A. Vancu. Optical Properties and Electronic Structure of Amorphous Germanium. *Physica Status Solidi (b)*, 15(2):627–637, 1966.

[65] P. Makuła, M. Pacia, and W. Macyk. How To Correctly Determine the Band Gap Energy of Modified Semiconductor Photocatalysts Based on UV–Vis spectra. *The Journal of Physical Chemistry Letters*, 9(23):6814–6817, 2018.

[66] J. H. Day. Thermochromism of inorganic compounds. *Chemical Reviews*, 68(6):649–657, 1968.

[67] J. H. Day. Thermochromism. *Chemical Reviews*, 63(1):65–80, 1963.

[68] G. Ferro, D. Carole, F. Cauwet, et al. Thermochromic properties of some colored oxide materials. *Optical Materials: X*, 15:100167, 2022.

[69] Cheng Y., X. Zhang, Ch. Fang, et al. Discoloration mechanism, structures and recent applications of thermochromic materials via different methods: A review. *Journal of Materials Science & Technology*, 34(12):2225–2234, 2018.

[70] Thermochromism in the ionic conductor, Cu_2HgI_4. [Online] https://people.umass.edu/mjknapp/Chem242/2004%20Experiments/CuHg2I4Lab.pdf]. Accessed on June 10th, 2024.

[71] Y. Cho, A. Yamaguchi, R. Uehara, et al. Temperature dependence on bandgap of semiconductor photocatalysts. *The Journal of Chemical Physics*, 152(23):231101, 2020.

[72] A. Hakami, S. Srinivasan, P. Biswas, et al. Review on thermochromic materials: development, characterization, and applications. *Journal of Coatings Technology and Research*, 19:377–402, 2022.

[73] M. Dey and Y. Sikdar. Thermochromics: A temperature sensitive smart Material. [Online] https://www.thebges.edu.in/wp-content/uploads/2023/03/5.-Thermochromics-A-Temperature-Sensitive-Smart-Material.pdf. Accessed on June 10th, 2024.

[74] P. M. Martin. *Handbook of Deposition Technologies for Films and Coatings.* Elsevier, Burlington, 2010.

[75] B. A. Movchan and A. V. Demchishin. Structure and properties of thick condensates of nickel, titanium, tungsten, aluminum oxides, and zirconium dioxide in vacuum. *Fiz. Metal. Metalloved.*, 28:653–662, 1969.

[76] W. R. Grove. On the Electro-Chemical Polarity of Gases. *Philosophical Transactions of the Royal Society of London*, 152:87–101, 1852.

[77] H. Frey and H. R. Khan. *Handbook of Thin Film Technology.* Springer Verlag Berlin-Heidelberg, Heidelberg, 2015.

[78] J. S. Chapin. Sputtering process and apparatus, Patent US4166018A, Jan. 1974.

[79] M. Ohring. *Materials Science of Thin Films: Deposition and Structure.* Academic Press, San Diego, 2002.

[80] P. Hruška. Study of hydrogen interactions with defects in thin metallic films. *PhD thesis, Faculty of Mathematics and Physics, Charles University*, 2018.

[81] J. A. Thornton. Influence of apparatus geometry and deposition conditions on the structure and topography of thick sputtered coatings. *Journal of Vacuum Science and Technology*, 11(4):666–670, 1974.

[82] O. Kylián, M. Drábik, O. Polonskyi, et al. Deposition of nanostructured fluorocarbon plasma polymer films by RF magnetron sputtering of polytetrafluoroethylene. *Thin Solid Films*, 519(19):6426–6431, 2011.

[83] NIST Basic Atomic Spectroscopic Data - Strong lines of Ti. [Online] https://physics.nist.gov/PhysRefData/Handbook/Tables/titaniumtable2.htm. Accessed on June 18th, 2024.

[84] NIST Basic Atomic Spectroscopic Data - Strong lines of Ar. [Online] https://physics.nist.gov/PhysRefData/Handbook/Tables/argontable2.htm. Accessed on April 7th, 2024.

[85] R. N. Zare, E. O. Larsson, and R. A. Berg. Franck-Condon factors for electronic band systems of molecular nitrogen. *Journal of Molecular Spectroscopy*, 15(2):117–139, 1965.

[86] H. Nassar, S. Pellerin, K. Musiol, et al. ${N_2}^+/N_2$ ratio and temperature measurements based on the first negative ${N_2}^+$ and second positive N_2 overlapped molecular emission spectra. *Journal of Physics D: Applied Physics*, 37(14):1904, 2004.

[87] H. M. Smith and A. F. Turner. Vacuum Deposited Thin Films Using a Ruby Laser. *Appl. Opt.*, 4(1):147–148, 1965.

[88] D. Dijkkamp, T. Venkatesan, X. D. Wu, et al. Preparation of Y-Ba-Cu oxide superconductor thin films using pulsed laser evaporation from high Tc bulk material. *Applied Physics Letters*, 51(8):619–621, 08 1987.

[89] T. Venkatesan. Pulsed laser deposition—invention or discovery? *Journal of Physics D: Applied Physics*, 47(3):034001, 2013.

[90] R. Eason. *Pulsed Laser Deposition of Thin Films: Applications-Led Growth of Functional Materials*. Wiley, Hoboken, 2006.

[91] Operation and Maintenance Manual for Surelite™ Lasers. [Online] https://static1.squarespace.com/static/5265c389e4b0e4777831dba7/t/5d7d352d5f172734866285e0/1568486705417/Surlite+Laser+User+Manual+.pdf. Accessed on June 22nd, 2024.

[92] User Manual FieldMaxII-TOP™ Laser Power/Energy Meter. [Online] https://content.coherent.com/file/fieldmaxiitop-user-manual.pdf. Accessed on June 22nd, 2024.

[93] Duo 1.6/Duo 1.6M/Duo 1.6 MC Rotary Vane Pump Operating Instructions. [Online] https://www.lesker.com/newweb/vacuum_pumps/pdf/manuals/kjlc-pfeiffer-duo1.6-operatingmanual.pdf. Accessed on June 22nd, 2024.

[94] HiPace 80 Turbopump Operating Instructions. [Online] https://www.idealvac.com/files/ManualsII/PfeifferHI_Pace80Turbo_OperatingInstructions.pdf. Accessed on June 22nd, 2024.

[95] CMR 364, 1 hPa F.S., DN 16 ISO-KF. [Online] https://www.lesker.com/newweb/vacuum_pumps/pdf/manuals/kjlc-pfeiffer-duo1.6-operatingmanual.pdf. Accessed on June 22nd, 2024.

[96] Balzers Compact FullRange Gauge PKR260. [Online] https://www.vacmarket.com/assets/Products/Pressure-Gauges/Full-Range-Gauges/Balzers/PKR260/balzers-PKR260-Full-Range-Gauge-Catalog-vacmarket.com.pdf. Accessed on April 5th, 2024.

[97] Selec Advanced, Full Featured PID Temperature Controller PID500. [Online] `https://www.jameco.com/Jameco/Products/ProdDS/2133261.pdf`. Accessed on April 5th, 2024.

[98] ISO 21920-2. Geometrical product specifications (GPS), Surface texture: Profile, Part 2: Terms, definitions and surface texture parameters. Technical report, International Organization for Standardization, Geneva, 2021.

[99] G. Binnig, C. F. Quate, and Ch. Gerber. Atomic Force Microscope. *Phys. Rev. Lett.*, 56:930–933, 1986.

[100] M. Saint Jean, S. Hudlet, C. Guthmann, et al. Van der Waals and capacitive forces in atomic force microscopies. *J. Appl. Phys.*, 86:5245–5248, 1999.

[101] P. Eaton and P. West. *Atomic Force Microscopy.* Oxford University Press, Oxford, 2010.

[102] V. Mironov. *Fundamentals of Scanning Probe Microscopy.* The Russian Academy of Sciences, Institute for Physics of Microstructures, Nizhniy Novgorod, 2004.

[103] D. Nečas and P. Klapetek. Gwyddion: an open-source software for SPM data analysis. *Central European Journal of Physics*, 10:181–188, 2012.

[104] J. Smith, S. Breakspear, and S. Campbell. AFM in surface finishing: Part II. Surface roughness. *Transactions of the Institute of Metal Finishing*, 81:55–58, 2003.

[105] M. Knoll and E. Ruska. Das elektronenmikroskop. *Z. Physik*, 78:318–339, 1932.

[106] M. von Ardenne. Die grenzen für das auflösungsvermögen des elektronenmikroskops. *Z. Physik*, 108:338–352, 1938.

[107] E. Abbe. Beiträge zur theorie des mikroskops und der mikroskopischen wahrnehmung. *Archiv f. mikrosk. Anatomie*, 9:413–468, 1873.

[108] J. I. Goldstein, D. E. Newbury, J. R. Michael, et al. *Scanning Electron Microscopy and X-Ray Microanalysis.* Springer, New York, 2018.

[109] FEI. Nova NanoSEM User Operation Manual. [Online] `https://static1.squarespace.com/static/57b26cc76b8f5b7524bf9ed2/t/642c492e21aca8137ebf1901/1680623921112/Nova+Nano+Extensive+Manual.pdf`. Accessed on March 3rd, 2024.

[110] Kammrath & Weiss GmbH - Heaters. [Online] `https://www.kammrath-weiss.com/en/heaters/`. Accessed on March 3rd, 2024.

[111] W. Friedrich, P. Knipping, and M. von Laue. *Interferenz-Erscheinungen bei Röntgenstrahlen.* Verlag der Kgl. Bayer. Akad. der Wiss, München, 1912.

[112] W. L. Bragg. The Diffraction of Short Electromagnetic Waves by Crystals. *Proceedings of the Cambridge Philosophical Society*, 17:43–57, 1913.

[113] M. Deutsch, G. Hölzer, J. Härtwig, et al. K_α and K_β X-ray Emission Spectra of Copper. *Phys. Rev. A*, 51:283–296, 1995.

[114] V. Valvoda, M. Polcarová, and P. Lukáč. *Základy strukturní analýzy*. Univerzita Karlova, Praha, 1992.

[115] J. Epp. *X-Ray Diffraction (XRD) Techniques for Materials Characterization*. Woodhead Publishing, Sawston, 2016.

[116] G. K. Williamson and W. H. Hall. X-ray line broadening from filed aluminium and wolfram. *Acta Metallurgica*, 1(1):22–31, 1953.

[117] P. Scherrer. Bestimmung der größe und der inneren struktur von kolloidteilchen mittels röntgenstrahlen. *Nachrichten von der Gesellschaft der Wissenschaften zu Göttingen, Mathematisch-Physikalische Klasse*, 98-100, 1918.

[118] S. D. Bakshi, D. Sinha, and S. G. Chowdhury. Anisotropic broadening of XRD peaks of α-Fe: Williamson-Hall and Warren-Averbach analysis using full width at half maximum (FWHM) and integral breadth (IB). *Materials Characterization*, 142:144–153, 2018.

[119] P. Scardi, M. Leoni, and R. Delhez. Line broadening analysis using integral breadth methods: A critical review. *Journal of Applied Crystallography*, 37:381–390, 2004.

[120] H. M. Rietveld. Line profiles of neutron powder-diffraction peaks for structure refinement. *Acta Crystallographica*, 22(1):151–152, 1967.

[121] H. M. Rietveld. A profile refinement method for nuclear and magnetic structures. *Journal of Applied Crystallography*, 2(2):65–71, 1969.

[122] R. J. Hill and C. J. Howard. Quantitative Phase Analysis from Neutron Powder Diffraction Data Using the Rietveld Method. *Journal of Applied Crystallography*, 20:467–474, 1987.

[123] G. Caglioti, A. Paoletti, and F. P. Ricci. Choice of collimators for a crystal spectrometer for neutron diffraction. *Nuclear Instruments*, 3(4):223–228, 1958.

[124] A. Le Bail. Whole powder pattern decomposition methods and applications: A retrospection. *Powder Diffraction*, 20:316–326, 2005.

[125] B. Toby and R. Dreele. GSAS-II: The Genesis of a Modern Open-Source All-Purpose Crystallography Software Package. *Journal of Applied Crystallography*, 46:544–549, 2013.

[126] K. Momma and F. Izumi. VESTA: A Three-Dimensional Visualization System for Electronic and Structural Analysis. *Journal of Applied Crystallography - J APPL CRYST*, 41:653–658, 2008.

[127] Integrating Sphere Theory and Applications. [Online] `https://www.labsphere.com/wp-content/uploads/2021/09/Integrating-Sphere-Theory-and-Applications.pdf`. Accessed on April 3rd, 2024.

[128] Spectralon Diffuse Reflectance Standards. [Online] `https://www.labsphere.com/wp-content/uploads/2023/01/Spectralon.pdf`. Accessed on April 3rd, 2024.

[129] Lavat, Rotary pump VR 1,5/12 documentation. [Online] `http://www.lavat.cz/katalog-pdf/6`. Accessed on April 5th, 2024.

[130] Pfeiffer Vacuum TMH/TMU 071 P turbomolecular drag pumps documentation. [Online] `https://www.ajvs.com/library/Pfeiffer_Vacuum_TMH_071_P_Manual.pdf`. Accessed on April 5th, 2024.

[131] Pfeiffer PCR 280 Operating Instructions. [Online] `https://www.idealvac.com/files/brochures/Pfeiffer_PCR_280.pdf`. Accessed on April 5th, 2024.

[132] Narran HR8 - compact spectrometer. [Online] `https://narran.cz/en/product/spectrometers/HR8_Manual.pdf`. Accessed on April 5th, 2024.

[133] P. Drude. Ueber die Gesetze der Reflexion und Brechung des Lichtes an der Grenze absorbirender Krystalle. *Annalen der Physik*, 268(12):584–625, 1887.

[134] H. Fujiwara. *Spectroscopic Ellipsometry Principles and Applications*. Wiley, New York, 2007.

[135] J. A. Woollam. *CompleteEASE™ Data Analysis Manual*. J. A. Woollam Co., Inc., Lincoln, 2015.

[136] E. Wiedemann. Ueber Fluorescenz und Phosphorescenz I. Abhandlung. *Annalen der Physik*, 270:446–463, 1888.

[137] V. Kiisk and R. Jaaniso. *Semiconductor Gas Sensors - Chapter Nine - Rare earth–doped oxide materials for photoluminescence-based gas sensors*. Woodhead Publishing, Sawston, 2020.

[138] R. Capelletti. *Luminescence - In book Encyclopedia of Condensed Matter Physics (pp. 178-189)*. Elsevier, Amsterdam, 2005.

[139] L. Volfová, S. A. Irimiciuc, S. Chertopalov, et al. Tailoring pulsed laser deposition fabricated copper oxide film by controlling plasma parameters. *Applied Surface Science*, 608:155128, 2023.

[140] I. N. Stranski and L. Krastanow. Zur Theorie der orientierten Ausscheidung von Ionenkristallen aufeinander. *Monatshefte für Chemie*, 71:351–364, 1938.

[141] G. R. Jones, Jackson M., and K. O'Grady. Determination of grain size distributions in thin films. *Journal of Magnetism and Magnetic Materials*, 193(1):75–78, 1999.

[142] M. Pelliccione and T. M. Lu. *Evolution of Thin Film Morphology: Modeling and Simulations*. Springer-Verlag Berlin Heidelberg, Heidelberg, 2008.

[143] D. Gerth, D. Katzer, and M. Krohn. Study of the thermal behaviour of thin aluminium alloy films. *Thin Solid Films*, 208(1):67–75, 1992.

[144] T. E. Volin and R. W. Balluffi. Annealing Kinetics of Voids and the Self-Diffusion Coefficient in Aluminum. *Phys. Stat. Sol. (b)*, 25:163–173, 1968.

[145] N. Kristensen, F. Ericson, J. Schweitz, et al. Hole formation in thin aluminium films under controlled variation of strain and temperature. *Thin Solid Films*, 197(1):67–83, 1991.

[146] Ch. Didier, W. K. Pang, Z. Guo, et al. Phase Evolution and Intermittent Disorder in Electrochemically Lithiated Graphite Determined Using in Operando Neutron Diffraction. *Chem. Mater.*, 32(6):2518–2531, 2020.

[147] C. A. Hampel. *The Encyclopedia of the Chemical Elements*. Reinhold Book Corp, New York, 1968.

[148] R. M. Wood. The Lattice Constants of High Purity Alpha Titanium. *Proceedings of the Physical Society*, 80(3):783, 1962.

[149] T. Novoselova, S. Malinov, W. Sha, et al. High-temperature synchrotron X-ray diffraction study of phases in a gamma TiAl alloy. *Materials Science and Engineering: A*, 371:103–112, 2004.

[150] A. Brager. An X-ray examination of titanium nitride III. *Acta Physicochimica (USSR)*, 9:617–632, 1939.

[151] J. Musil, J. Vlček, V. Ježek, et al. Production of Ti films with controlled texture. *Surface and Coatings Technology*, 76-77:274–279, 1995.

[152] A. Kavitha, K. Raman, P. Reddy, et al. The effect of annealing on the structural, optical and electrical properties of Titanium Nitride (TiN) thin films prepared by DC magnetron sputtering with supported discharge. *Journal of Materials Science: Materials in Electronics*, 27:10427–10434, 2016.

[153] J. Pflueger, J. Fink, W. Weber, et al. Dielectric properties of TiC_x, TiN_x, VC_x, and VN_x from 1.5 to 40 eV determined by electron-energy-loss spectroscopy. *Physical Review B*, 30:1155–1163, 1984.

[154] M. G. Krishna and K. A. Padmanabhan. Titanium Nitride based multifunctional thin films. *IOP Conference Series: Materials Science and Engineering*, 1221(1):012007, 2022.

[155] B. Hopp, T. Smausz, M. Lentner, et al. tability investigation of laser darkened metal surfaces. *Appl. Phys. A*, 598(123), 2017.

[156] Surface reflectivity of TiN thin films measured by spectral ellipsometry. *Surface Science*, 251-252:200–203, 1991.

[157] U. Guler, A. V. Kildishev, A. Boltasseva, et al. Plasmonics on the slope of enlightenment: the role of transition metal nitrides. *Faraday Discuss.*, 178:71–86, 2015.

[158] J. Gutpa, H. Shaik, K. N. Kumar, et al. PVD techniques proffering avenues for fabrication of porous tungsten oxide (WO_3) thin films: A review. *Materials Science in Semiconductor Processing*, 143:106534, 2022.

[159] Y. S. Zou, Y. C. Zhang, D. Lou, et al. Structural and optical properties of WO_3 films deposited by pulsed laser deposition. *J. Alloys Compd.*, 583:465–470, 2014.

[160] H. A. Wriedt. The O-W (oxygen-tungsten) system. *Bulletin of Alloy Phase Diagrams*, 10:368–384, 1989.

[161] K. R. Locherer and E. K. H. Salje. The refinement of a tetragonal phase of WO_3 using a novel PSD high temperature X-ray powder diffractometer. *Phase Transitions*, 69(1):85–93, 1999.

[162] F. Urbach. The Long-Wavelength Edge of Photographic Sensitivity and of the Electronic Absorption of Solids. *Phys. Rev.*, 92:1324–1324, 1953.

[163] NIST Basic Atomic Spectroscopic Data - Strong lines of Hg. [Online] `https://physics.nist.gov/PhysRefData/Handbook/Tables/mercurytable2.htm`. Accessed on April 7th, 2024.

[164] M. Vlček, J. Čížek, I. Procházka, et al. Defect studies of thin ZnO films prepared by pulsed laser deposition. *Journal of Physics: Conference Series*, 505:012021, 2014.

[165] G. E. Jellison and F. A. Modine. Parameterization of the optical functions of amorphous materials in the interband region. *Applied Physics Letters*, 69(3):371–373, 1996.

[166] G. E. Jellison and F. A. Modine. Erratum: "Parameterization of the optical functions of amorphous materials in the interband region" [Appl. Phys. Lett. 69, 371 (1996)]. *Applied Physics Letters*, 69(14):2137–2137, 1996.

[167] I. Tirca, I. Boerasu, M. S. Radu, et al. Refractive index of WO_3 thin films grown under various temperatures determined by the Swanepoel method. *Physica B: Condensed Matter*, 620:413266, 2021.

[168] M. Osiac, I. Boerasu, M. S. Radu, et al. Influence of the Iron as a Dopant on the Refractive Index of WO_3. *Materials (Basel)*, 14(14):5845, 2021.

[169] D. A. G. Bruggeman. Berechnung verschiedener physikalischer konstanten von heterogenen substanzen. I. Dielektrizitätskonstanten und Leitfähigkeiten der Mischkörper aus isotropen Substanzen. *Annalen der Physik*, 416(7):636–664, 1935.

List of Figures

1.1 Interference of light on a plane-parallel thin film 11
1.2 The intensity of transmitted and reflected light as a function of wavelength for a thin film composed of two materials with different transparencies 11
1.3 Graphical representation of energy vs. crystal momentum vector for a direct and an indirect band gap 13
1.4 Schematic diagram depicting the thermochromic properties of a transition metal oxide film undergoing a phase transition at the critical temperature T_c 16

2.1 Scheme of the sputtering process 20
2.2 Photographs of glow discharge plasma during MS deposition . . . 20
2.3 The effects of combined electric and magnetic fields in a planar magnetron 22
2.4 Front view of the whole MS deposition apparatus for BM deposition showing most of the key components 24
2.5 Photograph providing detailed views of our MS system for BM deposition 24
2.6 Schematic diagram of our MS system for BM deposition 25
2.7 An example of OES spectra showing a difference between deposition of reflective and black titanium films 27
2.8 Assessment of thickness homogeneity in our MS deposition system 27
2.9 Photography showing detail of a plasma plume during PLD 29
2.10 Schematic diagram of our laboratory PLD system and a few photographs of its components 31
2.11 Schematic diagram and photograph of our PLD vacuum chamber and its components 31
2.12 Screenshot of the LabVIEW graphical user interface programs developed for PLD 33
2.13 Photograph of the PLD sample holder from the inside 33

3.1 An example of a profilometric record for film thickness determination 35
3.2 A simplified schematic diagram of a basic AFM instrumentation. . 36
3.3 Illustration of probe-induced artefacts in AFM. 38
3.4 An illustration of the graphical user interface of Gwyddion software 38
3.5 Schematic diagram of an SEM and an interaction volume 41
3.6 Emission of various SEM signals 42
3.7 EDX spectrum of sample B-Al 03 43
3.8 Photographs of the SEM used in this work 43
3.9 Scheme of the two basic XRD geometries used for thin film characterization 46
3.10 Schematic of a diffraction peak showing different peak parameters and comparison between FWHM and IB 50
3.11 Diffraction pattern of LaB_6 standard measured in BB and GI geometries with two different X-ray tubes 51

3.12 An illustration of the graphical user interface of GSAS-II software 53
3.13 Instrumentation used for specular reflectance and transmittance measurements 55
3.14 The front view of our transmittance measurement system 56
3.15 The top view of our transmittance measurement system 57
3.16 A photo of the sample holder used for transmittance measurements 57
3.17 Reference optical spectrum of a halogen lamp used for the temperature-dependent transmittance measurements in Narran program interface 60
3.18 Optical transmittance spectrum of a fused silica glass and evaluation of its error 60
3.19 Scheme of an RCE type spectroscopic ellipsometry instrument. . . 62
3.20 A photography of experimental setup for spectral ellipsometry measurements 63
3.21 An illustration of the graphical user interface of CompleteEASE software 63
3.22 Schematic diagram of a PL measurement instrumentation 65
3.23 Photography of instrumentation used for PL measurements 65

4.1 A photography of prepared R-Al and B-Al samples on FS substrate 68
4.2 Thicknesses of R-Al and B-Al films deposited on FS and Si substrates as a function of deposition time 68
4.3 A photography of prepared R-Ti and B-Ti samples 69
4.4 Deposition voltage, current and power as a function of nitrogen content during the deposition of R-Ti and B-Ti films with deposition pressures corresponding to 1.0 Pa and 1.5 Pa 72
4.5 Deposition rate as a function of nitrogen content during the deposition of R-Ti and B-Ti films with deposition pressures corresponding to 1.0 Pa and 1.5 Pa 72
4.6 A photography of prepared WO_3 thin films 75
4.7 A photography of prepared WO_3:P thin films 75
4.8 Thickness of the WO_3 and WO_3:P films as a function of oxygen deposition pressure 76
4.9 A schematic diagram of the prepared multilayers 77
4.10 AFM and SEM images of R-Al and B-Al 78
4.11 SEM images of aluminium thin films deposited on FS and Si substrates I 79
4.12 SEM images of aluminium thin films deposited on FS and Si substrates II 80
4.13 Graph showing the evolution of mean grain size with film thickness for B-Al films grown on a Si(111) substrate. 83
4.14 Chemical composition obtained from EDX analysis of R-Al and B-Al films 83
4.15 SEM images of B-Al 04 film deposited on FS substrate at different temperatures 85
4.16 SEM images of B-Al 04 film deposited on Si(111) substrate at different temperatures 86
4.17 Unit cell of Al with space group $Fm\bar{3}m$ (225) 87

4.18 XRD patterns of R-Al and B-Al films deposited on FS substrates, measured in BB and GI geometry . . . 88
4.19 C-W plot and W-H plots of R-Al and B-Al films . . . 89
4.20 Comparison of XRD patterns of B-Al samples deposited on FS and Si(111) substrates for various film thicknesses . . . 91
4.21 C-W and W-H plots of B-Al films grown on FS and Si substrates 91
4.22 Spectrophotometric diffuse reflectance of B-Al films . . . 92
4.23 AFM and SEM images of R-Ti and B-Ti at RT . . . 94
4.24 SEM images of R-Ti and B-Ti taken at different temperatures . . 95
4.25 Theoretical diffraction pattern and unit cell of Ti with space group $P6_3/mmc$ (194) . . . 96
4.26 Theoretical diffraction pattern and unit cell of Ti with space group $Fm\bar{3}m$ (225) . . . 96
4.27 XRD patterns of R-Ti and B-Ti films deposited at different nitrogen content and deposition pressures . . . 98
4.28 Spectrophotometric diffuse reflectance of B-Ti films . . . 100
4.29 Root-mean-square roughness obtained from AFM as a function of oxygen deposition pressure for WO_3 films . . . 101
4.30 AFM images of RT-WO_3 series . . . 102
4.31 AFM images of HT-WO_3 series . . . 103
4.32 AFM images of RT-WO_3:P series . . . 104
4.33 AFM images of HT-WO_3:P series . . . 105
4.34 Theoretical diffraction pattern and unit cell of WO_3 with monoclinic crystal lattice and space group $P2_1/n$ (14) generated by VESTA software . . . 106
4.35 Theoretical diffraction pattern and unit cell of WO_3 with tetragonal crystal lattice and space group $P4/nmm$ (129:2) generated by VESTA software . . . 106
4.36 XRD patterns of RT-WO_3 and WO_3:P films . . . 108
4.37 XRD patterns of HT-WO_3 films . . . 108
4.38 W-H plots for HT-WO_3 7 and HT-WO_3 6 samples . . . 109
4.39 Optical transmittance spectra of pristine WO_3 thin films at ambient conditions . . . 110
4.40 Tauc plots for WO_3 and WO_3:P samples . . . 112
4.41 Optical spectra of Ar/Hg source for wavelength calibration . . . 113
4.42 Time-stability optical transmittance measurements . . . 114
4.43 Transmittance measurement for verifying the detector signal linearity 115
4.44 Optical transmittance spectra for fused silica glass at different temperatures . . . 116
4.45 Optical transmittance spectra of RT-WO_3 series thin films as a function of temperature . . . 117
4.46 Optical transmittance spectra of HT-WO_3 series thin films as a function of temperature . . . 117
4.47 Optical transmittance spectra of RT-WO_3:P series thin films as a function of temperature . . . 118
4.48 Optical transmittance spectra of HT-WO_3:P series thin films as a function of temperature . . . 118

4.49 PL spectra of ZnO:Eu films and ZnO:Eu@B-Al multilayers with various thicknesses excited by 365 nm LED lamp 121
4.50 PL spectra of ZnO:Eu films and ZnO:Eu@B-Al multilayers with various thicknesses excited by 355 laser 121
4.51 Spectroscopic ellipsometry results of HT-WO_3 7 sample at different temperatures 124
4.52 Spectroscopic ellipsometry results of HT-WO_3@B-Ti sample at different temperatures 126

List of Tables

1.1 Classification of various chromic phenomena and the responsible stimuli . . . 14

3.1 The most commonly used analytical functions for diffraction pattern peak approximation . . . 48

4.1 Deposition parameters for R-Al and B-Al samples prepared by MS 67
4.2 Deposition parameters for R-Ti and B-Ti samples prepared by MS 70
4.3 Deposition parameters for RT-WO_3 series prepared by PLD. . . . 73
4.4 Deposition parameters for HT-WO_3 series prepared by PLD. . . 73
4.5 Deposition parameters for RT-WO_3:P series prepared by PLD. . 74
4.6 Deposition parameters for HT-WO_3:P series prepared by PLD. . 74
4.7 Prepared multilayers based on B-Al for PL measurements 77
4.8 Parameters obtained from XRD patterns of B-Al and R-Al films using isolated peak fitting through C-W and W-H plots, and Rietveld refinement . . . 89
4.9 Parameters obtained from XRD patterns of B-Al films deposited on FS and Si(111) substrates using isolated peak fitting through C-W and W-H plots, and Rietveld refinement . . . 90
4.10 Parameters obtained from XRD patterns for R-Ti and B-Ti films through Rietveld refinement . . . 98
4.11 Comparison between measured position and intensity of diffraction peaks with the database tetragonal structure of WO_3 from CIF-file 109
4.12 Band gaps determined from Tauc plots for WO_3 and WO_3:P films 112
4.13 Fitting parameters obtained from the Tauc-Lorentz model of ellipsometric data for the HT-WO_3 7 sample . . . 125

List of Abbreviations

AC	Alternating current
AE	Auger electrons
AFM	Atomic Force Microscopy
B-Al	Black aluminium
B-Ti	Black titanium
BB	Bragg-Brentano (geometry)
BM	Black metal
BSE	Backscattered electrons
C-W	Cohen-Wagner
CCD	Charge-coupled device
CVD	Chemical vapour deposition
DC	Direct current
EDX	Energy dispersive X-ray spectroscopy
FCC	Face-centered cubic (structure)
FWHM	Full width at half maximum
GI	Grazing-incidence (geometry)
HCP	Hexagonal close-packed (structure)
HT	High temperature
IB	Integral breadth
LN_2	Liquid nitrogen
LSPR	Localised surface plasmon resonance
MS	Magnetron sputtering
MSE	Mean squared error
NIR	Near-infrared (light)
OES	Optical emission spectroscopy
PID	Proportional–integral–derivative (controller)
PL	Photoluminescence

PLD	Pulsed laser deposition
PVD	Physical vapour deposition
R-Al	Reflective aluminium
R-Ti	Reflective titanium
RF	Radio frequency
RT	Room temperature
SE	Secondary electrons
SEM	Scanning electron microscope
SZD	Structure zone diagrams
TCO	Transparent conductive oxide
TE	Thermal evaporation
UV	Ultraviolet (light)
VIS	Visible (light)
W-H	Williamson-Hall
XPS	X-ray photoelectron spectroscopy
XRD	X-ray diffraction